Finite element study of geosynthetic encased stone columns in sensitive soft clay

Author:
Zhang, Rongan

Publication Date:
2009

DOI:
https://doi.org/10.26190/unsworks/22567

FINITE ELEMENT STUDY OF GEOSYNTHETIC ENCASED STONE COLUMNS IN SENSITIVE SOFT CLAY

by

RONGAN ZHANG

Thesis submitted to School of Engineering and Information Technology
University College
The UNSW at ADFA
For the degree of Doctor of Philosophy

August 2009

DEDICATE TO MY FATHER

Your health is my happiness

DECLARATION

I hereby declare that this submission is my own work and to the best of my knowledge it contains no material published or written by another person, nor material which to a substantial extent has been accepted for the award of any other degree or diploma at UNSW or any other educational institution, except where due acknowledgement is made in the thesis. Any contribution made to the research by colleagues, with whom I have worked at UNSW or elsewhere, during my candidature, is fully acknowledged.

I also declare that the intellectual content of this thesis is the product of my own work, except to the extent that assistance from others in the project's design and conception or in style, presentation and linguistic expression is acknowledged.

Signed…………………………………………… Date………………..

Publications and Co-Authorship

Lo, S. R., Mak, J., Zhang, R., (2007). Geosynthetic Encased Stone Columns in Soft Clay. Proc of International symposium on earth reinforcement, Kyushu, Taylor and Francis, 751-756.

Lo, S. R., Mak, J., Gnanendran, C.T., Zhang, R., Manivanan, G., (2008). Long-term performance of a wide embankment on soft clay improved with prefabricated vertical drains. Can. Geotech. J. **45**(8): 1073-1091.

Zhang, R., Lo, S. R., (2008). Analysis of geosynthetic reinforced stone columns in soft clay. Gosynthetics Asia 2008 Proceedings of the 4th Asian Regional Conference on Geosynthetics. Shanghai, China

Lo, S. R., Zhang, R., Mak, J., (2009). Geosynthetic Encased Stone Columns in Soft Clay: A numerical study. Geotextiles and Geomembranes, Accepted.

The above publications are related to Section 5.2 & 5.3 of Chapter 5 in this thesis.

ACKNOWLEDGMENT

The author wishes to express his deepest gratitude and appreciation to his advisor Dr. Sik-Cheung Robert Lo for his guidance, encouragement and continuous support throughout the course of this research. Dr. Robert Lo's unique personality charm, rigorous research attitude, systematic work habits and optimistic attitude toward life benefit the author's academic studies and personal life in both past and future.

Valuable advice and suggestions given by Dr. C.T. Gnanendran are gratefully appreciated. Thanks are extended to Dr. Robert Niven for his sharing his valuable research experience.

Gratefully thanks to the former head of School Dr. Warren Smith for his advice, support and encouragement during the author's personal difficulties.

Special Thanks to Mr. Jim Baxter, Mr. David Sharp for their assistance during laboratory testing. Thanks are extended to the IT service of ACME for their support in providing assistance of using Unix environment of the APAC National facility.

Particular thanks to Mrs Denise Russel and Mrs Elizabeth Shock for their assistance in editing the author's thesis.

Many thanks to the Embassy of China, the educational office of Chinese embassy for their help and encouragement. Exceptional thanks to the former Minister-chancellor Mrs Xiaoyu Zhu for her kindness during the author's personal difficulties.

Thanks are due to the colleagues of the Australia Chinese Student Association for their co-operation, help, and support. Particular thanks to Mr Yong Liu from Wollongong university and Mrs Christine Ling from Tasmania university for their moral encouragement during the past year.

The author would like to thank Mr Dejin Hu, Mr Ovidu Craciun and all other Dr. Robert Lo and Dr. C.T. Gnanendran's students for their friendship and help.

The author want to express his extraordinary thanks to his girl friend Miss Fan Zhang for her love, kindness, understanding and selfless assistance.

The author with heartfelt love wishes to thank his parents, his sister and his two cousin brothers for their concern, solicitude and encouragement throughout the study.

Finally, as the Endeavour Australia Asia Award holder, the author wish to acknowledge the Cheung Kong Endeavour program and the UIPRS scholarship of supporting this research.

ABSTRACT

Some normally consolidated soft soils manifest strength sensitivity, ie these soil manifest strain softening when shear in an undrained mode. These soils, referred to as sensitive soft soils, have the typical features of strain hardening in drained shearing and strain softening in undrained shearing. The consolidation lines of these soils are also curved (concave upwards) in the semi-log space. However, under high consolidation stress or upon large shearing, these soils re-gain the features of re-constituted soil.

Ground improvement methods like stone columns were reported as not effective when installed in the sensitive soft clays. But mechanism of the un-effectiveness of the stone columns remains unknown because of lack of a suitable and simple model for simulating the stress-strain behaviours of sensitive soft soils. Although these soils have a meta-stable micro-structure, models that developed for simulating structured firm soils are not suitable for simulating sensitive soft soil features. Thus, a new model was formulated. The new model can degenerate back to a Modified Cam Clay model.

The ability of new model in simulating a range of behaviour was verified by using the finite difference (FD) method in solving the partial differential equations of the soil model for a range of tri-axial test conditions. The model was further implemented in coupled analysis formulation and coded into FEM program AFENA. Various cases with different soil parameters were then simulated and compared with the FD solutions for various triaxial tests so as to check the stability of the FEM code.

The coupled FEA was then used to simulate the performance of geosynthetic-encased stone columns. A new stone column element and a geo-encasement element were developed and coded into AFENA. The stone column simulations were then done for both non-sensitive soils (represented by Modified Cam Clay model) and sensitive soft soil (represented by the new model). Parametric study was conducted to examine the performance of the geo-encased stone columns in both types of soils. Furthermore, two different installation methods: wished-in installation and full displacement installation were studied numerically.

Cross comparison was done to investigate how the sensitive soft soil features interact with the installation method in affecting the performance of the geo-encased stone columns. A range of factors that influence the geosynthetic-encased stone columns performance installed in soft soils were also made clear.

TABLE OF CONTENT

NOTATIONS

$A(\alpha,\beta,\eta)$	Sensitive Soft Clay function
$[B]$	The strain nodal displacement transformation matrix
C_c	Compression index
C_h	Coefficient of consolidation in the horizontal direction
C_s	Recompression index
d(vol)	Volumatic change of the soil element
$\left[D^{ep}\right]$	The elasto-plastic stiffness matrix.
E	Young's modulus of the soil
G	Shear modulus
J_{2d}	Second invariant of the deviator stress tensor
K	Stiffness of stone
$[K]$	Element stiffness matrix
K_0^{NC}	Coefficient of earth pressure at rest for the normally consolidated state
K_0^{OC}	Coefficient of earth pressure at rest for the over consolidated state
M	Slope of the critical state line in $(q-p)$ space
M^*	Reference slope for the sensitive soft clay yield function
OCR	Over consolidation ratio
P_a	Atmospheric pressure
$P_{y,i}$	Initial yielding stress.
R	Radius of the stone column
S_u	Undrained shear strength
S_{ur}	Undrained shear strength of the reconstituted soil.
S_σ	The enhanced vertical yield stress ratio of the sensitive clay

U_{ex}	Excess pore water pressure
b	Sensitive Soft Clay parameter quantifying the rate of destructuring
c	Cohesion of fill material
e	Current void ratio
e^*	Equivalent void ratio
e_{cs}	Void ratio at unit mean normal pressure on the critical state line of the MCC model
e_i	In-situ void ratio
f	Modified Cam clay elliptical surface defined in the MCC model
f_s	SSC elliptical functional surface defined in the SSC model
k_h	Hydraulic conductivity in the horizontal direction
k_v	Hydraulic conductivity in the vertical direction
p	Mean effective stress on the f surface
p_c	p value at apex value of yield surface
p_{cg}	Apex value of the flue rule of SSC model
q	Deviator stress on the f surface
$\Delta_{y,i}$	Additional voids ratio of Sensitive clay compare to reconstituted clay at ICL condition at the yield point
Δe	Voids ratio difference between the consolidation curve and asymptotic slop ($p \rightarrow \infty$) of the consolidation curve of Sensitive clay at given stress state.
Δe_i	Additional voids ratio of Sensitive Soft Clay compare to re-constituted clay at in-situ condition.
Ψ	Dilation angle of fill material

α	Sensitive Soft Clay parameter that controls strain softening
β	Ratio of M^* / M
γ_s	Saturated unit weight
γ_w	Unit weight of pore water
ε_p^e	Elastic volumetric strain
ε_q^e	Elastic shear strain
ε_p^p	Plastic volumetric strain
ε_q^p	Plastic shear strain
λ	C_c/ln10
κ	C_s/ln10
μ	Poisson's ratio
η	Stress ratio
σ_{ij}	Current stress state on the f surface
σ_1	Maxim principal stress
σ_3	Minor principal stress
$\sigma_{r,s}$	The radial effective stress of soil
$\sigma_{z,s}$	The vertical effective stress of soil
φ_{cs}	Critical state friction angle

LIST OF TABLES

LIST OF FIGURES

CHAPTER ONE

INTRODUCTION

1.1 GENERAL

Constructions on soft clays have presented severe challenges to the geotechnical engineering community in the past decades. The low bearing capacity, high compressibility and the low permeability of the soft clay caused problems for both design and construction. When the soft clay manifests strength sensitivity, the problem may be even severe. Sensitive soft clays often contain meta-stable structure and this structure may provide a high degree of compressibility to the soil.

Soft sensitive clay has the following typical features:

1. the e-lnp line for isotropic consolidation is curved;
2. in drained shearing, the deviatoric stress-strain behaviour is strain hardening; and
3. in undrained shearing, strain softening phenomena may happen.

Thus a sensitive soft clay model is needed to simulate typical features of the sensitive soft soils caused by the meta-stable structure of the sensitive soils.

As the settlement of the sensitive soft clay is significantly high, ground improvement methods are needed. These methods include prefabricated vertical drain (PVD), surface and deep compaction**,** vacuum drainage, preloading, stone columns etc. Among these methods, stone columns method is one of the efficient ways of reducing both settlement and consolidation time.

Reports (e.g., Oh et al. (2007)) have documented that the stone columns are ineffective in reducing the settlement of a trial road embankment. Geosynthetic encasement was proposed (Kempfert et al. (2002), Raithel et al. (2002), Alexiew et al. (2005)) to enhance the performance of the stone columns. Nevertheless, the effectiveness of geosynthetic encased stone columns is relatively unknown especially when the sensitive soft clay is involved. Thus, numerical simulations are applied to examine the effectiveness of geosynthetic encasement stone columns in reducing the long time settlement and the consolidation time.

1.2 OUTLINE OF THE THESIS

The characteristics of sensitive soft clays (SSCs) are reviewed in Chapter 2. Numerical models that can provide hints for developing a suitable model for simulating the SSC behaviours are examined. Ground improvement methods for the soft soils, especially the geosynthetic encased stone column method are also discussed.

A new SSC model is developed in Chapter 3. It can simulate the characteristics of SSCs and can degenerate back to the Modify Cam Clay (MCC) model in situations that the SSC meta-stable structure has been destroyed. Mathematical formulations of the model are systematically described. The method for parameter determination is then presented.

In Chapter 4, the equations for simulating the undrained and drained triaxial tests using the finite displacement (FD) method are developed in an incremental form.

Element simulation of the triaxial tests is performed based on these equations. The implementation of the constitutive model in a fully coupled finite element analysis (FEA) is then described. The finite element solution algorithm is then coded into the finite element program AFENA. The FEA program is then used to simulate triaxial tests numerically. One-dimensional consolidation and multi-layer unit cell consolidation simulation are then conducted in order to check the numerical stability of the FEM code.

In Chapter 5, unit cell analysis of an embankment on soft clay improved by “wish-in” stone columns is presented for two different constitutive models, the MCC and the SSC. New elements are developed to simulate the geosynthetic encased stone columns. Locked-in strain of geosynthetic encasement is also simulated by using the new stone columns element. Parametric studies are also conducted to examine the effects of lower stone stiffness and reduced locked-in strain of the geosynthetic encasement.

Chapter 6 presents numerical simulation of the full displacement stone column installation method. The installation method is idealized by cavity expansion analysis.

Chapter 7 presents the numerical simulation of an embankment on soft clay improved by stone columns being installed by the full displacement installation method. The effective stress changes and excess pore water pressure from cavity expansion analysis of Chapter 6 are used to establish the input initial stress states.

Analyses is conducted with the same set of soil parameters as those used in Chapter 5. The only difference is a different installation method being simulated.

Chapter 8 presents an overall synthesis of the findings of Chapter 5 and Chapter 7. The focus of this chapter is to compare the geosynthetic encased stone column performance of the two installation methods. Detailed explanations are provided of the circumstances under which the geosynthetic encased stone columns can work efficiently.

Chapter 9 presents the conclusions drawn based on the simulations and discussions in the previous chapters. Recommendations for future work are made following the conclusions.

CHAPTER TWO

LITERATURE REVIEW

2.1 INTRODUCTION

Due to their low bearing capacities and high compressibility, soft soils are known as problematic soils and remain at the pioneering edge of geotechnical research. Normally, when embankments are constructed on soft clay foundations, different soil improvement methods are used in order to increase their bearing capacity and reduce settlement as well as consolidation time. The Mohr-Coulomb and MCC models have been widely used by geotechnical engineers over the past several decades to predict the deformation of soft clay foundations on which embankments are constructed. However, these predictions may be far from accurate, especially when the soft clay structure has a high sensitivity which can cause the construction design to be unsafe and millions of dollars to be wasted.

Reinforcement methods have been widely used in soft soil improvement to reduce uncertainty in the prediction of a soft soil foundation. However, the effects of the reinforcement, under particular drainage conditions and the subsequent embankment construction, have still not been fully addressed. Meanwhile, disturbance introduced into the field by installing stone columns and PVDs (prefabricated vertical drains) can cause combined effects that make a prediction even more unreliable.

In this chapter, the characteristics and behaviours of soft soil are examined. Relevant constitutive models of soft clay and structured soil are reviewed. Construction effects, especially the disturbance caused by the installation of reinforcement and improvements, are considered. Current testing methods and the effects of parameter determination for soft soil models are discussed.

The objectives of this chapter are to: provide an overview of current research into, and engineering methods applied to, soft soil improvement and the prediction of a soft soil foundation on which an embankment is constructed; and point out the significant importance of considering soft soil sensitivity in engineering designs for soft soil.

2.2 TERMINOLOGY

Depending on their sources, soils can be divided into three types: re-constituted, natural and remoudeled.

a) Reconstituted soil

As defined by Burland (1990), a reconstituted soil is one that has been thoroughly mixed at a water content equal to, or greater than, the liquid limit. Based on studying the properties of reconstituted soils or artificial materials such as Kaolinite, the Cam Clay framework was formulated elegantly by Roscoe and Burland (1968). This framework, known as the Cam Clay model, and later on the Modified Cam Clay

(MCC) model, has been widely used over past decades for the solutions of the engineering problems.

b) Natural soil

Although there is no common definition of a natural soil, it is generally accepted that it refers mainly to a soil that has been formed and developed in the field. These soils are generated by the long and complex chemical and mechanical processes of the natural environment. These processes normally including erosion and deposition by air and water, and they formulate different micro- and macro-structures differ from reconstituted soils. Thus, the MCC model, which was originally formulated by studying the behaviours of reconstituted soil, is unsuitable for simulating the natural soils. Details of the influence of a natural soil's structure will be explained in the next section.

c) Remoulded soil

When natural soil is sharing to a great extent, it is believed that the structure of the natural soil will be destroyed. At this time, the destructed natural soil is called remoulded soil. As the remoulded soil behaves similar with the reconstituted soil, its behaviour can be simulated by the MCC model which is intended to simulate the behaviour of reconstituted soil.

2.3 BEHAVIOUR OF SOFT SOILS

2.3.1 Structure of soil

Soil structure is defined as the arrangement of the solid parts of a soil and the pore space located between them (Marshall and Holmes 1979). Performances of soils vary significantly depending on how they are structured. While the structure of a soil is mainly dependent on from what it is developed, the environmental conditions under which it is formed, the soil's effective stress history, the organic materials present, etc. (Leroueil and Vaughan 1990).

The term "structure", as defined by Lambe and Whitman (1969), is the combination of the "fabric", the arrangement of the component particles and the "bonding", which is defined as those inter particle forces which are not of a purely frictional nature. A soil structure has been thought to be the result of a combination of factors, such as mineralogy, water chemistry during deposition, temperature, organic content, stress history, etc. Thus, the structure of a natural soil depends on the physical and chemical conditions that applied during the formation of the clay, which includes ageing, consolidation, loading and unloading, etc.

Burland (1990) introduced the term "intrinsic" to describe the properties of a reconstituted soil produced at a water content of 1.0 to 1.5 times the liquid limit and then consolidated under one-dimensional conditions. The intrinsic properties of reconstituted soils are those which can be captured by critical state soil mechanics. Thus, in this thesis, the term "structure" is simplified (Liu and Carter 1999) to include all the features of a natural soil that are different from those of a corresponding reconstituted soil.

Because of the structure of soils, the consolidation curve of a structured soil is normally above that of a corresponding remoulded soil. The characteristic of the consolidation curve of a structured soil is similar to that of a sensitive soft soil after yielding.

As most structured soils are over-consolidated, the OCR (over-consolidation ratio) affects their peak shear strengths. Based on an observation by Ladd and Foot (1974), the logarithm of undrained shear strength, S_u, normalized by the vertical consolidation stress, σ_v, plots linearly against the logarithm of the OCR, that is:

$$S_u/\sigma_v=K*OCR^N \quad (2\text{-}1)$$

where K and N are constants that, respectively, depend on the soil and the loading used to shear the soil.

Strain-softening phenomena can also happen in structured soils, but the mechanism involved is different from that of sensitive soft soils. From the above equation, it is clear that, when a soil is over-consolidated, its strength-softening is highly dependent on the OCR and the corresponding parameter, N. So, for an over-consolidated soil, strain-softening is the procedure of estimating the effects of over-consolidation during continuous shearing.

For soils with high OCRs, the process of strain-softening in an undrained test, as described by Liu and Carter (2002), is:

1. the soil is regarded as elastic for loading inside the yield surface;

2. when the current stress state reaches the yield surface, the soil begins yielding; and
3. then, when the soil reaches the yield surface with $\eta > M$ and the boundary conditions allow appropriate adjustment of the stress state, either strain softening or catastrophic failure occurs.

In this procedure, two particular important points which should be emphasized are:

1. strain softening occurs only when the stress path crosses the critical state line ($\eta > M$); and
2. the yield surface shrinks with the current stress when strain softening occurs.

Thus, the p, q curve of an undrained strain-softening path looks like that in Figure 2-1(a). It is clear that strain softening of the over-consolidated soil occurs on the left side of the critical state line.

2.3.2 Sensitive soft soil

Unlike normal structured soil, sensitive soft soil contains honeycomb structures (Shogaki 2006) that weaken its strength and make it very compactable compared with the corresponding remoulded soil. For example, Hongkong Marine Clay(Lumb and Holt 1968), Singapore Marine Clay (Pitts 1983), Canadian Batisan Clay (Leroueil et al. 1985), Canadian Sackville Silt Clay (Kerry et al. 1996), and Japan Ariake Clay (Shogaki 2006; Hong et al. 2006) have significantly higher C_v values and are much more compactable than the corresponding remoulded soils.

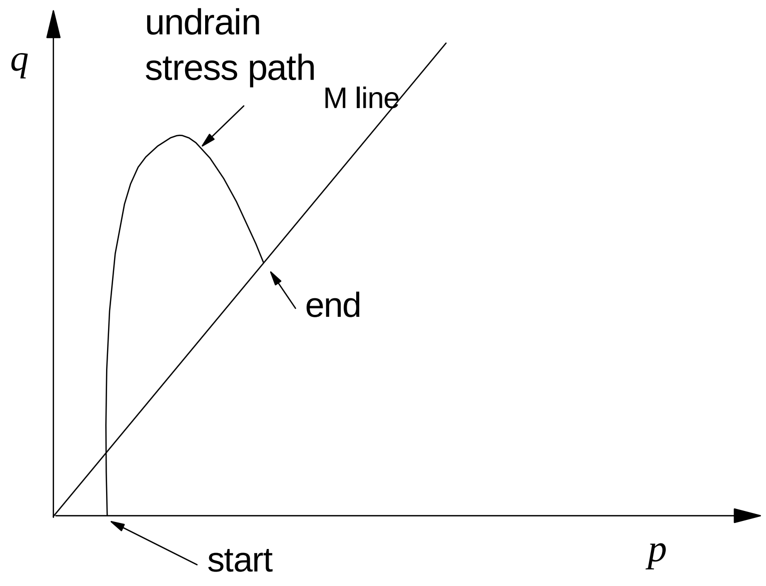

Figure 2.1(a): Undrained stress path of over-consolidated structured soil

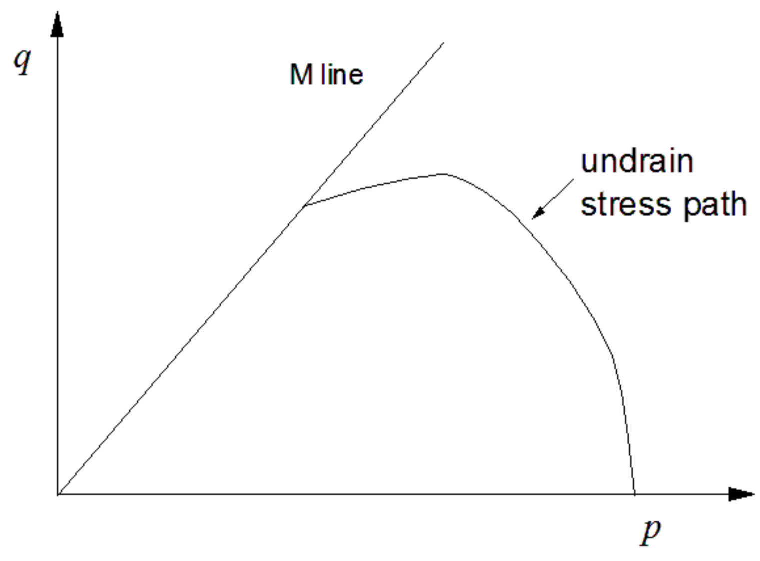

Figure 2.1(b): Undrained stress path of sensitive soft soil

The honeycomb structure of sensitive soft soil is very unstable and easily disturbed. When it is disturbed, its undrained shear strength decreases while its drained shear strength increases. Unlike a structured soil, its undrained stress-strain path is on the right side of the critical state line, as shown in Figure 2-1(b).

a) Soil sensitivity

Soil sensitivity is described as the degree to which a sensitive soft soil is structured compared with a reconstituted soil of the same soil material. Due to Leroueil and Hight (2002), this degree is classified in terms of strength sensitivity and stress sensitivity.

The undrained shear strength of a soil is defined as its maximum strength at the point at which yielding occurs due to the shear stress in the soil. In critical state soil mechanics, the shear strength means the stress state in the critical state in which plastic shearing could continue indefinitely without changes in the volumetric effective stress. But, for a structured soil, the peak value of its shear strength may occur before the stress state reaches the critical state. This phenomenon is caused by dilation of the soil, and the natural fabric of the soil must be destroyed in order to reach the state of constant volume shearing. The ratio between the pick strength of a soil and the strength of its corresponding reconstituted soil is defined as the undrained strength-sensitive rate and is written as:

$$S_t = \frac{S_u}{S_{ur}} \tag{2-2}$$

where S_u is the undrained shear strength of the undisturbed sensitive soft soil and S_{ur} is the undrained shear strength of the reconstituted soil. S_t reflects the enhanced resistance of the soil structure in sensitive soft soil and can be determined by vane shear tests.

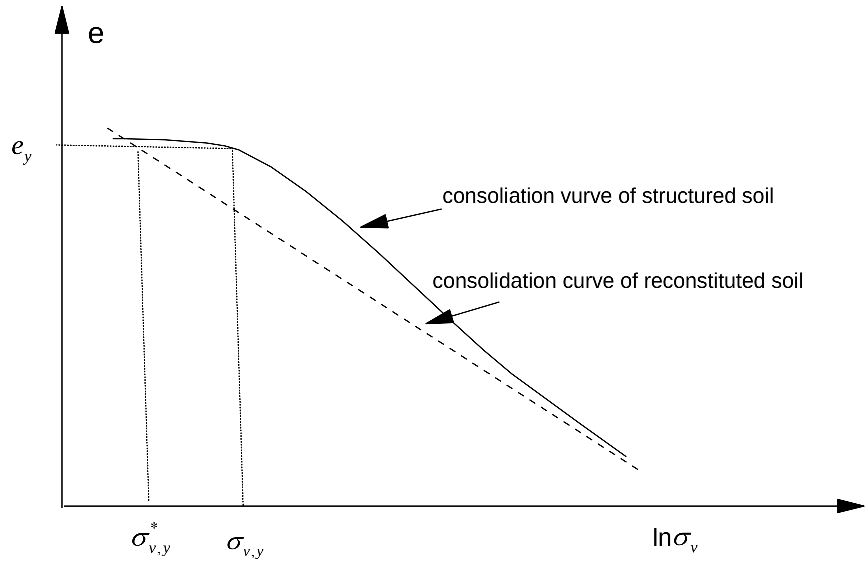

Figure 2.2: Consolidation curve of structured soil and corresponding reconstituted soil

As shown in Figure 2.2, the stress sensitivity (which is also referred to as the vertical stress OCR), as defined by Cotecchia and Chandler (2000), is the ratio of the vertical yield stress, σ_{vy}, of the sensitive soil to the vertical equivalent yield stress, σ_{vy^*} on the reconstituted soil consolidate to same void ratio.

$$S_\sigma = \frac{\sigma_{vy}}{\sigma_{vy^*}} \tag{2-3}$$

S_σ reflects the enhanced vertical yield stress ratio of the sensitive soil. Chang et al. (1997) and Chu et al. (2002) conducted studies of in-situ tests for estimating the S_σ value.

In a wider sense, sensitive soft soil belongs to the class of structured soils. However, in this thesis, it differs from normal structured soils in that:

1. it is normally consolidated or only slightly over–consolidated;
2. it has a honeycomb structure which cause high compressibility of the soil; and
3. strain softening on the undrained conditions and strain hardening in the drained conditions.

b) Undrained strain-softening feature

Both structured and soft sensitive soils have the feature of strain softening in undrained conditions. But, as mentioned above, a structured soil can experience strain-softening behaviour only when its OCR is high. The differences between strain softening of normally consolidated and highly over-consolidated soils are that, in the former:

1. strain softening occurs below the critical state line ($\eta < M$);
2. the yield surface does not need to shrink when strain softening occurs; and
3. structured soil also experiences strain softening in drained conditions whereas sensitive soft soil does not.

For sensitive soft soils, strain softening in undrained conditions occurs on the right side of the M line. We define it as “wet” strain softening (and, therefore, call the soil “wet” sensitive soil) to differentiate it from the normal strain-softening phenomena.

2.3.3 Review of existing constitutive models for structured soil

Unfortunately, previous research, including testing and numerical simulation, has not focused on the differences between the two types of strain-softening behaviours of structured and sensitive soft soils. The constitutive models generated to predict structured soils did not consider “wet” softening. Nevertheless, since sensitive soft soil behaves similarly to structured soil in isotropic consolidation after yielding, the constitutive models for structured soil will be examined.

The e-lnp plot of reconstituted soil is normally considered as a straight line while that of natural clay as a curve above the straight line of the reconstituted soil of the same soil material. As simplified by Burland (1990), the differences between natural and reconstituted soils are considered to be due to the “influence of the soil structure”. Since the e-lnp curve of a natural soil is above that of a reconstituted soil of the same soil type, at a given stress, the natural soil has a higher void ratio than does the reconstituted soil and, at a given void ratio, the stress of the natural soil is also higher than that of the reconstituted soil. Thus, apparently, the structured soil models can be divided according to whether they employ a stress sensitivity approach or an extra void ratio approach.

Since the differences between a natural clay and a reconstituted soil are considered to be due to "structure" effects, these models can be further divided by considering the plastic strain of the natural clay as a whole or by separating the effects of the plastic strain of the reconstituted soil and considering the "structure" effects separately.

a) Yield ratio approach

i) Damage strain approach

When taking the soil strain of a natural soil as a whole, most of these models introduce a concept of a damage-type mechanism (Nova 1977) which permits the reduction of the yield surface to bond degradation.

Cotecchia and Chandler (2000) proposed a yield ratio framework which used sensitivity as a means of quantifying structure in both volumetric and stress spaces for test data from Papadai clay. Within this framework, the behaviours of a natural clay can be described by its state, stress history and soil yield ratio only. Cotecchia (2003) pointed out that the soil yield ratio reduces with reductions in the plastic strain. Baudet and Stallebrass (2004) tried to adopt the yield ratio framework to describe the de-structuration of a soil structure by using soil sensitivity to represent the current structure during degradation.

In Baudet and Stallebrass's model (2004), the term "damage strain", which is defined in equation 2-4, is introduced, by assuming that the plastic volumetric strain and the shear strain have the same influence on degradation, as:

$$\delta\varepsilon^{d} = \sqrt{\delta\varepsilon_{p}^{p2} + \delta\varepsilon_{q}^{p2}} \qquad (2\text{-}4)$$

where $\delta\varepsilon_p^p$ and $\delta\varepsilon_q^p$ are increments of the plastic volumetric strain and the shear strain respectively for a given increment of stress.

The relationship of the increment of damage strain and the decrement of sensitivity are defined as:

$$\frac{\delta yr}{yr-1} = \chi \delta\varepsilon^d \qquad (2\text{-}5)$$

where yr is the yield ratio and χ is a factor of proportionality that is always negative.

The soil yield ratio and damage strain are combined with the MCC hardening rule to govern variations in the size of the sensitivity surface and form a destructuralization law as:

$$\delta yr = -\frac{k}{\lambda-\kappa}(yr - yr_f)\delta\varepsilon^d \qquad (2\text{-}6)$$

where λ and κ are the compression parameters, yr and yr_f are the sensitivity and the ultimate sensitivity in high confined stress.

A similar mechanism was also used in Postor's (1990), Kavvadas's (1995), Nova's (1995), Chazallon's (1998), Cotecchia and Chanler's(2000), and other models.

ii) Sub-loading approach

Some models consider the "structure" effects and inherent constitutive soil effects separately. These models include anisotropic models which have two yield surfaces based on the concept of sub-loading.

Wood (2000) adopted his bubble model framework (Wood 1989) for the extension of the MCC model to describe stiffness degradation with strain for over-consolidated clays. In that model, three surfaces were introduced, namely, the reference surface, the bubble surface and the structure surface.

All these surfaces have the same elliptical shape as the MCC model. The reference surface is the same as the MCC one, in that it describes the intrinsic behaviour of reconstituted soil. The bubble, which encloses the elastic domain, moves around with the outer surface following a kinematic hardening rule. The structure surface controls the process of de-structuration though its interaction with the bubble can simulate strain-softening effects during de-structuration.

Other models, like those of Asaoka (2000), Pedroso (2005), Callisto and Gajo (2002) and Noda (2005), can also be considered as they have similar formations, being based on the MCC model with the sub-loading concept.

b) Void ratio approach

i) Double logarithmic method

Butterfield (1979) studied the compression and consolidation characteristics of natural soil by adopting the double logarithmic method, that is, by assuming that the relationship between the void ratio and the mean effective stress is linear in the $\ln(e+\Delta)$ -lnp plot. Chai (2004) used this simplified relationship and incorporated it into the MCC model by modifying the hardening law of the model.

Numerical results presented by Chai (2004) showed that applying the double logarithmic hardening equation can simulate consolidation behaviour better than can the traditional e-lnp relation. This model is simple to use and easy to code in FEM by modifying the cam clay hardening law. But, normally, the $\ln(e+\Delta)$ -lnp relation is far from linear so this simple model finds it difficult to describe the de-structure process of natural soil.

ii) Extra void ratio approach

Oedometer tests (eg., Mesri 1975; Locat 1985) on both natural and reconstituted soils showed that natural soil has a higher void ratio than does reconstituted soil of the same soil material at the same stress state. Liu and Carter (2000, 2002, 2003), Liyanapathirana (2005), Hong (2006) and others developed models by considering the plastic strain of reconstituted soil and its “MCC part”, then adding extra terms into the MCC hardening function and, finally, twisting the MCC flow law to describe the “structure effects”.

Since Liu and Carter (2000, 2002, 2003) developed a series of models based on this extra void ratio approach, their models are explained here as examples.

In Liu and Carter’s model, the material idealization of the isotropic compression behaviour of a structured clay is illustrated in Figure 2.3. In this figure, e represents the void ratio for a structured clay, e^* is the void ratio for the corresponding reconstituted soil at the same stress state during virgin yielding, $p_{y,i}$ is the mean effective stress at the initial point of virgin yielding, and Δe is the difference in the void ratios between a structured soil and its corresponding reconstituted soil at the same stress. Thus:

$$e = e^{*} + \Delta e \qquad (2\text{-}7)$$

Liu and Carter (2000) proposed the following equation to describe the volumetric behaviour of structured soil during virgin isotropic compression.

$$e = e^{*} + \Delta(\frac{p_{y,i}}{p_c})^{b} \qquad (2\text{-}8)$$

in which Δ is the additional void ratio of p_c = $p_{y,i}$ and b is the parameter quantifying the rate of destruction and is referred to as the de-structuring index.

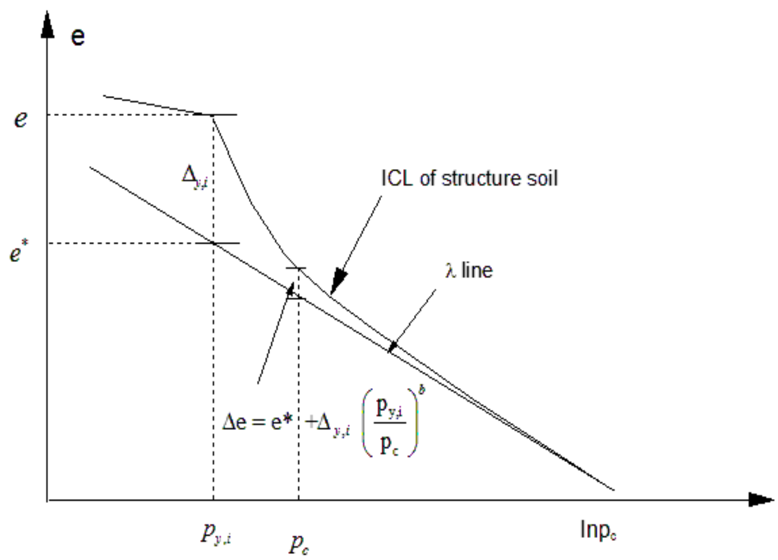

Figure 2.3: Isotropic consolidation curve of structured soil

In Liu and Carter's model, elastic behaviour and virgin yielding behaviour are divided by the soil's current yield surface and are described by the following yield function as:

$$f=(\frac{q}{0.5M\times p_c})^2+(\frac{p-0.5p_c}{0.5p_c})^2-1=0 \tag{2-9}$$

Following Schofield and Wroth's (Schofield and Wroth 1968) cam clay framework, virgin compression can be divided into two parts: elastic, which is dependent on the current mean effective stress; and plastic, which is dependent on the size of the current yield surface as:

$$d\varepsilon_V^e=k\frac{dp}{(1+e)p} \tag{2-10}$$

$$d\varepsilon_p^p=(\lambda-\kappa)\frac{dp_c}{(1+e)p_c}+b\Delta e\frac{dp_c}{(1+e)p_c} \tag{2-11}$$

In the MCC model, the associate flow law is assumed in order to apply a non-associate flow law. In Carter and Liu's (2002) paper, a new parameter, ω, which describes the influence of a soil's structure is introduced. The relationship of the shear plastic strain and the volume plastic strain is shown as:

$$\frac{d\varepsilon_q^p}{d\varepsilon_p^p}=\frac{2(1-\omega\Delta e)\eta}{M^2-\eta^2} \tag{2-12}$$

Parameter ω, when associated with parameters b and Δe, can successfully help the model simulate strain softening in undrained conditions when the soil is highly over-consolidated but, due to the limitation of the framework, the model cannot simulate "wet" strain-softening behaviour.

c) Other approaches

Konrad and Ayad (1997) firstly developed an idealised model and, later, a software called "CRACK" to simulate the destruction of a structured soil. Prasad (1998) modified the yield criteria by considering the microstructure of a natural soil. Kavvadas (2000) developed a model focused on the de-structuring process of highly over-consolidated structured soils. Hu and Pu (2004), Masia (2004) and Santagata (2005) applied empirical equations from oedometer and triaxial tests. Chen and Tang (2004) applied the moving boundary concept for the numerical solution of one-dimensional consolidation. Liu (2007) further extended his model by applying the sub-loading concept into the extra void ratio approach. Hawlader (2008) assumed the e-lnp relationship to be state-dependent.

These methods and models have contributed to the understanding of the structure phenomena and the simulation of natural soils. But all these models have two inherent disadvantages that prevent them from being able to simulate typical sensitive soil behaviour:

1. Although some of these models can simulate strain softening in undrained conditions, they can only simulate the strain softening of over-consolidated soil and are not suitable for simulating strain softening in "wet" sensitive clay.

2. These models need the yield surface to shrink in order to achieve strain softening. Thus, they cannot simulate typical sensitive soil phenomena, that is, simultaneous strain softening in undrained conditions and strain hardening in drained conditions.

d) Other strain softening models

Besides some of the structured soils models discussed have the ability of simulate the strain softening behaviour, a lot of sand models and creep model also can simulate strain softening. In this section, typical strain softening of san models and creep models are discussed in order to provide hints for modeling the sensitive soft soils.

Depends on the density, the sand can also experience strain softening behaviour (Chu and Lo (1992)). By twisting the Cam Clay flow rule and fitting the deviatoric stress and strain relationship curve with sand parameters, these models (Wood and Belkheir 1994; Yamamuro and Lade 1998; Thevanayagam and Mohan 2000) can simulate the strain softening of sand. But these models are difficult to be twisted to simulate the strain softening behaviour of sensitive soil because the sensitive soils have a typical curved e-lnp relationship and the sensitive soil eventually behave similar as the MCC when $p \rightarrow \infty$.

Some of the creep models (Adachi et al. 1998, Adachi and Oka, 2005) can also be applied to simulate the strain softening behaviour. These models are adopting the overstress theory (Perzyna 1963) to establish a constitutive framework to model the destructing of soil with time-dependency. Similar as the structure soil models discussed above, these models are also difficult to be twisted to simulate the typical sensitive soft soil features addressed in the previous section. In addition, applying Perzyna's (1963) overstress theory on simulating the destructing of the sensitive soft soil is unnecessary complicated.

2.4 GROUND IMPROVEMENT USING STONE COLUMNS

In the past few decades, various ground improvement methods have been used to improve the performance of soft soil, including: permeable vertical drains (PVD) (Hird et al. 1992; Indraratna and Balasubramaniam 1994; Bergado et al. 2002; Chu et al. 2004); stone columns (Barksdale and Bachus 1983; Murugesan and Rajagopal 2006; Wu and Hong 2008); vibro compaction (Baumann and Bauer 1974); vacuum pre-loading (Yan and Chen 1986; Chu et al. 2000); and deep soil mixing (Suzuki 1982; Bruce 1996).

The main function of PVD and vacuum pre-loading is to accelerate the rate of consolidation while the main function of deep soil mixing is the use of chemical agents to stabilize soft soils.

Stone columns can increase the bearing capacity of a soil and reduce the consolidation time and total settlement of an embankment (Mitchell and Huber 1985; Greenwood 1991; Watts 2000). The stone columns act as drains and consolidation settlements are accelerated and post construction settlement are minimized. When loads are applied on the soils reinforced with stone columns, a large portion of the total load is initially resisted by the relatively strong stone columns which are far more rigid compared to the surrounding cohesive soil. The remainder of the load is carried by surrounding soils. As the consolidation process continues, variations in the sharing of the total applied load between the stone columns and the soils takes place and the potion of load transferred from soils to the stone columns.

Despite the advantage of the stone column in the ground improvement, the stone column also has some obvious disadvantages thus as the installation of stone column cause disturbance to the surrounding soil and generate excess pore water pressure in the soils. Meanwhile, bulging failure may happen in the stone columns when the surrounding soil cannot provide enough support to the stone columns installed.

Thus the effectiveness of stone column method highly depends on the installation method and the soils that it is installed in. McKenna et al. (1975) reported cases in which stone columns installed in very soft clay were not restrained by the surrounding soil. This caused excessive bulging and led to the surrounding soft soil being squeezed into the voids of the aggregate (Garga and Medeiros (1995)). Oh et al. (2007) reported that the observed settlement of a trial embankment built on very soft sensitive clay being strengthened with stone columns indicated that the stone columns alone were not sufficiently effective in reducing settlement. This is because the strength and stiffness of a stone column is dependent on the effective stress confinement offered by the surrounding soils (Huges et al. 1975). As pointed out by

Black (2006), in weak deposits the lateral support is significantly low and the very soft clay cannot provide adequate confining stress to the stones.

To increase the lateral support for stone columns, an alternative system called "Geosynthetic Encased Stone Columns" (GESC) was introduced by Kempfert et al. (2002) and Raithel et al. (2002). The GESC uses a high modulus and a creep-resistant geotextile encasement that confines each compacted stone column, thereby increasing the bearing capacity of the stone columns and reducing the settlement of the construction. Moreover, the stone column tend to tense out the geo-synthetic encasement as the more load transferred to the columns during the consolidation process. Thus the geo-synthetic encasement can provide more confining stress to support the stone columns. A construction system utilising high stiffness and creep-resistant geotextiles for encasing stone columns is described in Alexiew et al. (2005).

The benefits of using geosynthetic to encase or wrap geomaterials are well-illustrated in studies on soil bag pile by Lohani et al. (2006). Murugesan and Rajagopal (2006) presented an axi-symmetric unit cell analysis to demonstrate the effectiveness of geosynthetic encasement in improving the performance of a stone column functioning as a single pile. However, as the surrounding clay was characterised by a non-linear elastic model, this makes it difficult to relate the computed results to the actual time-dependent performance when the stone columns act as reinforcements.

Murugesan and Rajagopal (2007) presented 1g-model test results to demonstrate the effectiveness of geosynthetic encasement in enhancing the axial load capacity of a short stone column under short-duration loading. However, the inherent scale effect and the rather atypical clay parameters reported (for example, the clay had a vane shear strength of 2.5 kPa at 47% moisture content) make it difficult to translate the findings to a field problem.

Wu and Hong (2008a) presented laboratory test results on geosynthetic encased granular columns in triaxial testing which showed that, at a low column strain of about 1% in the axial direction, the improvement due to geosynthetic encasement was several times less than that at the maximum test load. An alternative approach to the reinforcement of a stone column, by the inclusion of horizontal geosynthetic sheets at close intervals, was studied by Wu and Hong (2008b).

The studies discussed above focused on the performance of a stone column as a pile, i.e., with external load applied only to the column top not to the surrounding soil. As pointed out by Alexiew et al. (2005), the use of a large number of stone columns to enhance the ability of a soft clay layer to support a fill embankment involves complicated interaction mechanisms. The embankment weight was shared between the stone columns and the soft clay, in accordance with their relative stiffness values, and both were affected by the effective stress of the surrounding soft clay which changed with consolidation.

Numerical simulations of conventional stone columns had been done by Han and Ye(2001), Castro and Sagasetta(2008), Xie et al. (2009), etc. Han and Ye(2001) developed a simplified solution to demonstrate the relationship of the soil settlement and the ratio of stiffness of the stone column and soil. Castro and Sagasetta(2008), Xie et al. (2009) focus on the disturbed soil zone caused by installation methods.

Murugesan and Rajagopal (2006 and 2007) performed model tests and numerical analyses to study the behavior of a single geosynthetic-encased stone column without considering the behavior of the interface between different materials and long time coupled mechanism between stone column and the soils. M. Khabbazian et al(2009) use commercial program ABAQUS to check the bulging and Hoop tension force of the geosynthetic encased stone columns, but the simulation can not reflect the confining stress generated by the geosynthetic encasement during the consolidation process.

2.5 INSTALLATION TECHNIQUE

Stone column installation methods can be classified as the “replacement method” and the “displacement method”. Replacement means that the soil is removed from the hole and replaced by the stones. Displacement means that the soil is pushed out laterally and the stone feeds in.

The commonly used installation techniques in engineering practice are the vibro technologies in which vibro stone columns are implemented by using either rig-mounted or crane-mounted vibratory probes. Vibration, compaction and displacement are achieved by an eccentrically mounted weight.

The installation method chosen depends on the design requirement and ground conditions. The stone columns are installed using either top- or bottom-feed systems, either with or without jetted water. The top-feed method is used when a stable hole can be formed by the vibratory probe. At the site of a sensitive soil ground condition, the hole will collapse or partially collapse when the vibratory probe is retracted. The bottom-feed method mounts a pipe by the side of the probe to allow the stone to be perfused at the bottom of the hole with the probe staying inside the hole.

The wet method involves jetting in water as the probe penetrates to the full depth from the side of the probe and then replacing the surrounding soil with the jetted-in water. The stones are then pumped in and replace the water. The function of the water is to maintain a stable hole and increase the diameters of the stone columns, especially when the stone columns are installed in a weak deposit and the hole is easily capable of collapse. This method is mainly used for installation of large stone columns and significant efforts are required to manage its generated run-off, especially in environmentally sensitive areas.

When special efforts are addressed in the installation, the "replacement method" causes less disturbance to the soils when the stone column is installed. Techniques have been developed in the laboratory that cause less disturbance to the soils during installation. A construction procedure using this method is proposed by Ambily and Gandhi (2007) and is explained as follows:

1. a thin, open-ended seamless steel pope casement with a geosynthetic right inside is assumed to be pushed into the soft soil until it reaches the

bottom.(Slight grease is applied on both the inner and outer surfaces for easy penetration and withdrawal without creating any significant disturbance);

2. the soil inside the encasement is removed and replaced with stone;
3. the pipe casement is raised in stages ensuring that the bottom of the casement is below the top level of the placed stone gravel. Compaction is applied to achieve a uniform density of the stone columns and provide enough pre-strain of the geosynthetic encasement; and
4. procedure 3 is repeated until the column is completed to its full height.

Ambily and Gandhi (2007) claimed that the disturbance caused by the above “replacement” procedure would be very small, at least in laboratory conditions. This idealized “replacement” installation method can be regarded as the “wish-in” installation method if extremely careful work has been done.

CHAPTER THREE

DEVELOPMENT OF SENSITIVE SOFT CLAY MODEL

3.1 INTRODUCTION

Sensitive soft clays (SSCs) behave differently from clays in a reconstituted state which the MCC model has been widely used to simulate. Among these behaviours, SSCs show strain softening in undrained shearing but strain hardening in drained shearing. This phenomena is attributed to the meta-stable structure of SSC. Several constitutive models (Liu and Carter 2002; Baudet 2004) have been developed to simulate "structure phenomena" of structured soils. These models are not suit for sensitive soft clay as been discussed in Chapter 2.

The SSC model introduced here can simulate the strain softening behaviours of both "wet" and dry side in the undrained shearing without shrinkages of the yield surfaces while simulating the strain hardening behaviours of the same soils in drained shearing.

The Isotropic Consolidation Line (ICL) of SSC is quite similar with the structure soil described in Chapter 2. Unlike MCC, the ISL of SSC is a curve in the e-logp space. The void ratio of SSC is higher than the corresponding re-constituted soil at the same stress state. The void ratio difference is due to the meta-stable structure of the SSC. When the meta-stable structure of a sensitive soft clay is destroyed, say due to high stress or shearing, the SSC will eventually behave similar as the reconstituted clay. So the SSC model is formulated in a way that can degenerate back into the MCC model when the meta-stable structure influence is negligible. Therefore, in the SSC model, all the physical meaning of the MCC parameters are the same as they are in the MCC framework.

This chapter provides mathematical description of the SSC model. Function of each parameters and reasons for these parameters or functions chosen are explained in details. Methods for determining of the model parameters are also provided in this Chapter.

3.2 MATHEMATICAL DESCRIPTION OF THE SENSITIVE SSC MODEL

3.2.1 Examine prerequisite conditions for modelling strain softening of wet sensitive clay in critical state framework.

In order to achieve a model that can be used to simulate the strain softening character of wet sensitive clay, the following prerequisite conditions are examined.

Firstly, the non-associate flow rule is needed because the $f = g$ condition suppresses deviator strain softening unless the shrinkage of the yield surface with hardening is permitted. Therefore, the strain-hardening response in drained shearing implies that shrinkage of the yield surface with hardening should not be permitted. Thus, according to the associate flow rule, strain hardening in drained conditions and strain softening in undrained conditions will not happen.

Secondly, suitable yield loci, for simulating undrained strain softening, need to be introduced. Yield loci like those of MCC will guarantee there's no strain softening in the "wet" part of the soil in undrained conditions.

The yield loci of the MCC model is:

$$(1+\frac{q^2}{M^2 p^2})p = p_c \qquad (3\text{-}1)$$

in which p is the mean effective stress, q is the deviator stress, M is the slope of the critical state line in (q–p) space and p_c is the yield surface apex value.

The definition of the stress ratio is:

$$\eta = q/p \qquad (3\text{-}2)$$

The differential from equation (3-1) is:

$$\frac{2\eta}{M^2}dq = \left(\frac{\eta^2}{M^2}-1\right)dp + dp_c \qquad (3\text{-}3)$$

in which dq, dp, dp_c are the differential vectors of q, p, p_c.

In undrained conditions, dp is a negative value. When in the "wet" part, $\eta < M$. Thus, $\left(\frac{\eta^2}{M^2}-1\right)dp > 0$.

If the yield surface is not allowed to shrink, then $dp_c \geq 0$. Thus $dq > 0$.The strain softening phenomena won't occur in the "wet" part if the yield surface does not allow to shrink. Thus, to simulate the SSC features, non-associated flow rule and a different yield loci are essential.

3.2.2 Assumptions

Given the discussion above, the following six general assumptions are made for the SSC model.

1. The ICL line of SSC shown in Figure 3.1 is, obviously, not a straight line in the e-lnp plane. It is located above the ICL line of the re-constituted soil refer to as the λ line .

At a given mean effective stress, p, a corresponding void ratio, e, can be determined from the ICL line and written as:

$$e = e^* + \Delta e \qquad (3\text{-}4)$$

in which e^* is the corresponding void ratio on the λ line at the same mean effective stress, *p,* and Δe is the difference between the void ratio of the ICL and the λ line at the same mean effective stress, *p*. The Δe value corresponding to the yield point $p_{y,i}$ is defined as $\Delta_{y,i}$.

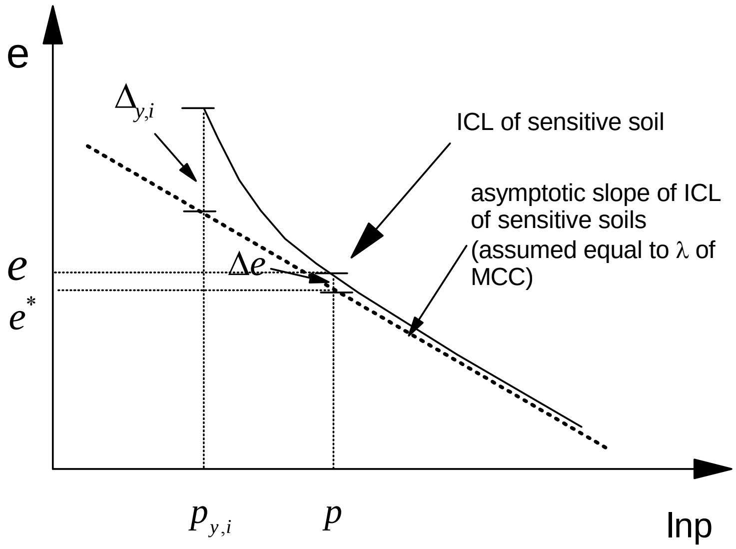

Figure 3.1: Isotropic consolidation curve of SSC

As shown in Figure 3.1, during the consolidation process, Δe decreases from $\Delta_{y,i}$ with increases in p from $p_{y,i}$ and, eventually, tends towards zero with $p \to \infty$ in isotropic consolidation.

2. Upon large shearing, the behaviour of SSC merges back to that of re-constituted soil, which we assume conforms to the MCC model, which has been widely used, as described in the literature on re-constituted soils. Meanwhile, when the difference between the SSC and the re-modelled soil is negligible, eg., $\Delta_{y,i} \approx 0$, the SSC model should approach the MCC model.

3. Critical State: the key concepts of critical state are the same as those of the MCC model.

4. Plastic Potential: The same plastic potential functional as that of MCC model. The MCC plastic potential is chosen because it is derived based on plastic energy dissipation that satisfies the constraints of critical State.

5. The modelling of elastic strain component is identical to MCC.

6. As discussed in section 3.2.1. Non associate flow rule and a suitable yield function that can simulate the strain softening behaviour in the "wet" part without the shrink of yield surface are needed.

3.2.3 Ingredients of the Sensitive Soft Clay model

a) Elastic properties

Based on the assumption 5, the recoverable changes in volume accompanying with any changes in the mean effective stress p and the recoverable shear strains accompanying any changes in the deviator stress q can be expressed by the following equations:

$$d\varepsilon_p^e = \kappa \frac{dp}{(1+e)p} \tag{3-5}$$

$$d\varepsilon_q^e = \frac{dq}{3G} \tag{3-6}$$

in which ε_p^e is the elastic volumetric strain; ε_q^e is the elastic shear strain; κ is the recompression index in the ln scale; and G is the shear modulus.

b) Plastic potential

Because the MCC plastic potential is derived based on plastic energy dissipation that satisfies the constraints of critical state, the same plastic potential functional as that of MCC model is maintained in this model.

$$g(p,q)=\frac{q^2}{M^2}+pp_g+p_g^2 \tag{3-7}$$

in which p_g is the mean effective stress at the apex of the plastic potential surface.

From this equation, When plastic deformation is occurring, the relationship between the volumetric plastic strain increment, $d\varepsilon_p^p$, and the deviator plastic strain increment , $d\varepsilon_q^p$, can be expressed as follows:

$$\frac{d\varepsilon_p^p}{d\varepsilon_q^p}=\frac{\partial g/\partial p}{\partial g/\partial q}=\frac{M^2(2p-p_g)}{2\eta}=\frac{M^2-\eta^2}{2\eta} \tag{3-8}$$

c) Yield function

As discussed in the previous section, the associate flow rule will guarantee there's no strain softening in the undrained condition on the "wet" side. Thus an A-function is introduced into the f function to distort the g function to achieve a non associate flow rule.

In SSC, the new yield loci by introducing A into g:

$$\frac{p}{p_c}=\frac{M^2}{M^2+A\eta^2} \tag{3-9}$$

It should be noted that if A→1, the yield function will degenerate to g, and thus become the yield function of MCC model.

Obviously "A" has the function of changing the shape of the yield loci as shown in Figure 3.2.

As discussed in the previous section, in order to achieve strain softening in the "wet" part without shrinkage of the yield loci, the peak value of the yield loci must also be in the "wet" side. This means that the yield loci should be flattened and that A should be no less than 1. The "distorted" shapes of the flattened yield loci with A = 4 are shown in the Figure 3.3

Having "A" as a constant value can fit the purpose of shifting the peak point of the yield loci ellipse into the wet side. The undrained stress path is shown in Figure 3.4 with the A being a constant value equal to 4.

But A as a constant value has the following obvious shortcomings:

- it cannot reflect the influence of the difference between the SSC and the corresponding re-modelled soil; and
- the yield loci cannot degenerate back to those of the MCC model.

Thus, the expression for A should have the following limiting conditions:

- The A function should include $\Delta_{y,i}$ to reflect the level of difference between SSCs and their corresponding remodelled soils;

- When $\Delta e \rightarrow 0$, the value of $A \rightarrow 1$, which makes the yield loci come back to the MCC model;
- A has to increase with η so that non-associativity increases as failure is approached. This is because non-associativity at η=0 is problematic and we need to have A=1 at η=0. So, the only way to get A>1 prior to reaching the M line is to have A increase with η; and
- A should reflect the impact of Δe, i.e., it should decrease when Δe decreases.

The above requirements imply that A is a function of Δe and η, i.e.,

$$A=A(\Delta e,\eta) \tag{3-10}$$

Thus, the yield loci of the sensitive soil can be written as:

$$\frac{p}{p_c}=\frac{[A(\Delta e,\eta)]^2 M^2}{[A(\Delta e,\eta)]^2 M^2+\eta^2} \tag{3-11}$$

and a simple A function is introduced as:

$$A(\Delta e,\eta)=\frac{M^2}{M^2-(\frac{\Delta e}{\Delta_{y,i}})^{\alpha}\eta^2} \tag{3-12}$$

in which α is a soil parameter. How the parameter α affects the shape of the yield loci is indicated in Figure 3.5.

The A function introduced above also has the following properties:

- as it is along the isotropic consolidation line, $\eta=0$, $A(\Delta e,\eta)\rightarrow 1$; and

- when $\Delta e \rightarrow 0$, $A(\Delta e, \eta) \rightarrow 1$, which enables the yield loci to degenerate back to those of the MCC model. Δe reflects the disturbance of the soil as when the structure been destroyed by disturbance, Δe become smaller.

Applying the above A function in the SSC model, the families of the yield loci are plotted in Figure 3.6(a).

As can be seen in Figure 3.6(a), the yield function has the shortcoming that the families of the yield loci come close together after the turning point, and eventually "bunch" near the critical state line. This may be due to numerical errors preventing the undrained shearing curve reaching the critical state line.

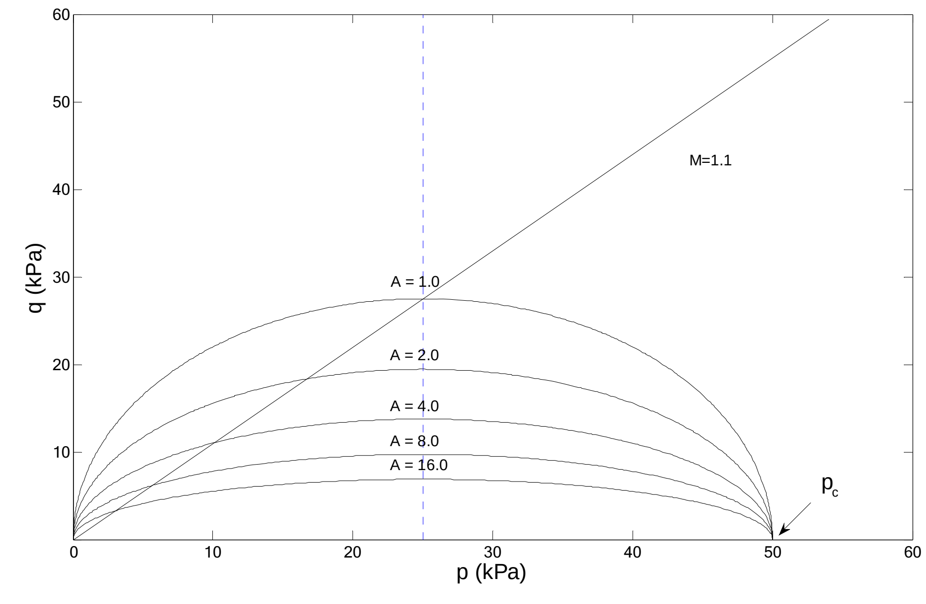

Figure 3.2: Yield loci with variations of A value but same p_c

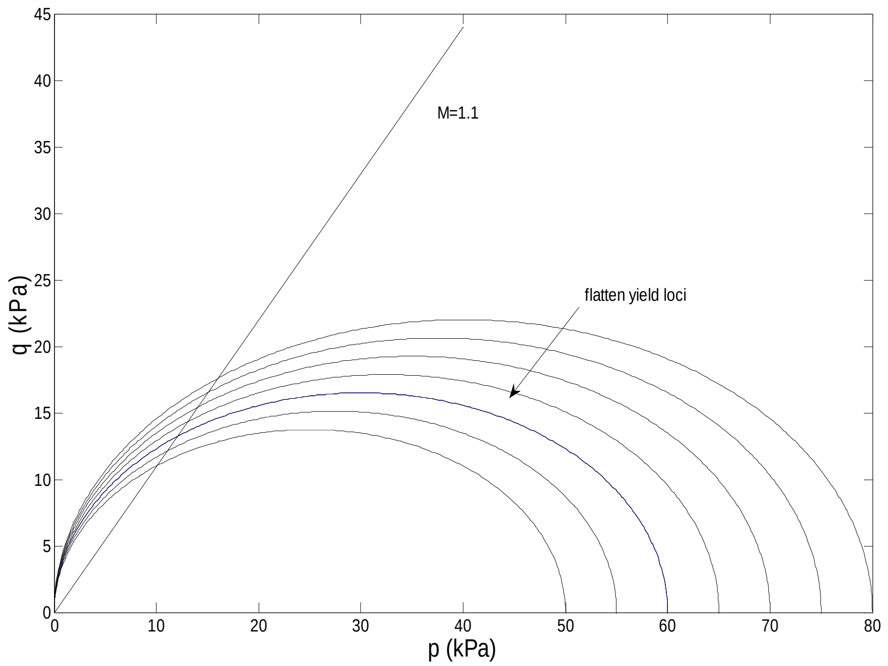

Figure 3.3: Evolutions of yield loci with A=4.0

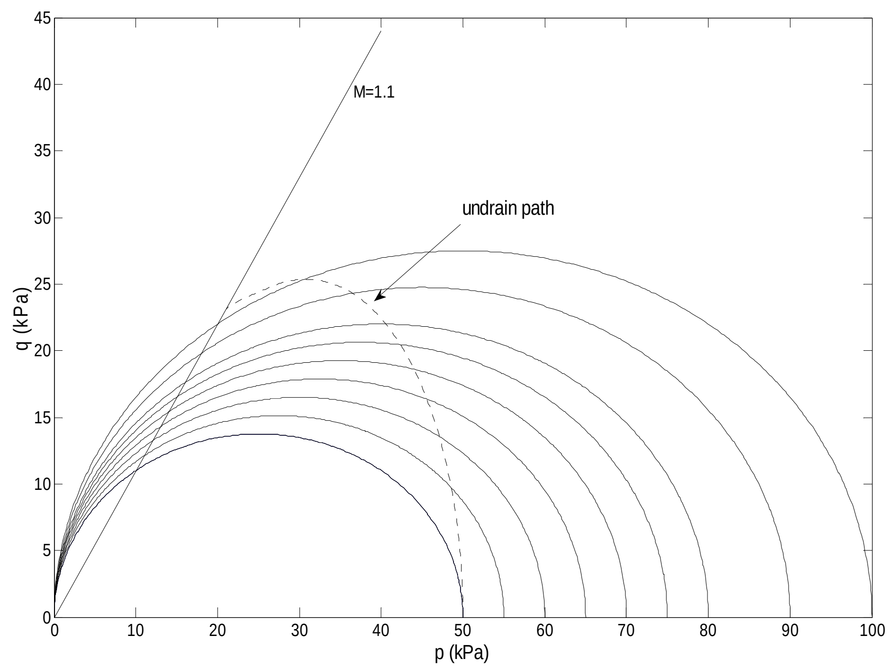

Figure 3.4: Softening paths in undrained conditions with A=4.0

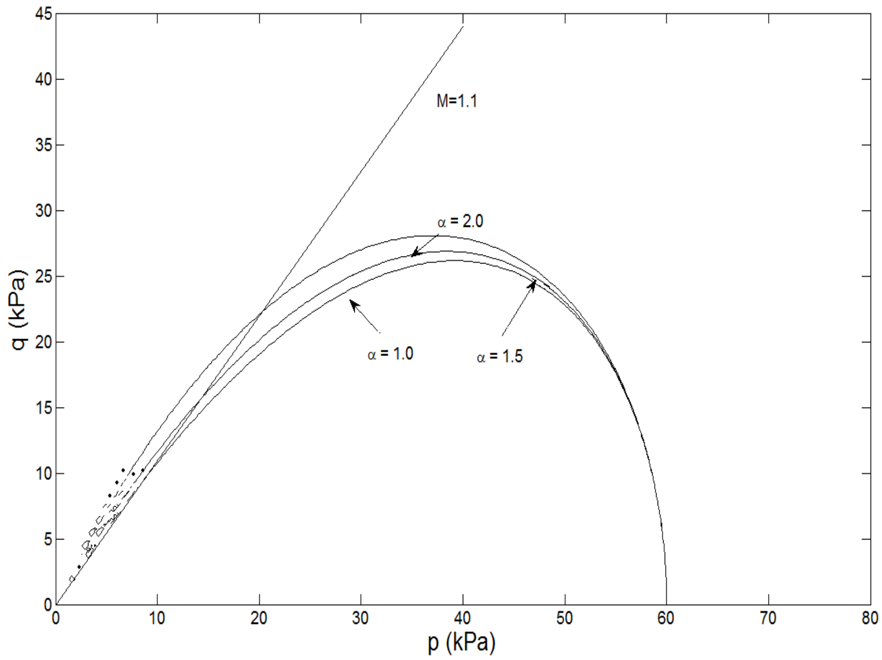

Figure 3.5: Changes of yield loci with changes of α

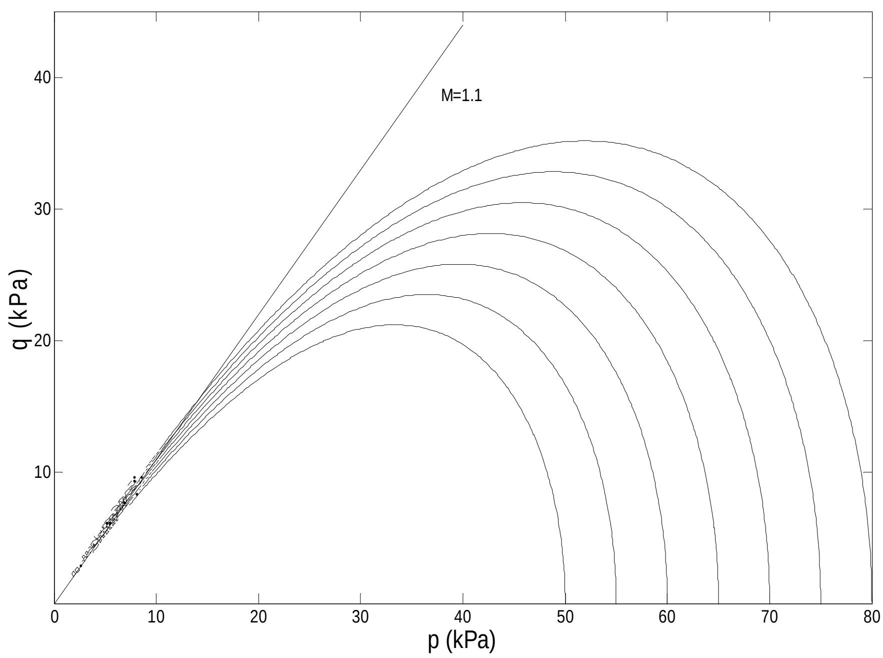

Figure 3.6(a): Growth of SSC yield loci with increase of P_c when β =1.0

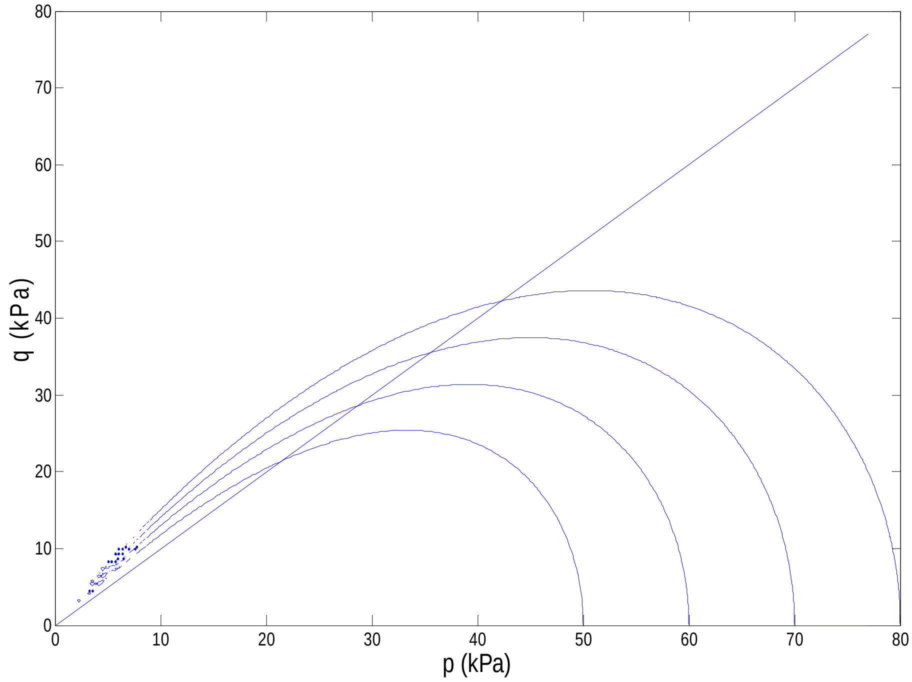

Figure 3.6(b): Growth of SSC yield loci with increase of P_c when β =1.2

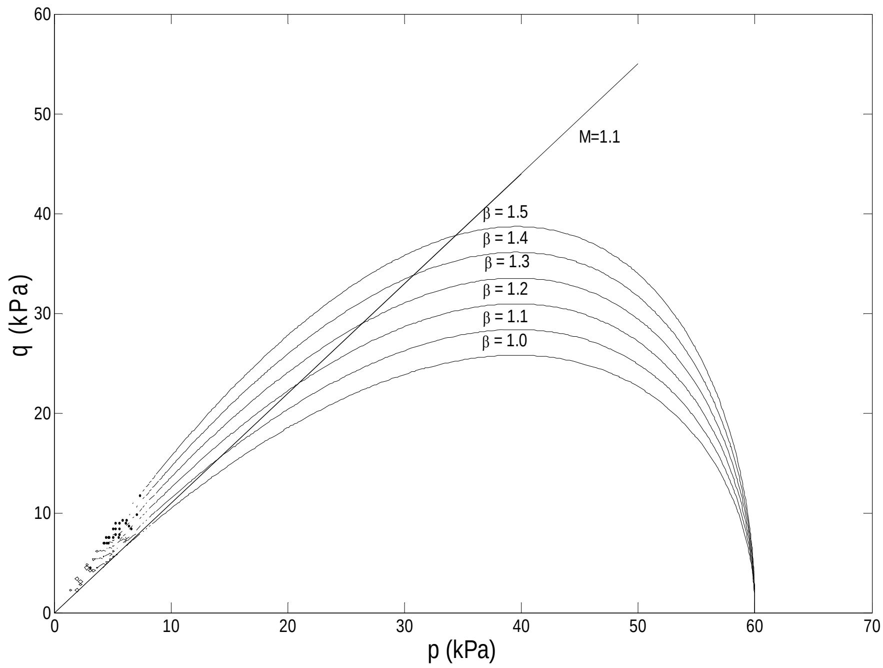

Figure 3.7: Changes of yield loci with changes of β

The above problem can be circumvented by replacing M with M^*, where M^*=βM and β is a soil parameter with a value higher than unity. Thus, the new A function is:

$$A(\Delta e, \eta) = \frac{M^{*2}}{M^{*2} - (\frac{\Delta e}{\Delta_{y,i}})^{\alpha} \eta^2} \tag{3-13}$$

and is re-written as:

$$A(\Delta e, \eta) = \frac{M^2 \beta^2}{M^2 \beta^2 - \left(\frac{\Delta e}{\Delta_{y,i}}\right)^{\alpha} \eta^2} \tag{3-14}$$

The resultant evolutions of the yield surfaces for β=1.2 are shown in Figure 3.6(b). Since the ESP starting from the "wet" side of the CSL, it ceases to move at the CSL and cannot enter the problematic region around M^*. The role of β is shown in Figure 3.7.

<u>d) Hardening rule</u>

Although the response of a SSC is very different from that of a stiff structure soil, the ICL of SSC is geometrically similar to the ICL during the de-structuring response of a stiff structure soil, as illustrated in Figure 3.1.

Therefore, the equations proposed by Liu and Cater (1999) for simulating the ICL during de-structuring are used. The e-lnp relationship in Figure 3.1 can be written as:

$$e = e^* + \Delta_{y,i} (\frac{p_{y,i}}{p_c})^b \tag{3-15}$$

In the ICL, by defining e^*_{IC} as the corresponding void ratio on the λ_{ICL} line when p_c=1.0, then, at a given p_c, e^* can be expressed as:

$$e^* = e^*_{IC} - \lambda \ln p_c \tag{3-16}$$

Thus,

$$e = e^*_{IC} - \lambda \ln p_c + \Delta_{y,i}(\frac{p_{y,i}}{p_c})^b \tag{3-17}$$

The differential from the above equation is:

$$de = \lambda \frac{dp_c}{p_c} + b\Delta e \frac{dp_c}{p_c} \tag{3-18}$$

Based on Assumption 5: The modelling of elastic strain component is identical to MCC, in the ICL:

$$de^e = \kappa \frac{dp_c}{p_c} \tag{3-19}$$

Thus:

$$de^p = (\lambda - \kappa)\frac{dp_c}{p_c} + b\Delta e \frac{dp_c}{p_c} \tag{3-20}$$

In which the subscript e and p means elastic and plastic components.

Within the critical state framework, the above expression of de^p is generally true for all load path with plastic yielding. Thus, the above equation can be expressed in term of plastic volumetric strain increment that serve as hardening function:

$$d\varepsilon_p^p = \frac{(\lambda - k + b\Delta e)}{1+e}\frac{dp_c}{p_c} \tag{3-21}$$

3.2.4 General plastic stress strain relationship

Differential of the yield loci:

$$\frac{\partial f}{\partial p}dp + \frac{\partial f}{\partial q}dq + \frac{\partial f}{\partial p_c}dp_c = 0 \tag{3-22}$$

From equation (3.14), (3.15), differentiation of f function gives:

$$\frac{\partial f}{\partial p} = \frac{M^2\beta^2 - A\eta^2 - 2A(A-1)\eta^2}{M^2\beta^2}p \tag{3-23}$$

$$\frac{\partial f}{\partial q} = \frac{2qA^2}{M^2\beta^2} \tag{3-24}$$

$$\frac{\partial f}{\partial p_c} = -p(1+\frac{b\alpha A(A-1)\eta^2}{M^2\beta^2 + A\eta^2}) \tag{3-25}$$

Substituting equation (3.21) and (3.23-3.25) into equation (3.22) and combine the flow rule expressed in equation (3.8), the general stress strain equation can be expressed as follows:

$$\begin{bmatrix} d\varepsilon_p^p \\ d\varepsilon_q^p \end{bmatrix} =$$

$$\frac{\lambda - k + b\Delta e}{\left[M^2\beta^2 + A\eta^2 + b\alpha A(A-1)\eta^2\right]p(1+e)}\begin{bmatrix} M^2 - A\eta^2\text{-}2A(1-A)\eta^2 & 2A^2\eta \\ \frac{2\eta[M^2 - A\eta^2 + 2A(1-A)\eta^2]}{(M^2-\eta^2)} & \frac{4A^2\eta^2}{(M^2-\eta^2)} \end{bmatrix}\begin{bmatrix} dp \\ dq \end{bmatrix}$$

(3-26)

3.3 PARAMETER DETERMINATIONS

Nine parameters are defined in this new SSC model, i.e, M, λ, κ, e^{*}_{IC}, $p_{y,i}$, $\Delta_{y,i}$, b, α and β. The first five are the same as those of the MCC model.

The new parameters, i.e., $\Delta_{y,i}$, b, α and β, have been introduced to describe the influence of its structure on a SSC's mechanical behaviour. Parameter $\Delta_{y,i}$ indicates the difference in the void ratio between the ICL and the λ line at the indicial yielding stress, $P_{y,i}$, of SSC. Parameter b indicates the destruction rate of SSC during virgin yielding. These two parameters can be determined directly from the isotropic compression test on an undisturbed SSC sample.

Since one-dimensional consolidation tests are much more convenient than the isotropic consolidation test and are widely used in geotechnical engineering practice, the approximate methods for obtaining these three parameters from one-dimensional consolidation tests are presented. To improve the accuracy of determining the initial yield stress, $p_{y,i}$, and the corresponding void ratio difference, $\Delta_{y,i}$, constant rate loading tests are also introduced.

Parameter β determines the peak deviator stress value of the undrained condition test and parameter α influences the amount of strain softening without changing the value of the peak deviator stress. These two parameters together can simulate the strain softening of SSC in undrained conditions.

Since the parameters adopted from the MCC model can be determined in the same way as those of the MCC model, only the new parameter determinations will be focused on. These new parameters, i.e., $\Delta_{y,i}$, b, α and β are divided into two groups: consolidation parameters ($\Delta_{y,i}$, b) and strain-softening parameters(α, β). The tests and methods used to determine them are discussed in detail in the following sub-section.

a) Consolidation parameter

For oedometer tests, the load is applied on the vertical direction. To convert the vertical effective stress into the mean effective stress, an approximation is made based on Jacky's empirical equation in which horizontal effective stress σ_h and vertical effective stress σ_v for a soil during one dimensional compression can be assumed as a constant value:

$$\frac{\sigma_h}{\sigma_v} \approx 1 - \sin\varphi_{cs} = k \tag{3-27}$$

Where φ_{cs} is the critical state friction angle measured from a triaxial compression test.

The consolidation curve from a typical constant rate of loading oedometer test can be drawn in e-logp space and the asymptotic slope of the consolidation line for SSCs is defined as $\lambda\big|_{k_0}$.

By drawing a vertical line from the consolidation curve to the $\lambda\big|_{k_0}$ line, the mean effective stress of the largest distance is assumed to be $p_i\big|_{k_0}$ and the corresponding void ratio difference between the consolidation curve and the $\lambda\big|_{k_0}$ line is defined as $\Delta_{y,i}\big|_{k_0}$.

The relationship of $p_{y,i}\big|_{k_0}$ and $p_{y,i}$ can be expressed as:

$$p_{y,i} = p_i\big|_{k_0}(1+\frac{A\eta^2}{M^2}) \tag{3-28}$$

From equation (3-27), the oedometer consolidation line can be assumed as a compression at constant η:

$$\eta = \frac{3(1-k)}{1+2k} \tag{3-29}$$

As at the initial yield point, $p_{y,i}$, $\Delta e = \Delta_{y,i}$, $\left(\frac{\Delta e}{\Delta_{y,i}}\right)^{\alpha}$ =1.

Assuming parameter β is determined (the method is explained in the next sub-section), the initial yield point on the ICL, $p_{y,i}$, can be determined by equation (3-28).

$\Delta_{y,i}$ and b value are then determined by try and error process of the curve fitting. One example of getting b value from actual testing data is indicated in Figure 3.8

b) Strain-softening parameters

Parameters α and β can be determined from undrained strain softening test results. For a test in undrained conditions, parameter β determines the peak deviator stress value and parameter α influences the amount of strain softening which can occur without changing this value. Thus, for an reasonable assumed undrained strain softening curve obtained from the undrained triaxial shearing test, β is determined first in order to fit the curve of the highest deviator stress value and then α is adjusted for the rest of the curve fitting. Procedures for the determination of parameters are shown in Figure 3.8(a), Figure 3.8(b) and Figure 3.9(c).

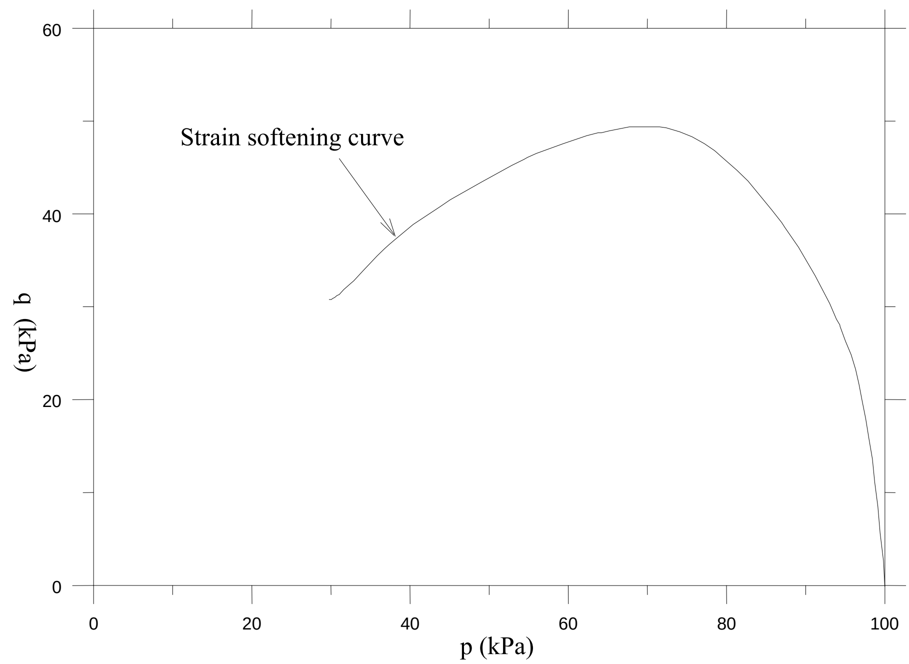

Figure 3.8(a): Strain-softening curve of undrained test

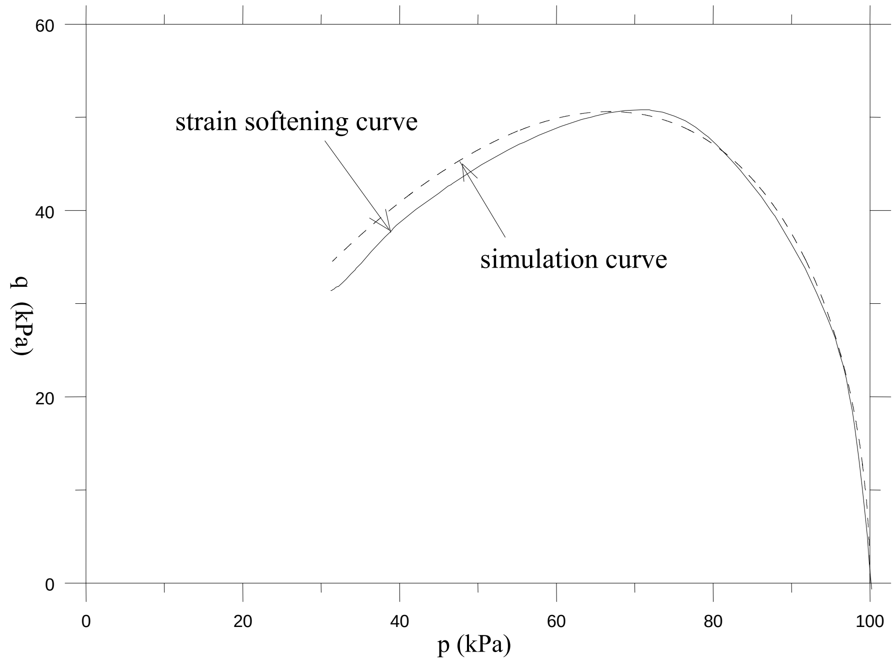

Figure 3.8(b): Simulation for β to fit highest Q value

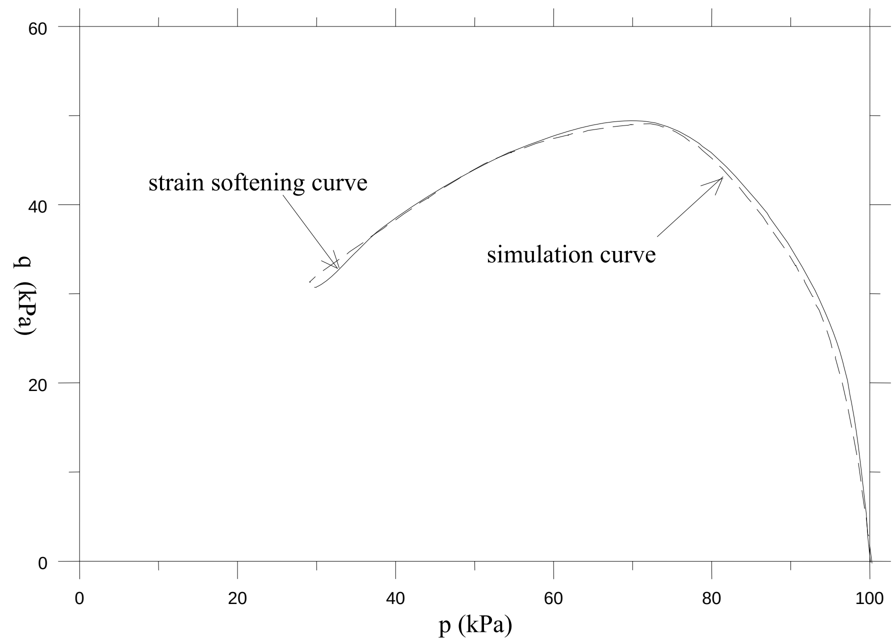

Figure 3.8(c): Simulation for adjusting α to fit strain softening curve

CHAPTER FOUR

SIMULATION WITH SENSITIVE SOFT CLAY MODEL

4.1 INTRODUCTION

To verify that the new sensitive soft clay (SSC) model can simulate typical behaviour, i.e., strain softening in undrained conditions while strain hardening in drained conditions, element simulations of triaxial tests are conducted by adopting the incremental stress-strain equation (3-26) of Chapter 3. This can be done by finite difference using spreadsheets. After verification, the new SSC model is coded into the finite element program, AFENA. Simulation results from AFENA are then compared with those from the simulation performed using spreadsheets. In this chapter, the procedure for forming the sensitive elasto-plastic matrix, $\left[D_{ep}\right]$, for SSC is presented and a coupled analysis formulation is presented following Britto and Gunn's (1987) procedure.

The sensitive elasto-plastic matrix, $\left[D_{ep}\right]$, reflects the relationship between the stress and strain, it containing the appropriate material properties of sensitive soil elements.

4.2 FINITE DIFFERENCE SIMULATIN OF TRIAXIAL TEST

The simulations of triaxial tests are undertaken to prove that the SSC model can simulate the SSC features in the right trend. For simplification, the boundary conditions and initial stress states of all elements of the triaxial test are assumed to be the same as those of the simulation. Thus, the simulation can be performed using the finite difference (FD) method and Microsoft Excel spreadsheets. The process is described below.

4.2.1 Simulation procedure

In the drained simulation, since the cell pressure is kept constant:

$$dq = 3dp \tag{4-1}$$

p and q increase simultaneously according to equation (4-1). The elastic strain is calculated by applying equations (3-5) and (3-6) while the volumetric and deviator plastic strains are calculated by equation (3-26).

In undrained triaxial conditions, $d\varepsilon_p = 0$,thus, the elastic volumetric and the volumetric strains are counterbalanced as:

$$d\varepsilon_p^e + d\varepsilon_p^p = 0 \tag{4-2}$$

In which $\delta\varepsilon_p^e$ and $\delta\varepsilon_p^p$ are expressed as equation (3-5) and (3-21) in Chapter 3.

Thus:

$$\kappa\frac{dp}{p} = -(\lambda - k + b\Delta e)\frac{dp_c}{p_c} \tag{4-3}$$

Then, the evolution of yield function in differential form is:

$$\frac{dp}{p}+\frac{2A^2\eta}{M^2+A\eta^2}d\eta-\frac{M^2+2A\eta^2-\eta^2}{M^2+A\eta^2}\frac{dp_c}{p_c}=0 \quad (4\text{-}4)$$

This equation indicates the geometry of a yield locus which provides a link between the changes in p and η which cause yielding and result in changes in p_c. Thus, a constraint on changes in p and η which leads to constant volume deformation of the soil can be expressed by the combination of equations (4-3) and (4-4) as:

$$(1+\frac{k}{\lambda-k}\frac{M^2+2A\eta^2-\eta^2}{M^2+A\eta^2})\frac{dp}{p}=\frac{2A^2\eta}{M^2+A\eta^2}d\eta \quad (4\text{-}5)$$

The FD method uses increments of the constant $\delta\eta$ and the typical calculation steps are:

i) step $\delta\eta$ and then obtain δp using equation (4-5) with $\delta\eta$ replaces $d\eta$ and δp replaces dp

ii) obtain δq using faction $\delta q=\eta\delta p$

iii) $q=q+\delta q$, $p=p+\delta p$

iv) calculate p_c using (p, q) from iii)

v) update p_c by take average of the current p_c value and p_c previous step

vi) recalculate (δq, δp), (q, p, p_c), by repeat step i)-iv)

vii) calculate $\delta\varepsilon_q$ from (δq, δp), (q, p), thus $\varepsilon_q=\varepsilon_q+\delta\varepsilon_q$

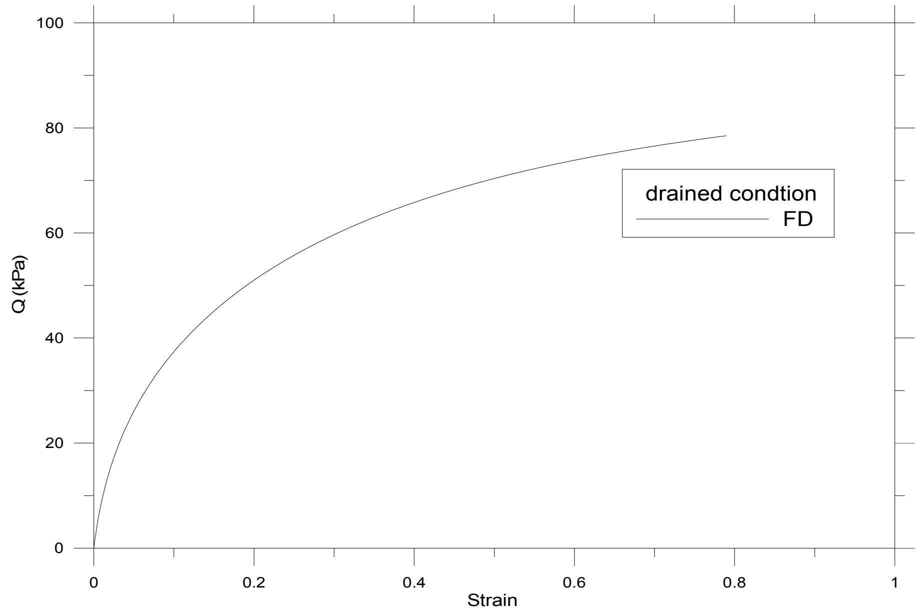

Figure 4.1: Deviator stress-strain relationship in drained condition (FD simulation)

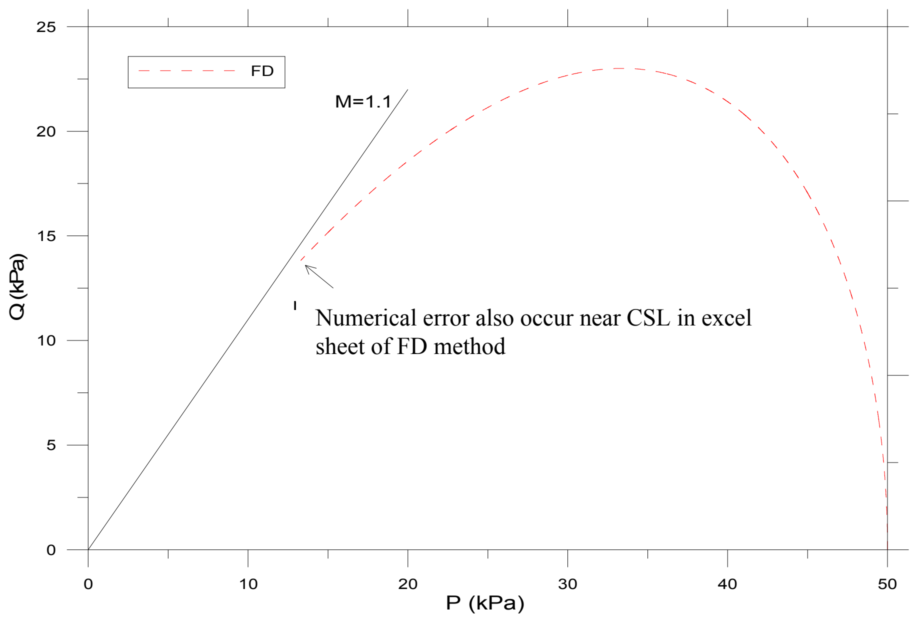

Figure 4.2(a): Stress path in undrained conditions (FD simulation)

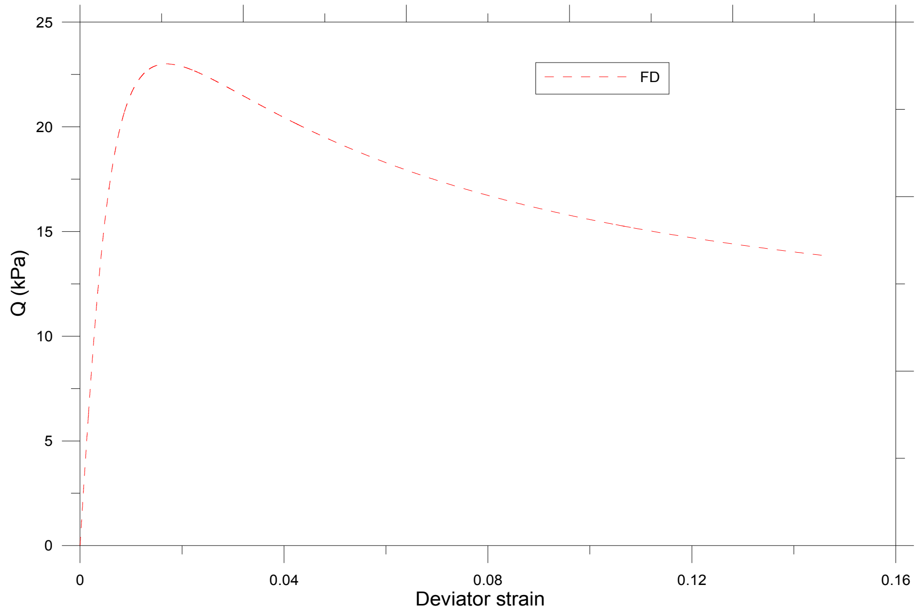

Figure 4.2(b): Deviator stress-strain relationship in undrained Conditions (FD simulation)

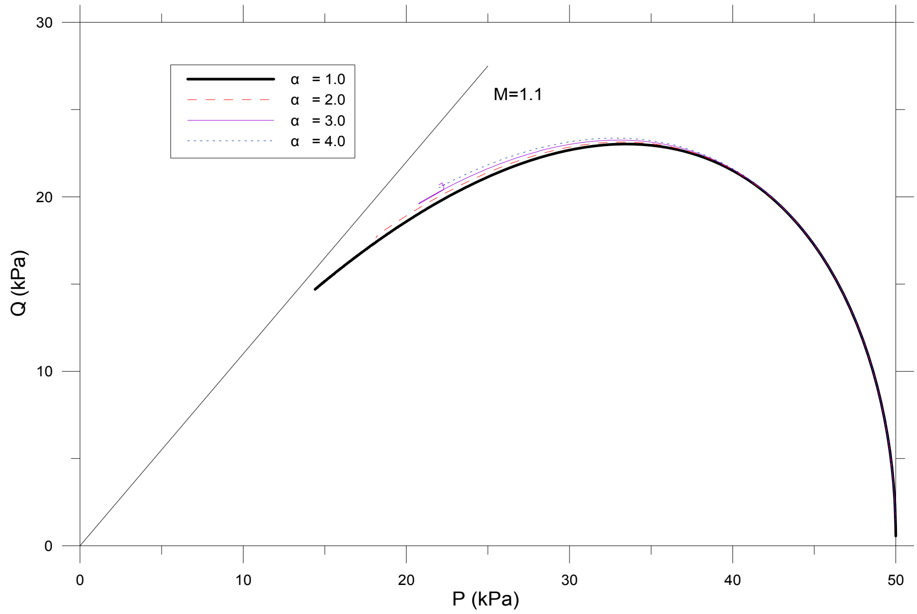

Figure 4.3(a): Stress paths with variations of α in undrained conditions (FD simulation)

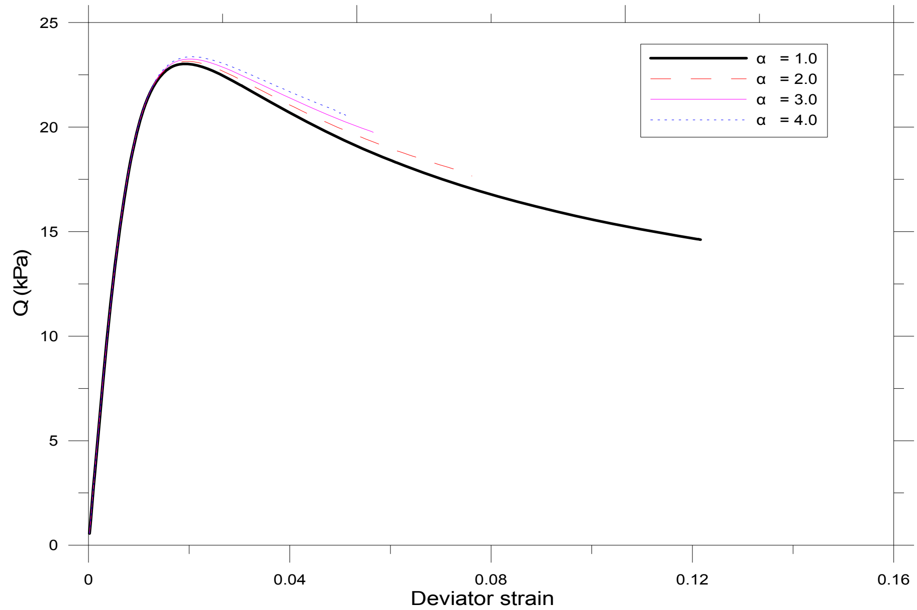

Figure 4.3(b): Deviator stress-strain relationships with variations of α in undrained conditions (FD simulation)

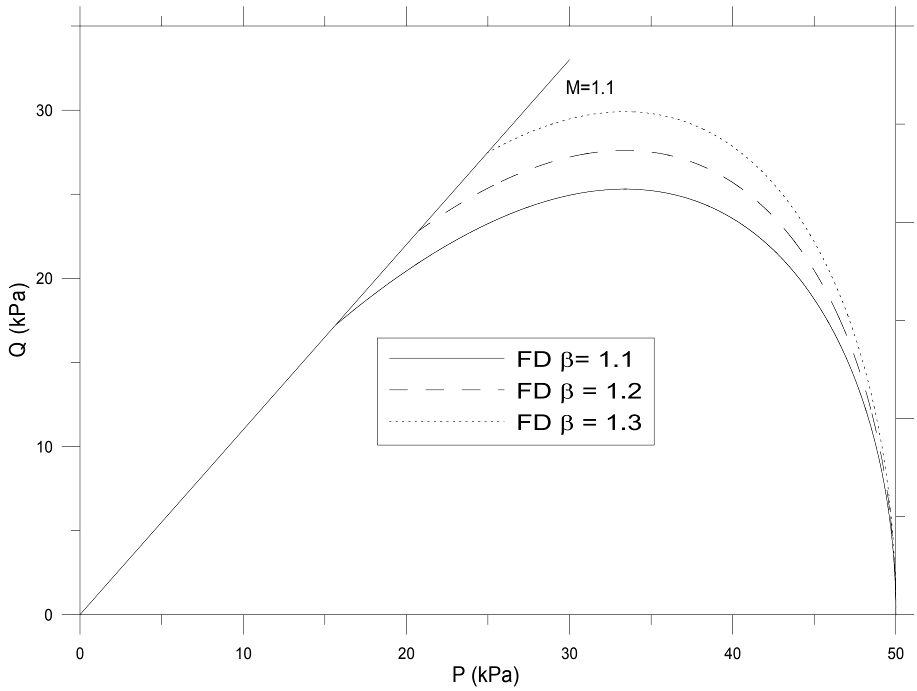

Figure 4.4(a): Stress paths with variations of β in undrained conditions (FD simulation)

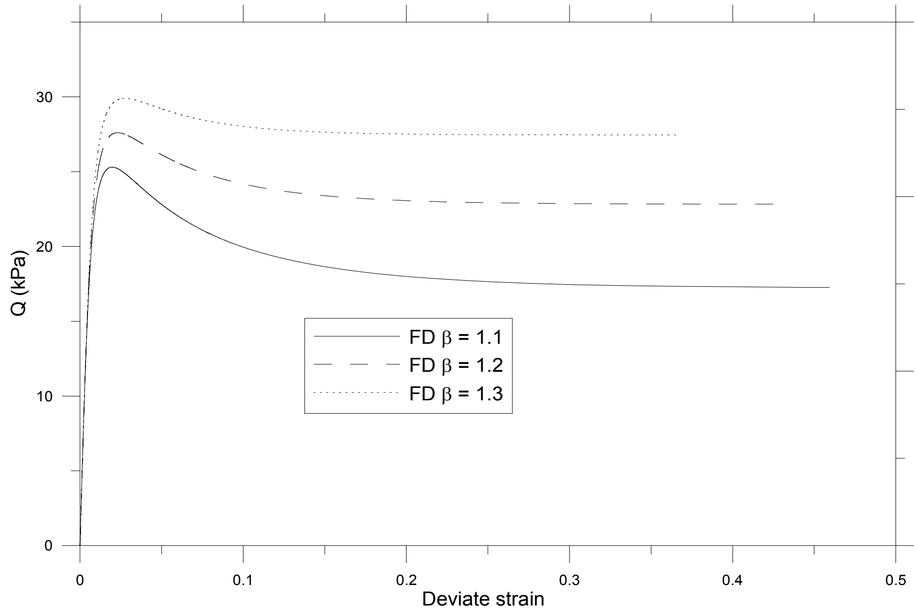

Figure 4.4(b): Deviator stress-strain relationships with variations of β in undrained conditions (FD simulation)

4.2.2 Simulation results

Soil parameters are listed in table 4-1. In order to clarify the need for parameter β, the simulation is conducted by assuming β=1.0 first. Simulation results from both the undrained and drained conditions are shown in Figures 4.1, 4.2(a) and 4.2(b). They show that the new model is suitable for simulating simultaneously both strain softening in undrained conditions and strain hardening in drained conditions.

But a phenomenon of concern is that, in undrained conditions, the mean effective stress, p, and the deviator stress, q, tend to decrease to zero when q/p approaches the M line. As shown in Figure 4.2(a), when the η value reaches nearly 97% of the M line, accumulated errors of p_c calculation eventually stopped the simulation..

To check the influence of the SSC model parameters on numerical errors, different α values are used in the undrained simulation while all other model parameters are unchanged. The simulation results are shown in Figures 4.3(a) and 4.3(b), in which it is obvious that numerical errors will occur when the η value approaches the M line. The larger the sensitive strain-softening parameter, α, the earlier the numerical errors occur.

Thus, as another parameter is needed in order to control the percentage of strain softening, parameter β is adopted.

The FD simulation results from different β are shown in Figures 4.4(a) and 4.4(b). They indicate that the numerical error will not occur when the strain-softening parameter, β, is large enough. From the simulations, it is clear that the larger the value of parameter β, the less strain softening will occur.

4.3 FINITE ELEMENT IMPLEMENTATION

After verification, the SSC model is then coded into the FEM program, AFENA. The procedure for forming the stiffness matrix and formulating the coupled analysis is explained below.

4.3.1 SSC stiffness matrix

Assuming that the incremental strain of SSC can be divided into elastic strain and sensitive plastic strain, then the incremental strain can be written as:

$$\{d\varepsilon\} = \{d\varepsilon^e\} + \{d\varepsilon^p\} \tag{4-6}$$

In which $\{d\varepsilon\}$ is the matrix of total strain, superscript e means elastic component while superscript p means plastic component.

When the material is elastic, the stress strain relationship can be expressed as:

$$\{d\sigma\} = \left[D^e\right]\{d\varepsilon^e\} \tag{4-7}$$

in which $\left[D^e\right]$ is the elastic stiffness matrix.

Thus:

$$\{d\sigma\} = \left[D^e\right]\{d\varepsilon\} - \left[D^e\right]\{d\varepsilon^p\} \tag{4-8}$$

In which $\{d\sigma\}$ is the matrix of total stress,

The general stress strain relationship can be expresses as:

$$\{d\sigma\} = \left[D^{ep}\right]\{d\varepsilon\} \tag{4-9}$$

in which $\left[D^{ep}\right]$ is the elasto-plastic stiffness matrix.

From the yield and hardening functions:

$$f(\sigma_{ij}, H) = 0 \tag{4-10}$$

In which, H is the hardening component. At a given H value, a yield surface can be determined in the stress space.

$$\left\{\frac{\partial f(\sigma)}{\partial \sigma}\right\}^T \{d\sigma\} = F'\left\{\frac{\partial H}{\partial \varepsilon^p}\right\}^T \left\{d\varepsilon^p\right\} \tag{4-11}$$

From equations (4-9) and (4-11):

$$\left\{\frac{\partial f(\sigma)}{\partial \sigma}\right\}^T \left[D^e\right]\{d\varepsilon\} = (F'\left\{\frac{\partial H}{\partial \varepsilon^p}\right\}^T + \left\{\frac{\partial f(\sigma)}{\partial \sigma}\right\}^T \left[D^e\right])\left\{d\varepsilon^p\right\} \tag{4-12}$$

From the plastic flow rule:

$$\left\{d\varepsilon^p\right\} = d\lambda\left\{\frac{\partial g}{\partial \sigma}\right\} \tag{4-13}$$

Substituting equation (4-13) into equation (4-12):

$$d\lambda = \frac{\left\{\frac{\partial f(\sigma)}{\partial \sigma}\right\}^T \left[D^e\right]}{(F'\left\{\frac{\partial H}{\partial \varepsilon^p}\right\}^T + \left\{\frac{\partial f(\sigma)}{\partial \sigma}\right\}^T \left[D^e\right])\left\{\frac{\partial g(\sigma)}{\partial \sigma}\right\}}\{d\varepsilon\} \tag{4-14}$$

From equations (4-7) and (4-8):

$$\left\{d\varepsilon^p\right\} = d\lambda\left\{\frac{\partial g}{\partial \sigma}\right\} = \frac{\left\{\frac{\partial g(\sigma)}{\partial \sigma}\right\}\left\{\frac{\partial f(\sigma)}{\partial \sigma}\right\}^T \left[D^e\right]}{(F'\left\{\frac{\partial H}{\partial \varepsilon^p}\right\}^T + \left\{\frac{\partial f(\sigma)}{\partial \sigma}\right\}^T \left[D^e\right])\left\{\frac{\partial g(\sigma)}{\partial \sigma}\right\}}\{d\varepsilon\} \tag{4-15}$$

Thus:

$$\{d\sigma\} = \left[\left[D^e\right] - \left[D^e\right] \times \frac{\left\{\frac{\partial g(\sigma)}{\partial \sigma}\right\}\left\{\frac{\partial f(\sigma)}{\partial \sigma}\right\}^T \left[D^e\right]}{(F'\left\{\frac{\partial H}{\partial \varepsilon^P}\right\}^T + \left\{\frac{\partial f(\sigma)}{\partial \sigma}\right\}^T \left[D^e\right])\left\{\frac{\partial g(\sigma)}{\partial \sigma}\right\}} \right] \{d\varepsilon\} \tag{4-16}$$

and

$$\left[D^{ep}\right] = \left[D^e\right](1 - \frac{\left\{\frac{\partial g(\sigma)}{\partial \sigma}\right\}\left\{\frac{\partial f(\sigma)}{\partial \sigma}\right\}^T \left[D^e\right]}{(F'\left\{\frac{\partial H}{\partial \varepsilon^P}\right\}^T + \left\{\frac{\partial f(\sigma)}{\partial \sigma}\right\}^T \left[D^e\right])\left\{\frac{\partial g(\sigma)}{\partial \sigma}\right\}}) \tag{4-17}$$

Thus, by differentiating the f, g and H functions:

$$\{\frac{\partial g(\sigma)}{\partial \sigma}\} = (2p - p_c)/3 + 1/M^2\{\sigma_{ii}\} \tag{4-18a}$$

$$\left\{\frac{\partial f(\sigma)}{\partial \sigma}\right\}^T = \left[(2p - p_c) + 2(p - p_c)(A-1) + \frac{2qA^2}{M^2\beta^2}\right]\{\sigma_{ii}\} \tag{4-18b}$$

and

$$F'\left\{\frac{\partial H}{\partial \varepsilon^p}\right\}^T = \frac{\lambda - k + b\Delta e}{1+e} \tag{4-18c}$$

in which σ_{ii} , is the principal stress.

4.3.2 Finite element formulation for coupled consolidation

The principle of virtual work is applied to the equilibrium and continuity equations in order to obtain the FEM equations. Applying this principle to the equilibrium equations gives the relationship for the load increment as:

$$\begin{aligned}&\int_V \{\delta\varepsilon\}^T \{\delta\sigma\}\, dV + \int_V \{\delta\varepsilon\}^T \{\delta U_W\}\, dV \\ &= \int_V \{\delta d\}^T \{\delta F_b\}\, dV + \int_S \{\delta d\}^T \{\delta F_s\}\, dS\end{aligned} \tag{4-19}$$

where: $\delta\varepsilon$ is the strain vector; $\delta\sigma$ is the incremental effective stress vector; δU_W is the incremental pore water pressure vector; δd is the displacement vector; δF_b is the incremental body force vector; and δF_s is the incremental surface load vector.

The displacements are assumed to vary over FEM mesh according to:

$$\{\delta d\} = [N]\{\delta a\} \tag{4-20}$$

where $[N]$ is the matrix of the shape functions and δa is the vector of the nodal displacements.

The same shape functions as for displacement $[N]$ are applied to the variations of excess pore water pressure and are given by:

$$\{\delta U_W\} = [N]\{\delta u\} \tag{4-21}$$

where δu is the nodal excess pore water pressure.

The strain increment vector, $\delta\varepsilon$, is related to the incremental nodal displacement vector, δa, as:

$$\{\delta\varepsilon\} = [B]\{\delta a\} \quad (4\text{-}22)$$

where [*B*] is the strain nodal displacement transformation matrix.

The incremental volumetric strain vector, δ*v*, within a typical element, can be expressed as:

$$\{\delta v\} = \{m\}^T [B]\{\delta a\} \quad (4\text{-}23)$$

where vector *m* is defined as:

$$\{m\} = \begin{bmatrix} 1 \\ 1 \\ 1 \\ 0 \end{bmatrix} \quad (4\text{-}24)$$

The discretised form of the equilibrium equation can be obtained by substituting equations (4-20)-(4-24) in equation (4-19), so that:

$$\left[K^e\right]\{\delta a\} + [L]\{\delta u\} = \{\delta F\} \quad (4\text{-}25)$$

where

$$\left[K^e\right] = \int_V [B]^T \left[D^e\right][B] dV \quad (4\text{-}26)$$

$$[L] = \int_V [B]^T \{m\}[N] dV \quad (4\text{-}27)$$

and

$$\{\delta F\} = \int_V [N]^T \{\delta F_b\} dV + \int_S [N]^T \{\delta F_s\} dS + \int_V \{\delta\sigma\} dV \quad (4\text{-}28)$$

where $\delta\sigma$ is the vector of the stresses of the SSC model and is given by:

$$\{\delta\sigma\} = [B]^T [D^{ep}]\{\varepsilon\} \tag{4-29}$$

in which D^{ep} is defined as in equation (4-17).

Applying the principle of virtual work to the two-dimensional continuity gives the following expression:

$$\int_{vol} \{\delta u\} \left[\frac{k_{11}}{\gamma_w} \frac{\partial^2 U_w}{\partial x_{11}{}^2} + \frac{k_{33}}{\gamma_w} \frac{\partial^2 U_w}{\partial x_{33}{}^2} + \frac{\partial v}{\partial t} \right] d(vol) = 0. \tag{4-30}$$

Where: k_{11} and k_{33} are the hydraulic conductivities in the 1- and 3- coordinate directions respectively; γ_w is the unit weight of pore water; v is the seepage velocity; and t is the time, d(vol) is the volumetric change. The excess pore water pressure gradient is obtained as:

$$\begin{bmatrix} \dfrac{\partial U_w}{\partial x_{11}} \\ \dfrac{\partial U_w}{\partial x_{33}} \end{bmatrix} = [E]\{\delta u\} \tag{4-31}$$

where the matrix [*E*] is obtained by differentiating the shape functions [*N*] with respect to x_{11} and x_{33}.

Substituting equations (4-21)-(4-24) and equation (4-31) into equation (4-30) results in the following FEM equations:

$$[L]^T \frac{d\{a\}}{dt} - \phi_k \{u\} = \int_S [N]^T \{V_n\} dA \tag{4-32}$$

where

$$L = \int_V [B]^T m[N] dv \tag{4-33}$$

and

$$\phi_k = \int_{vol} [E]^T [k][E] \frac{1}{\gamma_w} d(vol) \tag{4-34}$$

where V_n is the prescribed boundary seepage velocity and $[k]$ is the permeability matrix given as:

$$[k] = \begin{bmatrix} k_{11} & 0 \\ 0 & k_{33} \end{bmatrix} \tag{4-35}$$

Integrating equation (4-32), with respect to time, results in:

$$\begin{aligned} &[L]^T \{\delta a\} - \phi_k \left[(1-\beta)\{u(t)\} + \beta\{u(t+\Delta t)\} \right] \\ &= \int_S [N]^T \left((1-\beta)\{v_n(t)\} + \beta\{v_n(t+\Delta t)\} \right) \Delta t dA \end{aligned} \tag{4-36}$$

where the value of β defines the way in which u varies during the time interval.

Booker and Small (1975) considered the stability of integration schemes using different values of β and showed that, for stability, $\beta \geq 0.5$. Britto and Gunn (1987) adopted $\beta = 1$ and this value also works proper for the new SSC model, thus the same value is adopted in SSC model. Then equation (4-36) becomes:

$$[L]^t \{\delta a\} - \phi_k \Delta t \{\delta u\} = \phi_k \Delta t \{u\} + \int_S [L]^T V_n(t+\Delta t) \Delta t dA = \{\Delta F_S\} \tag{4-37}$$

Equations (4-25) and (4-37) can be used to establish a solution at a time, $t+\Delta t$, from the solution at time, t. In summary, the fully coupled FEM equations can be written as:

$$\begin{bmatrix} [K] & [L] \\ [L]^T & -\phi_k \Delta t \end{bmatrix} \begin{bmatrix} \{\delta a\} \\ \{\delta u\} \end{bmatrix} = \begin{bmatrix} \{\delta F\} \\ \{\delta F_w\} \end{bmatrix} \tag{4-38}$$

where: $[K]$ is the element stiffness matrix; δF is the normal finite element incremental load term, and δF_w is the load term corresponding to a prescribed water seepage on the boundary.

4.4 FINITE ELEMENT SIMULATION

The numerical analyses described in this section have two main purposes: firstly, to verify whether there are severe numerical errors arising from the high non-linear simulation and coupled analysis and, if there any, to find reasonable changes for the yield function and other methods to avoid or minimise them; and secondly, to study the effects of parameters α and β on the behaviour prediction. In order to meet the second purpose, triaxial analyses are performed with different values of α and β while keeping all the other parameters and test conditions unchanged.

4.4.1 Triaxial test simulation

To verify the code, triaxial test simulations are first conducted using the same soil parameters as in the FD method. Figure 4.5 presents the FEM meshes used to isotropically simulate consolidated drained and undrained triaxial SSC behaviours. They consist of 72 LST elements with 175 nodes for both the drained and undrained analyses. Every LST element has 6 integration points and 2 degrees of freedom per node in the non-coupled analysis and 9 integration points and 3 degrees of freedom per node in the coupled analysis. Axisymmetric conditions are assumed and the boundary conditions are shown in Figure 4.6. Smooth contact is assumed between the loading cap and the soil sample in each analysis and the initial stress states are set to be uniform in order to make the results comparable with FD methods. Both drained and undrained triaxial simulations are conducted, and with prescribed boundary displacement.

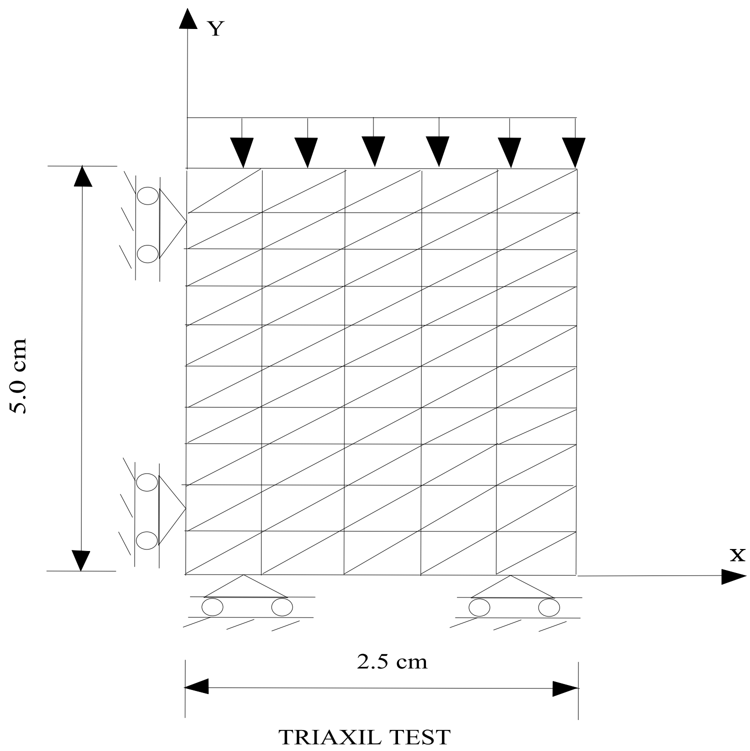

Figure 4.5: Triaxial test simulation

Table 4-1 Soil parameters

Soil	**Parameter**	**Value**
MCC	M	1.1
	ϕ	27.7 ^{o}
	λ	0.28
	κ/λ	0.2
	e_{cs}	2.95
SSC	Δ	0.30
	b	1.0

Note:

SSC parameters α, β, and $p_{y,i}$ changes during the paramatic study and the value is listed in text.

Begin with β = 1.0, simulation results from the tests in both drained and undrained conditions are shown in Figures 4.6, 4.7(a) and 4.7(b). As can be seen in Figure 4.6, the stress-strain curves are slightly different for the two different methods. Figure 4.7(a) and Figure 4.7(b) show that the stress paths and stress-strain curves of the undrained tests are about the same for each method. However, a numerical issue may arise when the soil approaches the critical state as the stress path shoots up to the critical state line when η nearly approaches M.

Although this phenomenon may not happen when the parameter changes, it remains of concern that numerical problems may need to be considered when the soil approaches the critical state. The deviator stress-strain curves of the drained and undrained tests show a relatively small difference. The strain difference may be caused by an accumulative error resulting from the calculation of p_c which cannot be precise due to the f function being an implicit equation.

a) Change $P_{y,i}$

$P_{y,i}$ is changed to a different value to further verify the code and the simulation results are shown in Figures 4.8 to 4.11. Comparison of the simulation results from the FD and FEM methods shows that they are still approximately the same when $P_{y,i}$ .changes. The sightly difference of the simulation results of FD and FEM are caused by numerical errors of FEM and approximation of the FD method. The difference is relatively small and not sensitive with the change of parameter $P_{y,i}$

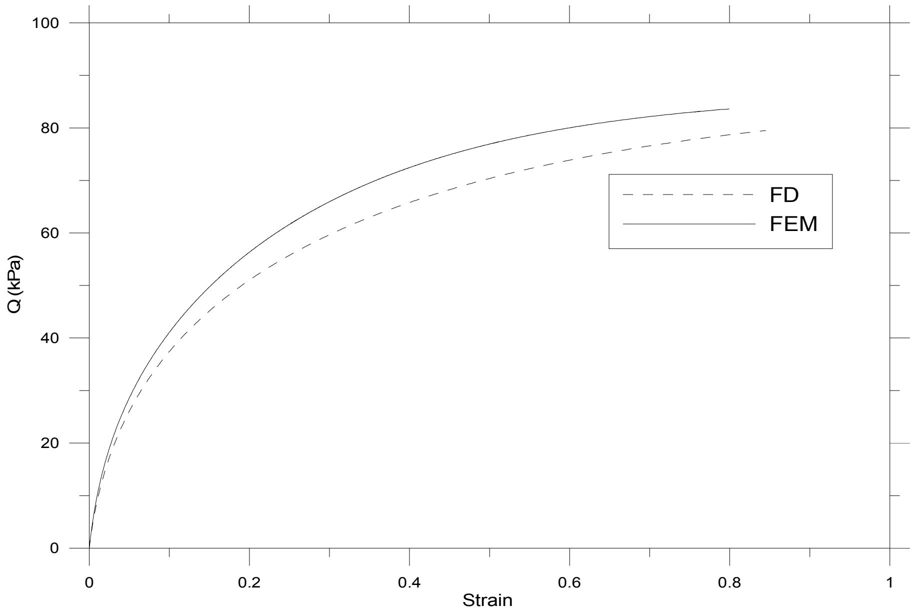

Figure 4.6: Comparison of stress-strain curves in drained conditions (P_0 = 50 kPa, β = 1.1)

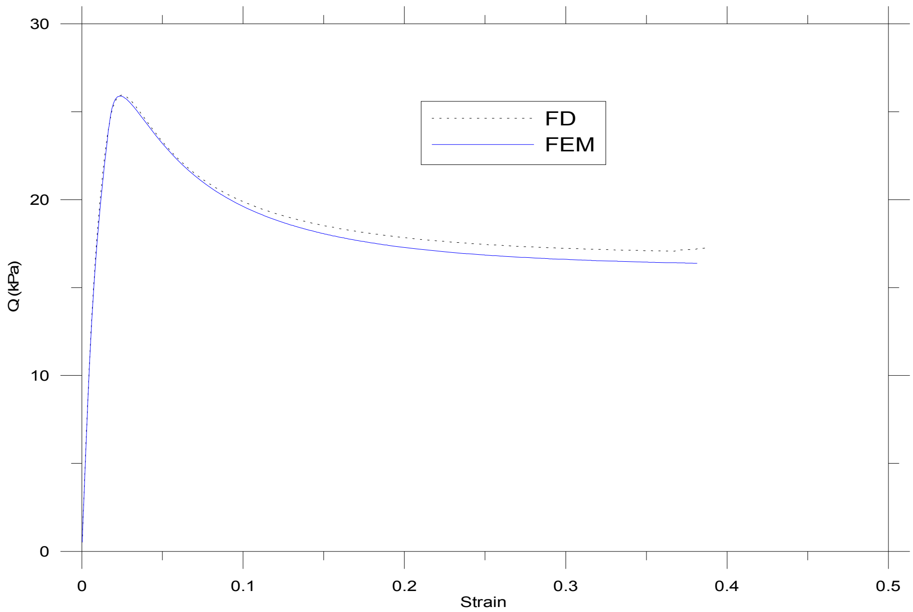

Figure 4.7(a): Comparison of stress paths in undrained conditions (P_0 = 50 kPa, β = 1.1)

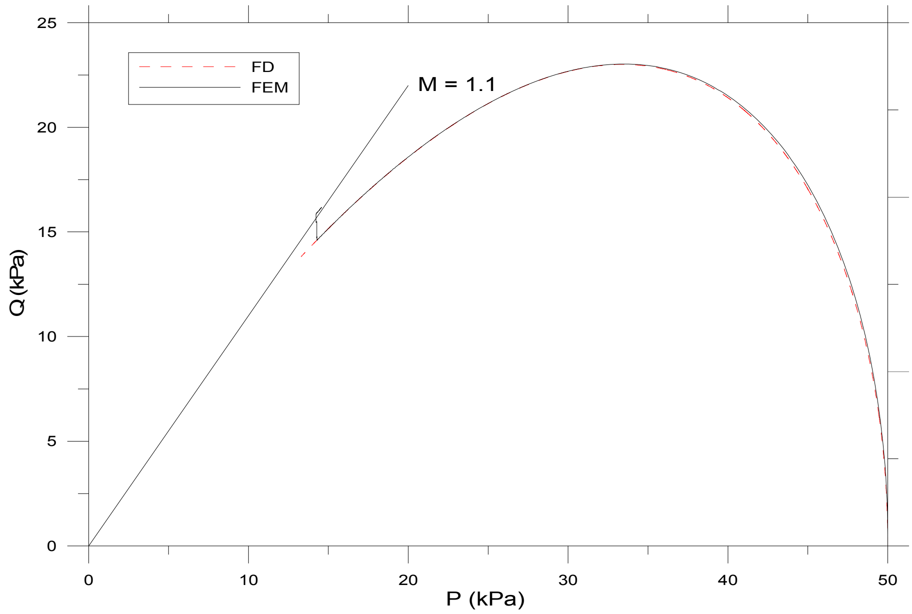

Figure 4.7(b): Comparison of stress-strain curves in undrained conditions (P_0 = 50 kPa, β = 1.1)

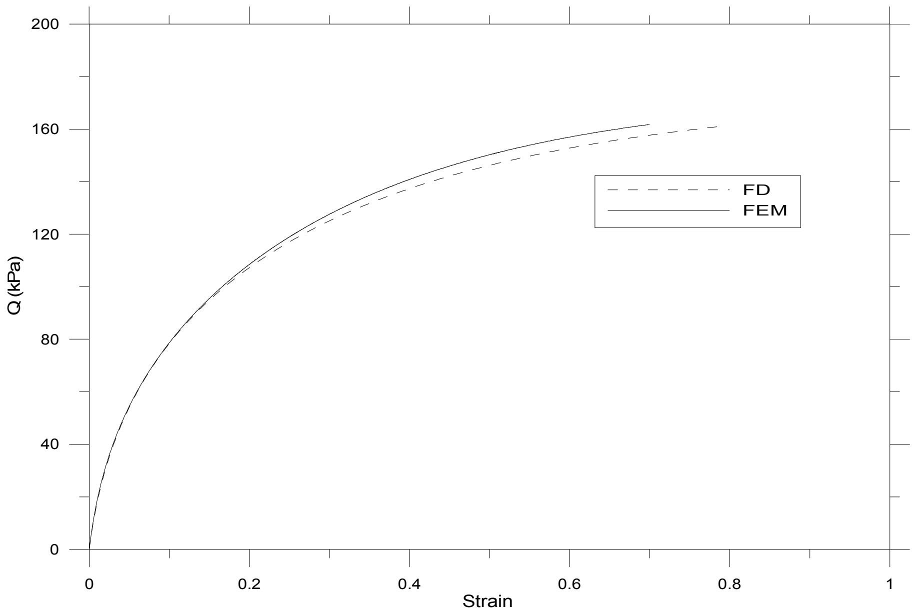

Figure 4.8(a): Comparison of stress-strain curves in drained conditions (P_0 = 100 kPa, β = 1.1)

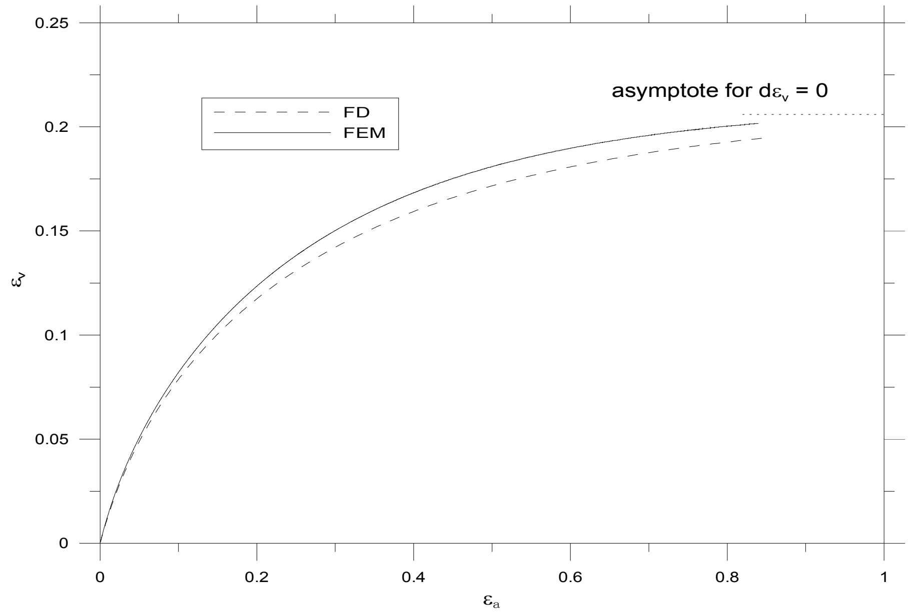

Figure 4.8(b): Comparison of volumetric and deviator strains

(P_0 = 100 kPa, β = 1.1)

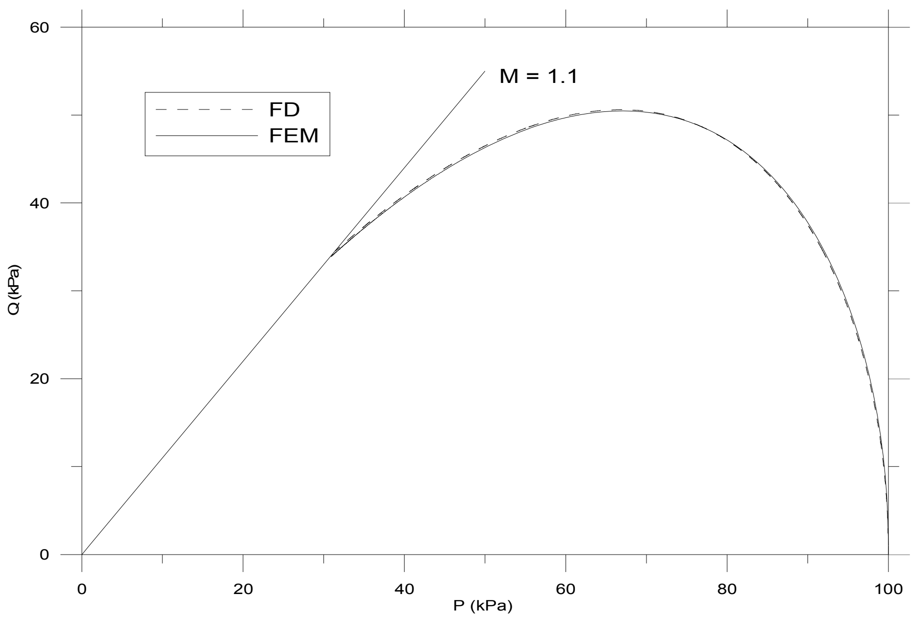

Figure 4.9(a): Comparison of stress paths in undrained conditions

(P_0 = 100 kPa, β = 1.1)

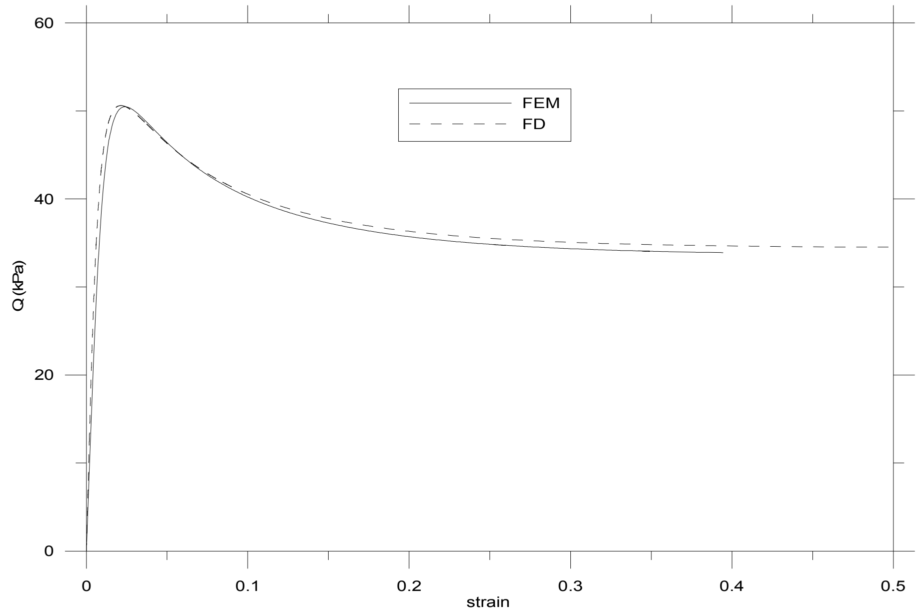

Figure 4.9(b): Comparison of stress-strain curves in undrained conditions

(P_0 = 100 kPa, β = 1.1)

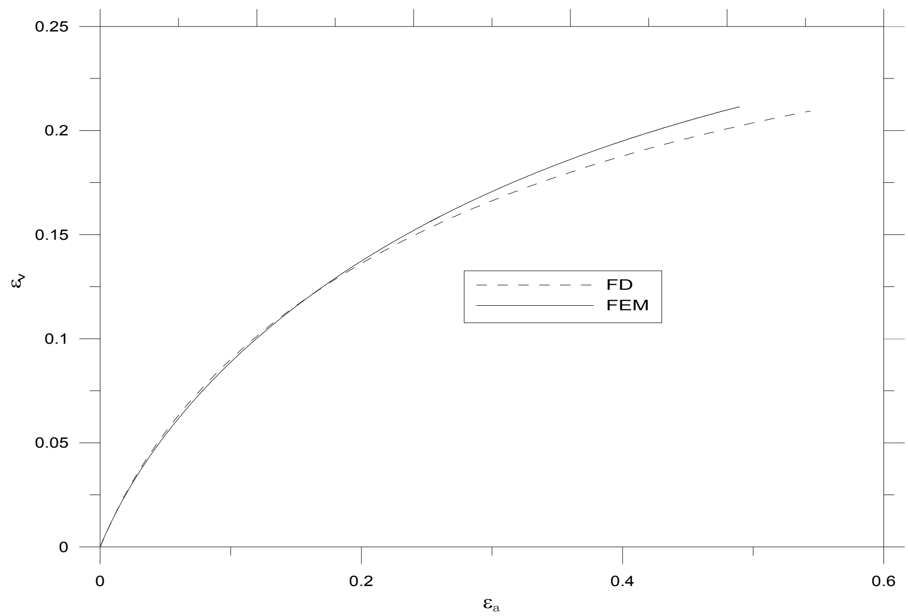

Figure 4.10(a): Comparison of volumetric and deviator strains

(P_0 = 500 kPa, β = 1.1)

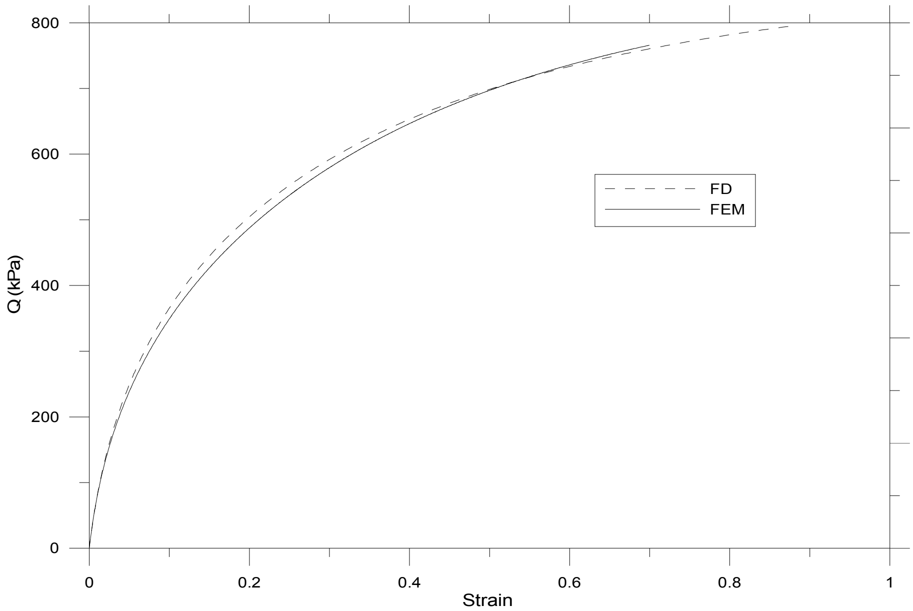

Figure 4.10(b): Comparison of stress-strain curves in drained conditions ($P_0 = 500$ kPa, $\beta = 1.1$)

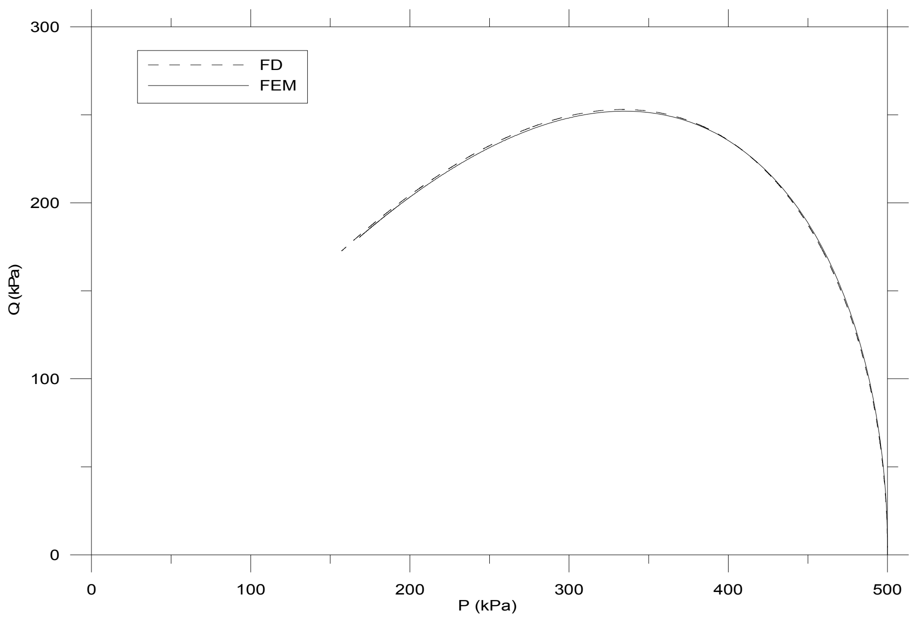

Figure 4.11(a): Comparison of stress paths in undrained conditions ($P_0 = 500$ kPa, $\beta = 1.1$)

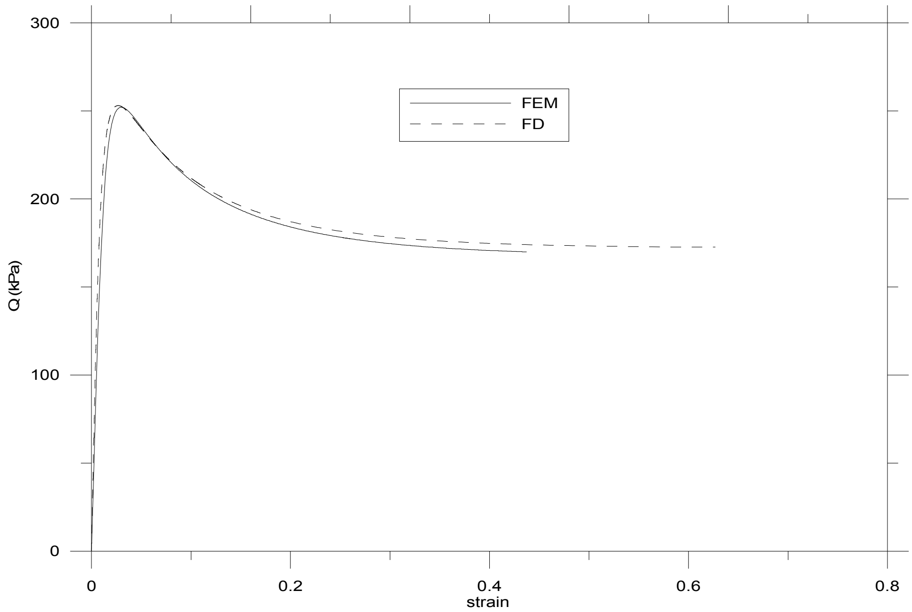

Figure 4.11(b): Comparison of stress-strain curves in undrained conditions (P_0 = 500 kPa, β = 1.1)

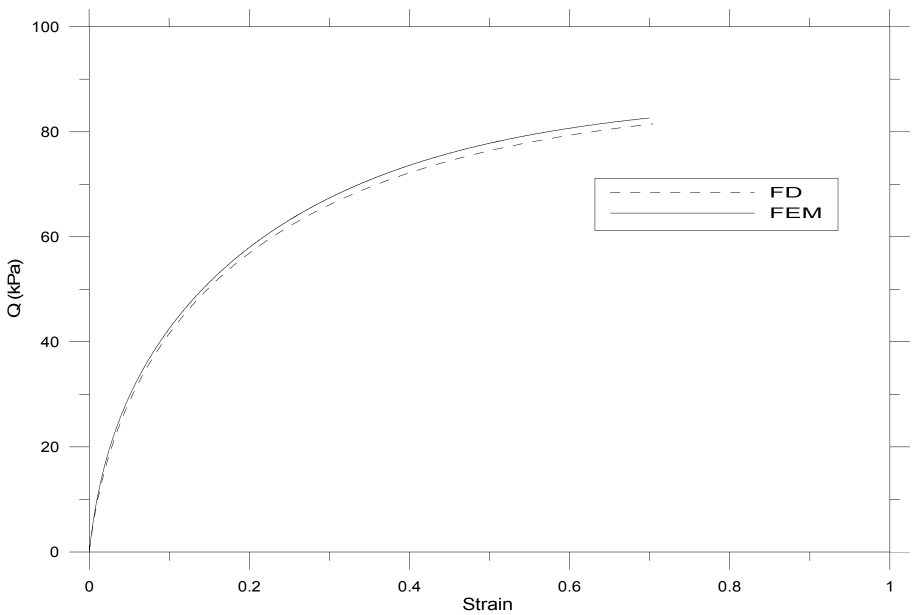

Figure 4.12(a): Comparison of stress-strain curves in drained conditions (P_0 = 50 kPa, β = 1.2)

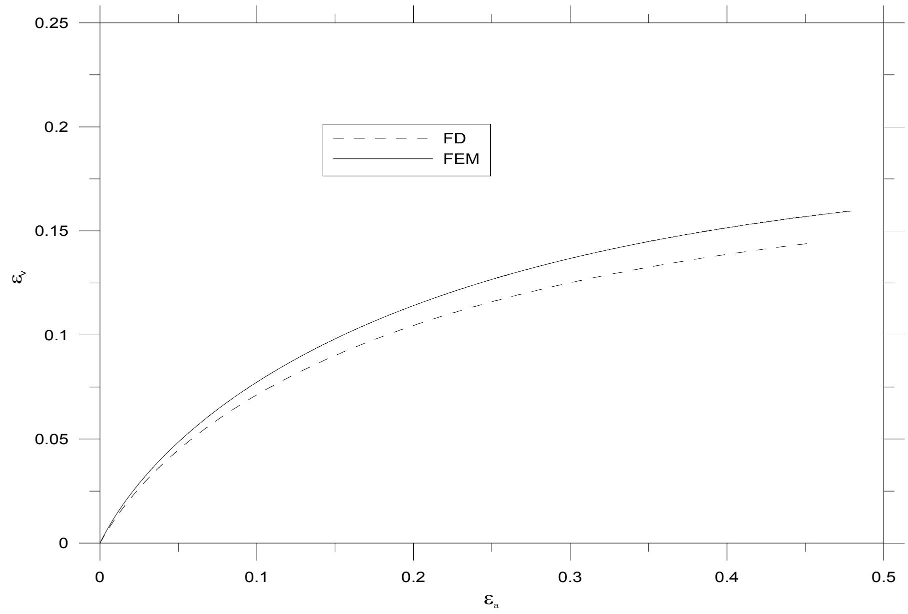

Figure 4.12(b): Comparison of volumetric and deviator strains

(P_0 = 50 kPa, β = 1.2)

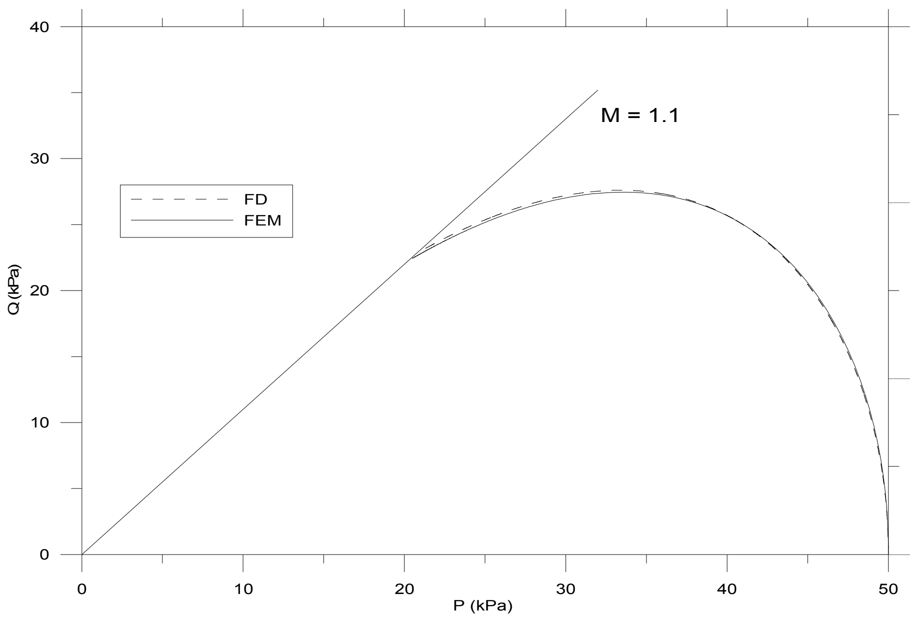

Figure 4.13(a): Comparison of stress paths in undrained conditions

(P_0 = 50 kPa, β = 1.2)

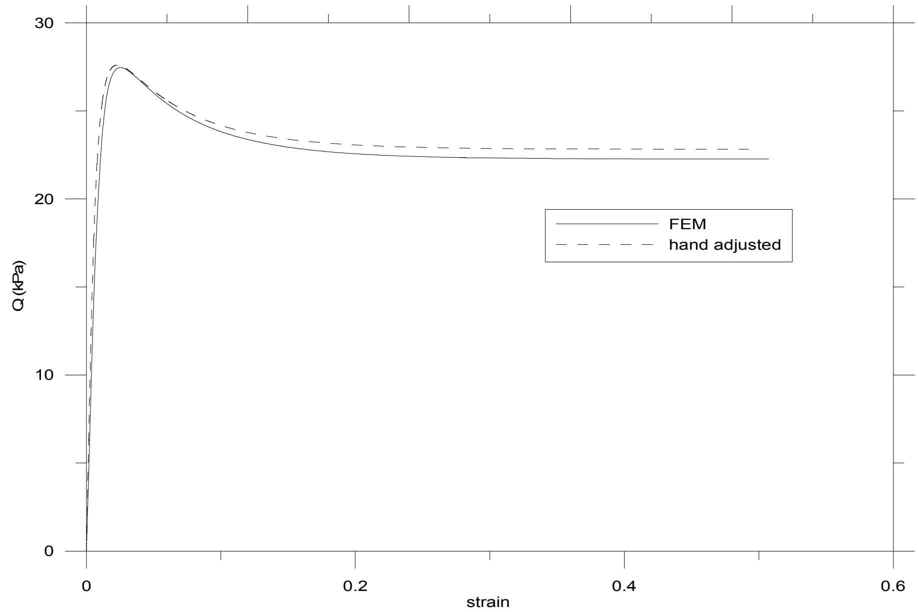

Figure 4.13(b): Comparison of stress-strain curves in undrained conditions (P_0 = 50 kPa, β = 1.2)

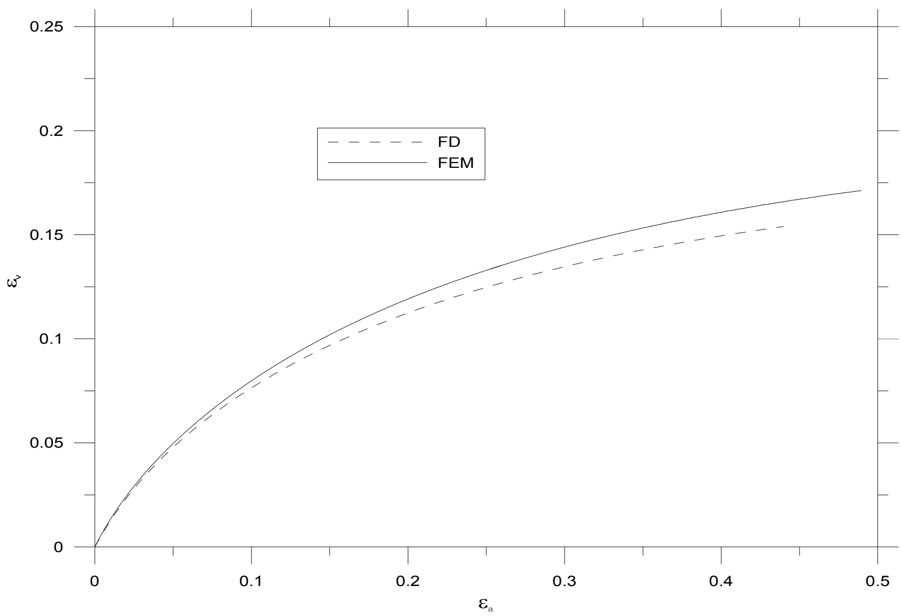

Figure 4.14(a): Comparison of volumetric and deviator strains (P_0 = 100 kPa, β = 1.2)

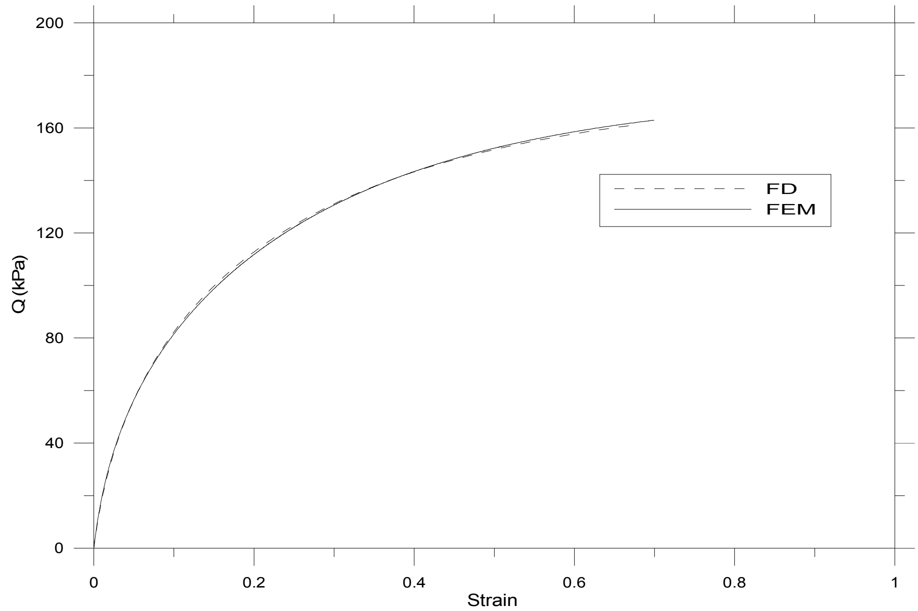

Figure 4.14(b): Comparison of stress-strain curves in drained conditions (P_0 = 100 kPa, β = 1.2)

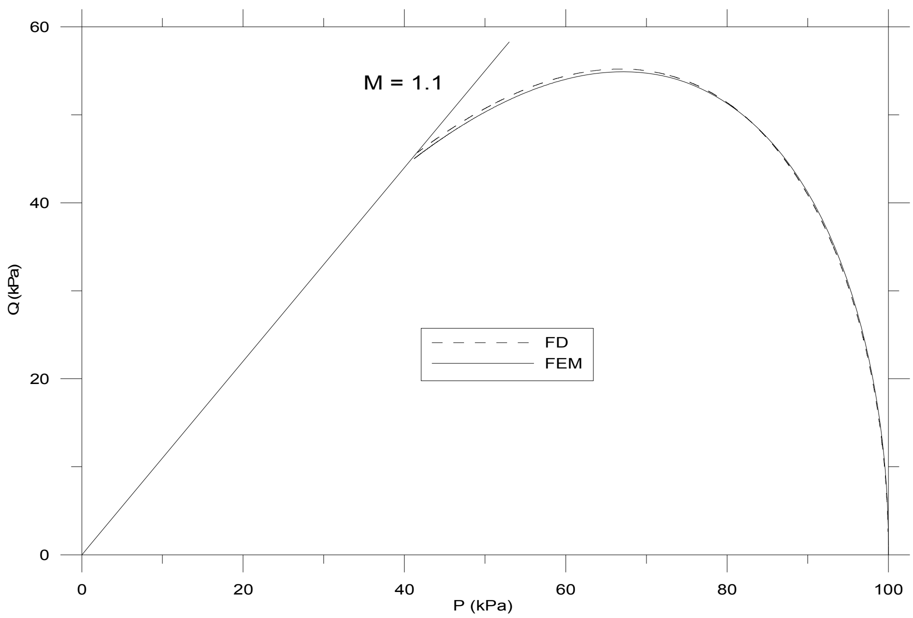

Figure 4.15(a): Comparison of stress paths in undrained conditions (P_0 = 100 kPa, β = 1.2)

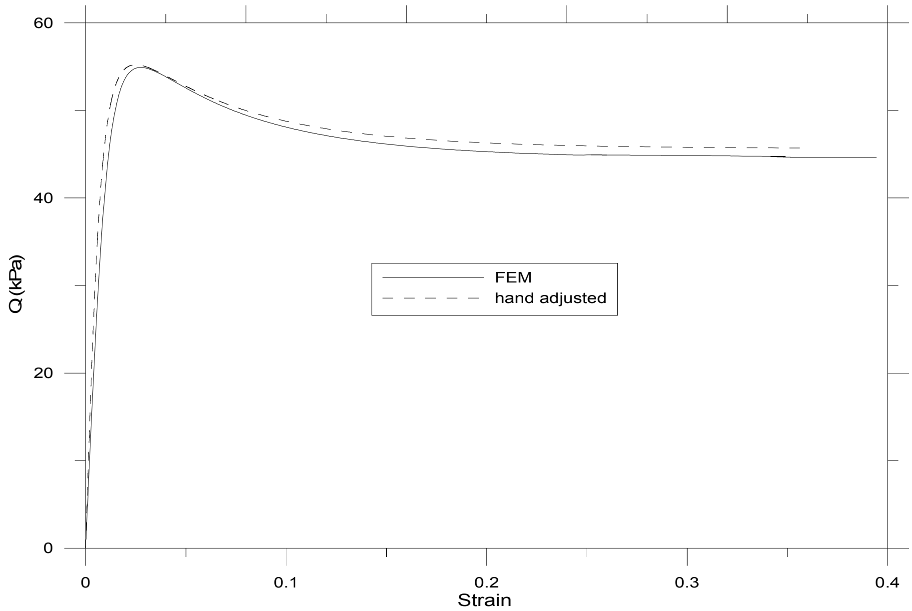

Figure 4.15(b): Comparison of stress-strain curves in undrained conditions (P_0 = 100 kPa, β = 1.2)

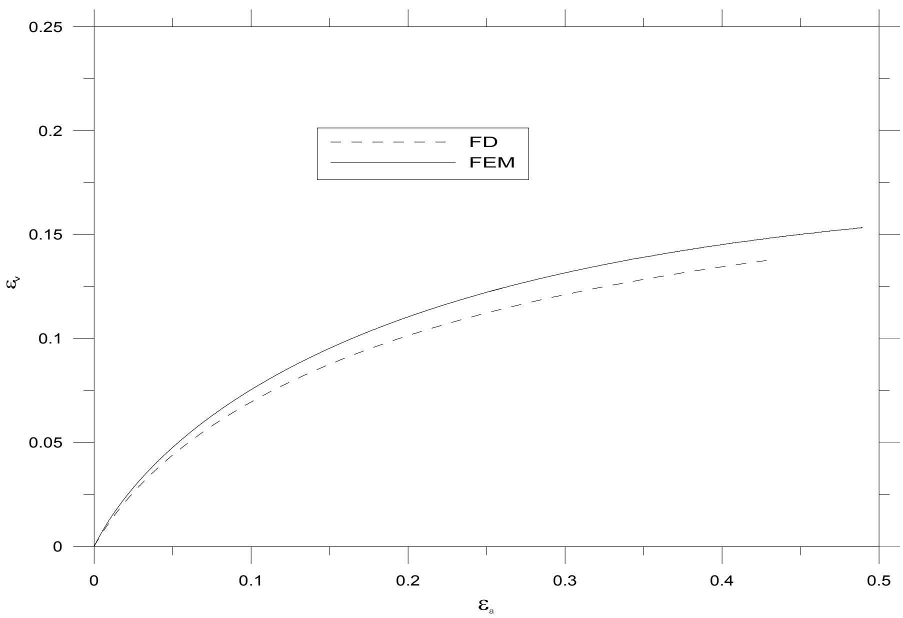

Figure 4.16(a): Comparison of volumetric and deviator strains (P_0 = 50 kPa, β = 1.3)

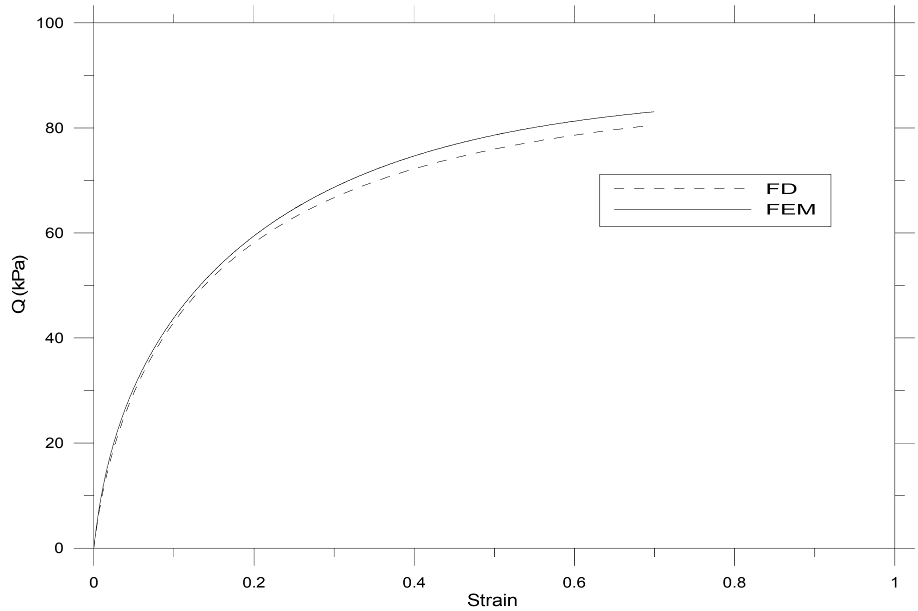

Figure 4.16(b): Comparison of stress- strain curves in drained conditions (P$_0$ = 50 kPa, β = 1.3)

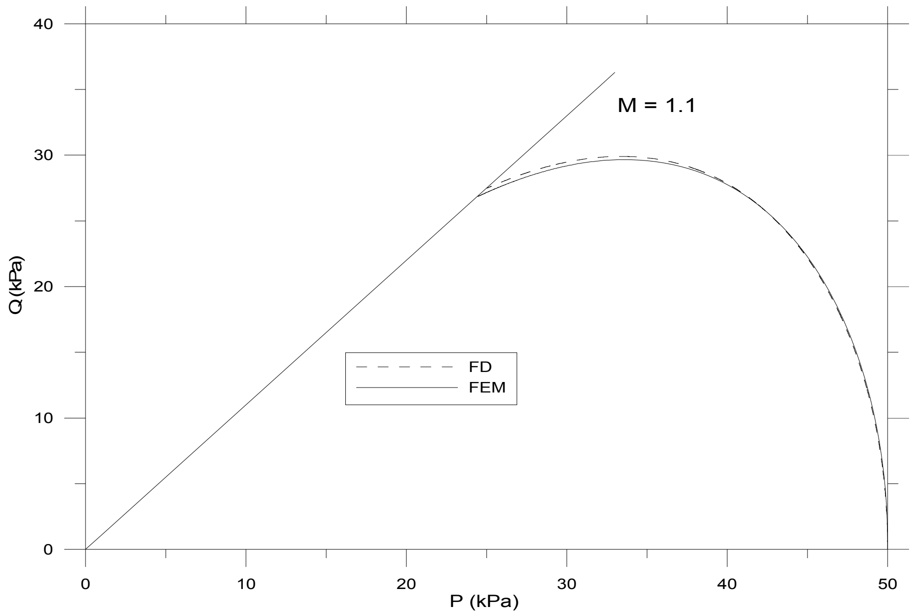

Figure 4.17(a): Comparison of stress paths in undrained conditions (P$_0$ = 50 kPa, β = 1.3)

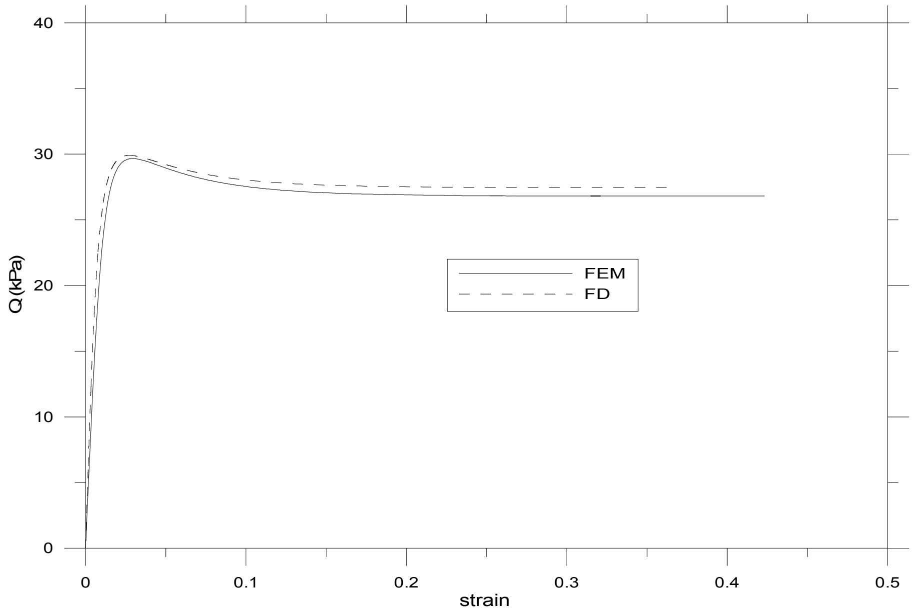

Figure 4.17(b): Comparison of stress-strain curves in undrained conditions (P_0 = 50 kPa, β = 1.3)

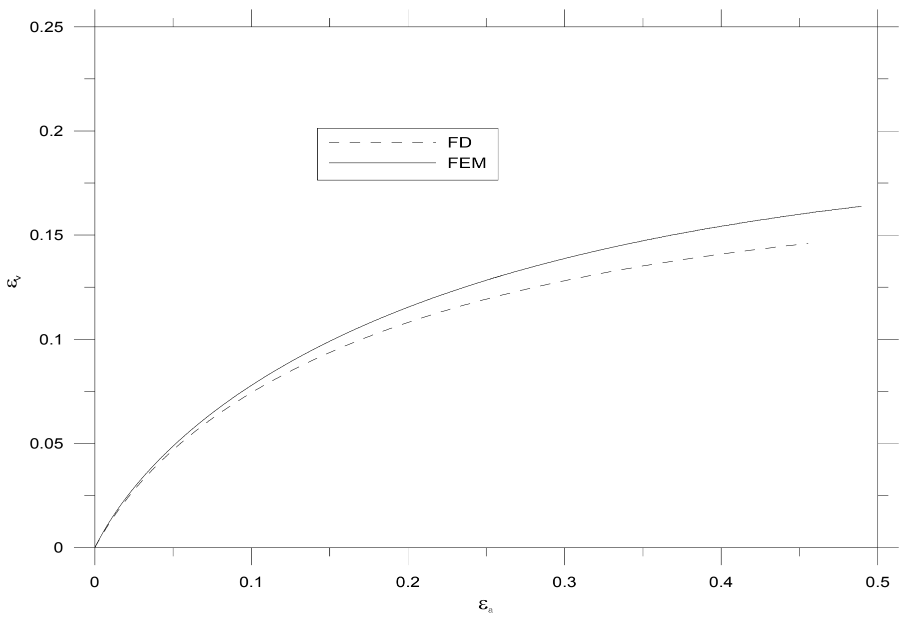

Figure 4.18(a): Comparison of volumetric and deviator strains (P_0 = 100 kPa, β = 1.3)

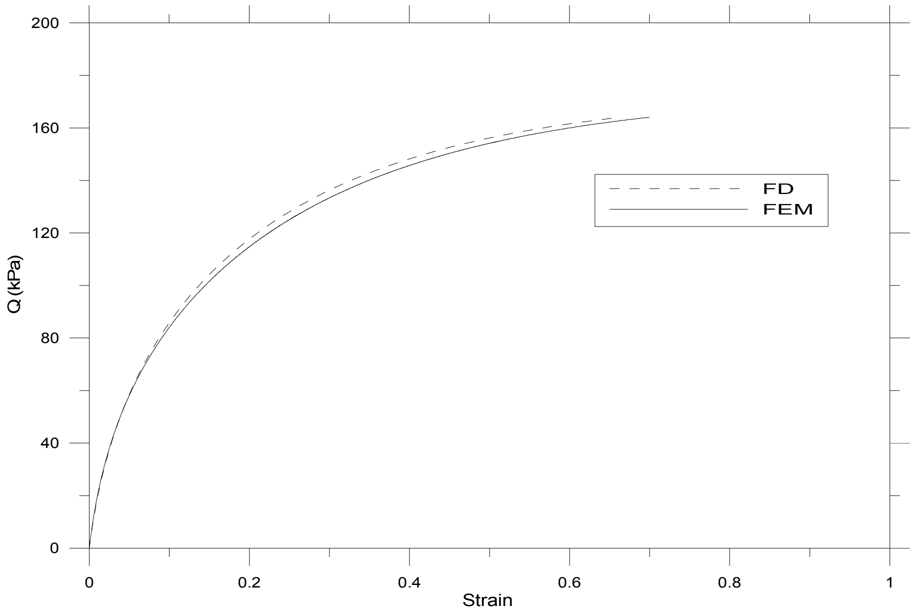

Figure 4.18(b): Comparison of stress-strain curves in drained conditions (P_0 = 100 kPa, β = 1.3)

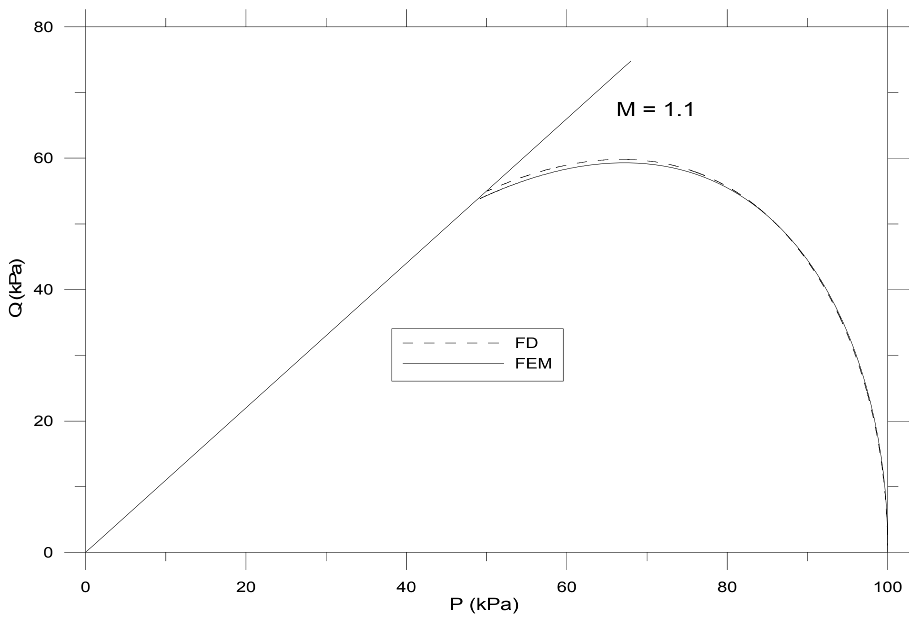

Figure 4.19(a): Comparison of stress paths in undrained conditions (P_0 = 100 kPa, β = 1.3)

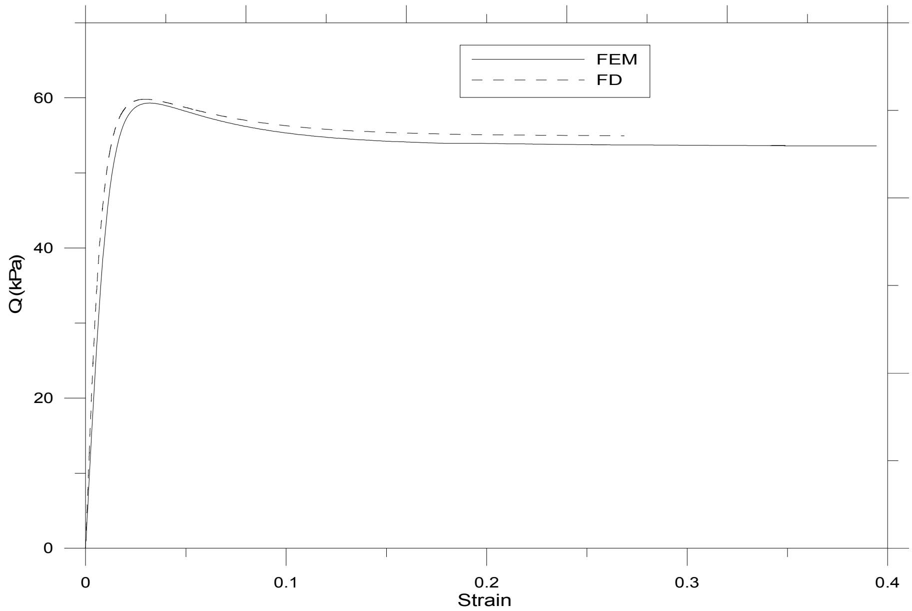

Figure 4.19(b): Comparison of stress-strain curves in undrained conditions (P_0 = 100 kPa, β = 1.3)

<u>b) Change β</u>

The simulation results using different β are plotted in Figures 4.12 to 4.19. Comparison of the two methods shows that the differences between them are very small when the strain-softening parameter β changes. Depends on the parameter is choosing, the stress curve may or may not shoot up to the M line when η approaching M.

Simulation results with varies range of parameters show that there's no outstanding difference between the two methods. Depends on the soil parameters are chosen, numerical error may occur when the stress state approaching the critical state line in both methods.

4.4.2 One-dimensional consolidation

To check the numerical stability of the FEM code of the SSC model, loading and unloading simulations are performed in one-dimensional conditions.

The height of the soil is assumed to be 5cm and the radius of the soil is assumed to be 2.5cm. The FEM mesh soil sample consists of 12 6-noded axisymmetric iso-parametric elements and 39 nodes with three degrees of freedom per node. The soil is assigned to be either the MCC or the SSC model. The soil parameters are assigned as the same of the triaxial test simulations. The bottom boundaries are modelled as being restrained from movement both horizontally and vertically (fixed supports). The side boundaries and the axials are restrained from movement only in the horizontal direction (roller supports). The top boundaries are assigned as permeable while all other boundaries are assigned as impermeable.

In the case of the SSC model, the parameters assigned are the same as the MCC parameters but are much small, i.e., $\Delta_{y,i}$=0.001. The numerical results show that there's no obvious difference between the models when the SSC parameter $\Delta_{y,i}$ is very small. These results indicate that the SSC model can degenerate back to the MCC model when the meta-stable structure of the SSC is not obvious.

Comparison of the consolidation curves after yielding for the two cases are shown in Figure 4.20 in which it can be seen that the consolidation curve of the SSC model is above that of the MCC model. When the stress becomes large enough, the two consolidation curves eventually almost merge together.

4.4.3 Unit cell consolidation simulation

To further check the numerical stability of the FEM code of the SSC model, the unit cell consolidation is simulated. The main purpose of this simulation is to check whether there are significant numerical issues between the boundary of the SSC and MMC soils.

The radius of the unit cell is assumed to be 2m and the height of the unit cell is 10m. The top 4m soils are assumed to be MCC soil while the bottom 10m is assumed to be SSC soils. The soil parameters are exactly the same as the soils in section 4.4.2 of the one-dimensional consolidation simulation.

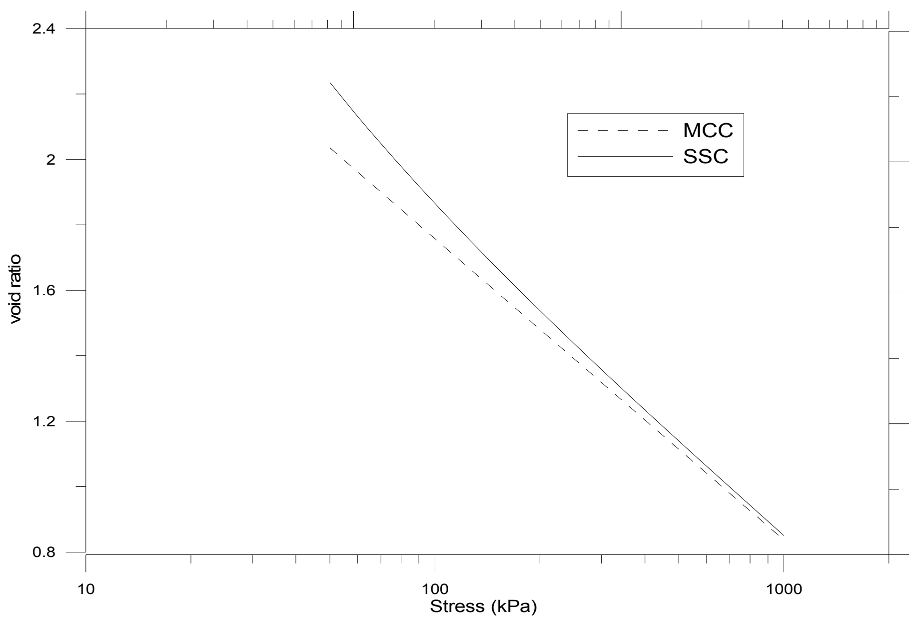

Figure 4.20: Comparison of one-dimensional consolidation curves

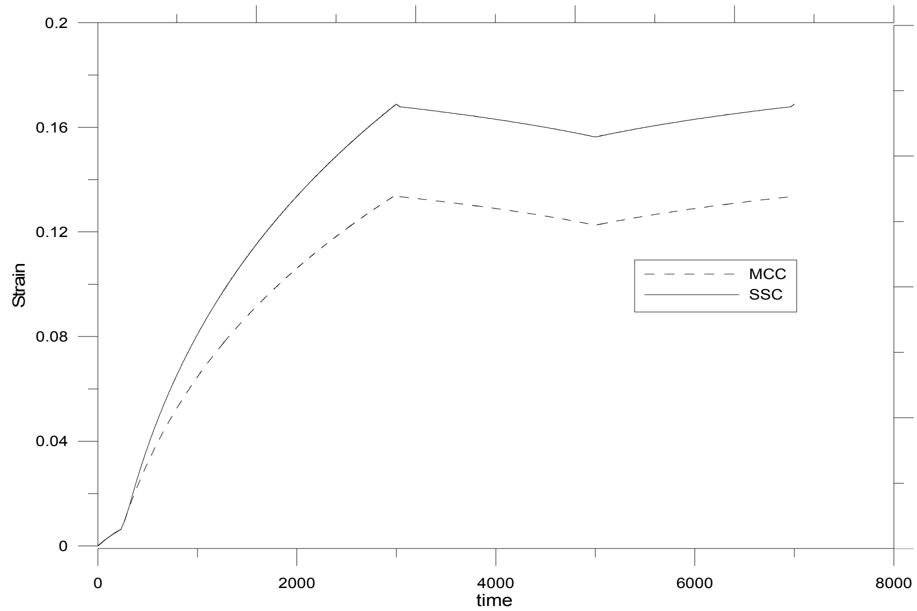

Figure 4.21: Comparison of time-strain curves for one-dimensional consolidations

The FEM mesh of the double-layer one-dimensional consolidation simulation contains 80 6-noded axisymmetric isoparametric elements and 187 nodes with three degrees of freedom per node. The bottom boundaries are modelled as being restrained from movement both horizontally and vertically (fixed supports). The side boundaries and the axials are restrained from movement only in the horizontal direction (roller supports). The top boundaries are assigned as permeable while all other boundaries are assigned as impermeable.

The simulation is performed by applying displacement control. The soil is compressed with displacement of 1.5m at the top (15% strain) in 3000 time-steps.

Then, it is unloaded to 1.25m (12.5% strain) in 500 time-steps and reloaded back to 1.5m (15% strain) in 500 time-steps.

The numerical simulation results shown in Figure 4.21 indicate that, at the same stress, the SSC is softer than the MCC. During the unloading and reloading states, as changes in the strain of the two soils are the same, it is confirmed that there is no severe numerical issue related to unloading and reloading during the interface of the two different types of soil.

4.5 CONCLUSIONS

From the above sections, the new SSC model can simulate the typical SSC soil behaviour very well. Simulation results of the FD methods and the FEM are about the same, thus the numerical code coded into the FEM program AFENA does not have sever numerical problems and is suitable for solving practical engineer problems.

CHAPTER FIVE

STONE COLUMNS WITH WISH-IN INSTALLATION

5.1 INTRODUCTION

Stone columns have been widely used as a ground improvement technique for many years. Potential functions of the stone columns are increase in bearing capacity, reduction in post-construction settlement time (by accelerating settlement rate), and reduction in total settlement. Design procedures for determining the bearing capacity of stone columns are well documented in FHWA (1983). The prediction of settlement is, however, less certain. For a road embankment section that leads to a piled abutment, the role of stone columns in limiting settlement is crucial. Applying a generous safety factor to the bearing capacity does not necessarily guarantee compliance with settlement limits.

Stone columns may be used to support a column load in a manner similar to that of piles, i.e., the external load is applied to the top of a stone column and not to the surrounding soil. In a road embankment situated on soft clay, stone columns function more as soil reinforcement and their mechanism is much more complicated. Immediately after the imposition of fill loading, most of the total stress is taken by pore water pressure in the clay and, thus, the stone columns only play a small role in resisting the fill loading so that, indeed, the initial settlement will be small. It is only with the dissipation of pore water pressure over time that the clay will settle and the weight of the fill will “arch over” to the stone columns.

During this process, the stone columns will be strained both axially and radically, the latter leading to increase in the confining stress from the surrounding soil due to the cavity expansion mechanism. Some of the fill loading will still be transferred to the clay as increase of effective stress also leads to increases in the confining stress. Therefore, this mechanism involves the interaction of the stone columns and the dissipation of pore water pressure in the surrounding soft clay. The latter is a coupled process between mechanical behaviour (as governed by the effective stress principle) and the flow of pore water (as governed by Darcy's law).

Stone columns in a typical SSC near the coast between New South Wales and south-east Queensland are selected for a case study of the effects of a soft clay structure on reducing the performance of stone columns. As the observed settlement of a trial embankment built on that kind of clay, when strengthened with stone columns, indicated that stone columns are not effective in reducing settlement. It is hypothesised that very soft clay does not provide adequate confining stress to stone columns.

As pointed out by Christoulas et Al. (1997), distributions of fill load depend on the relative stiffness of the stone columns and the soil between their spacing. The stiffness of a stone column is affected by the selection of its material and the pre-confining stress of the geosynthetic, if it is geosynthetic–encased. The stiffness of a soil is affected by its initial properties and its disturbance during stone column installation. These influencing factors, in total, determine the relative stiffness of stone columns and the soil between their spacing. Thus, the installation method, the selection of stone material and the pre-straining of the geosynthetic should be considered.

Depends on the methods of the stone column installation, the disturbance of the soil is different. In extreme are the wish-in installation which has no disturbance of the surrounding soil and the other is full displacement installation method which cause nearly biggest disturbance of the surrounding soil among the current installation methods.

In this Chapter, the wish-in installation method is assumed and disturbance to the soil due to the installation of stone columns is not considered. Disturbance of the soil caused by the full-displacement installation method will be studied in Chapters 6 and Chapter 7.

Thus, in this Chapter, numerical studies on the performance of pre-strained geosynthetic encased stone columns are presented. New elements are designed to simulate both the geosynthetic and geosynthetic encased stone columns. As the MCC model is widely used in current engineering design, stone columns installed in MCC soils are examined first. Varies conditions including no pre-straining geosynthetic encasement, reference parameters and reduction of T_{pre} or K are analysed. Reduction of T_{pre} refers to in the real construction, the pre-strain and the stone stiffness may not be able to reach the maxim designed value. But on average, 50% of the maxim value is very conservative and highly achievable. The SSC model, with the same MCC parameters but extra SSC parameters is then introduced. The above cases are simulated with SSC model to examine the performs of the geosynthetic encased stone columns installed in the SSC soils.

As the primary issue in this study is the development of settlement over time after the completion of stone column installation, a fully coupled analysis is performed. To reduce the computational effort, a unit cell idealisation is adopted to simplify the analysis.

Table 5-1 Dimensions of unit cell

Items	**Dimensions (m)**
Embankment height	4.0
Sand blanket thickness	1.0
Diameter of stone column	0.6
Depth of groundwater table	0.0
Thickness of soft clay	10.0

Note: unit cell radii vary for different cases: 2.0m and 1.3m

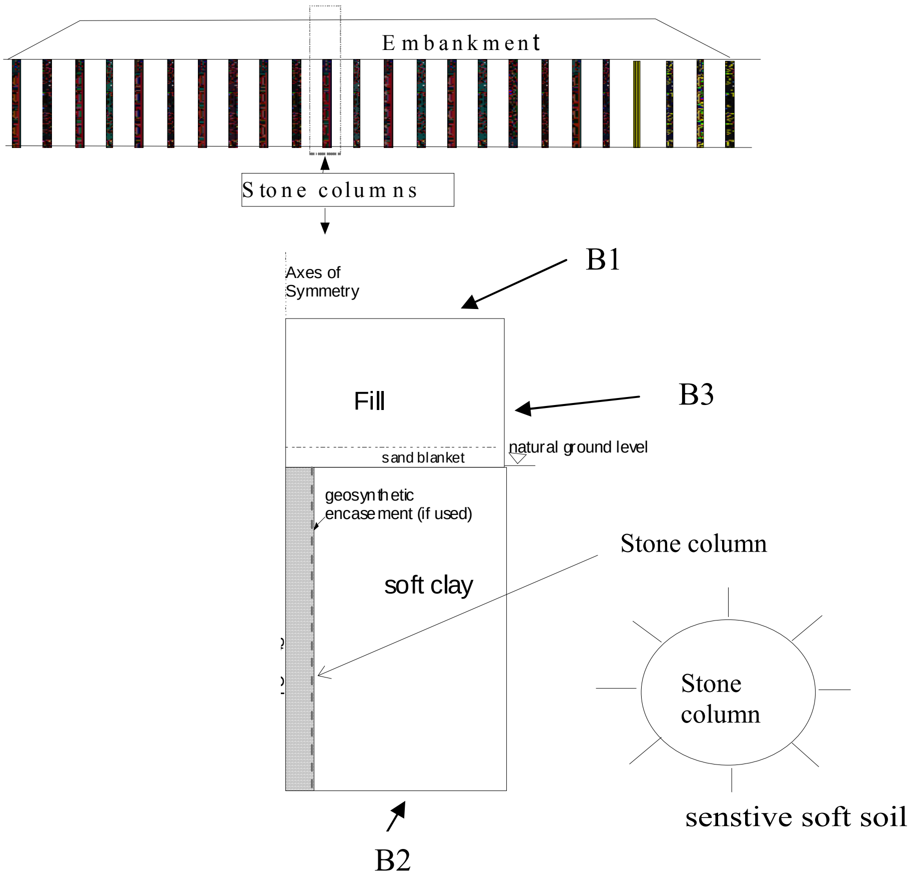

Figure 5.1(a) Idealization of stone column

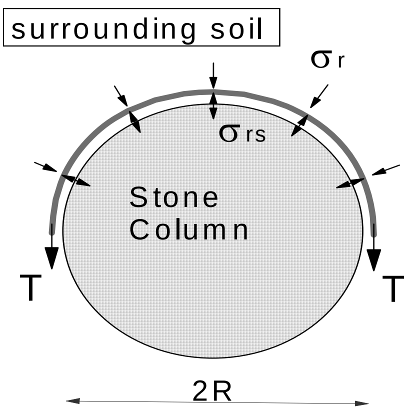

Figure 5.1(b) Hoop tension and radial stress in stone column if geosynthetically encased

5.2 Numerical idealisation

5.2.1 Unit cell idealisation

The numerical simulations examine conditions in which the fill area is large relative to the thickness of the SSC and a large number of stone columns are installed. To simplify the simulations for analysis purposes, a unit cell idealisation is adopted, as shown in Figure 5.1(a), which is a reasonable approximation of areas away from the edges of an embankment. It is assumed that the stone columns are installed in a regular rectangular or triangular pattern with a centre-to-centre spacing (denoted as S). Based on equivalence in the externally loaded area per stone column, the radius of the unit cell may be approximated as 0.55S for a square pattern and 0.525S for a triangular pattern.

Since the normal space for an installed stone column is from around 1.3m to 2.0m, stone column spaces of these dimensions are selected as representative cases. Listed in Table 5-1 are the assumed dimensions of the unit cell: the height of the embankment is 4.0m; the thickness of the SSC is 10.0m; the depth of the ground watertable is set to 0.0m; the 1.0m-thick sand blanket is well above groundwater level; and the diameter of the stone column is 0.6m. The top boundary of the clay layer is idealised as a free-draining boundary whereas the outer and bottom boundaries of the unit cell are modelled as impermeable. The fill, sand blanket and stone columns are idealised as highly permeable materials.

5.2.2 Geosynthetic encasement

As shown in Figure 5.1(b), the radial stress acting on a stone column, $\sigma_{r,s}$, is induced by the radial stress of the surrounding clay, $\sigma_{r,c}$, and the hoop tension, T, in the geosynthetic encasement. Thus:

$$\sigma_{r,s} = \sigma_{r,c} + T/R \tag{5-1}$$

where R is the radius of the stone column. The second term can be viewed as the additional effective radial stress due to the geosynthetic encasement. Both T and $\sigma_{r,c}$ can be decomposed into two parts: the initial value (i.e., after stone column installation); and increases due to the placement of fill and time-dependent deformation. Therefore, equation (5-1) can be re-written as:

$$\begin{aligned} \sigma_{r,s} &= \sigma_{r,c}(i) + T(i)/R + \Delta\sigma_{r,c} + \Delta T/R \\ &= \sigma_{r,c}(i) + \sigma_{r,p} + \Delta\sigma_{r,c} + \Delta T/R \end{aligned} \tag{5-2}$$

where (i) denotes the initial (as-installed) state, σ_{rp}=T(i)/R, and Δ indicates increases due to loading. It should be noted that the as-installed hoop tension, T(i), is generally non-zero and its magnitude depends on the installation method employed. It is essential to have T(i) included in the modelling. One can also express increases in stress in a stone column by:

$$\Delta\sigma_{r,s} = \Delta\sigma_{r,c} + \Delta T/R \tag{5-3}$$

To enable the stones to develop adequate strength and stiffness, $\sigma_{r,s}$ has to be of an adequate magnitude. If a sufficiently high $\sigma_{r,c}$(i) can be generated, then both T(i) and ΔT are not needed. Indeed, the value of $\Delta\sigma_{r,c}$ will also be low because of axial strain and, thus, the radial expansion of a stone column will be small. However, one can compensate for a low $\sigma_{r,c}(i)$ value, which may be due to the surrounding clay being very soft, by geosynthetic encasement which gives non-zero values for T(i) and ΔT.

The value of T(i) is governed by two considerations: i) the pre-straining action due to installation; and ii) the triaxial extension failure of the stones at the top zones. Compaction of the stones and the consequent radial expansion of a stone column and its prefabricated geosynthetic encasement to its final diameter will pre-strain the geosynthetic encasement. This pre-straining will induce a pre-loading, T_{pre}, in the geosynthetic encasement. As the pre-straining action is related to the radial expansion of a stone column as a result of compaction of the stones, T_{pre} may be approximated to be constant, i.e., as an input parameter to the analysis. However, near the top of the stone columns, the magnitude of T(i) is limited by the maximum radial stress, the condition of the triaxial extension failure of the stones, and is defined by:

$$\sigma_{r,s}(i) = K_p \sigma_{z,s}(i) \qquad (5\text{-}4a)$$

where $\sigma_{z,s}(i)$ is the in-situ vertical stress (due to the self-weights of the stones), $K_p=(1+\sin\phi)/(1-\sin\phi)$, and ϕ is the secant friction angle of the stones. Equation (5-4a) leads to:

$$T_{ext}(i) = RK_p \sigma_{z,s}(i) \qquad (5\text{-}4b)$$

where $T_{ext}(i)$ denotes the calculated hoop tension based on the triaxial extension failure of the stones. Therefore, T(i) is less than both $T_{pre}(i)$ and $T_{ext}(i)$. Assuming the water table to be at natural ground level (NGL), the resultant T(i) profile is given by

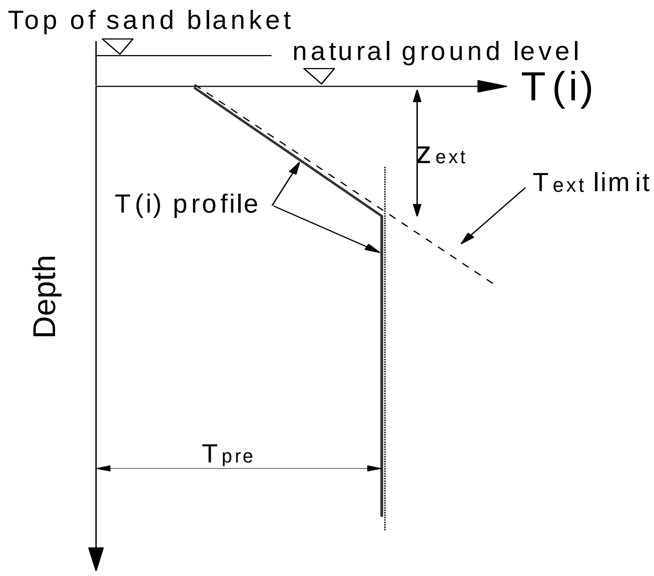

Figure 5.2 Initial hoop tension

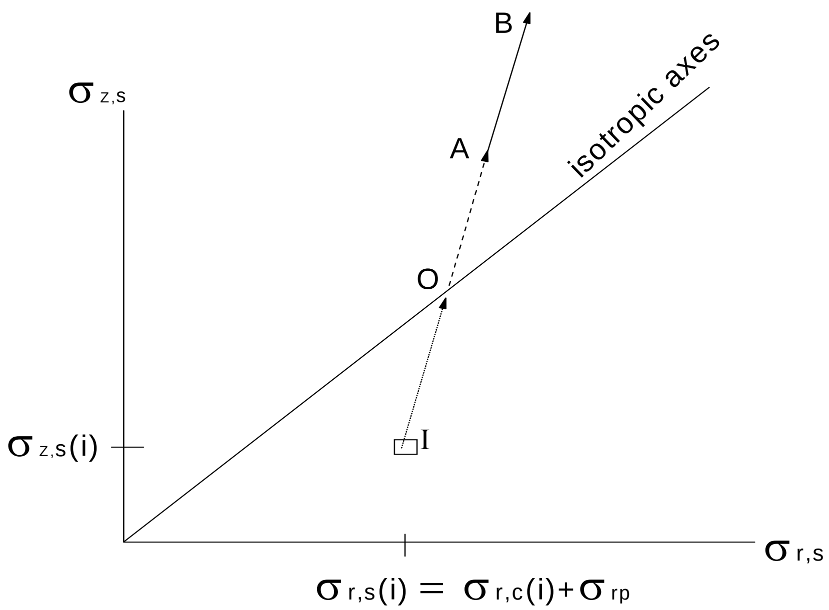

Figure 5.3 Effective stress path of typical stone column element

the bi-linear solid line in Figure 5.2. The link in the bi-linear relationship corresponds to the condition of $T_{pre}=T_{ext}$, which occurs at the depth, z_{ext}, and is given by:

$$z_{ext} = \frac{T_{pre}/RK_p - \gamma_b t_b}{\gamma'_s\left(1 - \rho K_0/K_p\right)} \tag{5-5a}$$

where: γ'_s = effective unit weight of stones; γ_b = unit weight of sand blanket; ρ = ratio of effective unit weight of clay to that of stones (=0.65); t_b = thickness of sand blanket (=1m); K_o = at-rest earth pressure coefficient of soft clay; and z_{ext} is measured from NGL. In calculating K_p, noting that $\rho K_o/K_p$<<1, equation (5-5a) can be approximated as:

$$z_{ext} = \frac{1}{\gamma'_s}\left(\frac{T_{pre}}{RK_p} - \gamma_b t_b\right) \tag{5-5b}$$

5.2.3 Material models

a) Fill

The fill is modeled as a Mohr-Coulomb elastic-plastic material with a non-associative flow rule. The parameters adopted for the analysis are listed in Table 5-2.

b) Geosynthetic encasement

The geosynthetic encasement is modeled as a cross-anisotropic elastic element. The horizontal stiffness is taken to be 2000 kN/m for the reference analysis. The axial stiffness is taken to be 2% of the horizontal stiffness, in line with Lo et al. (2007), so that it will not "numerically" act as a vertical cylindrical reinforcing tube. The

Poisson's ratio is taken to be zero to eliminate cross-coupling between the axial and radial stresses. The use of an elastic element inherently implies that tensile rupture of the geosynthetic will not occur and, therefore, the locked-in tension, T(i), will not influence the behaviour of the geosynthetic. However, T(i) will induce a higher initial radial stress in the stones, as represented by the term σ_{rp} in equation (5-2). This will lead to a higher radial stress in the stones in all stages of the analysis, the effects of which can be modeled by a stone column element, as explained in the next section.

<u>c) Stone column</u>

The stone column is modeled as a free-draining material. A stone column element is introduced into AFENA (Carter and Balaam, 1995) and is, in fact, a modified Mohr-Coulomb elastic-plastic element with a non-linear elastic part similar to that in the Duncan-Chang model (Duncan and Chang, 1970). However, a criterion for selecting unloading and loading stiffnesses is introduced, as explained below.

The stress path followed by an element along the centre of a stone column can be schematically illustrated, as in Figure 5.3. This illustration is also considered to be an approximation of other stone column elements. As a result of T(i) and the corresponding locked-in confining stress in the stones, $\sigma_{r,p}$=T(i)/R and $\sigma_{z,s}<\sigma_{r,s}$. Therefore, in the early phase of embankment loading, denoted by "IO" in Figure5.5, any increase in $\sigma_{z,s}$ due to embankment loading will lead to a reduction in the stress ratio and move towards the isotropic stress state. Thus, the element will behave in an "unloading mode", for which the Young's modulus is given by the Janbu's equation, i.e., the initial Young's modulus of the Duncan-Chang equation, as:

$$E_0 = k\left(\frac{\sigma_{r,s}}{p_a}\right)^n p_a$$
$$= k\left(\frac{\sigma_{rp} + \sigma_{r,c}(i) + \Delta\sigma_{r,s}}{p_a}\right)^n p_a \qquad (5\text{-}6)$$

In which k and n are Duncan-Chang parameters determine the initial Young's modulus.

Once the stress state crosses and traces away from the isotropic axes, the Young's modulus is calculated using the Duncan-Chang equation as:

$$E = E_0\left(1 - r_f S\right)^2 \qquad (5\text{-}7)$$

In which r_f is the destroying ratio.

where E_0 (initial Young′s modulus) is given by:

$$S = \frac{(\sigma_1 - \sigma_3)(1 - \sin\phi)}{2\sigma_3 \sin\phi + 2c.\cos\phi} \qquad (5\text{-}8)$$

It is recognized that, as the stress path crosses the stiffness response, and before it reaches state "A" (defined by a stress ratio equal to that of the as-installed state "I"), the stiffness actually transitions from that in equation (5-6) to that in equation (5-7). However, for the sake of simplicity, the criterion for moving away from the isotropic stress state is used to trigger the use of the Duncan-Chang equation for loading.

The parameters assigned for the analysis are given in Table 5-2. It should be noted that the Duncan-Chang parameters are inferred conservatively from triaxial test results obtained from a well-graded sandy gravel compacted to maximum dry density, as determined by the Standard Proctor test. These results give a curved failure surface, the approximation for which uses the linear Mohr-Coulomb failure function, and leads to a small non-zero cohesion intercept of 15 kPa.

In the simplified analysis presented in Lo et al. (2007), the average Young's modulus, $\overline{E}$, calculated using equations (5-6) and (5-8) and neglecting $\Delta\sigma_{r,s,}$ is used and gives:

$$\begin{aligned}\overline{E} &= \frac{1+(1-r_f)^2}{2}\left(\frac{\sigma_{r,s}(i)}{p_a}\right)^n p_a \\ &\approx 0.5\left(\frac{\sigma_{r,s}(i)}{p_a}\right)^n p_a\end{aligned} \qquad (5\text{-}9)$$

The results of the preliminary analysis show that significant portions of the stone column elements are close to the Mohr-Coulomb failure function at an early stage of time-stepping. This may present a numerical problem (in the form of a lower bulk modulus), as discussed in Lo (2001). To suppress such a problem, the Poisson's ratio is taken to be a function of S, following Lo (2001), and is expressed as:

$$\mu = \mu_0 + (0.496 - \mu_0)\sqrt{S} \qquad (5\text{-}10)$$

Thus, the Poisson's ratio in Table 5-2 is, in fact, μ_0.

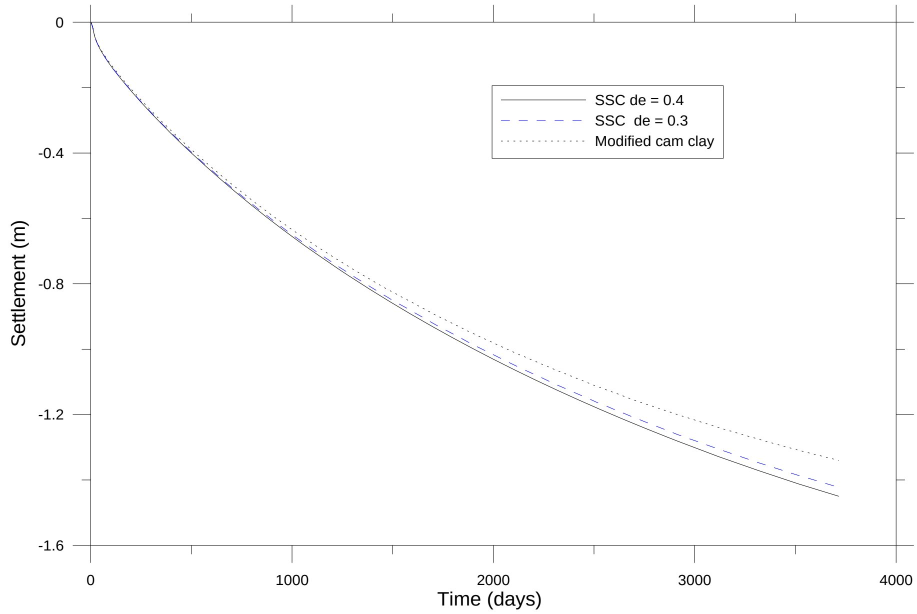

Figure 5.4(a) Displacements without stone columns

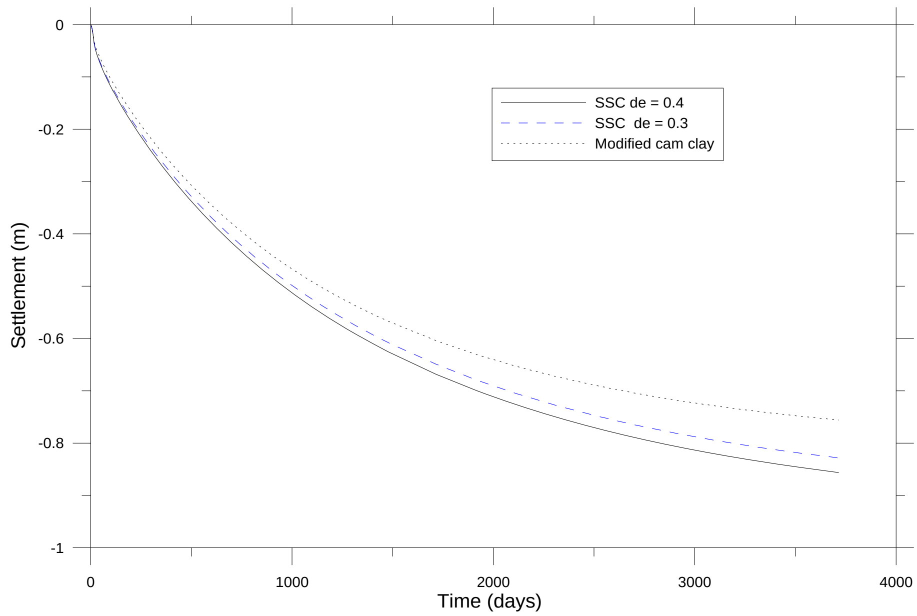

Figure 5.4(b) Displacements with non-geo-grid reinforcement stone columns

d) Soft clay

The whole depth of the soft clay is modeled by the MCC model first when its depth is between 4.0m and 10.0m from NGL. Then, it is modeled by the SSC model using the same MCC parameters, with its depth from NGL up to 4.0m remaining modeled by the MCC model with the same MCC properties as before. The relevant MCC and SSC parameters are given in Tables 5-2 and 5-3 respectively. For verification purpose, $\Delta = 0.0$ is chosen and compare the results with that using the MCC model, simulation results shown that the two results are the same which indicate that the SSC model can degenerate back to the MCC model when the SSC feature is negligible. In Table 5-3, the average of the three maximum tested values of Δ is chosen as the input parameter for the analysis. The upper boundary values, determined by Cottenina's (2000) method, are compared in Figure 5.4 for the parameter sensitivity check.

The comparison shows that Δ is not very sensitive in the range of 0.3-0.4 even in a 2.0m radius unit cell. In this chapter, the average value, Δ=0.3, is used rather than the upper boundary value, Δ=0.4. In-situ stress is assigned based on an effective unit weight of 6 kN/m^3 and K_o=(1-sinϕ)=0.535 for normally consolidated clay. As the analysis models the coupled process of time-dependent dissipation of pore water pressure, permeability parameters are also needed. The horizontal permeability of the soft clay is assumed to be 2.3x10^{-10}m/s, and a horizontal to vertical permeability ratio of 2 is assigned. A typical undrained shear strength profile is also assumed, from which it is inferred, following Potts and Ganendra (1991), that the top 3m is over-consolidated even though the soil is soft. Over-consolidation is characterized by p_c, the effective mean stress at the apex of the MCC ellipse. The value of p_c is assumed to be 70 kPa at NGL and to reduce to 40 kPa at a 3m depth.

5.2.4 Construction consequence

A coupled analysis is introduced to simulate long-term effects and the following construction sequence is modelled:

1. Initialize in-situ stress of soft clay deposit under green field conditions;
2. Place sand blanket in for 4 days;
3. Turn appropriate regions of soft clay into stone column elements and activate geosynthetic elements;
4. Build embankment in a layer-by-layer manner at a rate of 0.25m/day; and
5. Time-step for 10 years so as to track dissipation of excess pore water pressure and, thus, development of settlement after completion of embankment.

It should be noted that the sand blanket needs to be placed first in order to form a platform to support the equipment required for installing the stone columns. Furthermore, step 3 above automatically simulates the effects of pre-straining due to installation.

5.2.5 Finite element mesh

Figure 5.5 presents the FEM meshes used to simulate the stone columns in SSC. They consist of 72 linear strain triangular (LST) elements with 175 nodes. Every LST element has 6 integration points and 3 degrees of freedom per node in the coupled analysis using the MCC model and 9 integration points and 3 degrees of freedom per node in the coupled analysis using the SSC model. Axisymmetric conditions are assumed and the boundary conditions are shown in Figure 5.1. The top boundary (B1) is modelled as permeable whereas the bottom (B2) is assigned to be impermeable and is restrained from movement both horizontally and vertically (fixed supports). The boundaries denoted by 'B3' are modelled as impermeable and are restrained from movement in only the horizontal direction (roller supports).

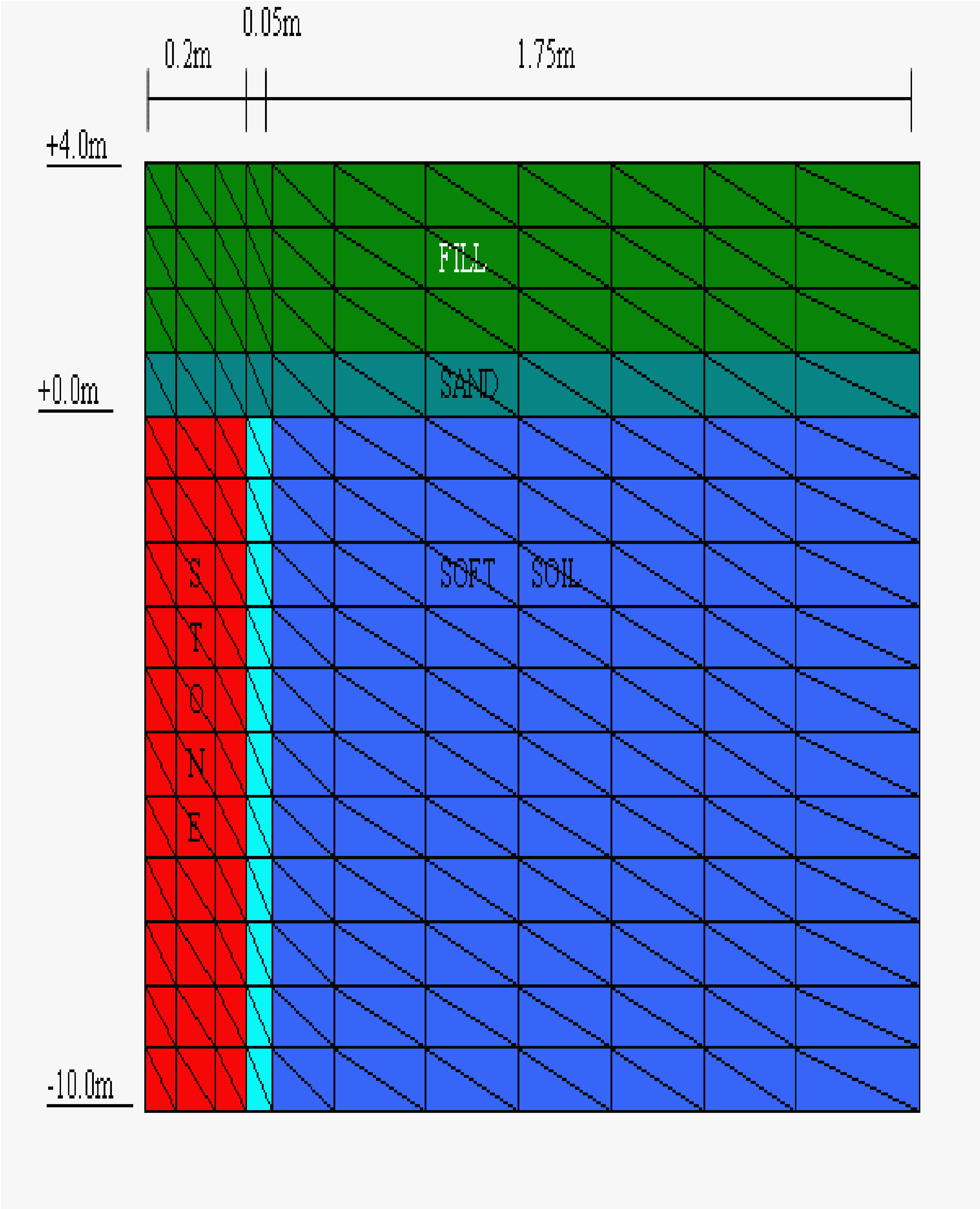

Figure 5.5 Mesh file of stone column

Table 5-2 Soil parameters (MCC model)

Material	**Parameter**	**Value**
Fill	ϕ	30^{o}
	c	20 kPa
	ψ	5^{o}
	Young's modulus	30×10^{3} kPa
	Unit weight	20 kN/m^3
Soft clay	M	1.1
	ϕ	27.7^{o}
	λ	0.65
	κ/λ	0.1
	e_{cs}	4.1
	k_r	2.3×10^{-10}m/s
	k_r/k_z	2.0
Stone	ϕ	45^{o}
	μ	0.30
	c	15 kPa
	k	2000
	n	0.65
	r_f	0.7

Note:

ϕ = friction angle;

c = cohesion;

μ = Poisson's ratio

ψ = dilatancy angle;

k_r = permeability in radial (horizontal direction);

k_z = permeability in vertical direction;(M, λ, κ, e_{cs}) are parameters for modified MCC model; and

(k, n, r_f) are parameters for Duncan-Chang model.

Table 5-3 SSC model parameters

Material	**Parameter**	**Value**
SSC	Δ	0.3
	P_{ci}	40 kPa
	b	2
	α	1.0
	β	1.1

Note:

Δ is the difference between the void ratio of SSC and the corresponding remodelling soil at a given corresponding P_{ci} on the isotropic consolidation line;

P_{ci} is a chosen stress state with its value being less than that of the initial yield point (according to the discussion in Chapter 3, P_{ci} can be any reasonable value less than the initial yield stress – 40kPa is chosen for calculations for convenience);

b is the SSC parameter describing the isotropic consolidation curve of SSC;

α is a parameter describing the amount of undrained strain softening; and

β is an undrained strain-softening parameter which determines the height of the strain-softening curve.

The geosynthetic-stone and geosynthetic-clay interfaces are assumed to be at full strength. This is because the installation of a stone column will automatically lead to undulating interfaces which are internal drainage nodes. Therefore, preferential slippage cannot occur and there is no need to introduce any special internal interface element.

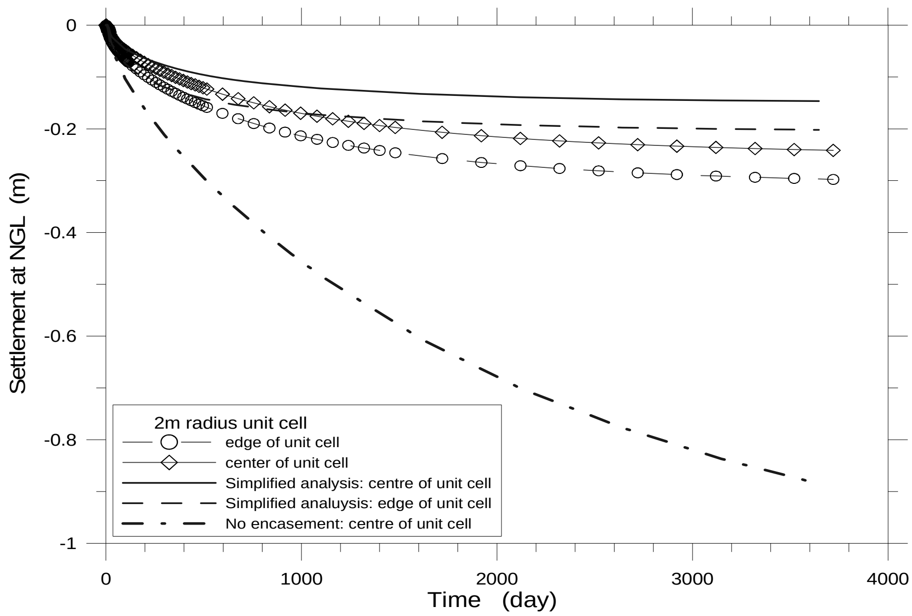

Figure 5.6(a) Settlement responses of reference analysis: comparison of settlement-time plots (2.0m radius unit cell, MCC model only)

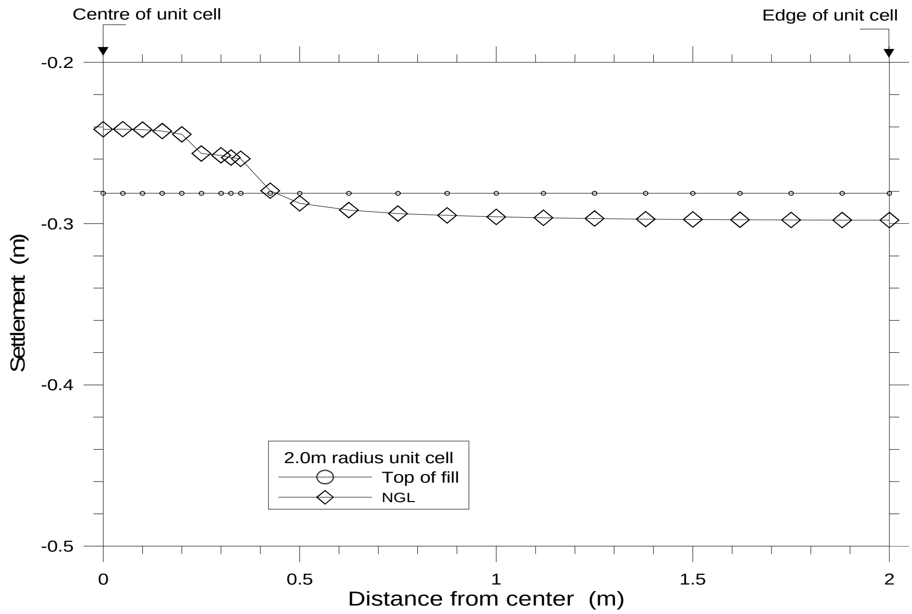

Figure 5.6(b) Settlement responses of reference analysis: settlement profiles at 10 years (2.0m radius unit cell, MCC model only)

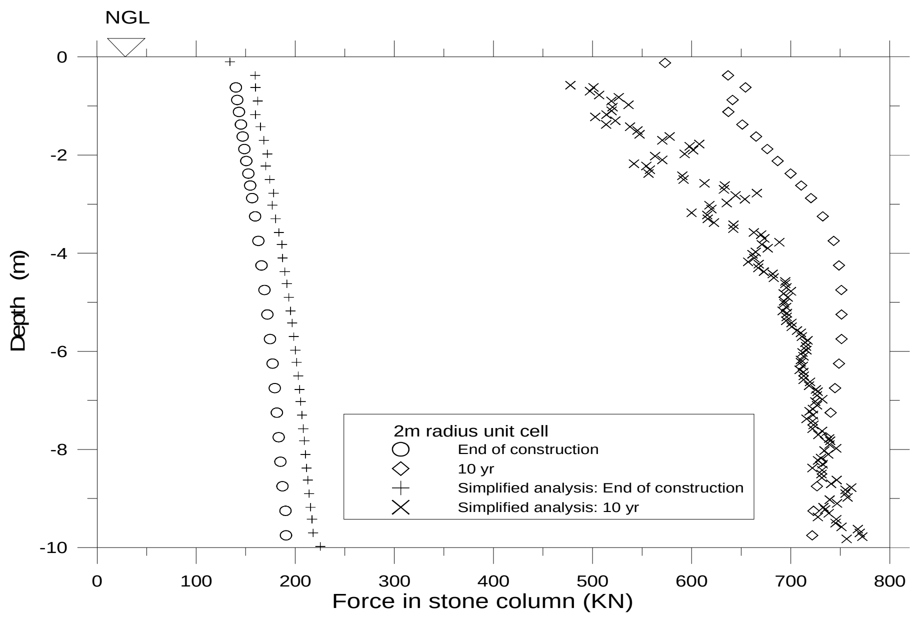

Figure 5.7 Distributions of column forces with depth: reference analysis (2.0m radius unit cell, MCC model only)

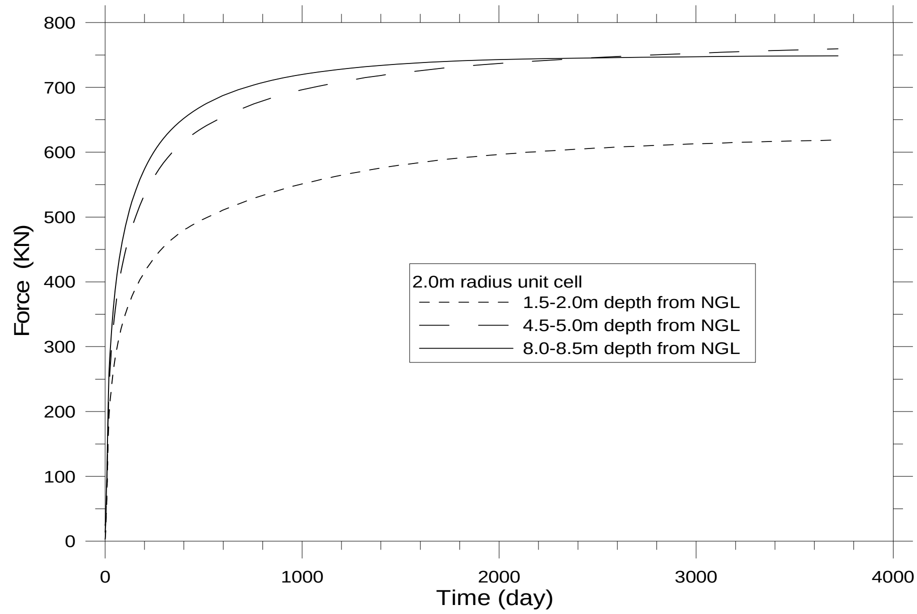

Figure 5.8 Evolutions of column forces with time: reference analysis

(2.0m radius unit cell, MCC model only)

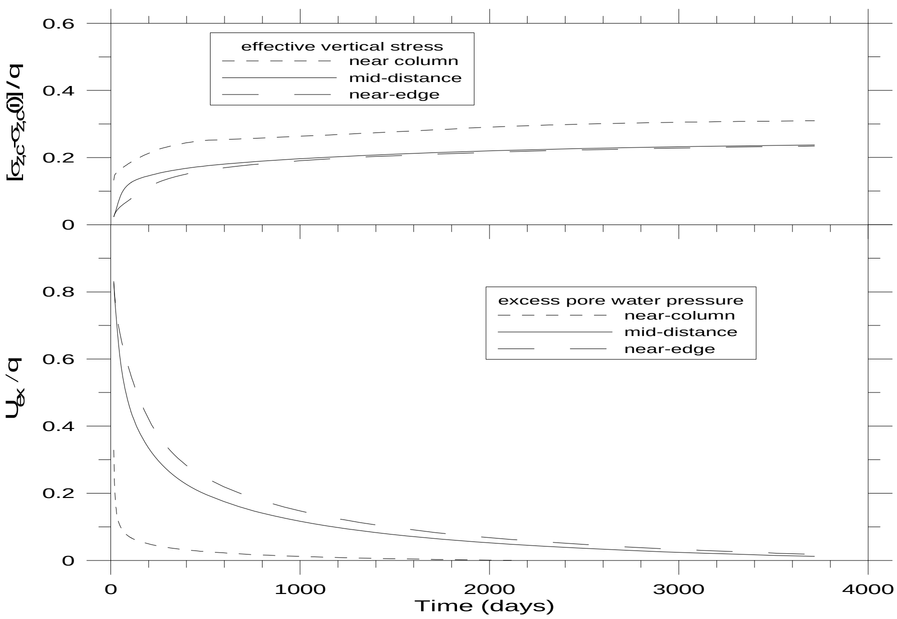

Figure 5.9. Consolidation responses in clay: reference analysis

(2.0m radius unit cell, MCC model only)

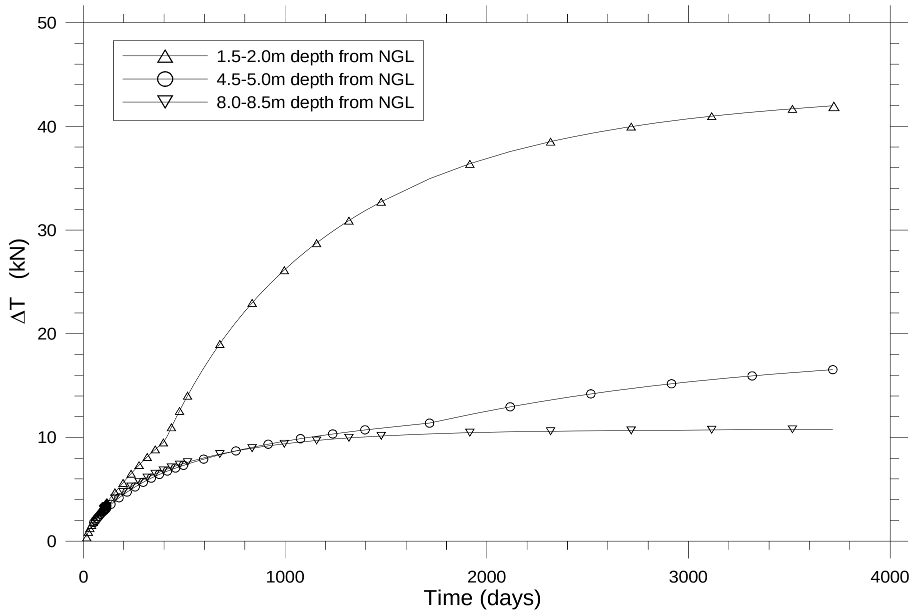

Figure 5.10 Increases in geosynthetic tension with time: reference analysis (2.0m radius unit cell, MCC model only)

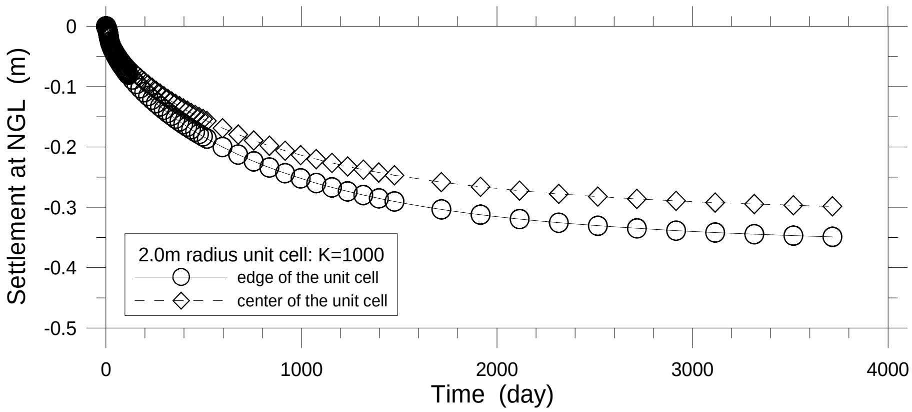

Figure 5.11(a) Settlement-time plots: reduced stone stiffness K=1000 (2.0m radius unit cell, MCC model only)

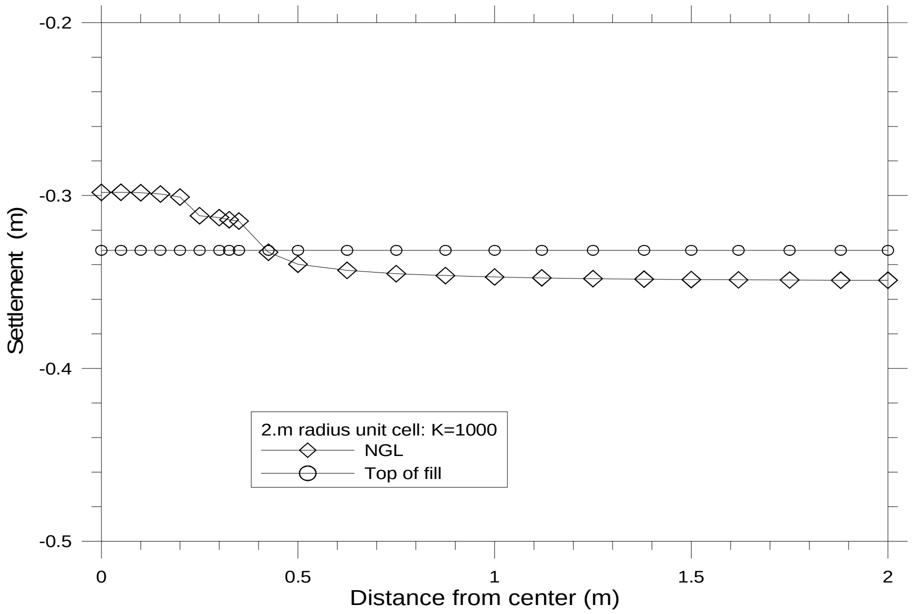

Figure 5.11(b) Settlement profiles: reduced stone stiffness K=1000

(2.0m radius unit cell, MCC model only)

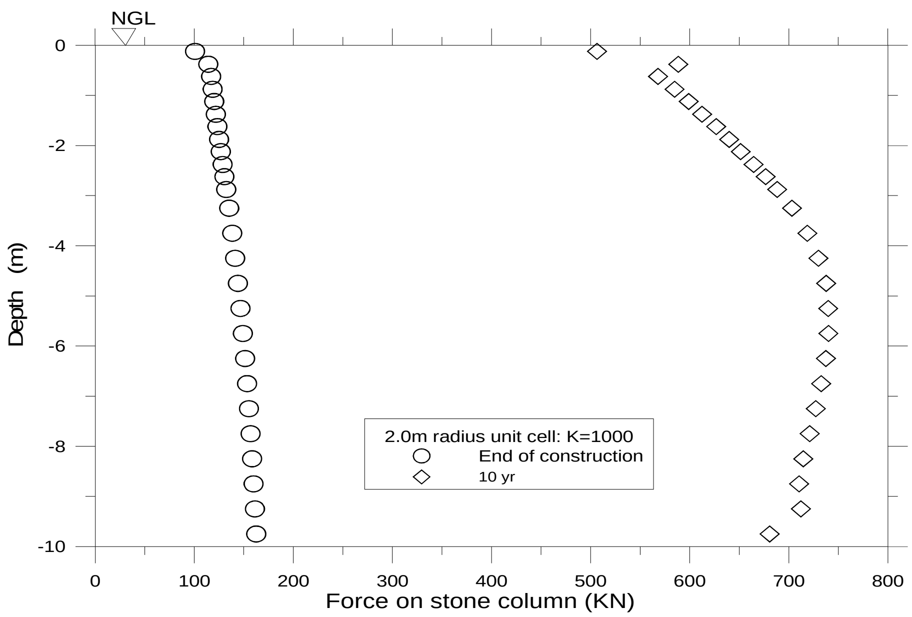

Figure 5.12 Distributions of column forces: reduced stone stiffness K=1000

(2.0m radius unit cell, MCC model only)

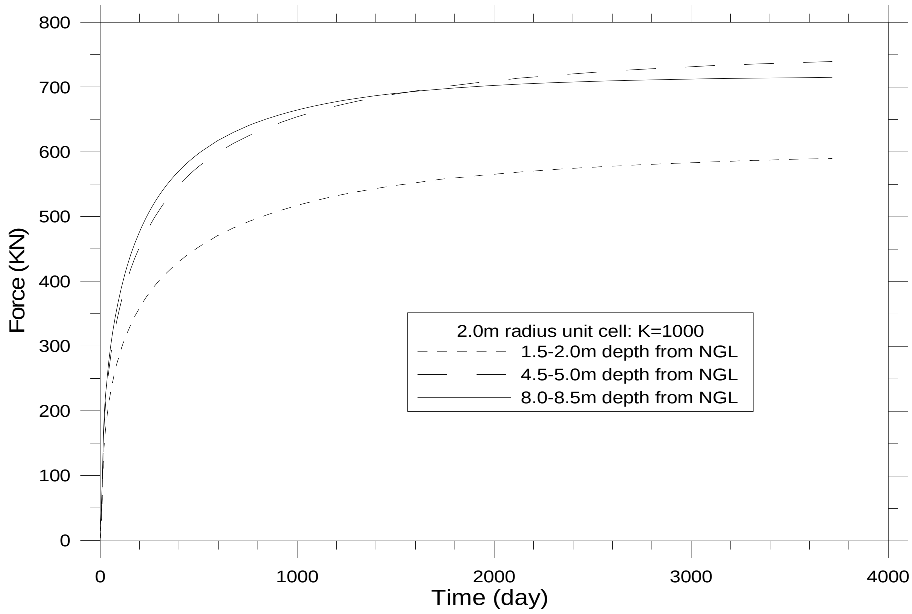

Figure 5.13 Evolutions of column forces with time: reduced stone stiffness K=1000 (2.0m radius unit cell, MCC model only)

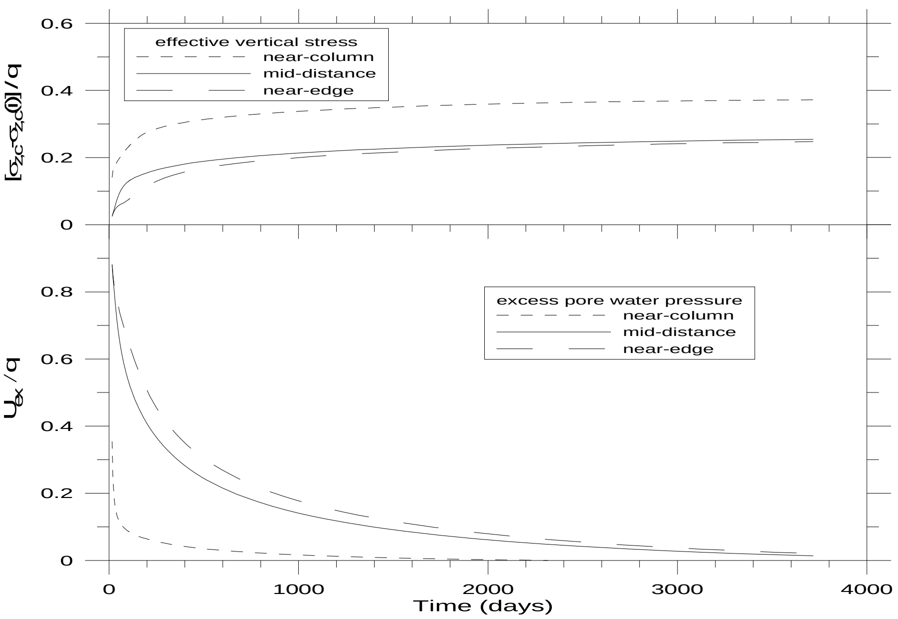

Figure 5.14 Consolidation responses in clay: reduced stone stiffness K=1000 (2.0m radius unit cell, MCC model only)

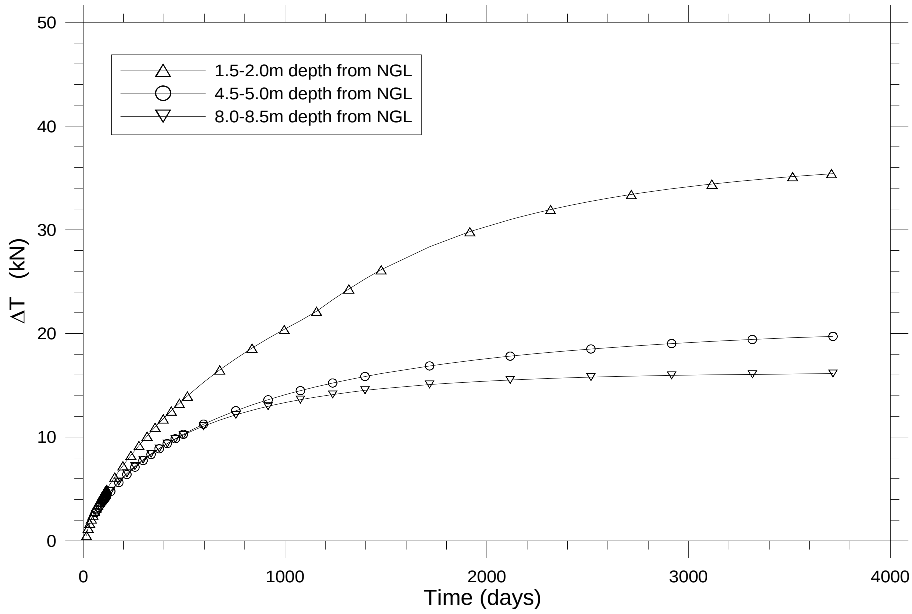

Figure 5.15 Increases in geosynthetic tension with time: reduced stone stiffness K=1000 (2.0m radius unit cell, MCC model only)

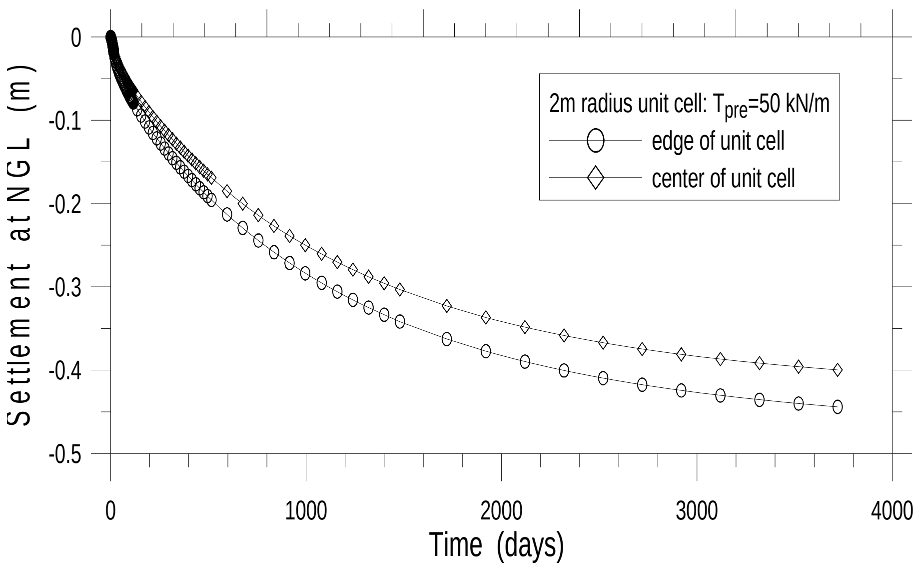

Figure 5.16(a) Settlement-time plots: reduced locked-in stress Tpre=50kN/m (2.0m radius unit cell, MCC model only)

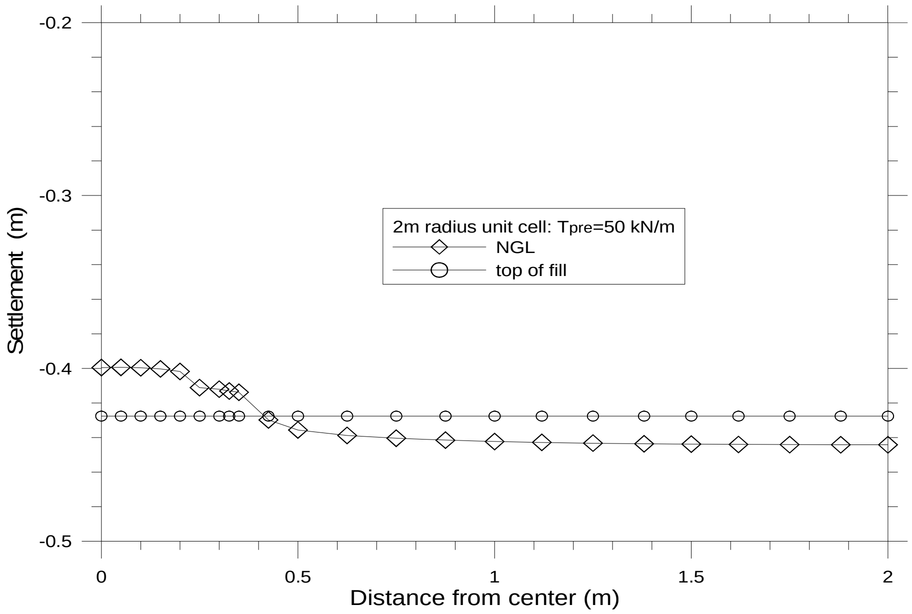

Figure 5.16(b) Settlement profiles: reduced locked-in stress Tpre=50kN/m

(2.0m radius unit cell, MCC model only)

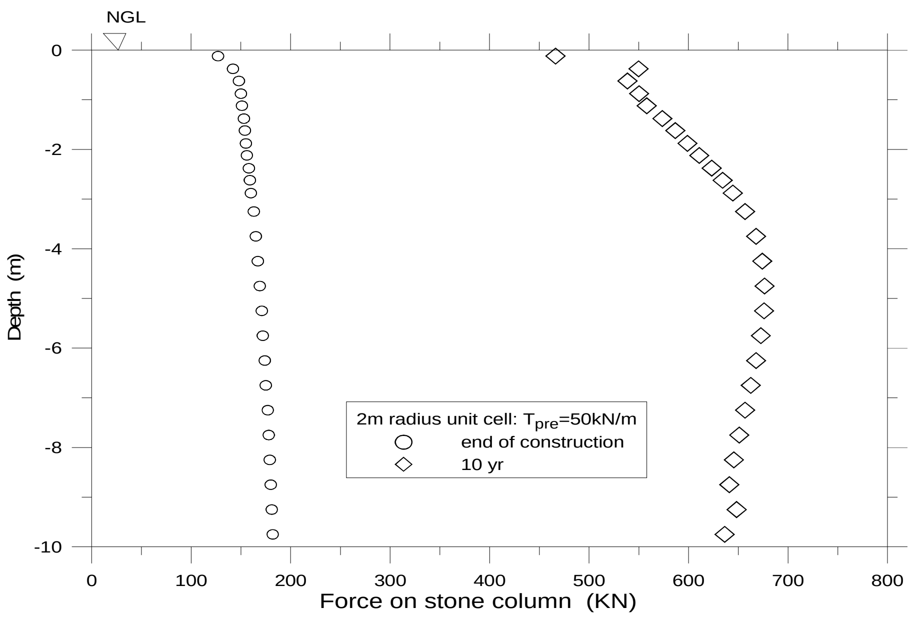

Figure 5.17 Distributions of column forces: reduced locked-in stress

Tpre =50kN/m (2.0m radius unit cell, MCC model only)

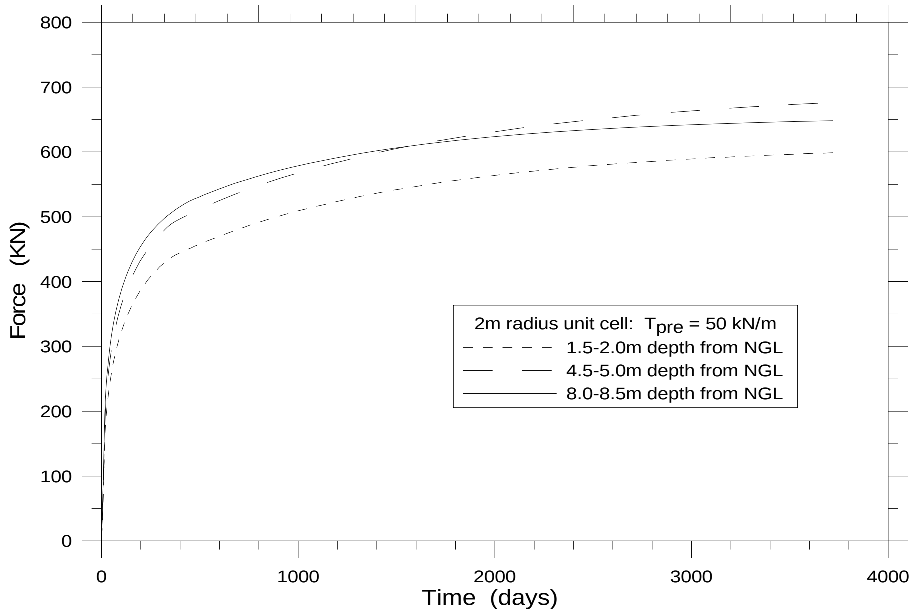

Figure 5.18 Evolutions of column forces with time: reduced locked-in stress Tpre=50kN/m (2.0m radius unit cell, MCC model only)

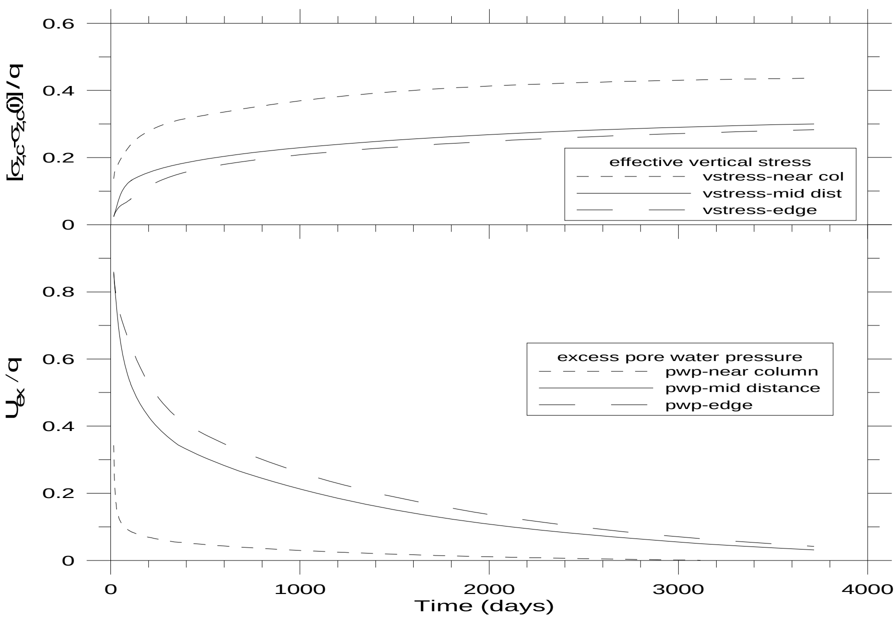

Figure 5.19 Consolidation responses in clay: reduced locked-in stress Tpre=50kN/m (2.0m radius unit cell, MCC model only)

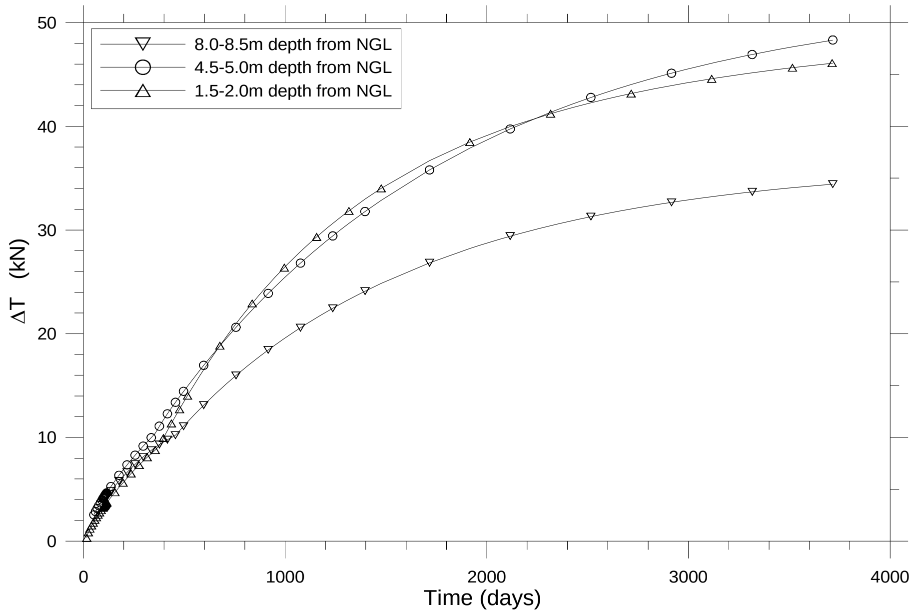

Figure 5.20 Increases in geosynthetic tension with time: reduced locked-in stress Tpre=50kN/m (2.0m radius unit cell, MCC model only)

5.3 STONE COLUMN IN MCC SOIL WITH 2.0M UNIT CELL

5.3.1 Reference parameters

An analysis conducted, based on the dimensions listed in Table 5-1, the material models presented in section 5.2, the material parameters listed in Table 5-2, and with a T_{pre} of 100 kN/m, is referred to as the reference analysis.

<u>a) Settlement</u>

Plots showing the developments of settlement at NGL with time are presented in Figure 5.6(a). The settlement-time relationships computed by the simplified analysis presented in Lo et al. (2007) are also plotted in this figure. It is evident that the settlements predicted by the reference analysis are higher than those of the simplified analysis. However, the overall trends are essentially the same in both analyses.

The incorporation of geosynthetic encasement considerably reduces settlement at both the column and edge of unit cell locations. Without pre-straining of the geosynthetic encasement, settlement at the top of the stone column in 10 years is approximately 0.77m. However, by applying geosynthetic encasement with T_{pre}=100 kN/m, this is reduced to 0.24m and settlement at the edge of the unit cell attains a higher, but still relatively small, value of 0.30m at 10 years. Furthermore, the stone column essentially ceases settlement after 2000 days.

Settlement profiles at NGL and the top of the fill are plotted in Figure5.6(b). The settlement profile at NGL manifests a "bump" near the perimeter of the stone column. However, as that at the top of the fill is smooth, a high-quality road surface is provided. The two profiles "intersect" which implies that, at the edge of the unit cell, the settlement is "less than" that at NGL. This is because settlement at the top of the fill is related to the end of construction. At the centre of the unit cell, settlement at the top of the fill is significantly higher than that at NGL because the fill above the stone column is subjected to significantly higher stress due to the stone column force.

b) Force in stone column

Distributions of the computed column forces with depth are presented in Figure 5.7 for two time-steps: end of construction and after 10 years. Profiles from the simplified analysis (presented in Lo et al. 2007) are plotted to allow comparisons of the two analyses. Evidently, the computed results from the simplified analysis are similar to those from the current analysis.

The profile at the end of construction is different from that at 10 years because of coupling between the reinforcing role of a stone column and the consolidation of the soft clay. At an early stage, when the extent of consolidation of the soft clay is small, the pore water pressure in it provides significant support to the fill loading. It is only with development of consolidation that a greater portion of the fill loading is transferred to the stone column; this justifies the need for a coupled analysis.

The column force at 10 years increases with depth until a maximum value of ~750 kN is achieved at about mid-depth. This is due to negative drag-down from the surrounding clay that tends to settle more than does that of the stone column. Evolutions of the column forces with time are examined in further detail (at three depths) in Figure 5.8. At all three depths, the column forces increase with time; at the mid-depth and near the toe of the stone column, they attain asymptotic values at about 1500 days and, at the top of the stone column, approach an asymptotic value at ~2000 days.

<u>c) Coupled behaviour</u>

The coupling between column force and consolidation behaviour is highlighted by plotting increases in the vertical effective stress, [$\sigma_{z,c}$-$\sigma_{z,c}$(i)], and dissipation of the excess pore water pressure, u_{ex}, with time for three radial locations at the mid-depth of the soft clay (Figure 5.9). It should be noted that (i) denotes the start of embankment construction. For ease of comparison, both [$\sigma_{z,c}$-$\sigma_{z,c}$(i)] and u_{ex} are normalized relative to the average fill loading, q, where q = unit weight of fill for an embankment height = 80 kPa. All plots commence from 16 days when the embankment is at its full height. The three radial locations are: next to the stone column; at the mid-distance between the stone column and the edge of the unit cell; and next to the edge of the unit cell.

As expected, dissipation of the excess pore water pressure proceeds with increases in the vertical effective stress. The maximum value of u_{ex}/q is only 0.82 because of some dissipation occurring during embankment construction. Dissipation of the excess pore water pressure and increases in the effective stress are significantly faster next to the stone column than in the other two locations. This is due to the drainage provided by the stone. At all three locations, increases in the effective stress after 300 days are slight.

However, significant dissipation of the excess pore water pressure continues to occur at the mid-distance and edge locations which can be a result of load being re-distributed to the stone column. This explanation is consistent with the evolutions of column forces shown in Figure 5.8. When u_{ex}/q essentially approaches zero, the $[\sigma_{z,c}-\sigma_{z,c}(i)]/q$ value is ~0.30 near the column and ~0.22 in the other two locations. The soil element next to the stone column still has a higher $[\sigma_{z,c}-\sigma_{z,c}(i)]/q$ value compared with those of the other two locations. These two features imply that the consolidation process also leads to significant embankment loading being re-distributed to the stone column.

The coupling between consolidation and geosynthetic tension is manifested in the ΔT versus time relationships in which $\Delta T = T - T(i)$ = increases in geosynthetic tension after embankment construction. Figure5.10 presents three ΔT-time plots corresponding to three depths: near-top, mid-depth, and near-toe. All three show increases in ΔT with time (and, hence, consolidation). Increases in a stone column force with consolidation lead to axial and radial deformations of the stone column which, in turn, induce ΔT. This ΔT provides further confinement to the stones and enables the stone column to continue attracting more load as consolidation proceeds.

The ΔT values for the mid-depth and bottom locations are small relative to T(i). This is because, at these two locations, $T(i) = T_{pre} = 100$ kN/m which already provides very high confinement and consequent stiffness to the stones. At the near-top location, $z<z_{ext}$ and, therefore, $T(i)=T_{ext}<T_{pre}$, as explained in equation (5-5a) and illustrated in Figure 5.3. The lower confinement provided by a smaller T(i) value at the near-top location leads to higher straining of the stones which, in turn, generates significantly higher ΔT values.

5.3.2 Influence of lower stone stiffness

The influence of lower stone stiffness is examined by repeating the analysis using the Duncan-Chang parameter, K, reduced to 1000, while all other parameters are identical to those of the reference analysis. This stiffness value is considered to be relatively low for compacted stones.

a) Settlement and force in stone column

The computed evolutions of settlement with time at NGL are presented in Figure 5.11(a), while the settlement profiles at NGL and foundation level are plotted in Figure 5.11(b). The overall trends of both the plots and profiles are similar to those of the reference analysis(Figure 5.6(a) and Figure 5.6(b)). The computed settlement with time is higher and the settlement profile at the top of the fill is smooth. However, this increase in settlement is only ~20% in spite of a 50% reduction in stiffness. This somewhat unexpected small increase can be explained by examining the computed distributions of the column forces with depth presented in Figure 5.12.

As can be seen in the figure, distributions for both the end of construction and at 10 years are only marginally less than are those of the reference analysis (Figure 5.7). Thus, at a high value of T_{pre} (which is the case for both analyses), the performance of the unit cell is not sensitive to the stiffness of the compacted stones. The underlying mechanism for such a "forgiving" and desirable attribute will be explained in a subsequent paragraph that examines coupling between the development of geosynthetic tension and the consolidation process. The time-dependent nature of the stone column forces is illustrated in Figure 5.13 which shows their evolutions with time at three depths. It is evident that the contribution of stone columns to resisting the fill loading is time-dependent.

b) Coupled behaviour

The computed $[\sigma_{z,c}-\sigma_{z,c}(i)]/q$-time and u_{ex}/q-time relationships for three radial locations at the mid-depth of the soft clay are plotted in Figure 5.14 following the same rationale and format as in Figure 5.9 for the reference analysis. These three plots display characteristics similar to those of the reference analysis, viz:

- increases in $\sigma_{z,c}$ after 300 days are slight at all three locations but significant dissipation of u_{ex} continues to occur at the mid-distance and edge locations.

This is because the dissipation of u_{ex} can also occur as a result of the embankment load being distributed to the stone column;

- the soil element next to the stone column attracts a higher effective stress than do those at the other two locations which is a result of its interaction with the stone column (in addition to that due to drainage); and
- even when u_{ex} is essentially dissipated, the ratios $[\sigma_{z,c}-\sigma_{z,c}(i)]/q$ for all three locations are significantly less than unity because of the load carried by the stone column increasing during the consolidation process.

At 10 years, the value of $[\sigma_{z,c}-\sigma_{z,c}(i)]/q$ near the stone column is 20% higher than that of the reference analysis even though the stiffness parameter of the stones is reduced by 50% in this analysis. This is consistent with the evolutions of settlement and stone column forces with time, as presented in Figures 5.8 and 5.13.

The coupling between consolidation and geosynthetic tension is manifested in the ΔT versus time relationships presented in Figure 5.15 following the same format as in Figure 5.10 for the reference analysis. All three plots show increases in ΔT with time. The trends displayed are similar to those of the reference analysis, thus indicating similar coupling during the consolidation process.

5.3.3 Effects of locked-in stress in geosynthetic

The influence of a lower locked-in force in a stone column is studied by repeating the analysis with T_{pre} reduced to 50 kN/m (i.e., halved) but with all other parameters being identical to those of the reference analysis.

a) Settlement and force in stone column

The computed evolutions of settlement with time at NGL and the settlement profiles at both NGL and foundation level are presented in Figures 5.16(a) and 5.16(b) respectively. Although the development of settlement with time and the overall shapes of the settlement profiles follow patterns similar to those of the reference analysis (Figures 5.6(a) and 5.6(b)), the settlement values are considerably higher in this analysis.

At the centre-line location (i.e., at the stone column's centre), the settlement is 0.40m which is ~67% higher than that of the reference analysis and, at the edge location, the computed settlement is 0.445m, ~48% higher than that of the reference analysis. Despite such increases in this analysis, the computed profile along the top of the fill is still smooth, thus giving a high-quality riding surface for a pavement. However, these settlement values are still significantly lower than are those without geosynthetic encasement.

Distributions of the column forces with depth at the end of construction and at 10 years are plotted in Figure 5.17. The overall shapes are similar to those of the reference analysis (Figure5.7). Once again, the distribution of the column forces at 10 years is considerably different from that at the end of construction, thus re-confirming that the contribution of column forces to resisting the fill load is time-dependent. For the distribution at 10 yr, the column force in general was distinctly smaller, but only by a small extent. The force at a 1m depth is 554 kN which is 86%

of that given by the reference analysis (with a higher T_{pre} of 100 kN/m). The maximum column force is 676 kN which is 90% of that from the reference analysis.

The underlying mechanism for such an “apparently unexpected” behaviour will be explained in a subsequent paragraph that examines coupling between the development of geosynthetic tension and the consolidation process. The time-dependent nature of stone column forces is illustrated in Figure 5.18. It is evident that the contribution of a stone column to resisting the fill loading is time-dependent and follows a similar trend to that of the reference analysis (Figure5.8).

b) Coupled behaviour

The computed $[\sigma_{z,c}-\sigma_{z,c}(i)]/q$-time and u_{ex}/q-time relationships for three radial locations at the mid-depth of the soft clay are plotted in Figure 5.19 following the same rationale and format as in Figure 5.9 for the reference analysis. These three plots display characteristics similar to those of the reference analysis, viz:

- increases in $\sigma_{z,c}$ after 300 days are slight at all three locations but significant dissipation of u_{ex} continues to occur at the mid-distance and edge locations. This is because dissipation of u_{ex} also occurs as a result of the embankment load being distributed to the stone column;
- the soil element next to the stone column attracts a higher effective stress compared with those at the other two locations as a result of its interaction with the stone column (in addition to that due to drainage); and

- even when $u_{ex}/q \rightarrow 0$, the ratios $[\sigma_{z,c}-\sigma_{z,c}(i)]/q$ are significantly less than unity at all three locations because the load carried by the stone column increases during the consolidation process.

At 10 years, the values of $[\sigma_{z,c}-\sigma_{z,c}(i)]/q$ in this analysis are significantly higher than those of the reference analysis, by about ~40% next to the stone column and ~30% at the other two locations. This is because of the higher settlement and smaller load carried by the stone column as a result of a 50% reduction in T_{pre} being adopted.

The coupling between consolidation and geosynthetic tension is manifested in the ΔT versus time relationships presented in Figure 5.20 following the same format as in the reference analysis (Figure 5.10). Although all these plots show increases in ΔT with time (and, hence, consolidation), the magnitudes of ΔT in this analysis are considerably higher than those in the reference analysis at all three locations. Thus, the system is trying to compensate for a lower locked-in geosynthetic tension by generating higher ΔT during the consolidation process. The lower T(i) values lead to higher axial and radial deformations of the column which, in turn, induce higher ΔT values which provide additional confinement, thereby enabling the stone column to continue attracting higher loads.

5.4 STONE COLUMN IN MCC SOIL WITH 1.3M UNIT CELL

5.4.1 Reference parameters

Apart from their radii, the dimensions of the 1.3m and 2.0m radius unit cell stone columns are the same (Table 5-1) as are their material parameters (Table 5-2). Since the stone column strengthen a smaller area of soft soil. T_{pre} for reference condition was adopted by the ratio of the area strengthened by the column. This gives $T_{pre} = 100\times(1.3/2.0)^2 = 42$ kN/m. Substituting this T_{pre} value into equation (5-5) gives Z_{ext}=1.2m.

<u>a) Settlement</u>

The numerical simulated evolutions of settlement with time are presented in Fig 5.21(a). The settlement-time relationships computed by assuming non-pre-strained geosynthetic encased stone columns are also plotted in this figure. Without geosynthetic encasement, settlement at the top of the stone column at 10 years is approximately 0.47m while, at NGL at the edge of the stone column, it is about 0.48m. These settlement values are about 60% those of the 2.0m radius unit cell with no pre-straining (Figure 5.6(a)). This is due to the reduced radius of the unit cell. The application of geosynthetic encasement with T_{pre}=42 kN/m reduces settlement at the top of the stone column to only 0.1m. Settlement at the edge of the unit cell attains a higher, but still very small, value of only 0.126m at 10 years. Essentially, this stone column ceases settlement after 600 days, much earlier than that of the 2.0m radius unit cell.

The settlement profiles at NGL and the top of the fill are plotted in Figure 5.21(b). The latter profile remains "bump-free" which is similar to that of the 2.0m radius unit cell stone column (Figure5.6(b)). Since settlements at both the top of the stone column and the edge of the unit cell are very small compared with the depth of the soil, the settlement profile at NGL has only a little “bump” between the stone column and the surrounding soil. Note that the settlement at NGL is computed from the beginning of the construction while the settlement on top fill is computed after construction. At the centre of the unit cell, settlement at the top of the fill is slightly higher than that of the NGL.

<u>b) Force in stone column</u>

Distributions of the computed column forces with depth at the end of construction and after 10 years, showing maximums of about 220 kPa and 375 kPa respectively, are presented in Figure 5.22. Evolutions of the column forces with time are plotted in Figure 5.23 at three depths: near-top, mid-depth and near-toe. At all three depths, the column forces increase with time as the excess pore water pressure disappears from the surrounding soil, and they approach asymptotic values at about 200, 300 and 400 days at the bottom, mid- and top depths respectively.

Comparing the 2.0m and 1.3m radius unit cell reference parameters cases, there are the following differences:

- although the values of their column forces at the end of construction are about the same, after 10 years, that of the 1.3m case is only half that of the 2.0m case. This is caused by dimensional effects because the soil volume in the stone column spacing of the 2.0m radius unit cell is 2.5 times that of the 1.3m radius unit cell; and

- the time needed for the 1.3m radius stone column force to reach its ultimate value is significantly shorter than that for the 2.0 radius stone column force, namely, about one year compared with more than 5 years.

c) Coupled behaviour

The computed $[\sigma_{z,c}-\sigma_{z,c}(i)]/q$-time and u_{ex}/q-time relationships for three radial locations at the mid-depth of the soft clay are plotted in Figure 5.24 following the same rationale and format as the reference analysis of the 2.0m radius unit cell (Figure5.9).

The maximum value of u_{ex}/q is less than 0.6 which can be explained by dissipation occurring during embankment construction. The process of dissipation of the excess pore water pressure is complete at about 500 days at all these locations. Increases in the effective stress at the near-stone column location stop shortly after construction and, at that time, a slight strain softening is highly likely to happen. This is caused by the combined effects of:

- the drainage provided by the stone columns;
- the non-uniformity of soil consolidation (soil near the stone columns consolidates faster than does that far from them); and
- the transfer of the weight of the fill from the soil to the stone columns.

The effective stresses at the mid-distance and near-edge locations continuously increase until about 200 and 500 days respectively. This shows that, at the edge of the stone column, the effective stress in the soil continues increasing with dissipation of the excess pore water pressure. At the mid-distance, after the effective stress reaches a constant value, the embankment loading is re-distributed to the stone column during the process of dissipation and does not further affect the effective stress of the soil. The results show that the soils at the mid-distance and near-edge locations reach about the same maximum effective stress values after the coupled process.

The coupling between consolidation and geosynthetic tension is manifested in the ΔT versus time relationships presented in Figure 5.25 following the same format as the reference analysis of the 2.0m radius stone column (Figure 5.10). All three plots show increases in ΔT over time due to the consolidation process. The trends displayed are also similar to those of the 2.0m radius reference analysis except that increases in the value of ΔT are much smaller. This is believed to be due to the impact of the dimensional effect of the 1.3m radius stone columns.

5.4.2 Influence of lower stone stiffness

The influence of lower stone stiffness is examined by repeating the analysis with the Duncan-Chang parameter, K, reduced to 1000, while all other parameters are identical to those of the reference analysis of the 1.3m radius unit cell. This stiffness value is considered to be relatively low for compacted stones.

<u>a) Settlement and force in stone column</u>

The computed evolutions of settlement with time are presented in Figure 5.26(a) and the settlement profiles at NGL and foundation level are plotted in Figure 5.26(b). The overall trends of both the settlement-time plots and settlement profiles are similar to those of the reference analysis (Figures 5.21(a) and 5.21(b)). Settlement of the soil at the top of the stone column at 10 years is about 0.15m and that at the edge of the unit cell 0.17m. The computed settlement at the top of the fill is smooth with a value of 0.14m at 10 years.-Compared to the reference analysis, the settlement increase about 50%. This result shows that the stone column performance is sensitive with K.

The distribution of the stone column force is shown in Figure 5.27. The maximum stone column force at the end of construction is 47kN less than that of the reference analysis. The column force is 360kN after 10 year which is about 15kN less than that of the reference analysis. The time-dependent nature of the stone column forces is illustrated in Figure 5.28 which shows their evolutions with time at three depths. These trends are similar to those of the reference analysis (Figure 5.23) except that the asymptotic force values are smaller.

b) Coupled behaviour

The computed $[\sigma_{z,c}-\sigma_{z,c}(i)]/q$-time and u_{ex}/q-time relationships for three radial locations at the mid-depth of the soft clay are plotted in Figure 5.29 following the same rationale and format as in Figure 5.24 for the reference analysis. These three plots display characteristics similar to those of the reference analysis except that:

- the complete dissipation of excess pore water pressure takes longer; at the near-stone column location about 50 days longer while, at the mid-distance and edge of unit cell locations, about 250 days longer;
- the trends of $[\sigma_{z,c}-\sigma_{z,c}(i)]/q$ with time are similar to those of the reference analysis at both the mid-distance and edge of the near-edge locations.

Meanwhile, at the near-column location, $[\sigma_{z,c}-\sigma_{z,c}(i)]/q$ takes much longer to reach its peak value and the "strain-softening phenomenon" is more obvious which is believed to be due to the same mechanism as in the reference analysis; and

- the increase of $[\sigma_{z,c}-\sigma_{z,c}(i)]/q$ is significantly higher than in the reference analysis at the near-stone column location. At 10 years, the values at the mid-distance and near edge are only 20% higher than those of the reference analysis while, at the near-stone column location, the value is about 70% higher. This may be due to the weaker of the stone columns causing the soil next to the stone columns to attract more fill load.

The coupling between consolidation and geosynthetic tension is manifested in the ΔT versus time relationships presented in Figure 5.30 following the same format as in Figure 5.25 for the reference analysis. All three plots show increases in ΔT with time and similar trends to those of the reference analysis, thus indicating similar coupling during the consolidation process. A significant ΔT increase is found at the mid-depth but, at the top and bottom depth locations, the ΔT become only slightly larger compared with the reference case. This can be explained by the column forces shown in Figures 5.22 and 5.27 in which increments at the mid-depth are obviously higher than those at the top and bottom locations.

5.4.3 Effects of locked-in stress in geosynthetic

The influence of a lower locked-in force in a stone column is studied by repeating the analysis with T_{pre} reduced to 21 kN/m while the other parameters are identical to those of the reference analysis.

a) Settlement and force in stone column

The computed evolutions of settlement with time are presented in Figure 5.31(a) and the settlement profiles at NGL and foundation level are plotted in Figure 5.31(b). They follow patterns similar to those of the reference case (Figures 5.26(a) and 5.26(b)). Settlement of the soil at the top of the stone column at 10 years is about 0.12m and that at the edge of the unit cell is 0.14m. This analysis gives settlement values 20% higher at the centre-line and ~10% higher at the edge of the unit cell locations than those of the reference analysis. The computed profile along the top of the fill is still smooth with a settlement value of 0.11m. Considering the 50% drop in the locked-in stress, these settlement values are only slightly higher than those of the reference analysis.

Distributions of the column forces with depth at the end of construction and at 10 years are plotted in Figure5.32. Compared with the reference analysis (Figure 5.22), the distribution of column forces at the end of construction and after 10 year remains nearly the same in shape but lightly smaller in value. Developments of the stone column forces at three typical locations are plotted in Figure 5.33. The shapes of the force versus time plots are fairly similar to those of the reference case (Figure 5.23) at each location but with the asymptotic value being about 3% less.

b) Coupled behaviour

The computed $[\sigma_{z,c}-\sigma_{z,c}(i)]/q$-time and u_{ex}/q-time relationships for three radial locations at the mid-depth of the soft clay are plotted in Figure 5.34. Despite similarities to the reference case (Figure 5.24), these three plots display the following characteristics:

- the dissipation of excess pore water pressure takes slightly longer at all three locations. However, the differences are so small that, when plotted in the same format as the reference analysis, there is no obvious difference between the two sets of plots. At all three locations, about 600 days are needed for the excess pore water pressure to dissipate;
- the increscent trends of $\sigma_{z,c}$ are similar to those of the reference case at both the mid-distance and the near-edge locations. However, at the near–stone column location, $[\sigma_{z,c}-\sigma_{z,c}(i)]/q$ takes longer to reach its peak value although its shape is similar to those of the other two locations. Unlike in the reference analysis, no "strain-softening phenomenon" is found; and
- $[\sigma_{z,c}-\sigma_{z,c}(i)]/q$ is 25% higher than that of the reference analysis at the near-stone column location. After 10 years, the values of $[\sigma_{z,c}-\sigma_{z,c}(i)]/q$ at the mid-distance and near edge locations are only 10% higher than those of the reference analysis.

The coupling between consolidation and geosynthetic tension is manifested in the ΔT versus time relationships presented in Figure 5.35. All three plots show increases in ΔT with time and their trends are similar to those of the reference analysis (Figure

5.25). The ultimate ΔT values at all three locations are slightly higher than those of the reference analysis. However, their differences do not exceed 1 kPa.

5.5 STONE COLUMN IN SSC SOIL WITH 2.0M UNIT CELL

5.5.1 Reference parameters

The simulation using the SSC model adopts the same MCC parameters as the MCC simulation and determines them by following the methods described in Chapter 3 and listed in Table 5-3. The analysis conducted in this section is the same as in section 5.3 except that it uses the SSC model rather than the MCC model.

a) Settlement

Settlements developing with time at NGL are presented in Figure 5.36(a) which includes the computed settlement-time relationships geosynthetic encasement not pre-strained. If the geosynthetic encasement has no pre-strain, the settlement at the top of the stone column in 10 years is approximately 0.87m and at the edge of unit cell is 0.89m. The application of geosynthetic encasement with T_{pre}=100 kN/m reduces this settlement to 0.30m. Settlement at the edge of the unit cell attains a higher, but still relatively small, value of 0.365m at 10 years and continues after that time.

The settlement profiles at NGL and at the top of the fill are plotted in Figure 5.36(b). That at NGL manifests an approximately 0.065m high “bump” near the perimeter of the stone column. However, that at the top of the fill is smooth and thus provides a high-quality road surface, with a value of about 0.346m settlement after 10 years.

b) Force in stone column

Distributions of the computed column forces with depth are presented in Figure 5.37 for both the end of construction and at 10 years. The maximum column force at the end of construction is 240kN. The maximum column force after 10 years is about 875kN. The stone column forces increase steadily with increases in depth until maximum value is achieved near the bottom. Evolutions of the column forces with time are examined in further detail (at three depths) in Figure 5.38. At all three depths, the column forces increase with time.

c) Coupled behaviour

The computed $[\sigma_{z,c}-\sigma_{z,c}(i)]/q$-time and u_{ex}/q-time relationships for three radial locations at the mid-depth of the soft clay are plotted in Figure 5.39 following the same rationale and format as in the reference analysis of the 2.0m radius unit cell using the MCC model (Figure 5.9).

The maximum value of u_{ex}/q is about 0.82 which can be explained by dissipation occurring during embankment construction. The process of dissipation of the excess pore water pressure does not stop until 10 years. Increases in the effective stresses at the mid-distance and edge locations continue although the increments lessen over time. The curve of the effective stress development with time at the near-stone column location is different from those at the other two locations. The $[\sigma_{z,c}-\sigma_{z,c}(i)]/q$ continues to increase to about 0.19 at approximately 250 days and then begins to drop to 0.15 over a 550-day period. After that, $[\sigma_{z,c}-\sigma_{z,c}(i)]/q$ again continues to increase to about 0.2 at the end of 10 years.

This strain softening phenomenon may be explained by the combination of SSC characteristics and the following coupled consolidation process:

- at the beginning of loading, most of the loads from the fill are supplied by the water pressure. As the consolidation process begins, the fill weights tend to "shift" from above the soils to the stone columns. The soil near the stone column will act like reinforcement and will "share" part of the weight transferred from the edge. This can be seen in the plots of before 250 days. The value of $[\sigma_{z,c}–\sigma_{z,c}(i)]/q$ near the stone column is about 2 times and 1.5 times higher than at the edge-and mid-distance locations respectively; and

- meanwhile, because the permeability of the soil is low and drainage is provided by the stone columns, the pore water pressure dissipates from the soil near the stone column much faster than it does at the mid-distance and near the edge. This is shown in the plots of excess pore water pressure dissipation with time. Thus, consolidation of the soil near the stone columns will also be faster than that of the soil far from them. As the soil consolidates, the "back up" role or "share" of the fill load will decrease. The drop in the "share" of the fill load may exceed the effective stress gained from dissipation of the excess pore water pressure. These combined effects may cause the phenomenon evident in the effective stress with time curve from 250 to 800 days; and

- when the consolidation process becomes relatively stable, the soil continues to gain effective stress increments from dissipation of the excess pore water pressure and the sharing stress from the soils at the edge side which consolidate more than do those on the stone side. Thus, the effective stress of the soil will continue to increase after 10 years.

The coupling between consolidation and geosynthetic tension is manifested in the ΔT versus time relationships presented in Figure 5.40 following the same format as in the reference analysis of the 2.0m radius stone column using only the MCC model (Figure 5.10). All three plots show increases in ΔT with time due to the consolidation process. However, these increases are "delayed" because, before about 500 days, the soil does not provide much support for the geosynthetic encasement and it is only as the consolidation process continues that it becomes much stronger and then provides greater support. This phenomenon is more obvious at the mid-depth and near-bottom locations.

5.5.2 Influence of lower stone stiffness

The influence of lower stone stiffness is examined by repeating the analysis with the Duncan-Chang parameter, K, being reduced to 1000 while all the other parameters are identical to those of the reference analysis.

<u>a) Settlement and force in stone column</u>

The computed evolutions of settlement with time are presented in Figure 5.41(a) and the settlement profiles at NGL and foundation level are plotted in Figure 5.41(b). The overall trends of both the settlement-time plots and settlement profiles are similar to those of the reference analysis (Figures 5.36(a) and 5.36(b)). The computed settlement at the top of the fill is smooth with a value of 0.39m at 10 years.

Settlements at the top of the stone column at 10 years are about 0.36m and that of the soil at the edge of the unit cell is 0.41m. Compared with the reference analysis, increases in settlement are about 20% at the top of the stone column and, approximately 10% at the edge of the stone column. Considering the reduction in stiffness of 50%, these differences are relatively small.

The distributions of stone column forces are plotted in Figure 5.42. After 10 years, the maximum force in the stone column located near the bottom is only reduced by about 20 kN (less than 5%) compared with the reference analysis (Figure 5.37). This is consistent with the small difference of the settlement. The time-dependent nature of the stone column forces is illustrated in Figure5.43 which displays the evolutions of column forces with time at three depths. The trends are similar to those of the reference analysis (Figure 5.38) at each location .

b) Coupled behaviour

The computed $[\sigma_{z,c}-\sigma_{z,c}(i)]/q$-time and u_{ex}/q-time relationships for three radial locations at the mid-depth of the soft clay are plotted in Figure 5.44. The u_{ex}/q-time relationships are very similar to those of the reference analysis (Figure 5.39) but with the excess pore water pressure dissipating more slowly. The dissipation process does not end until 10 years.

The overall trends of the $[\sigma_{z,c}-\sigma_{z,c}(i)]/q$-time relationship curves are also close to those of the reference analysis. The obvious differences are:

- the $[\sigma_{z,c}-\sigma_{z,c}(i)]/q$ at each location is higher than in the reference case. This is somewhat expected because the lower the stiffness of the stone, the less load will transfer to the stone columns; and
- the $[\sigma_{z,c}-\sigma_{z,c}(i)]/q$-time curve at the near-stone column location experiences a rapid increase at the beginning. Compared with the reference analysis, this increase is 30% higher and takes about 50 days less before the strain-softening phenomenon occurs. The strain-softening process ends at about 2000 days and does not rise again. The possible reason for this phenomenon is the same as explained for the reference analysis.

The coupling between consolidation and geosynthetic tension is manifested in the ΔT versus time relationships presented in Figure 5.45 following the same format as in Figure 5.40 for the reference analysis. The overall trends are similar to those of the reference case with ΔT increasing with time. At the middle and bottom depth locations, two-stage increases can be seen but they are not as obvious as in the reference analysis. The asymptotic ΔT value at these two locations is about 5kPa lower than it is in the reference case.

5.5.3 Effects of locked-in stress in geosynthetic

The influence of a lower locked-in force in a stone column is studied by repeating the analysis with T_{pre} reduced to 50 kN/m while the other parameters are identical to those of the reference analysis.

a) Settlement and force in stone column

The computed evolutions of settlement with time are presented in Figure 5.46(a) and the settlement profiles at NGL and foundation level are plotted in Figure 5.46(b). The developments of settlement with time and the overall shapes of the settlement profiles follow similar patterns to those of the reference analysis (Figures. 5.36(a) and 5.36(b)). Settlement at the top of the stone column at 10 years is about 0.486m and that of the soil at the edge of the unit cell is 0.53m. These values increase by 60% and 47% respectively and are significantly higher than those of the reference analysis.

Distributions of the column forces with depth at the end of construction and at 10 years are plotted in Figure 5.47. The distribution shapes at the end of construction remain nearly the same as in the reference analysis (Figure 5.37) with the maximum value 35kN less. The overall shapes of the after 10 years column force distributions are similar to those of the reference analysis, but the maximum stone force value reduces by about 75 kPa at the bottom of the unit cell. The developments of stone column forces with time at three typical locations are plotted in Figure 5.48. The shapes of the force versus time plots are similar to those of the reference analysis (Figure 5.38) at each location. The asymptotic values are 10%-20% less than those of the reference analysis.

<u>b) Coupled behaviour</u>

The u_{ex}/q-time relationships for three radial locations at the mid-depth of the soft clay are plotted in Figure 5.49. The overall trends of the curves are similar to those of the reference analysis (Figure 5.39) but the dissipation rates are slower.

The computed $[\sigma_{z,c}-\sigma_{z,c}(i)]/q$-time relationships for three radial locations at the mid-depth of the soft clay are also plotted in Figure 5.49. Despite their similarities to the reference analysis, these three plots display the following characteristics:

- the $[\sigma_{z,c}-\sigma_{z,c}(i)]/q$-time relationship curves at the mid-distance and edge locations are similar to those of the reference case. However, the asymptotic value of the effective stress at the mid-distance is slightly higher and the $[\sigma_{z,c}-\sigma_{z,c}(i)]/q$ at the edge location eventually reaches close to the same value as the mid-distance location at 10 years; and
- the strain-softening phenomenon also happens The effective stress curve at the near-stone column location also experiences rapid increases at the beginning, reaching its maximum value of 0.25 in about 60 days. Then, the strain softening happens smoothly until it reaches the stable value of 0.24 at about 2000 days. The possible reason is the same as that of the reference analysis.

The coupling between consolidation and geosynthetic tension is manifested in the ΔT versus time relationships presented in Figure 5.50. All three plots exhibit the same shape and show increases in ΔT with time due to the consolidation process. The asymptotic value of ΔT at the bottom location increases only a little. The ΔT values at the top and mid-depth locations increase significantly, by about 30 kPa. This increase is very high considering that the T_{pre} is only 50 kN/m.

5.6 STONE COLUMN IN SSC SOIL WITH 1.3M UNIT CELL

5.6.1 Reference parameters

Apart from their radii, the dimensions of the 1.3m radius and 2.0m radius unit cell stone columns are the same (Table 5-1) as are the MCC parameters and SSC material parameters (Tables 5-2 and 5-3). A T_{pre} of 42 kN/m is referred to as the reference analysis with the reason explained in section 5.4.

a) Settlement

The numerical simulated evolutions of settlement with time are presented in Figure 5.51(a). The settlement-time relationships computed by assuming no pre-straining geosynthetic encased stone columns are also plotted in this figure. With no pre-straining, the settlement at the top of the stone column at 10 years is approximately 0.50m while that at NGL at the edge of the stone column is about 0.52m. These settlement values are about half those of the 2.0m radius unit cell without geosynthetic encasement (Figure 5.41(a)/Figure 5.36(a)). These reductions are caused by the dimension reduction of the unit cell radius.

The application of geosynthetic encasement with T_{pre}=42kN/m reduces the settlement at the top of the stone column to only 0.12m while that at the edge of the unit cell attains a higher, but still very small, value of only 0.14m at 10 years. Essentially, the stone column ceases settlement after 800 days.

The settlement profiles at NGL and the top of the fill are plotted in Figure 5.51(b). There is a "bump" of about 0.02m between the stone and the surrounding soil at NGL. At the top of the fill is "bump-free".

b) Force in stone column

Distributions of the computed column forces with depth at the end of construction and after 10 years are presented in Figure 5.52. The column forces at the end of construction and at 10 years are about 245 kPa and 420 kPa respectively. Evolutions of the column forces with time are plotted in Fig 5.53 at three depths; near-top, mid-depth and near-toe. At all three depths, the column forces increase with time as the excess pore water pressure dissipates from the surrounding soil. The stone column forces approach asymptotic values at about 300, 400 and 600 days at the bottom, middle and top depth locations respectively.

Compared with the 2.0m radius unit cell reference parameters case (Figure 5.38), the 1.3m case has the following differences:

- the value of the column force at the end of construction is about the same as that of the 2.0m reference analysis while, after 10 years, it is only half that of the 2.0m case. This is because the soil volume in the stone column spacing of the 2.0m radius stone column is 2.5 times as that of the 1.3m radius stone column; and
- the time required for the stone column force to increase to the asymptotic value for the 1.3m radius stone column is significantly shorter than for that of the 2.0 radius stone column, that is, less than 2 years compared with longer about 10 years.

c) Coupled behaviour

The computed $[\sigma_{z,c}-\sigma_{z,c}(i)]/q$-time and u_{ex}/q-time relationships for three radial locations at the mid-depth of the soft clay are plotted in Figure 5.54 following the same rationale and format as in the reference analysis of the 2.0m radius unit cell (Figure 5.39).

The maximum value of u_{ex}/q is less than 0.6 which can be explained by dissipation occurring during embankment construction. The process of dissipation of the excess pore water pressure ends up at about 500 days at all these locations. Increases in the effective stress of the near-stone column location stops shortly after construction at which time a slight strain softening is likely to occur. This is caused by the combined effects of:

- the drainage provided by the stone columns;
- the non-uniformity of soil consolidation, that is, the soil near the stone columns consolidates faster than does the soil far from them; and
- the transfer of the weight of the fill from the soil to the stone columns.

There are continuous increases in the effective stress at the mid-distance and near-edge locations until about 300 and 500 days respectively. This shows that, at the edge of the stone column, the effective stress in the soil continues to increase with dissipation of the excess pore water pressure. At the mid-distance, after the effective stress reaches a constant value, the embankment loading is re-distributed to the stone column by the process of dissipation and does not affect the effective stress of the soil any more. The soil at the mid-distance and near-edge locations reaches about the same ultimate effective stress value after the coupled process.

The coupling between consolidation and geosynthetic tension is manifested in the ΔT versus time relationships presented in Figure 5.55 following the same format as that of the reference analysis of the 2.0m radius stone column (Figure 5.40). All three plots show increases in ΔT with time due to the consolidation process. The shapes of the ΔT versus time curves are about the same at the three different depths. Compared with the 2.0m radius reference case, the ΔT are much smaller. This is believed to be due to the impact of the dimension effect of the unit cell.

5.6.2 Influence of lower stone stiffness

The influence of lower stone stiffness is examined by repeating the analysis with the Duncan-Chang parameter, K, reduced to 1000, while all the other parameters are identical to those of the reference analysis of the 1.3m radius unit cell. This stiffness value is considered to be relatively low for compacted stones.

<u>a) Settlement and force in stone column</u>

The computed evolutions of settlement with time are presented in Figure 5.56(a) and the settlement profiles at NGL and foundation level are plotted in Figure 5.56(b). The overall trends of both the settlement-time plots and profiles are similar to those of the reference analysis Figures. 5.51(a) and 5.51(b)). The computed settlement at the top of the fill is smooth with a value of 0.155m at 10 years. Settlement at the top of the stone column at 10 years is about 0.17m and that of the soil at the edge of the unit cell is 0.195m. Compared with the settlement of the reference analysis (Figure 5.51), these values increase about 40% when the stiffness reduces to 50%.

The distributions of stone column forces are plotted in Figure 5.57. After 10 years, the maximum force in the stone column located near the bottom is reduced by about 15 kN compared with the reference analysis (Figure 5.52). The time-dependent nature of the stone column forces is illustrated in Figure 5.58 which displays the evolutions of column forces with time at three depths. The trends are similar to those of the reference analysis (Figure 5.53) at each location .

b) Coupled behaviour

The computed $[\sigma_{z,c}-\sigma_{z,c}(i)]/q$-time and u_{ex}/q-time relationships for three radial locations at the mid-depth of the soft clay are plotted in Figure 5.59 following the same rationale and format as in Figure 5.54 for the reference analysis. These three plots display characteristics similar to those of the reference analysis except that:

- the dissipation of excess pore water pressure takes longer to complete, about 50 days, at the near-stone column location and approximately 300 days at the mid-distance and edge of unit cell locations;
- the increscent trends of $\sigma_{z,c}$ are similar to those of the reference case in the mid-distance and edge of the near-edge locations but, at the near-column location, $[\sigma_{z,c}-\sigma_{z,c}(i)]/q$ takes much longer to reach its peak value and the "strain softening phenomenon" is more obvious. This phenomenon occurs for the same reason as it does in the reference case; and
- the increase of $\sigma_{z,c}$ is significantly higher than in the reference case at the near-stone column location. At 10 years, the values of $[\sigma_{z,c}-\sigma_{z,c}(i)]/q$ at the mid-distance and near-edge locations are only 20% higher than those of the

reference analysis while, at the near-stone column location, the value is about 70% higher. This may be due to the weaker of the stone columns causing the soil next to them to attract more fill load.

The coupling between consolidation and geosynthetic tension is manifested in the ΔT versus time relationships presented in Figure 5.60 following the same format as in Figure 5.55 for the reference analysis. All three plots show increases in ΔT with time and similar trends to those of the reference analysis. The shapes of the ΔT with time are also similar to those of the reference analysis but with values about several kN/m higher. Differences between the ΔT values at all locations are very small.

5.6.3 Effects of locked-in stress in geosynthetic

The influence of a lower locked-in force in a stone column is studied by repeating the reference analysis with T_{pre} reduced to 21 kN/m while the other parameters are identical to those of the reference analysis.

<u>a) Settlement and force in stone column</u>

The computed evolutions of settlement with time are presented in Figure 5.61(a) and the settlement profiles at NGL and foundation level are plotted in Figure 5.61(b). Developments of settlement with time and the overall shapes of the settlement profiles follow similar patterns to those of the reference case (Figures. 5.51(a) and 5.51(b)). The computed profile along the top of the fill is still smooth with a settlement value of 0.127m. Settlement at the top of the stone column at 10 years is about 0.135m and that of the soil at the edge of the unit cell is 0.16m.

This analysis gives settlement values only slightly smaller than those of the reference analysis - about 10% higher at both the centre-line location of the stone column and at the edge of the unit cell. Considering the 50% drop in the locked-in strain, these settlement values are only slightly higher than those of the reference case.

Distributions of the column forces with depth at the end of construction and at 10 years are plotted in Figure 5.62. Those at the end of construction remain nearly the same as in the reference analysis (Figure 5.52). Overall shapes at 10 years are similar to those of the reference analysis but with slightly smaller values at each location. Developments of the stone forces in three typical locations are plotted in Figure 5.63. The shapes of the force versus time plots are fairly similar to those of the reference case (Figure 5.53) at each location, with the asymptotic force values being about 1% less than in the reference analysis.

b) Coupled behaviour

The computed $[\sigma_{z,c}-\sigma_{z,c}(i)]/q$-time and u_{ex}/q-time relationships for three radial locations at the mid-depth of the soft clay are plotted in Figure 5.64. Despite similarities to the reference case (Figure 5.54), these three plots display the following characteristics:

- the dissipation of excess pore water pressure takes slightly longer at all three locations, about 500 days. However, as the differences are very small when plotted in the same format as the reference case, there is no obvious difference among the plots.;

- the increscent trends of $\sigma_{z,c}$ are similar to those of the reference case at the mid-distance and edge of the near-edge locations with only slightly higher values. At the near-column location, $[\sigma_{z,c}-\sigma_{z,c}(i)]/q$ takes about 400 days to reach its peak value. Its shape in the development with time plot is similar to those at the other two locations. Unlike the reference case, no "strain softening phenomenon" is found; and
- the increase of $\sigma_{z,c}$ is significantly higher than in the reference case at the near-stone column location. At 10 years, the values of $[\sigma_{z,c}-\sigma_{z,c}(i)]/q$ at the mid-distance and near-edge locations are only 10% higher than those of the reference analysis. The value is about 25% higher at the near-stone column location. This may due to the weaker of the stone columns causing the soil next to the stone columns to attract more fill load.

The coupling between consolidation and geosynthetic tension is manifested in the ΔT versus time relationships presented in Figure 5.65. All three plots show increases in ΔT with time and their trends are similar to those of the reference analysis (Figure5.55). The ultimate ΔT values are slightly higher than those of the reference case at all three locations but these differences do not exceed 1.5 kPa.

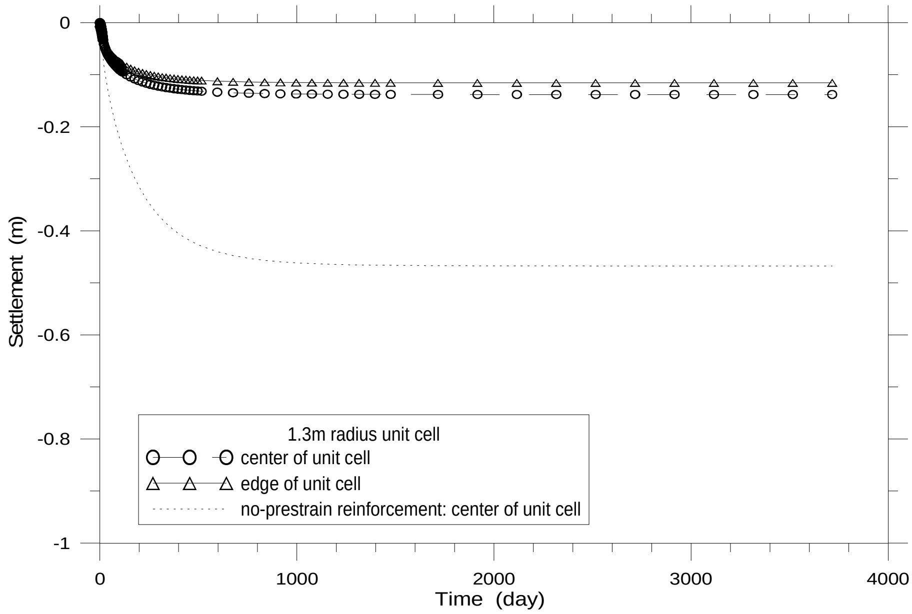

Figure 5.21(a) Settlement responses of reference analysis: comparison of settlement-time plots (1.3m radius unit cell, MCC model only)

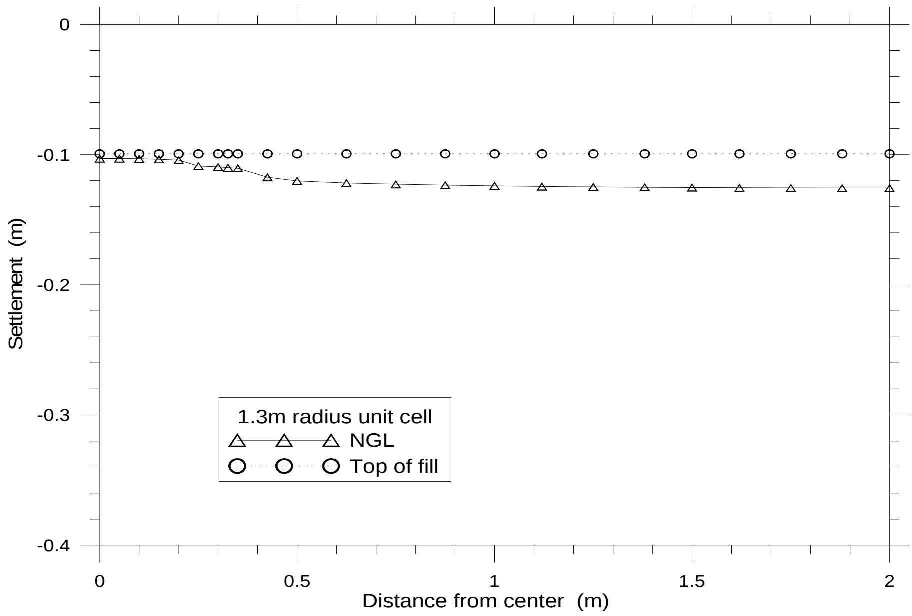

Figure 5.21(b) Settlement responses of reference analysis: settlement profiles at 10 years (1.3m radius unit cell, MCC model only)

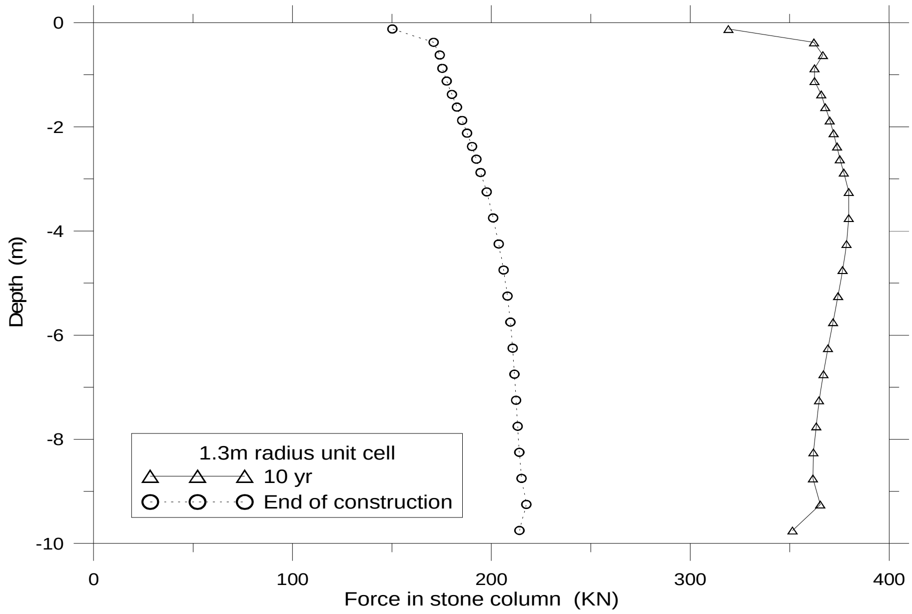

Figure 5.22 Distributions of column forces with depth: reference analysis (1.3m radius unit cell, MCC model only)

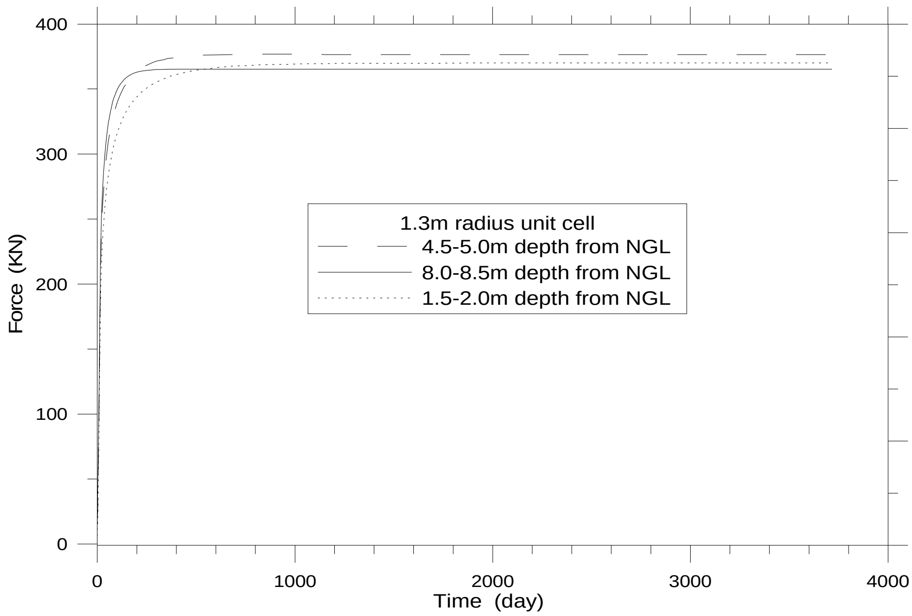

Figure 5.23 Evolutions of column forces with time: reference analysis (1.3m radius unit cell, MCC model only)

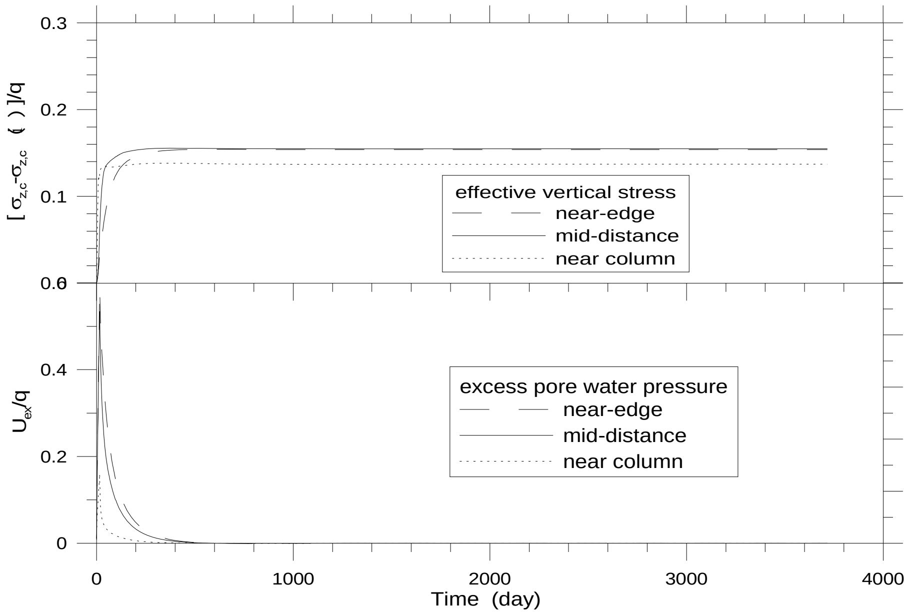

Figure 5.24 Consolidation responses in clay: reference analysis

(1.3m radius unit cell, MCC model only)

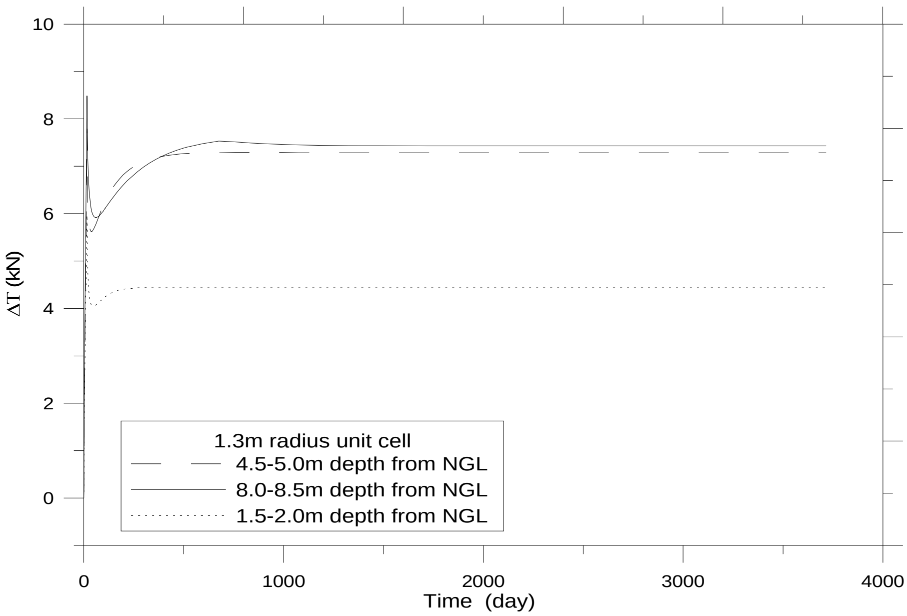

Figure 5.25 Increases in geosynthetic tension with time: reference analysis

(1.3m radius unit cell, MCC model only)

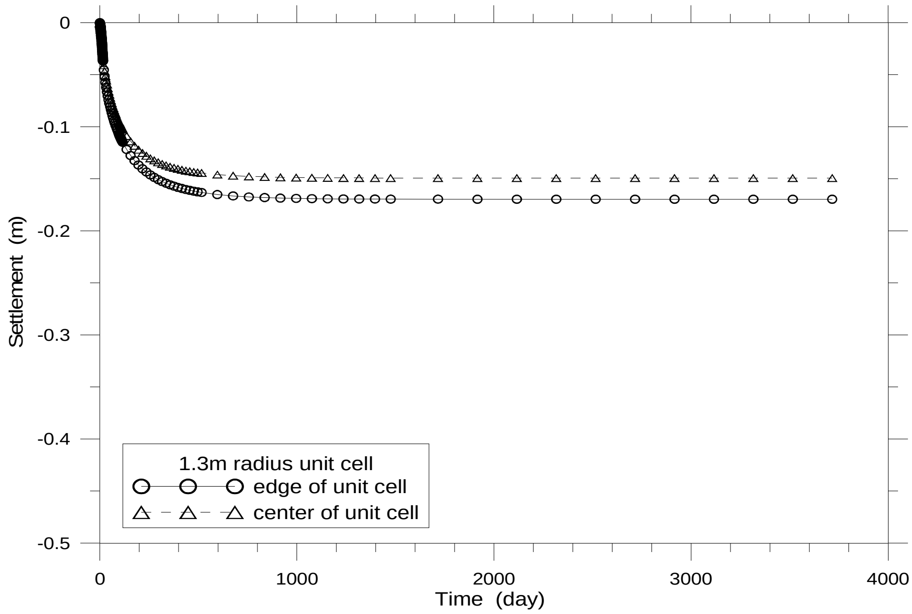

Figure 5.26(a) Settlement-time plots: reduced stone stiffness K=1000

(1.3m radius unit cell, MCC model only)

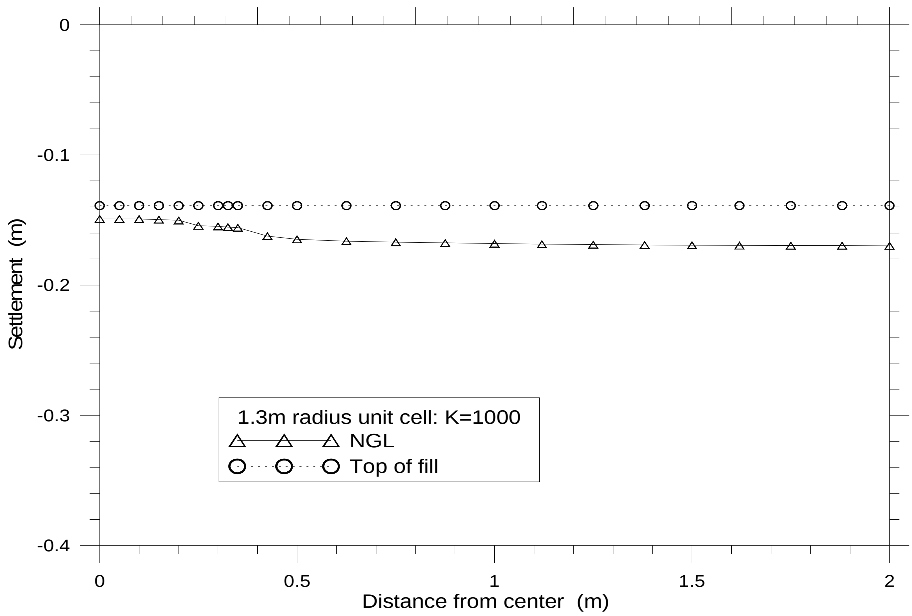

Figure 5.26(b) Settlement profiles: reduced stone stiffness K=1000

(1.3m radius unit cell, MCC model only)

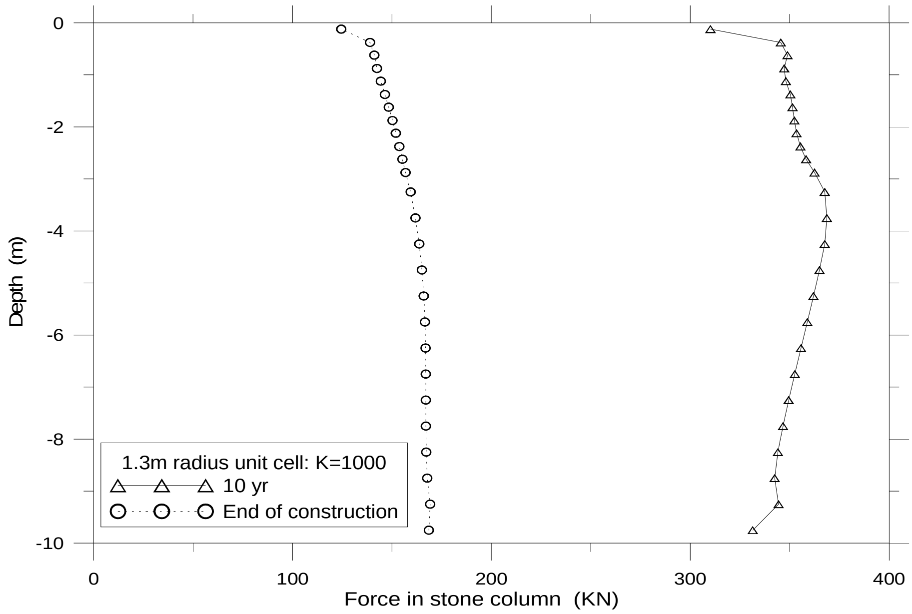

Figure 5.27 Distributions of column forces: reduced stone stiffness K=1000 (1.3m radius unit cell, MCC model only)

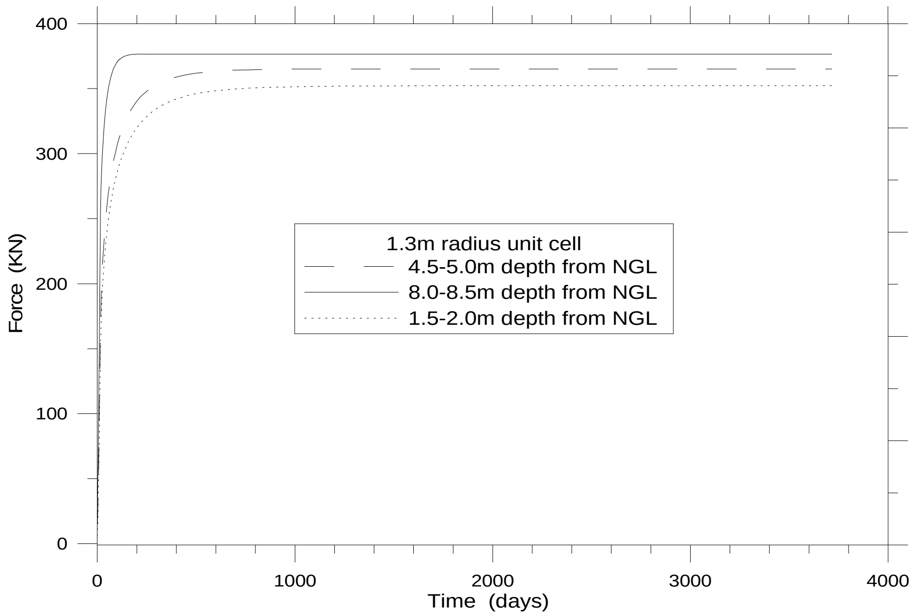

Figure 5.28 Evolutions of column forces with time: reduced stone stiffness K=1000 (1.3m radius unit cell, MCC model only)

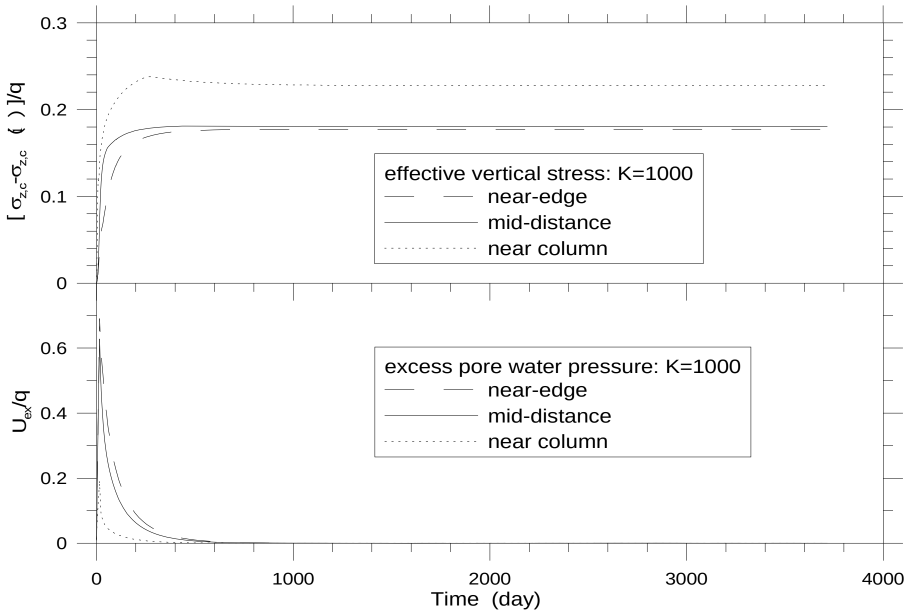

Figure 5.29 Consolidation responses in clay: reduced stone stiffness K=1000 (1.3m radius unit cell, MCC model only)

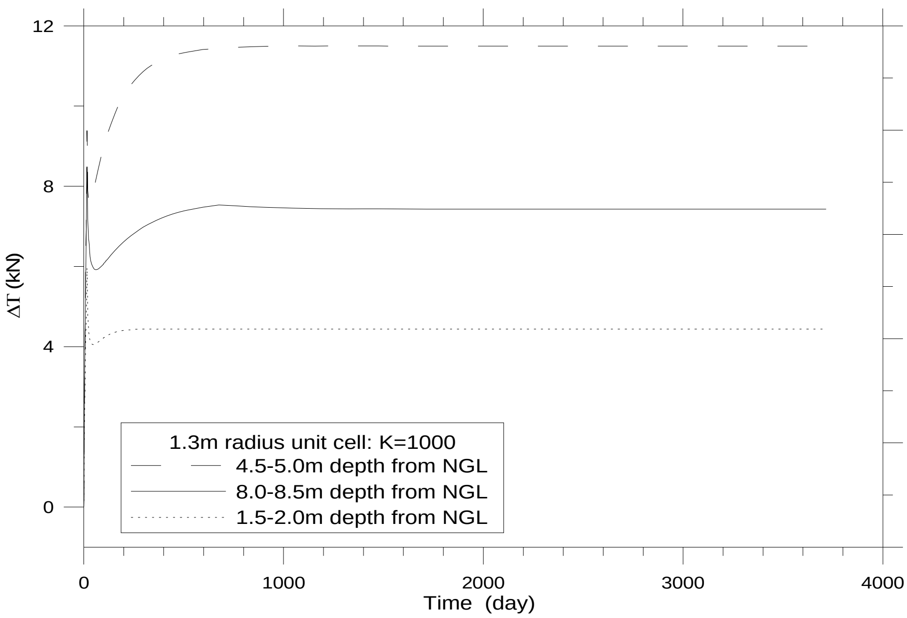

Figure 5.30 Increases in geosynthetic tension with time: reduced stone stiffness K=1000 (1.3m radius unit cell, MCC model only)

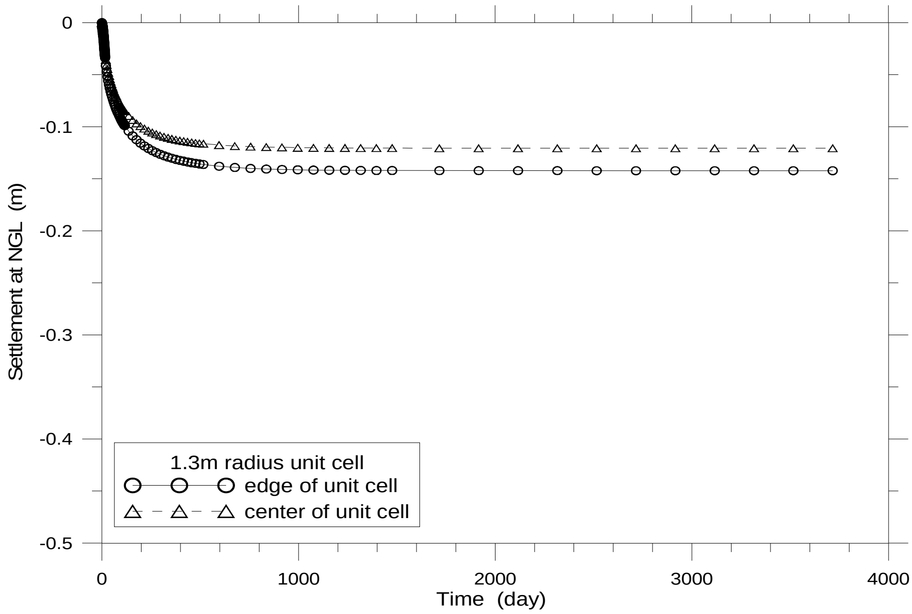

Figure 5.31(a) Settlement-time plots: reduced locked-in stress Tpre=21kN/m (1.3m radius unit cell, MCC model only)

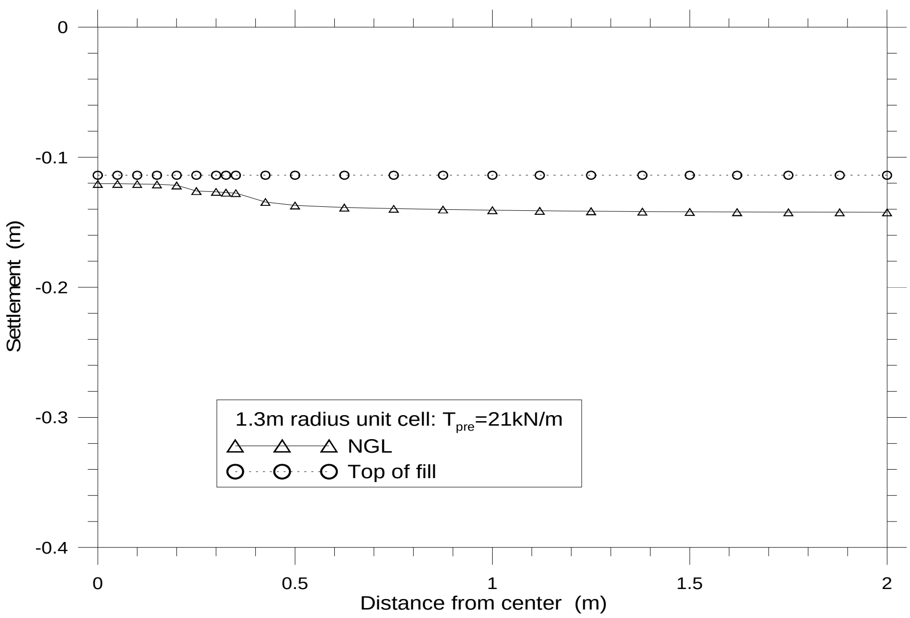

Figure 5.31(b) Settlement profiles: reduced locked-in stress Tpre=21kN/m (1.3m radius unit cell, MCC model only)

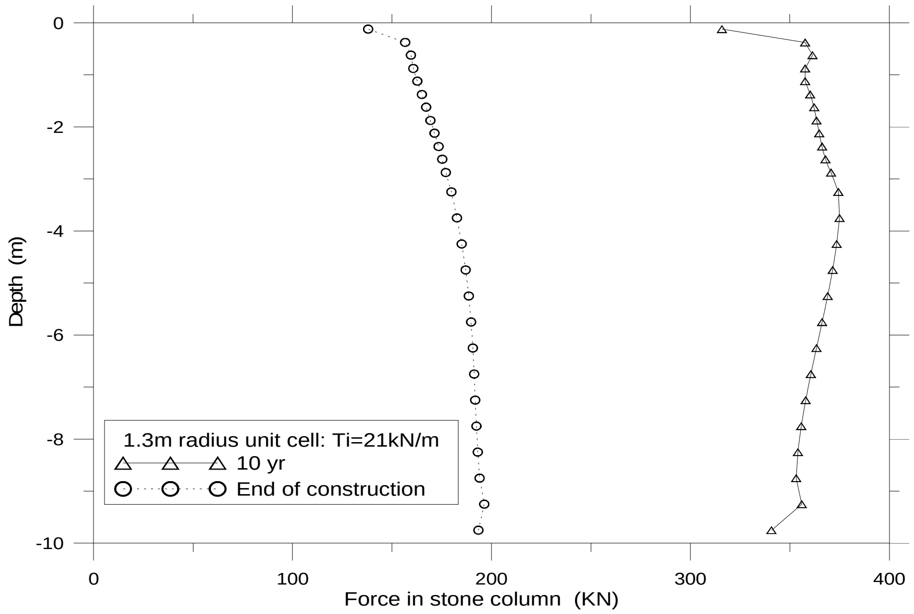

Figure 5.32 Distributions of column forces: reduced locked-in stress Tpre=21kN/m (1.3m radius unit cell, MCC model only)

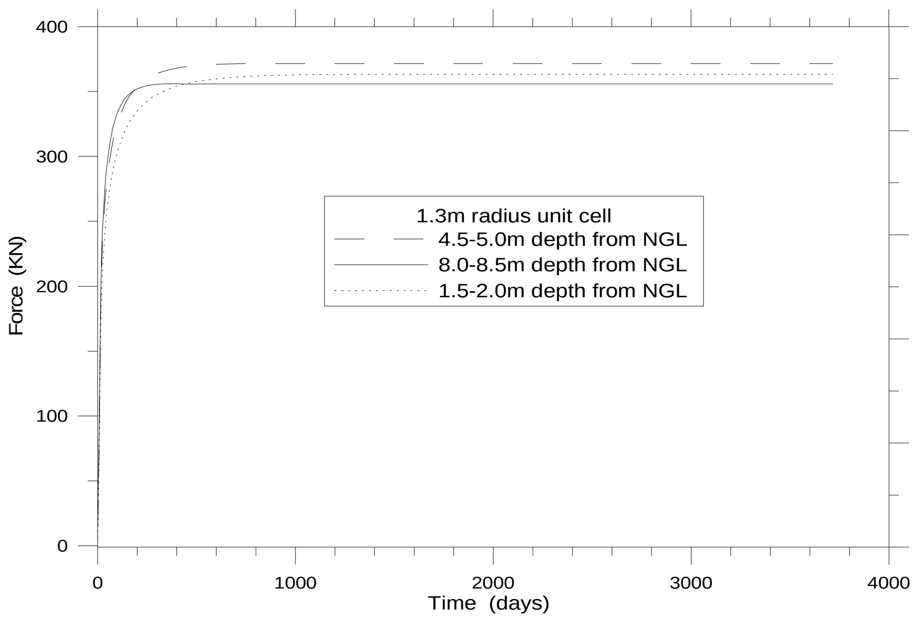

Figure 5.33 Evolutions of column forces with time: reduced locked-in stress Tpre=21kN/m (1.3m radius unit cell, MCC model only)

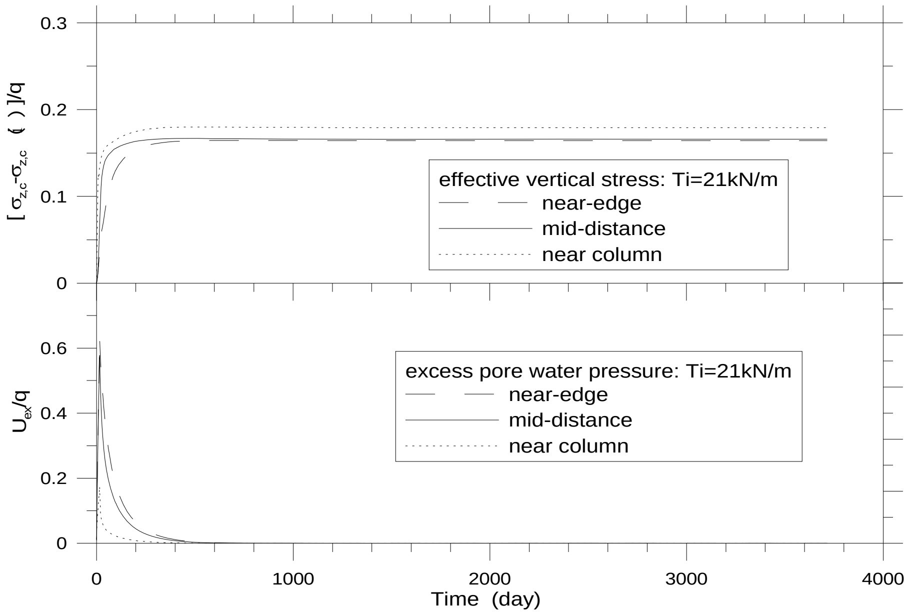

Figure 5.34 Consolidation responses in clay: reduced locked-in stress Tpre=21kN/m (1.3m radius unit cell, MCC model only)

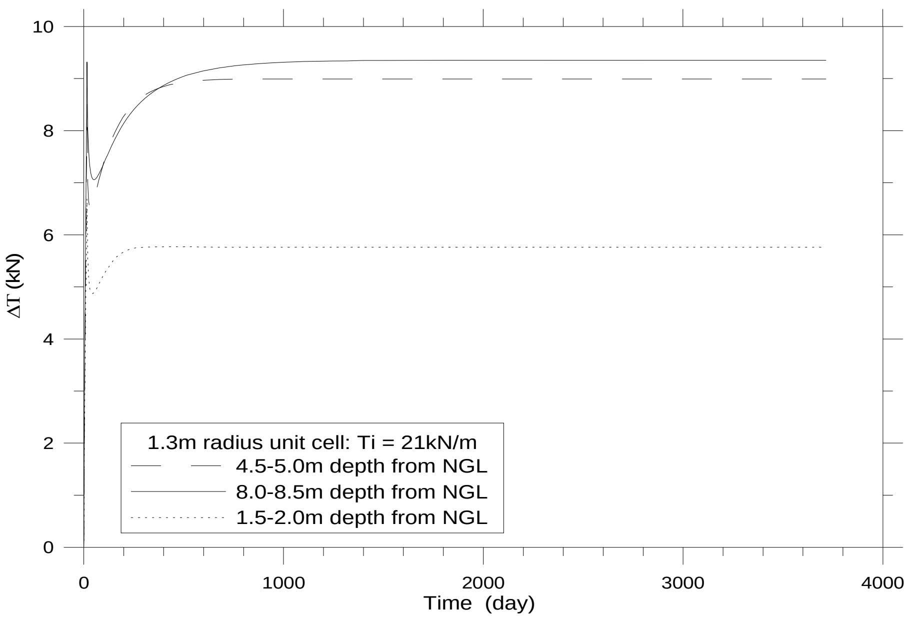

Figure 5.35 Increases in geosynthetic tension with time: reduced locked-in stress Tpre=21kN/m (1.3m radius unit cell, MCC model only)

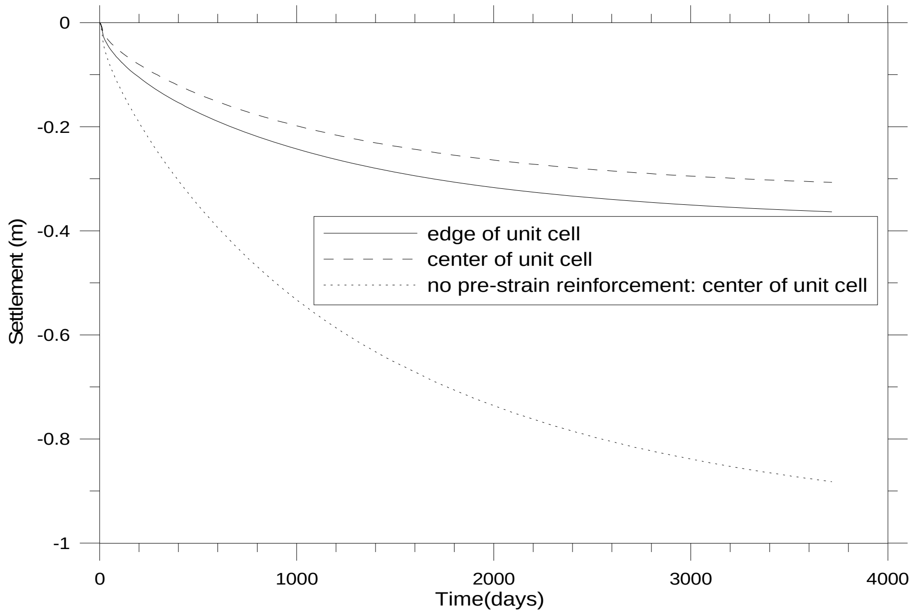

Figure 5.36(a) Settlement responses of reference analysis: comparison of settlement-time plots (2.0m radius unit cell, SSC model applied)

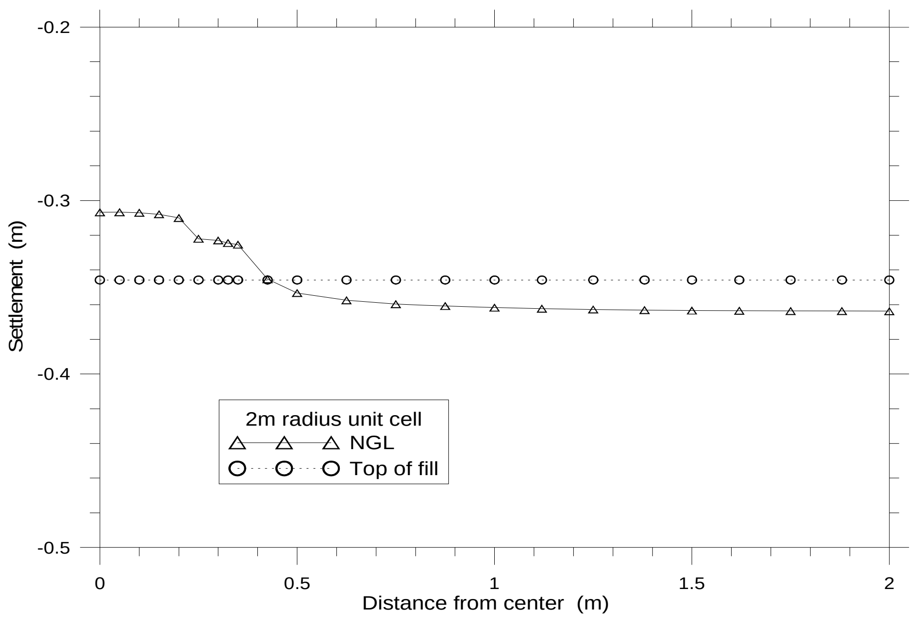

Figure 5.36(b) Settlement responses of reference analysis: settlement profiles at 10 years (2.0m radius unit cell, SSC model applied)

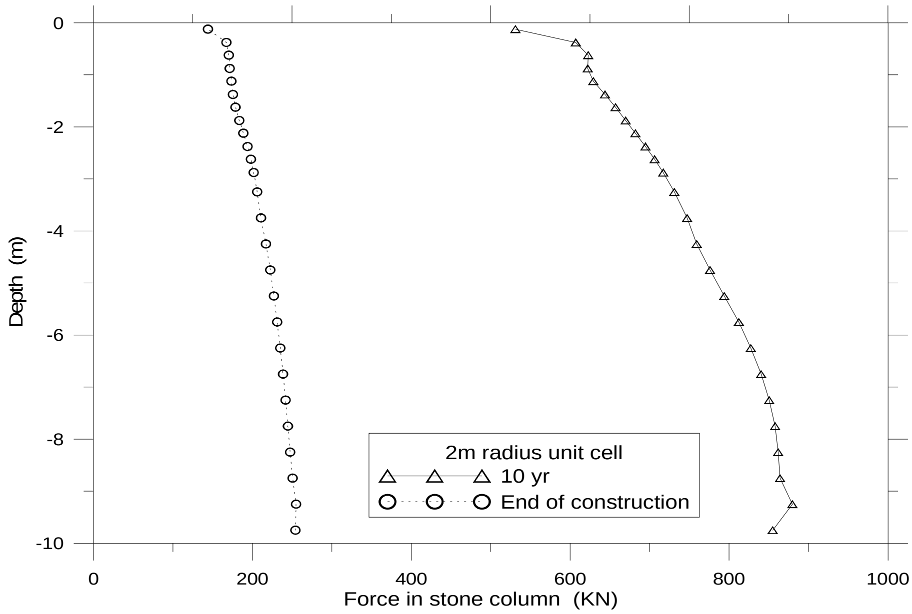

Figure 5.37 Distributions of column forces with depth: reference analysis (2.0m radius unit cell, SSC model applied)

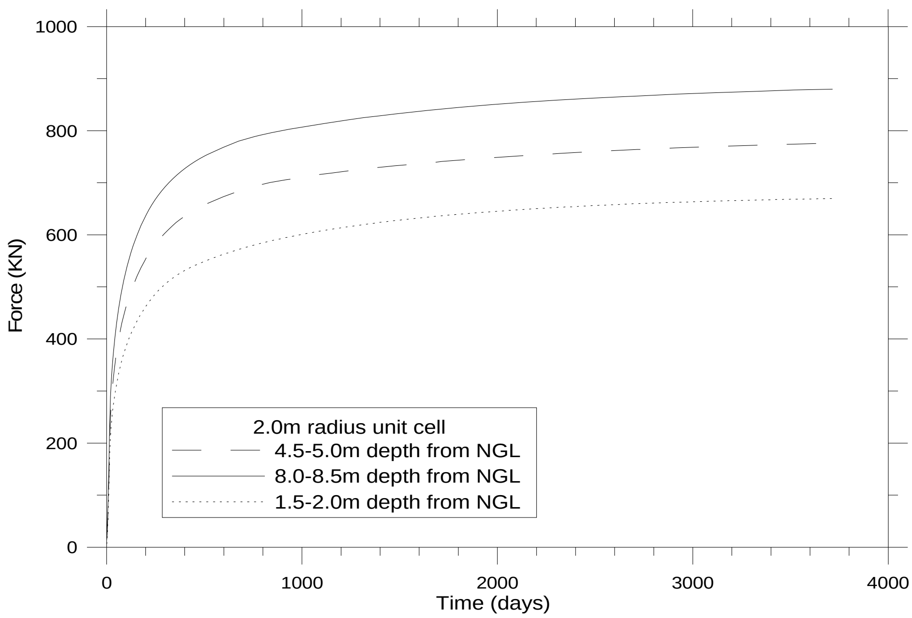

Figure 5.38 Evolutions of column forces with time: reference analysis (2.0m radius unit cell, SSC model applied)

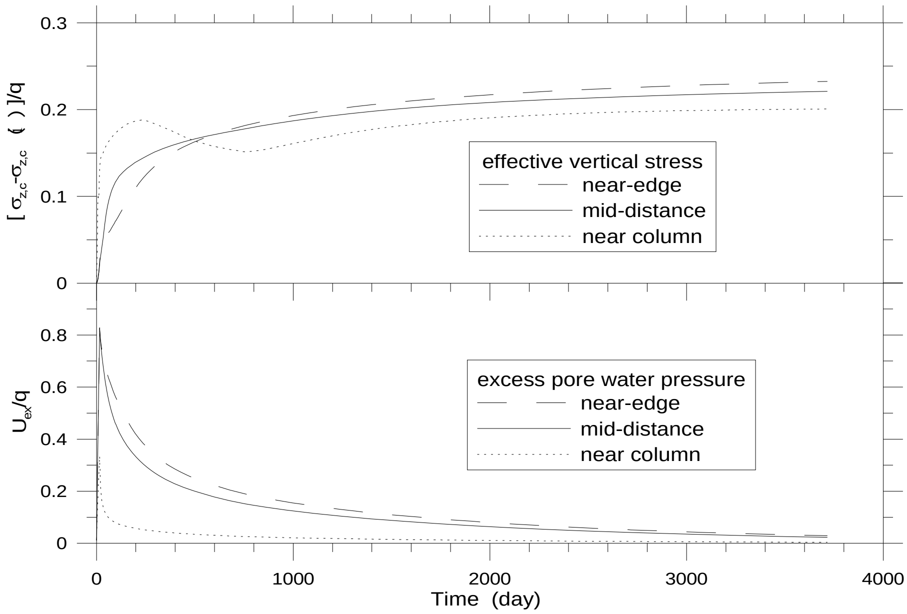

Figure 5.39 Consolidation responses in clay: reference analysis

(2.0m radius unit cell, SSC model applied)

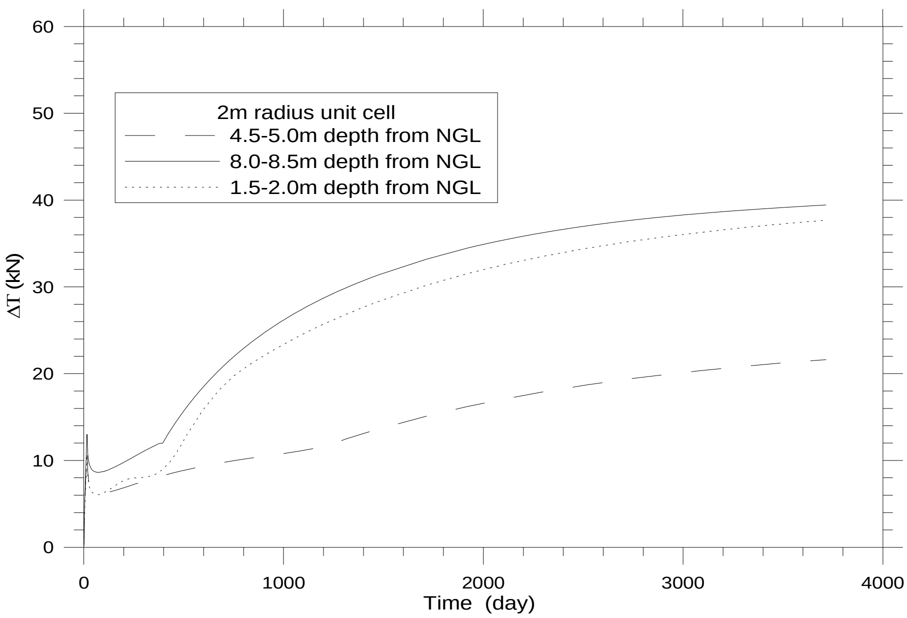

Figure 5.40 Increases in geosynthetic tension with time: reference analysis

(2.0m radius unit cell, SSC model applied)

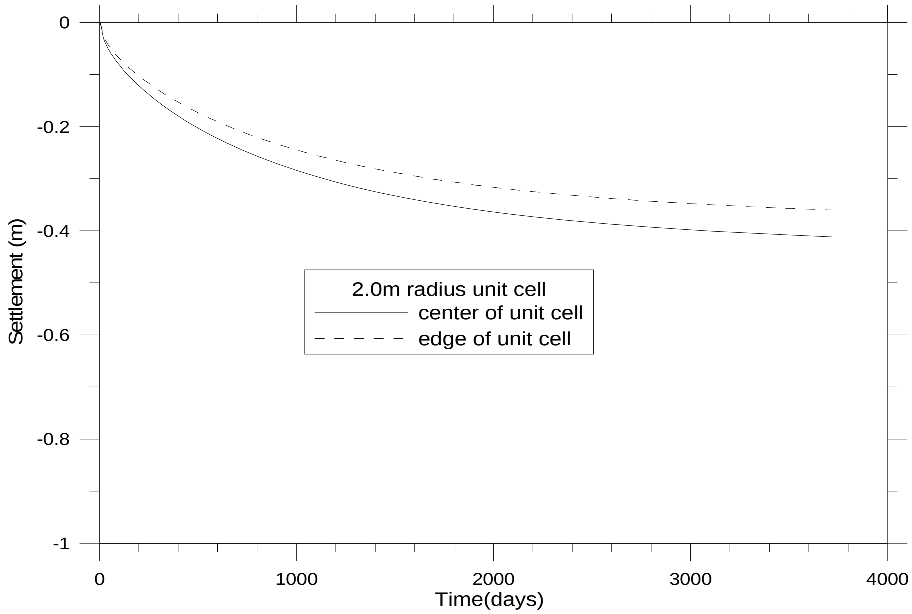

Figure 5.41(a) Settlement-time plots: reduced stone stiffness K=1000

(2.0m radius unit cell, SSC model applied)

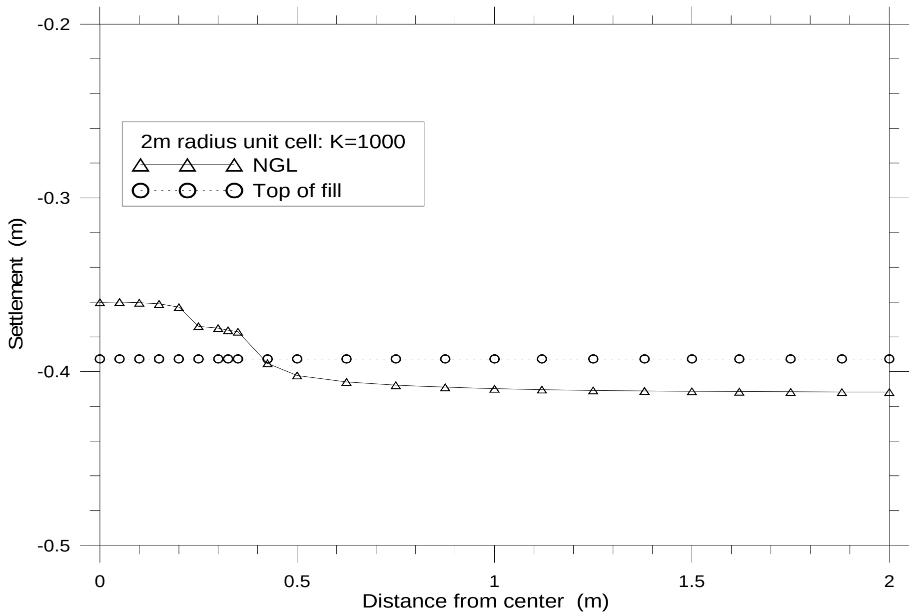

Figure 5.41(b) Settlement profiles: reduced stone stiffness K=1000

(2.0m radius unit cell, SSC model applied)

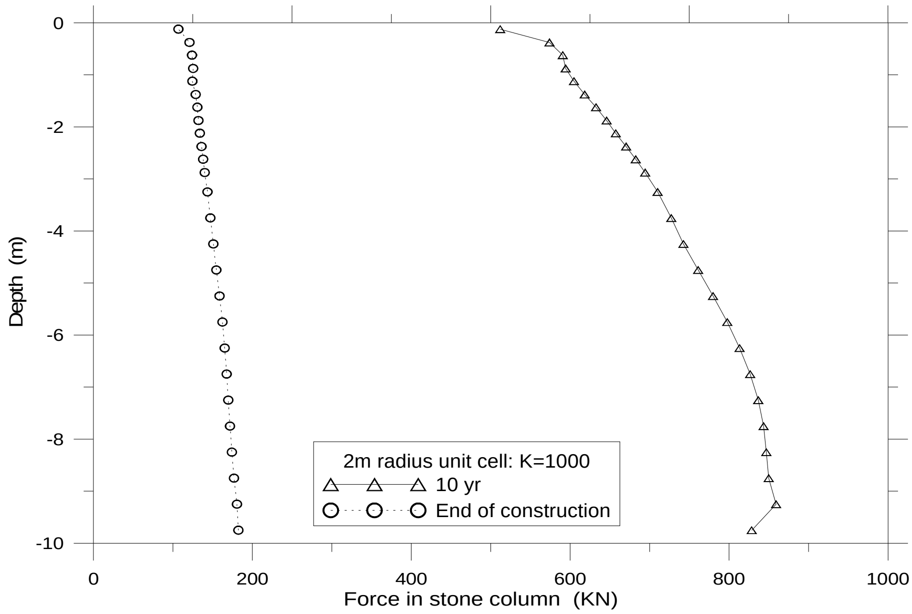

Figure 5.42 Distributions of column forces: reduced stone stiffness K=1000 (2.0m radius unit cell, SSC model applied)

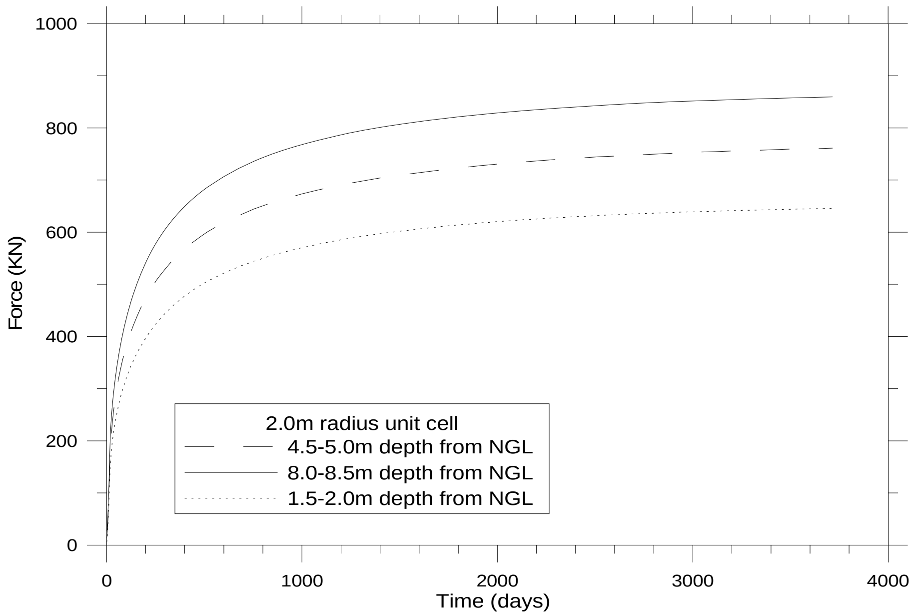

Figure 5.43 Evolutions of column forces with time: reduced stone stiffness K=1000 (2.0m radius unit cell, SSC model applied)

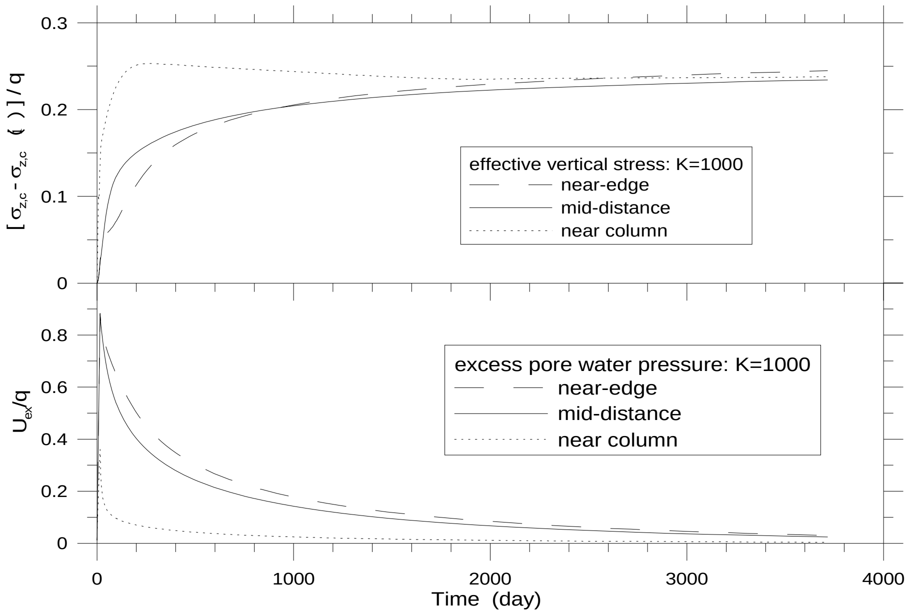

Figure 5.44 Consolidation responses in clay: reduced stone stiffness K=1000 (2.0m radius unit cell, SSC model applied)

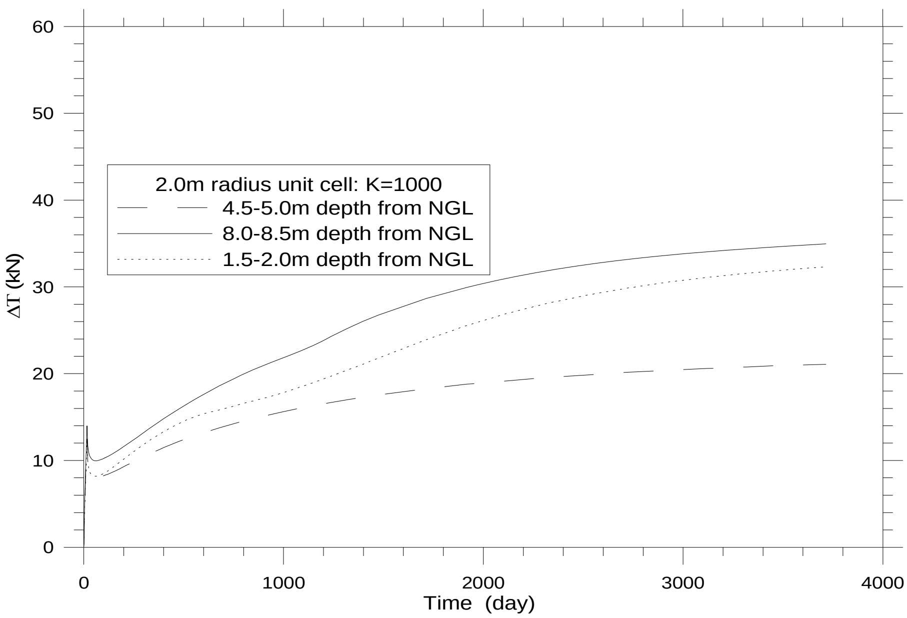

Figure 5.45 Increases in geosynthetic tension with time: reduced stone stiffness K=1000 (2.0m radius unit cell, SSC model applied)

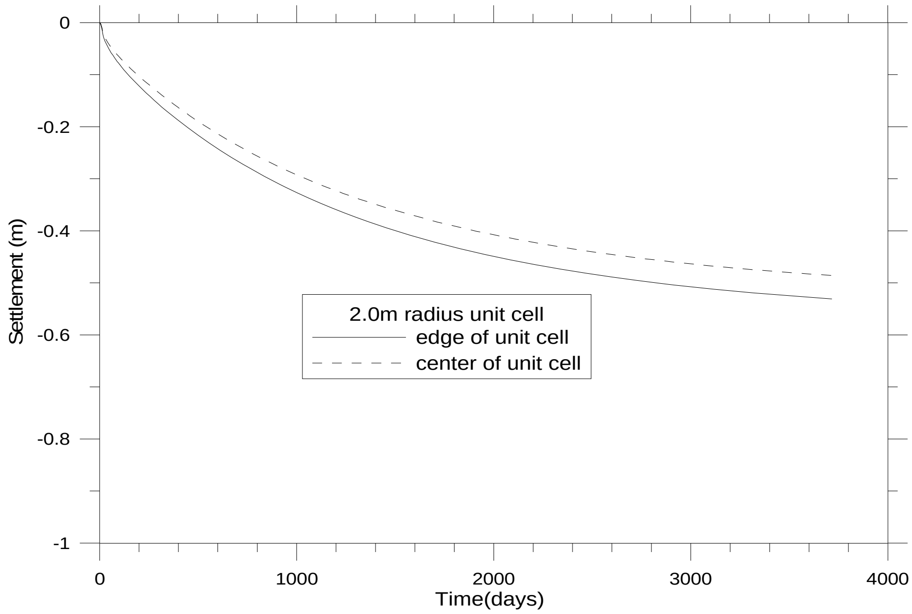

Figure 5.46(a) Settlement-time plots: reduced locked-in stress Tpre=50kN/m

(2.0m radius unit cell, SSC model applied)

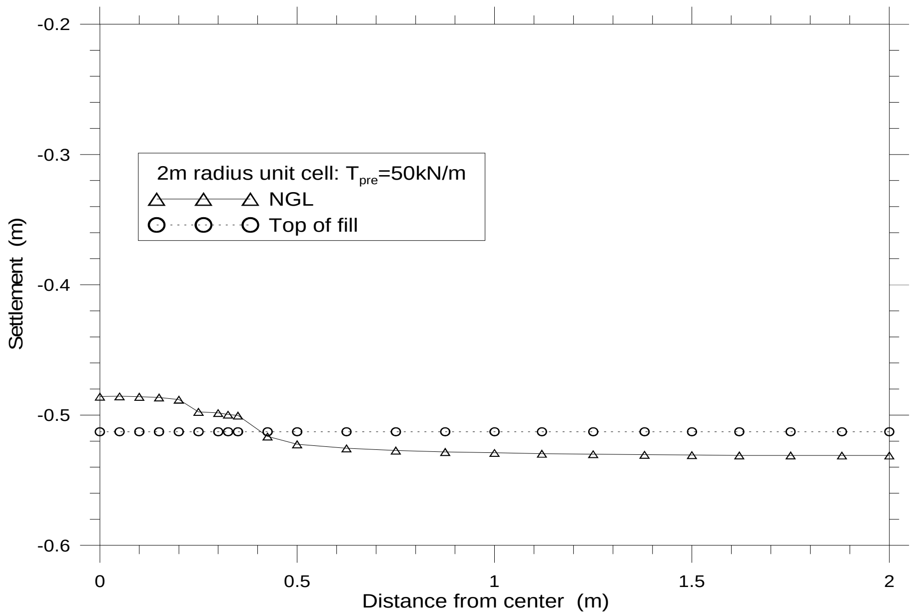

Figure 5.46(b) Settlement profiles: reduced locked-in stress Tpre=50kN/m

(2.0m radius unit cell, SSC model applied)

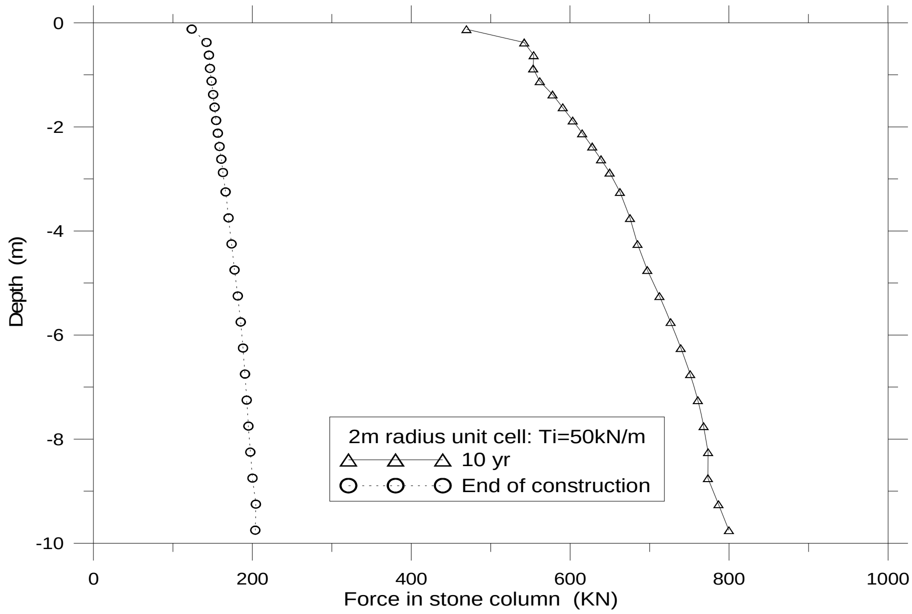

Figure 5.47 Distributions of column forces: reduced locked-in stress Tpre=50kN/m (2.0m radius unit cell, SSC model applied)

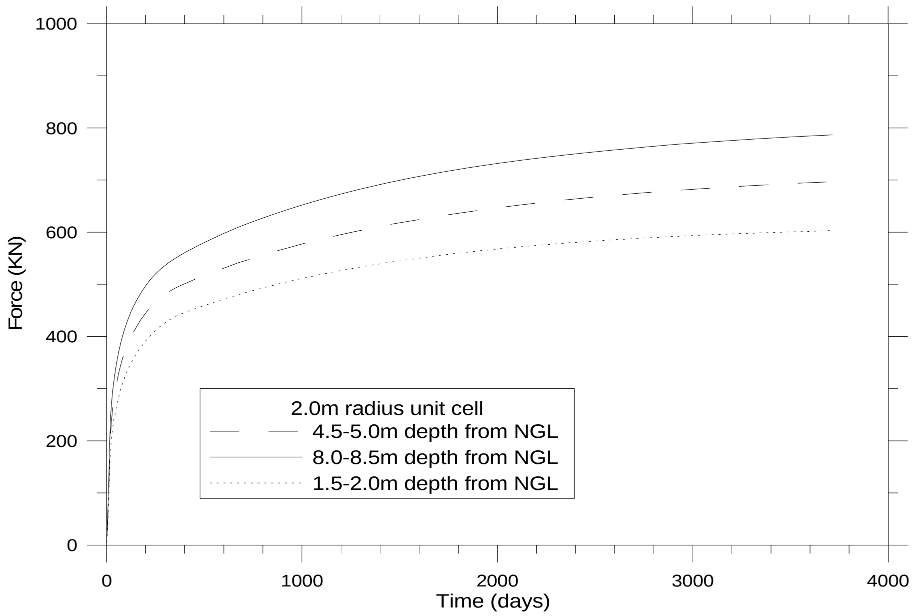

Figure 5.48 Evolutions of column forces with time: reduced locked-in stress Tpre=50kN/m (2.0m radius unit cell, SSC model applied)

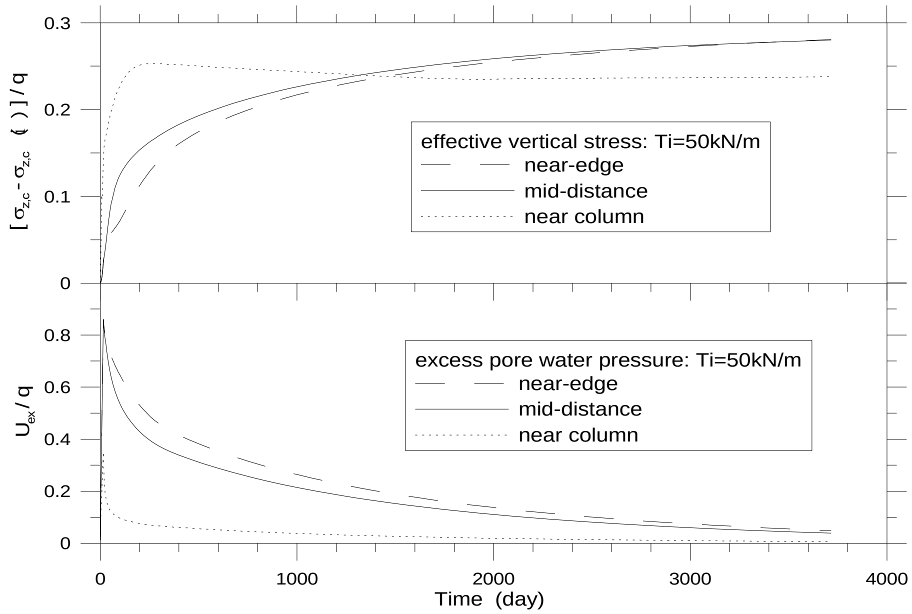

Figure 5.49 Consolidation responses in clay: reduced locked-in stress Tpre=50kN/m (2.0m radius unit cell, SSC model applied)

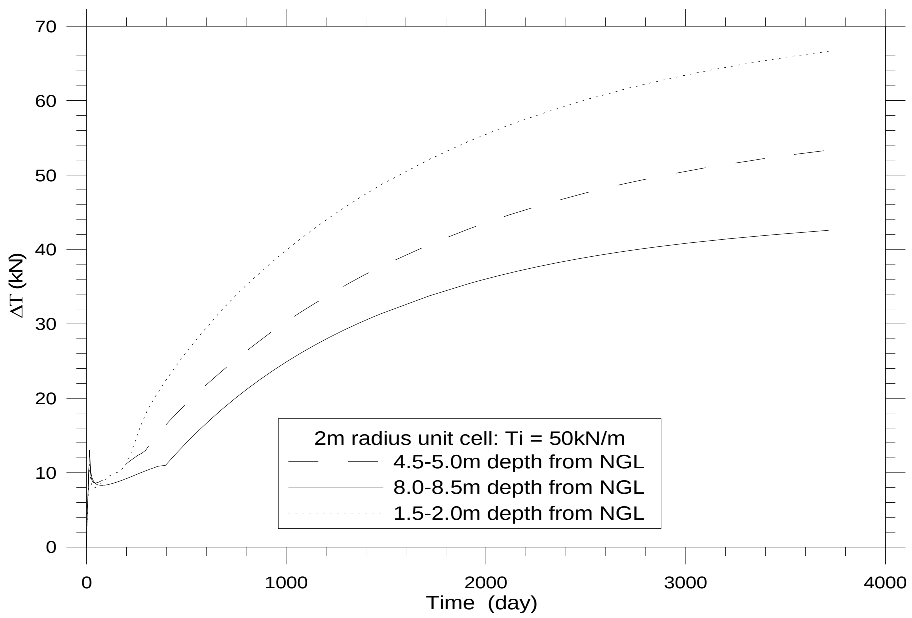

Figure 5.50 Increases in geosynthetic tension with time: reduced locked-in stress Tpre=50kN/m (2.0m radius unit cell, SSC model applied)

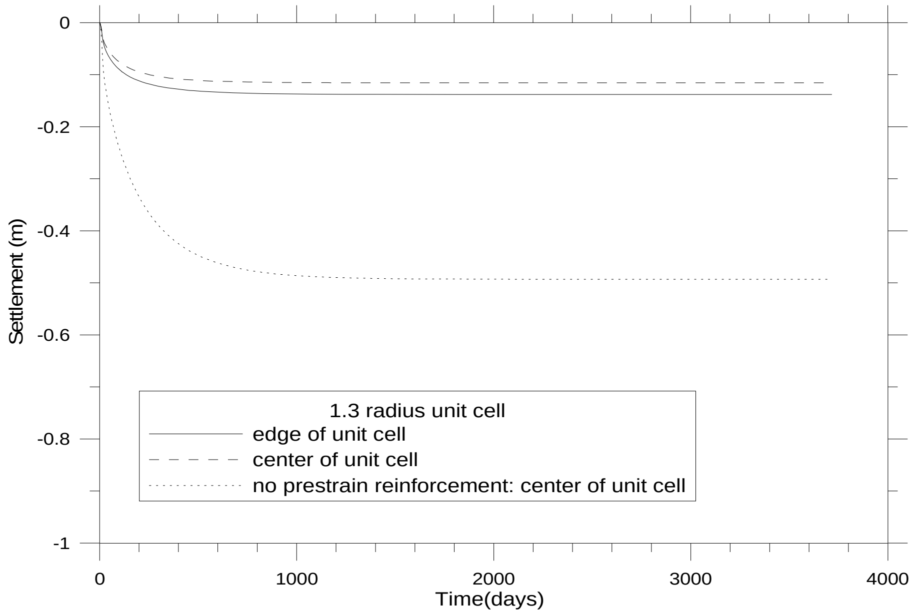

Figure 5.51(a) Settlement responses of reference analysis: comparison of settlement-time plots (1.3m radius unit cell, SSC model applied)

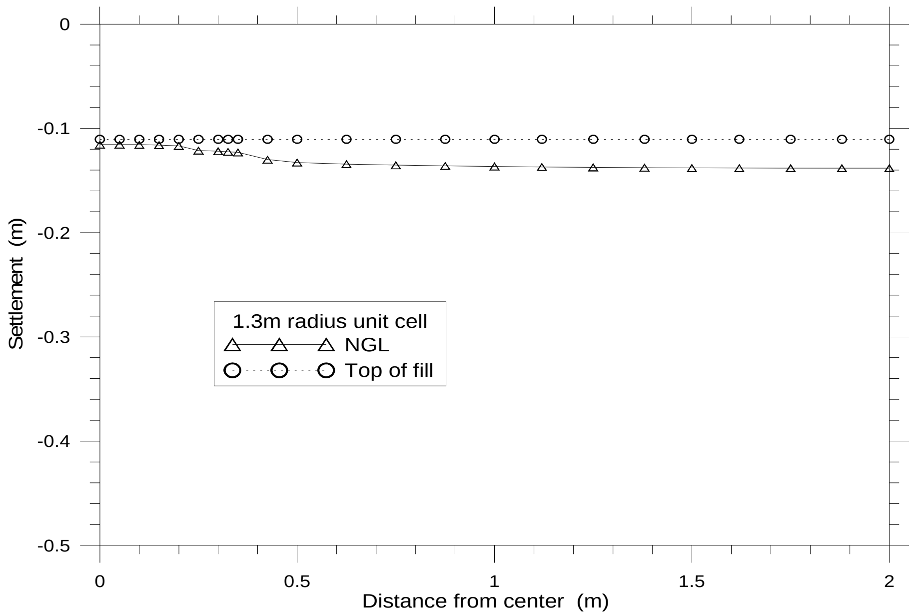

Figure 5.51(b) Settlement responses of reference analysis: settlement profiles at 10 years (1.3m radius unit cell, SSC model applied)

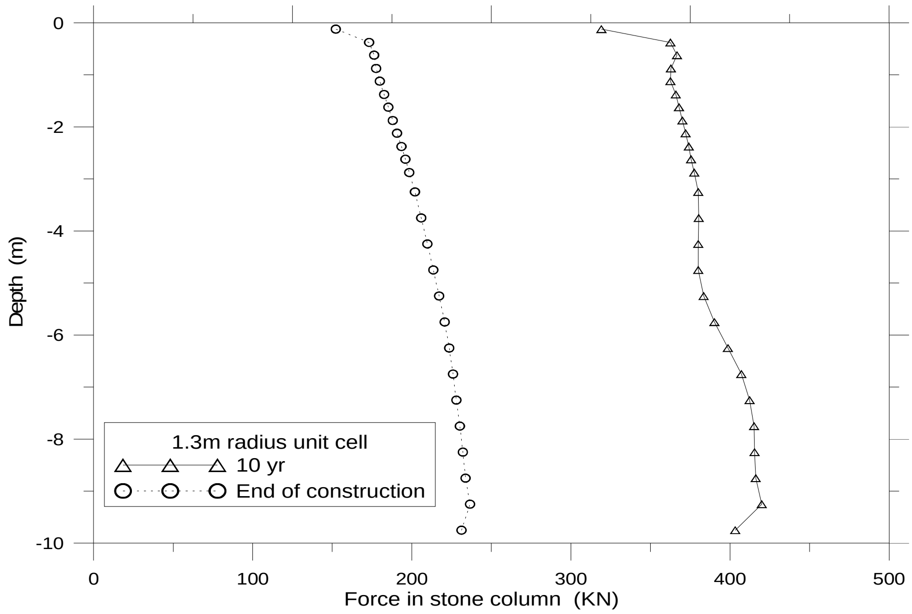

Figure 5.52 Distributions of column forces with depth: reference analysis (1.3m radius unit cell, SSC model applied)

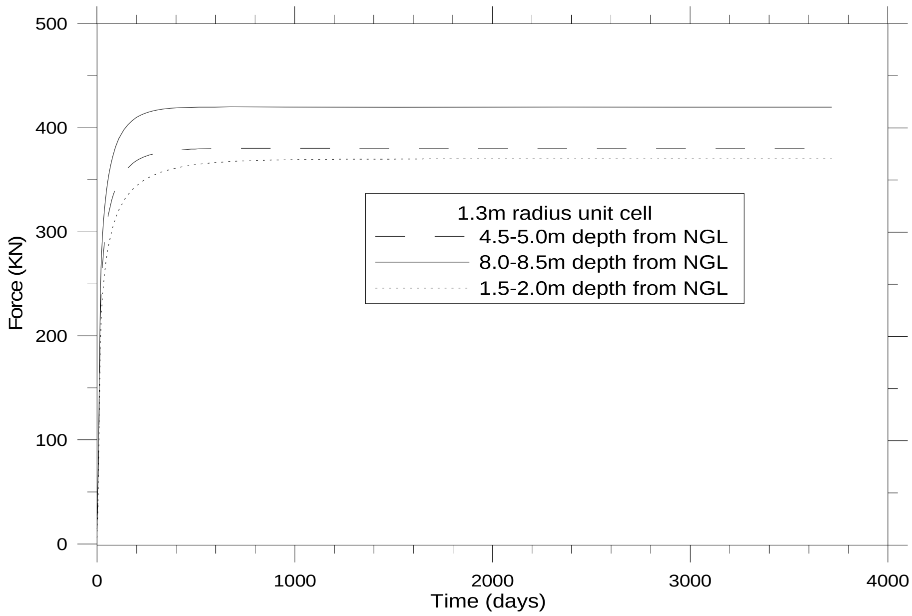

Figure 5.53 Evolutions of column forces with time: reference analysis (1.3m radius unit cell, SSC model applied)

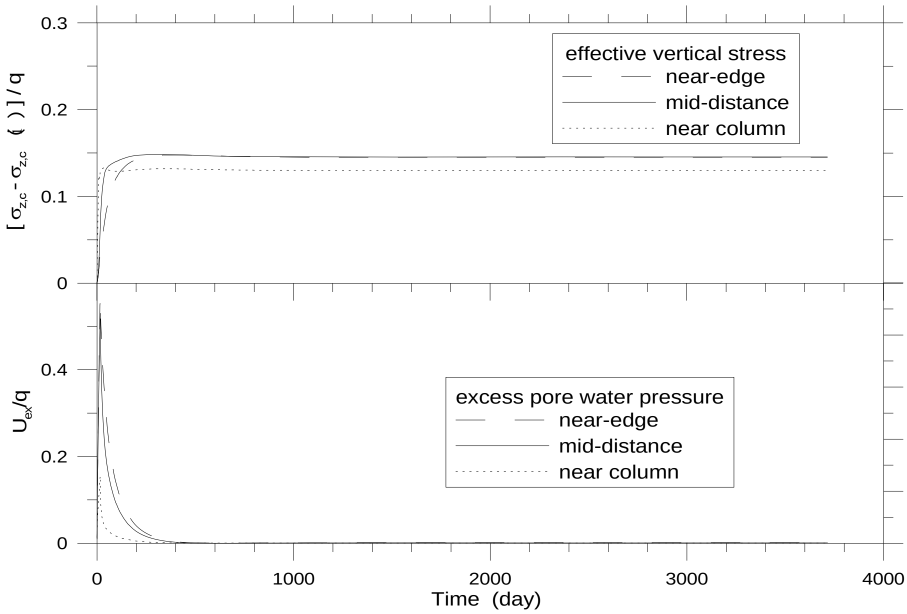

Figure 5.54 Consolidation responses in clay: reference analysis

(1.3m radius unit cell, SSC model applied)

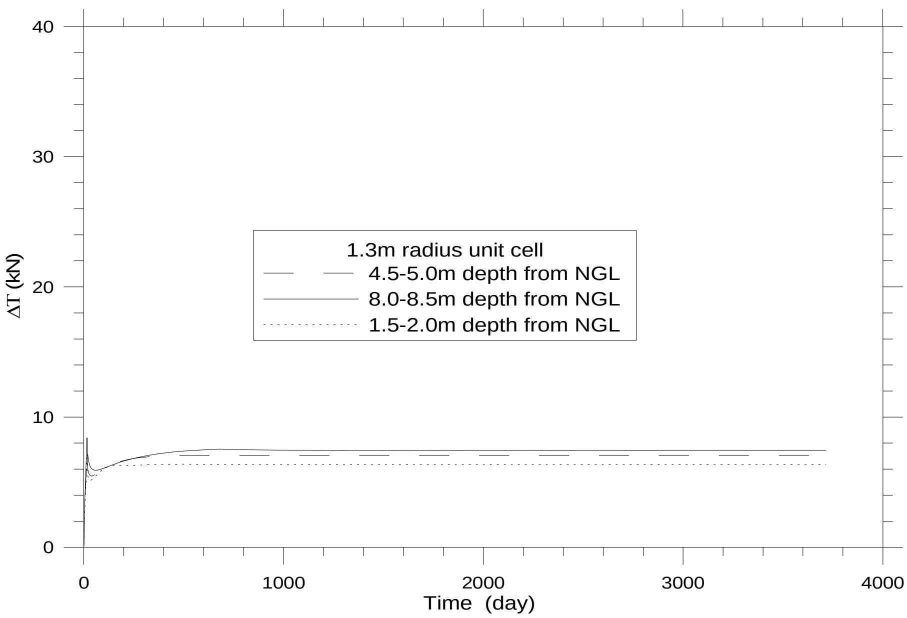

Figure 5.55 Increases in geosynthetic tension with time: reference analysis

(1.3m radius unit cell, SSC model applied)

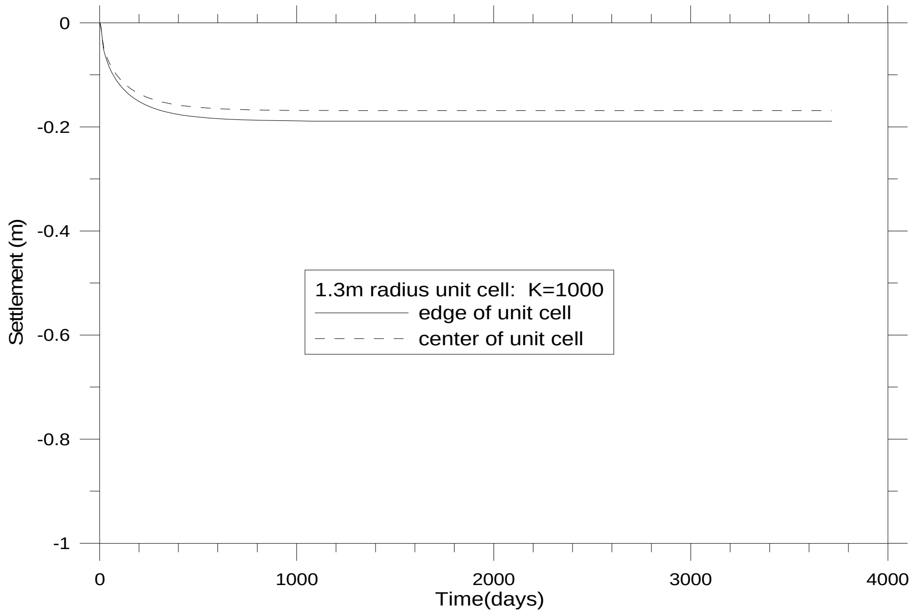

Figure 5.56(a) Settlement-time plots: reduced stone stiffness K=1000

(1.3m radius unit cell, SSC model applied)

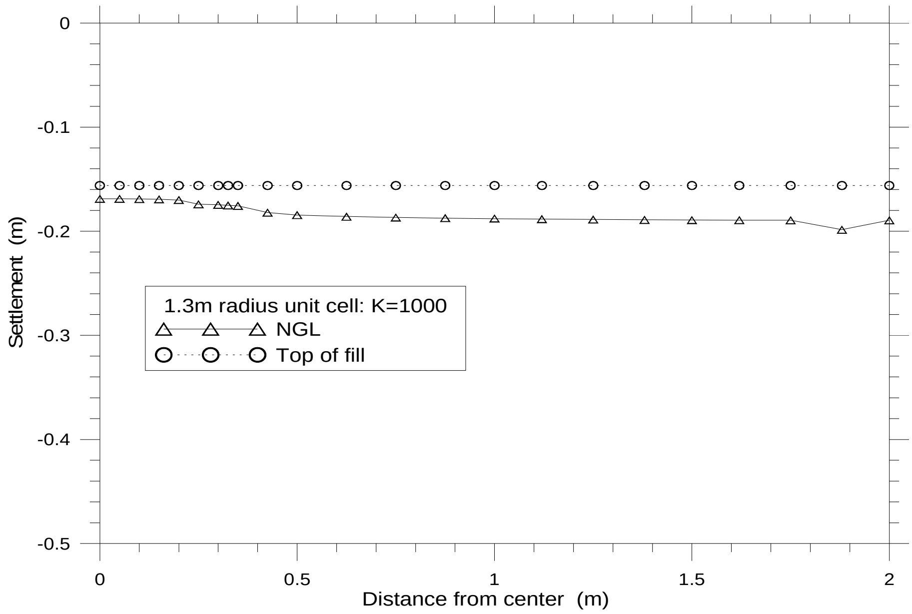

Figure 5.56(b) Settlement profiles: reduced stone stiffness K=1000

(1.3m radius unit cell, SSC model applied)

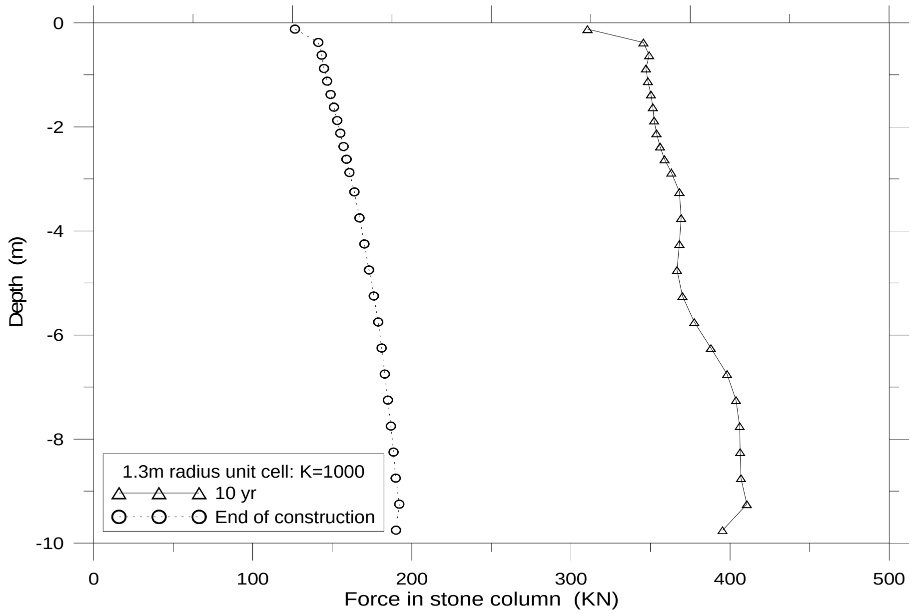

Figure 5.57 Distributions of column forces: reduced stone stiffness K=1000 (1.3m radius unit cell, SSC model applied)

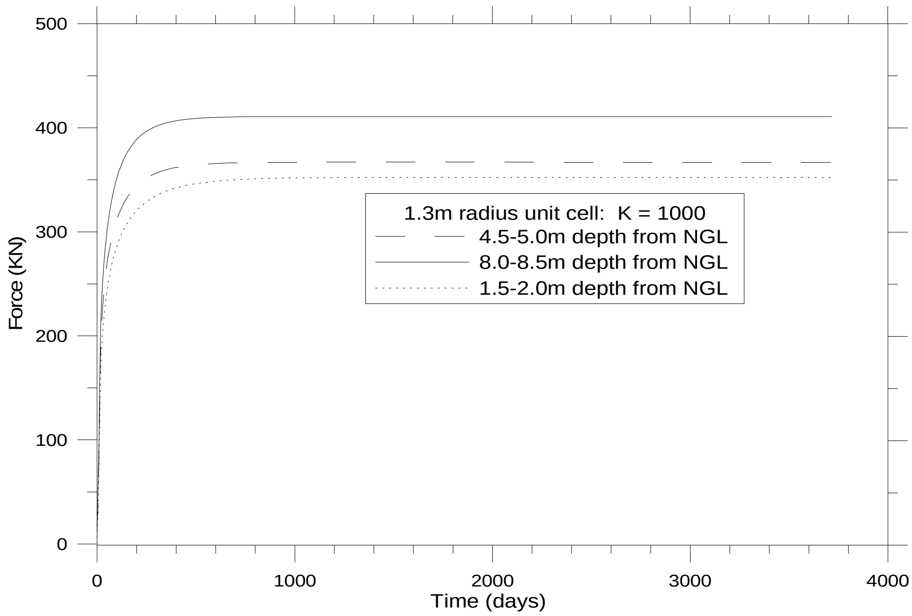

Figure 5.58 Evolutions of column forces with time: reduced stone stiffness K=1000 (1.3m radius unit cell, SSC model applied)

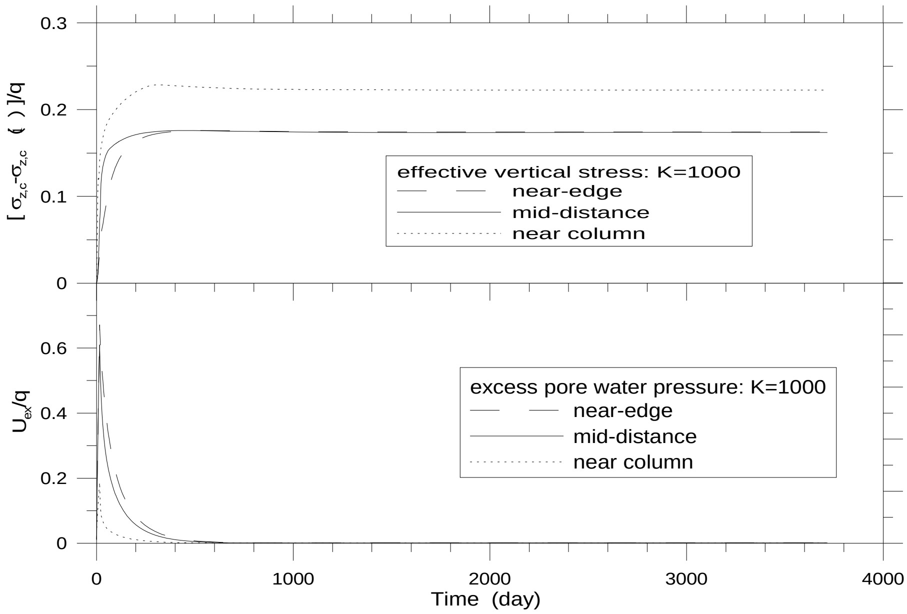

Figure 5.59 Consolidation responses in clay: reduced stone stiffness K=1000 (1.3m radius unit cell, SSC model applied)

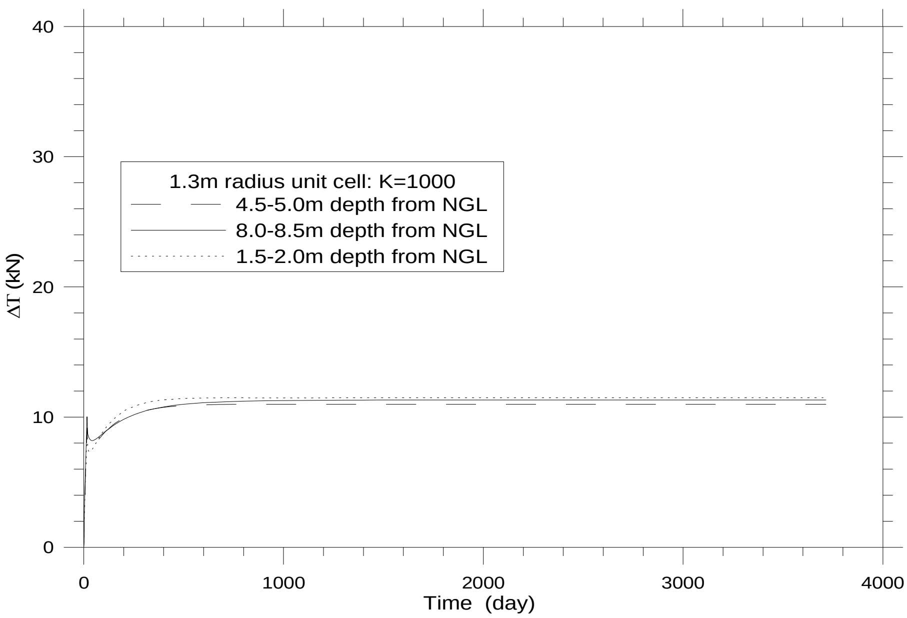

Figure 5.60 Increases in geosynthetic tension with time: reduced stone stiffness K=1000 (1.3m radius unit cell, SSC model applied)

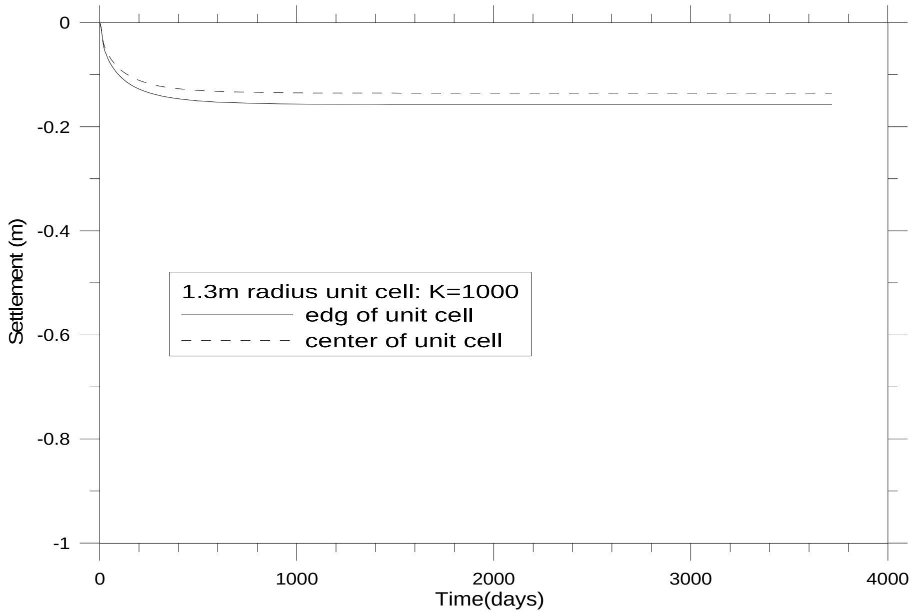

Figure 5.61(a) Settlement-time plots: reduced locked-in stress Tpre=21kN/m (1.3m radius unit cell, SSC model applied)

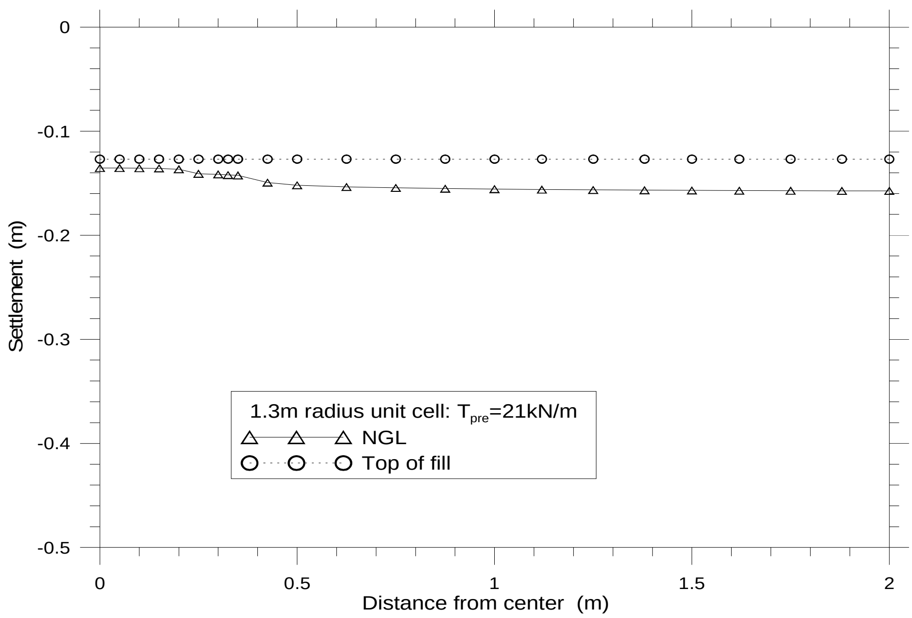

Figure 5.61(b) Settlement profiles: reduced locked-in stress Tpre=21kN/m (1.3m radius unit cell, SSC model applied)

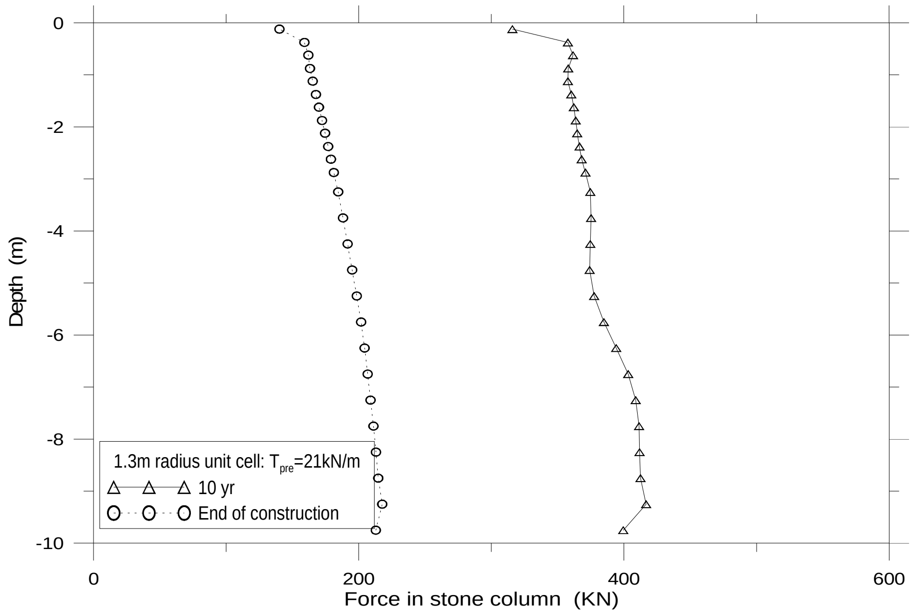

Figure 5.62 Distributions of column forces: reduced locked-in stress Tpre=21kN/m (1.3m radius unit cell, SSC model applied)

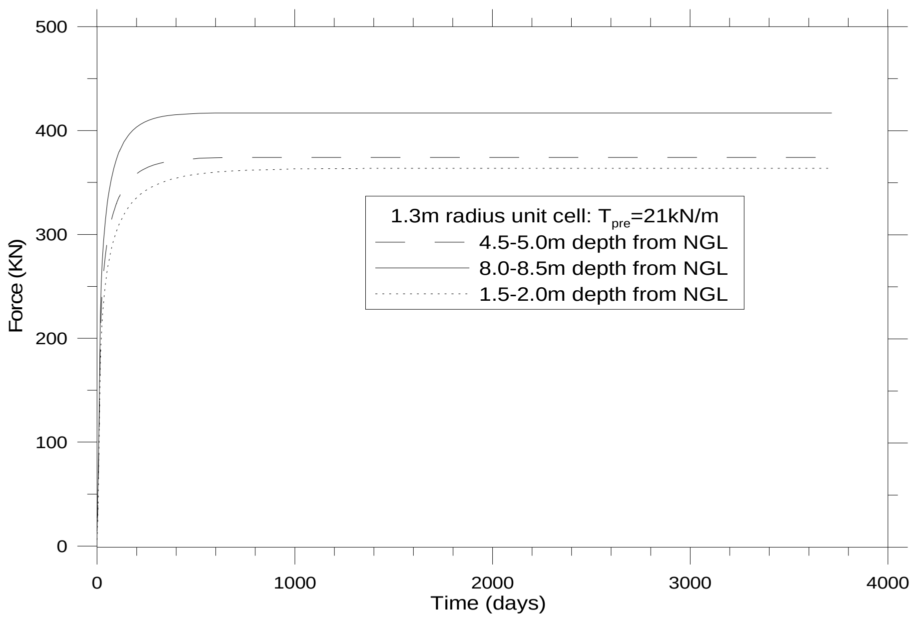

Figure 5.63 Evolutions of column forces with time: reduced locked-in stress Tpre=21kN/m (1.3m radius unit cell, SSC model applied)

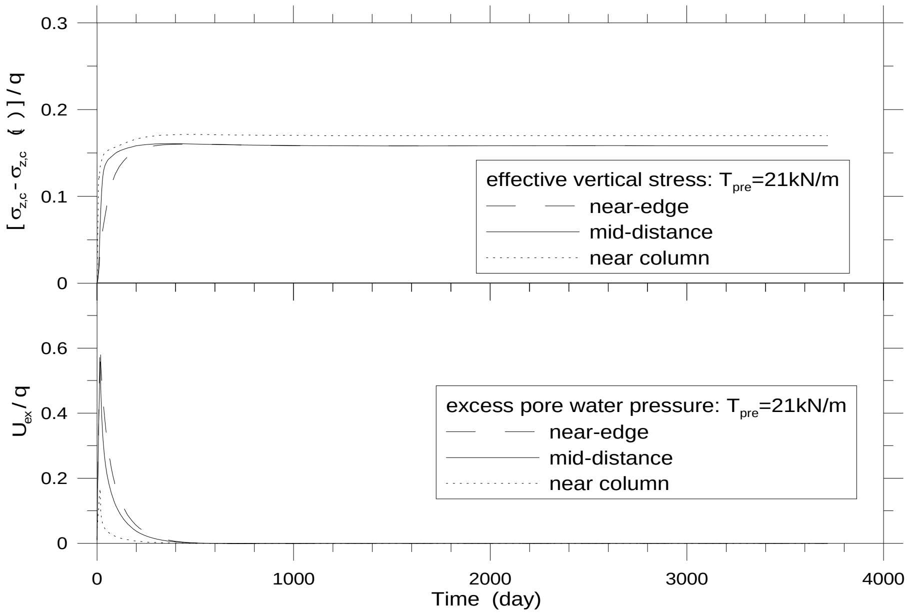

Figure 5.64 Consolidation responses in clay: reduced locked-in stress Tpre=21kN/m (1.3m radius unit cell, SSC model applied)

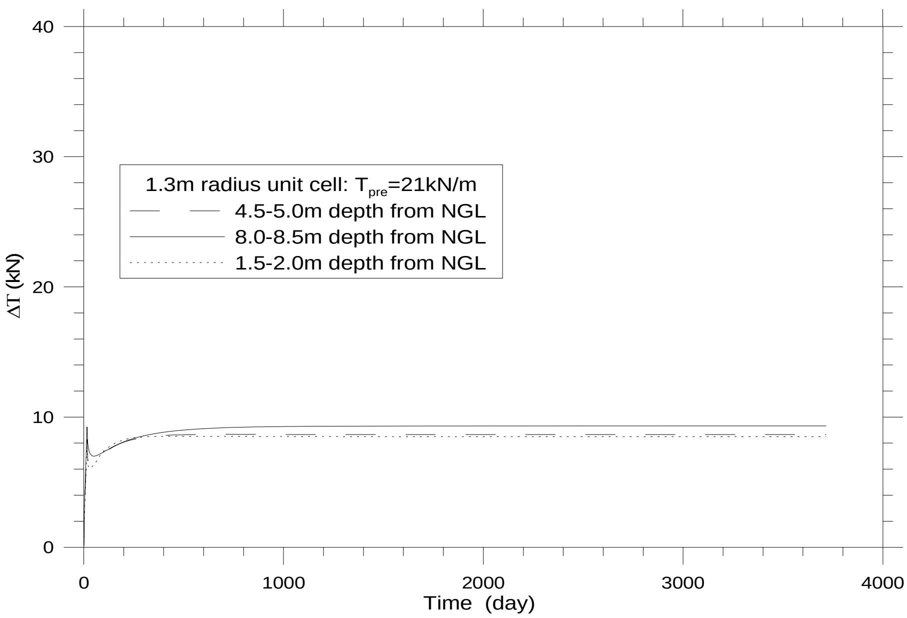

Figure 5.65 Increases in geosynthetic tension with time: reduced locked-in stress Tpre=21kN/m (1.3m radius unit cell, SSC model applied)

Table 5-4 Simulation results of “wish-in” stone columns

	settlement @ NGL (m)		Force (kN)		Increase of soil stress (after 10yr)		
	center	edge	EoC	10yr	next to column	middle-distance	near edge
MCC - 2.0m							
T_{pre} = 0	0.77	0.78	128	448			
Reference	0.24	0.30	198	750	0.3	0.22	0.22
T_{pre} halved	0.4	0.445	180	676	0.42	0.3	0.28
K halved	0.297	0.35	160	740	0.38	0.26	0.26
MCC -1.3m							
T_{pre} = 0	0.47	0.48	142	280			
Reference	0.1	0.126	220	375	0.13	0.15	0.15
T_{pre} halved	0.12	0.14	200	371	0.17	0.16	0.16
K halved	0.15	0.17	173	360	0.225	0.18	0.175
SSC- 2.0m							
T_{pre} = 0	0.87	0.89	137	466			
Reference	0.3	0.365	240	875	0.2	0.22	0.23
T_{pre} halved	0.486	0.53	205	800	0.24	0.28	0.28
K halved	0.36	0.41	194	855	0.24	0.24	0.25
SSC- 1.3m							
T_{pre} = 0	0.5	0.52	153	335			
Reference	0.12	0.14	245	420	0.13	0.15	0.15
T_{pre} halved	0.135	0.16	215	410	0.16	0.15	0.15
K halved	0.17	0.195	197	405	0.22	0.17	0.17

5.7 DISCUSSION

5.7. 1 Unit cell radius effects in MMC model

a) Geosynthetic encasement without pre-straining

The after 10yr settlement at NGL, stone column forces and $[\sigma_{z,c}-\sigma_{z,c}(i)]/q$ values are listed in Table 5-4 for comparing purpose. From the table, the unit cell radius has a significant impact on the performance of geosynthetic encased stone columns. When the geosynthetic encasement has no pre-straining, the settlements at NGL at the centers of the 2.0m and 1.3m radius unit cells are 0.77m and 0.47m respectively. The 40% difference is due to the radius size effect.

At the end of construction, the maximum column force of the 2.0m unit cell radius is about 128kN while the value of the 1.3m radius is 142kN. The difference of the stone column force is very small. After 10 years, the maximum column force of the 2.0m unit cell radius increases to 448kN while the value of the 1.3m radius is only 280kN. The column force of the 2.0m unit cell is significantly higher than that of the 1.3m radius.

b) Reference parameters

The settlement values at NGL of the 2.0m radius unit cell with reference parameters are 0.24m at the centre and 0.30m at the edge. The settlement values of the 1.3m radius unit cell with reference parameters are 0.1m at the centre and 0.126m at the edge. The settlement values of 1.3m radius are only about 40% of those of the 2.0m radius. This comparison shows that reducing the unit cell radius can significantly enhance the performance of stone column.

At the end of construction, the maximum column force of the 2.0m unit cell radius is about 198kN while the value of the 1.3m radius is 220kN. Column force of the 2.0m radius unit cell is slightly smaller than that of the 1.3m radius. After 10 years, the maximum column force of the 2.0m unit cell radius increases to 750kN while the value of the 1.3m radius is only 375kN. The column force of the 2.0m unit cell is double of that of the 1.3m radius.

Times required for the settlement and stone column forces to reach their ultimate values are significantly reduced. This is due to the dissipation of excess pore water pressure being much faster in the 1.3m radius than in the 2.0m radius. As shown in Figure 5.9 and Figure 5.24, about 400-500 days are needed for the excess pore water pressure to dissipate out when the unit cell radius is 1.3m. The time needed for the dissipation of pore water pressure in 2.0m radius is about 10 years.

Increases in the effective stress of the 2.0m radius unit cell are also higher than those of the 1.3m radius unit cell. The $[\sigma_{z,c}-\sigma_{z,c}(i)]/q$ value next to the column is about 130% higher than that of the 1.3m radius unit cell. The values at the mid-distance and edge of unit cell location are 46% higher than those of 1.3m radius unit cell.

c) Impact on stone stiffness

The performance of stone column due to the compacted stones also depends on the unit cell radius. The settlement values at NGL of the 2.0m radius unit cell are 0.297m at the centre and 0.35m at the edge. The corresponding settlement values of the 1.3m radius unit cell are 0.15m at the centre and 0.17m at the edge. The settlement values of 1.3m radius are only about 50% of those of the 2.0m radius. This comparison shows that reducing the unit cell radius can significantly enhance the performance of stone column.

Comparing with the reference analysis: When the unit cell radius is 2.0m, increases in settlement are only about 24% at the top of the stone column and 17% at the edge location in spite of a 50% reduction in stiffness. When the unit cell radius is 1.3m, the settlement values increase 50% at the centre and 35% at the edge. This comparison showns that the performance of stone column is sensitive with K when the unit cell radius is 1.3m but not sensitive with K when the radius is 2.0m.

At the end of construction, the maximum column force of the 2.0m unit cell radius is about 160kN while the value of the 1.3m radius is 173kN. Column force of the 2.0m radius unit cell is slightly smaller than that of the 1.3m radius. After 10years, the maximum column force of the 2.0m unit cell radius increases to 740kN while the value of the 1.3m radius is only 360kN. The maximum column force of the 2.0m unit cell is more than 100% higher than that of the 1.3m radius.

Increases in the effective stress of the 2.0m radius unit cell are also higher than those of the 1.3m radius unit cell. The $[\sigma_{z,c}-\sigma_{z,c}(i)]/q$ values of the 2.0m radius unit cell are more than 40% higher than those of the 1.3m radius unit cell.

d) Impact of locked-in strain

The performance of a unit cell due to locked-in strain also depends on its radius. The settlement values at NGL of the 2.0m radius unit cell are 0.4m at the centre and 0.445m at the edge. The settlement values of the 1.3m radius unit cell with T_{pre}

dropped into half of the reference parameter are 0.12m at the centre and 0.14m at the edge. The settlement values of 1.3m radius are only ~ 30% of those of the 2.0m radius. This comparison shows that reducing the unit cell radius can significantly enhance the performance of stone column.

Comparing with the reference analysis: When the unit cell radius is 2.0m, increases of settlement are about 67% at the top of the stone column and 48% at the edge location when T_{pre} drop 50%; when the unit cell radius is 1.3m, the settlement values increase 20% at the centre and 11% at the edge. This comparison shows that the performance of stone column is sensitive with T_{pre} when the unit cell radius is 2.0m but not sensitive with T_{pre} when the unit cell radius 1.3m.

At the end of construction, the maximum column force of the 2.0m unit cell radius is about 180kN while the value of the 1.3m radius is 200kN. Column force of the 2.0m radius unit cell is slightly smaller than that of the 1.3m radius. After 10 years, the maximum column force of the 2.0m unit cell radius increases to 676kN while the value of the 1.3m radius is only 371kN. The maximum column force of the 2.0m unit cell is significantly higher than that of the 1.3m radius.

Increases in the effective stress of the 2.0m radius unit cell are also higher than those of the 1.3m radius unit cell. The $[\sigma_{z,c}-\sigma_{z,c}(i)]/q$ value next to the column is about 150% higher than that of the 1.3m radius unit cell. The values at the mid-distance and edge of unit cell location are75% higher than those of the 1.3m radius.

5.7. 2 Unit cell radius effects in SSC model

a) Geosynthetic encasement without pre-straining

From the table 5-4, the unit cell radius has a significant impact on the performance of geosynthetic encased stone columns. When the geosynthetic encasement has no pre-straining, the settlements at NGL at the centers of the 2.0m and 1.3m radius unit cells are 0.87m and 0.5m respectively. The 43% difference is due to the radius effect.

At the end of construction, the maximum column force of the 2.0m unit cell radius is about 137kN while the value of the 1.3m radius is 153kN. The difference of the stone column force is very small. After 10 years, the maximum column force of the 2.0m unit cell radius increases to 466kN while the value of the 1.3m radius is only 335kN. The column force of the 2.0m unit cell is significantly higher than that of the 1.3m radius.

b) Reference parameters

The settlements at NGL of the 2.0m radius unit cell with reference parameters are 0.3m at the centre and 0.365m at the edge. The settlements value of the 1.3m radius unit cell with reference parameters are 0.12m at the centre and 0.14m at the edge. The settlement values of 1.3m radius are only about 40% of those of the 2.0m radius. This comparison shows that reducing the unit cell radius can significantly enhance the performance of stone column.

At the end of construction, the maximum column force of the 2.0m unit cell radius is about 240kN while the value of the 1.3m radius is 245kN. Column force of the 2.0m radius unit cell is slightly smaller than that of the 1.3m radius. After 10years, the maximum column force of the 2.0m unit cell radius increases to 875kN while the value of the 1.3m radius is only 420kN. The maximum column force of the 2.0m unit cell is about twice as that of the 1.3m radius.

Times required for the settlement and stone column forces to reach their ultimate values are significantly reduced. This is due to the dissipation of excess pore water pressure being much faster in the 1.3m radius than in the 2.0m radius. As shown in Figure 5.39 and Figure 5.54, about 400 days are needed for the excess pore water pressure to dissipate out when the unit cell radius is 1.3m. The time needed for the dissipation of pore water pressure in 2.0m radius is about 10 years.

Increases in the effective stress of the 2.0m radius unit cell are also higher than those of the 1.3m radius unit cell. The $[\sigma_{z,c}-\sigma_{z,c}(i)]/q$ value next to the column is about 54% higher than that of the 1.3m radius unit cell. The values at the mid-distance and edge of unit cell location are 47% higher than those of the 1.3m radius.

c) Impact on stone stiffness

The performance of stone column due to the compacted stones also depends on the unit cell radius. The settlements at NGL of the 2.0m radius unit cell are 0.36m at the centre and 0.41m at the edge. The corresponding settlement values of the 1.3m radius unit cell are 0.17m at the centre and 0.195m at the edge. The settlement values of 1.3m radius are only about 50% of that of the 2.0m radius. This comparison shows that reducing the unit cell radius can significantly enhance the performance of stone column.

Comparing with the reference analysis: When the unit cell radius is 2.0m, increases of settlement are only about 20% at the top of the stone column and 11% at the edge location in spite of a 50% reduction in stiffness. When the unit cell radius is 1.3m, the settlement values increase 42% at the centre and 39% at the edge. This comparison shown that the performance of stone column is sensitive with K when unit cell radius is 1.3m but not sensitive with K when the radius is 2.0m.

At the end of construction, the maximum column force is about 194kN of the 2.0m unit cell radius while the value of the 1.3m radius is 197kN. Column force of the 2.0m radius unit cell is slightly smaller than that of the 1.3m radius. After 10years, the maximum column force of the 2.0m unit cell radius increases to 855kN while the value of the 1.3m radius is only 405kN. The maximum column force of the 2.0m unit cell is 110% higher than that of the 1.3m radius.

Increases in the effective stress of the 2.0m radius unit cell are also higher than those of the 1.3m radius unit cell. At the next to stone column location, $[\sigma_{z,c}-\sigma_{z,c}(i)]/q$ values of the 2.0m radius unit cell are 10% higher than those of the 1.3m radius unit cell. At the mid-distance and near the edge location, the values are more than 40% higher than that of the 1.3m radius.

<u>d) Impact of locked-in strain</u>

The performance of a unit cell due to locked-in strain also depends on its radius. The settlements at NGL of the 2.0m radius unit cell are 0.486m at the centre and 0.53m at the edge. The corresponding settlement value of the 1.3m radius unit cell are 0.135m at the centre and 0.16m at the edge. The settlement values of 1.3m radius is only ~

30% of that of the 2.0m radius. This comparison shows that reducing the unit cell radius can significantly enhance the performance of stone column.

Comparing with the reference analysis: When the unit cell radius is 2.0m, increases in settlement are about 60% at the top of the stone column and 45% at the edge location as T_{pre} drop 50%; when the unit cell radius is 1.3m, the settlement value increase 13% at the centre and 14% at the edge. This comparison shows that the performance of stone column is sensitive with T_{pre} when the unit cell radius is 2.0m but not sensitive with T_{pre} when the unit cell radius 1.3m.

At the end of construction, the maximum column force is about 194kN of the 2.0m unit cell radius while the value of the 1.3m radius is 215kN. Column force of the 2.0m radius unit cell is slightly smaller than that of the 1.3m radius. After 10years, the maximum column force of the 2.0m unit cell radius increases to 800kN while the value of the 1.3m radius is only 410kN. The column force of the 2.0m unit cell is significantly higher than that of the 1.3m radius.

Increases in the effective stress of the 2.0m radius unit cell are also higher than those of the 1.3m radius unit cell. The $[\sigma_{z,c}-\sigma_{z,c}(i)]/q$ value next to the column is about 50% higher than that of the 1.3m radius unit cell. The values at the mid-distance and edge of unit cell location are 87% higher.

5.7. 3 Impact of soil models

In this sub-section, the difference of performance of a stone column installed in MCC and SSC will be examined. The comparison is based on the calculation results from the above conditions using both the MCC and SSC models.

a) 2.0m radius unit cell

Settlement is higher when the stone column is installed in SSC. Settlements of non-pre-strained geosynthetic encasement for MCC and SSC are 0.77m and 0.89m respectively. This 0.12m increase is due to the SSC characteristics.

When the geosynthetic encasement becomes pre-strained, the settlements of both the MCC and SSC cases drop dramatically. When the reference parameters are used, settlements at NGL of the unit cell using MCC only drop to 0.24m at its centre and 0.30m at its edge. Settlements at NGL of the stone column unit cell installed in SSC drop to 0.30m at its centre and 0.36m at its edge. The settlement difference between the SSC and MCC cases is 0.06m, about half that of when the geosynthetic does not have locked-in strain. The “bump” at NGL, which is roughly the difference between settlements at the centre and edge of the unit cell, remains nearly the same in both MCC and SSC, about 0.06m in height. The top of the fill remains flat and there is no bump in either case.

The consolidation process takes longer in SSC. Consolidation of the MCC ceases after about 2000 days but, for SSC, it does not end even after 10years.

The maximum stone column force at 10 years of the stone installed in SSC is much higher than of that installed in MCC, 875 kN compared with 750 kN respectively. In addition, the stone column force for SSC still does not reach the asymptotic value even after 10 years.

The $[\sigma_{z,c}-\sigma_{z,c}(i)]/q$ value of SSC is significantly lower than that of MCC in the near-stone column location being 0.2m compared with 0.31m while, at the middle location, it is slightly less and, at the edge location, nearly the same. This reduction in increases in the effective stress is consistent with increases in the column forces. In the SSC case, more fill is transferred to the stone column and less fill load is supported by the SSC.

Stone stiffness effects

The stone stiffness effects in both MCC and SSC are nearly the same. When the stiffness of the stone is reduced by 50%: settlements at the top of the stone column increase by 20% for both cases and, at the edge of the unit cells at NGL, they increase by 17% for MCC and by14% for SSC.

In both MCC and SSC, the stone forces reduce slightly when the stiffness of the stone is reduced by 50%. The effective stress changes in SSC are less than those in MCC: increases of 20% at the next-to-stone column, 10% at the middle distance and 5% at the edge of the unit cell locations for SSC and 40% next to the stone column and around 20% at the other two locations for MCC.

The computed results show that, in both MCC and SSC, stone column performance is not sensitive to stone stiffness in the 2.0m radius unit cell.

Impacts on locked-in strain

There are no dramatic differences of the settlement changes between MCC and SSC when the locked-in strain reduced. When it reduces by 50%, settlements at the edges of the unit cells at NGL increase by around 47% for SSC and 55% for MCC and, at the top of the stone column, by 60% for SSC and 67% for MCC.

In both MCC and SSC, the stone force experiences about a 10% reduction when the locked-in strain is reduced by 50%. The effective stress changes in SSC are larger than those in MCC at the next-to-stone column location and nearly the same at the other two locations. For SSC and MCC, there are 80% and 40% increases at the next to stone column, 27% and 28% at the middle distance, and 22% and 20% at the edge of the unit cell, locations respectively.

The above comparisons indicate that stone column performance is sensitive to locked-in strain for both MCC and SSC, with the stone column installed in SSC being relatively less sensitive.

b) 1.3m radius unit cell

Settlement of the stone column installed in SSC is higher than that of the stone column installed in MCC when the locked-in strain is the same. Settlement of the non-pre-strained geosynthetic encasement of MCC is 0.47m and that of SSC 0.50m. This 0.03m difference in settlement is due to the SSC characteristics.

When the geosynthetic encasement becomes pre-strained to the reference parameters, settlements of both the MCC and SSC drop dramatically. Settlements at NGL of the stone column unit cells for the MCC only and the SSC cases drop to 0.1m and 0.12m at their centers and 0.126m and 0.14m at their edges respectively. These settlement differences of 0.02m are about 2/3 of those when the geosynthetic does not have locked-in strain.

The consolidation process takes longer in SSC than in MCC, nearly 800 days compared with 300 days.

The maximum stone column force after 10 years for the stone installed in SSC is much higher, 420 kN, than that installed in MCC, 375 kN.

The $[\sigma_{z,c}-\sigma_{z,c}(i)]/q$ values of SSC are about 5%-6% less than MCC at each location. This is because SSC is weak and more load of the fill is transferred to the stone columns.

Stone stiffness effects

When the stiffness of the stones is reduced by 50%, settlements at NGL at the edges of the unit cells increase by around 36% for SSC and 40% for MCC and, at the top of the stone columns, by 40% for SSC and 50% for MCC.

In both MCC and SSC, the stone forces reduce slightly when the stiffness of the stone is reduced by 50%. The effective stress changes in SSC are less than those in MCC, being increases of 20% and 40% at the next to stone column location, 10% and about 20% at the middle distance and 5% and about 20% at the edges of the unit cell locations respectively.

When the stone stiffness is reduced by 50%, the value of $[\sigma_{z,c}-\sigma_{z,c}(i)]/q$ at the next to stone column location is 60% higher than in the reference case for MCC and 70%

higher than in the reference case for SSC. The percentage increases at the other two locations are about 20% higher than in the reference cases for both MCC and SSC.

As discussed above, stone column performance is sensitive to stone stiffness for both MCC and SSC although relatively less so for the latter.

<u>Impacts on locked-in strain</u>

There are no obvious differences in the locked-in strain between MCC and SSC. When it is reduced by 50%, settlements at NGL at the edge of the unit cell locations increase by around 10-15% for both MCC and SSC.

In both MCC and SSC, stone force changes are very small when the locked-in force is reduced to 50%, being 3% and 1% decreases respectively. Effective stress changes in MCC and SSC are also relatively small, being 25% and 30% increases at the next to stone column locations and about 10% and 9% increases at the other two locations respectively.

Thus, in the 1.3m radius unit cell, the performance of the stone column is not sensitive to the locked-in strain when installed in either MCC or SSC.

5.8 CONCLUSION

Conclusions drawn from the above discussion are:

1. Unit cell radius has a significant impact on the stone column performance.

2. When the radius of the unit cell is 2.0m, the performance of the stone column is more sensitive to the lock in strain than to the stiffness of the stone.

3. When the radius of the unit cell is 1.3m, the performance of the stone column is more closely related to the stiffness of the stone than to the lock in strain; and
4. Sensitivities of stone column performance to both pre-strain and stone stiffness are less in SSC than in MMC.

CHAPTER SIX

MODELLING FULL DISPLACEMENT INSTALLATION OF STONE COLUMNS

6.1 INTRODUCTION

Stone columns are installed by either replacement or displacement of the in-situ soils or by a combination of these methods using a variety of equipment and installation techniques. No matter what kind of installation methods are used, the disturbance to the surrounding soil is unavoidable.

The "wish-in" stone column method discussed in Chapter 5 assumes that the stone has been installed by the "replacement method" with idealized installation and nearly no disturbance to the surrounding soils.

The other extreme is "full displacement installation method". The soil is considered to be pushed laterally to the designed dimension of the stone columns during installation. This procedure can be further idealized by a cavity expansion analysis and be simulated numerically by coupled FEM to examine how the installation method will affect the surrounding soils.

6.2 NUMERICAL IDEALISATION

In this chapter, the "full displacement" installation method is idealized as full-depth cavity expansion in a unit cell. To simplify the simulation and check the trend of the cavity expansion results of different depths, one-layer cavity expansion analysis is conducted first. The one-layer cavity expansion results were then normalized by the initial stress before the cavity expansion of that layer to examine the dependence of the cavity expansion results if any on depth. A full-depth cavity expansion of unit cell is then conducted and compared with the one-layer cavity expansion simulation. The results of the full-depth cavity expansion are utilized as the initial stress for the simulation of stone column installed by full displacement installation method in the next Chapter. As the one-layer cavity expansion has only one selected depth from the unit cell, only the numerical idealization of the full-depth cavity expansion will be explained in details in this section.

6.2.1 Unit cell idealization

The stone column installation simulated in this chapter is assumed to be conducted in a large fill area. Both the depth of the soil and the lateral displacement caused by the installation are negligible compared with the fill area. Thus, to simplify the simulation, a unit cell idealization as shown in Figure 6.1 can be adopted for the analysis purpose. This idealization is reasonable approximation of areas away from the edges of the embankment.

The thickness of the soft clay is about 10.0m. The radial dimension of the unit cell is assumed to be 100m,10 times of the thickness of the soft clay. The ground watertable is set to 0.0m. The top boundary of the clay layer is idealized as a free draining boundary whereas the bottom boundary of the unit cell is modelled as impermeable. The inside boundary of the unit cell is assumed permeable and the outside boundary is assumed impermeable. The stone columns are assumed to be installed by the "full displacement" method, which can be idealized as cavity expansion from the centre of the unit. To avoid numerical errors, the cavity expansion is begin at 0.05m away from the central line of the unit cell and expanded to 0.35m which is the radius of the stone columns with geosynthetic encasement. The speed of the expansion is 0.3m in 2 hours.

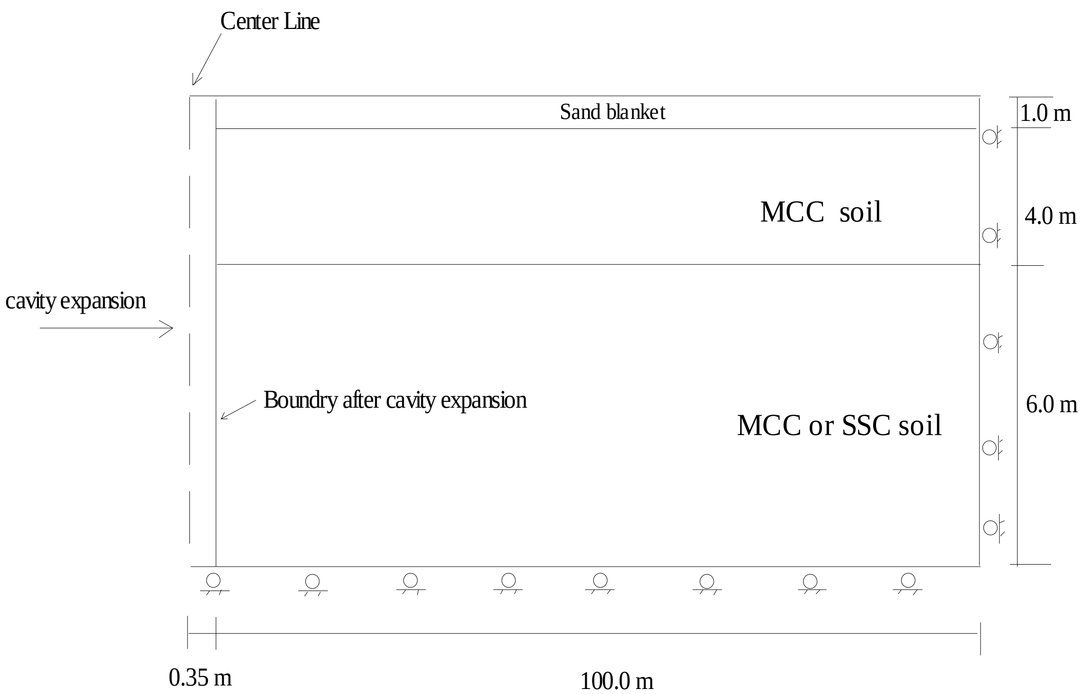

Figure 6.1: Idealization of the unit cell

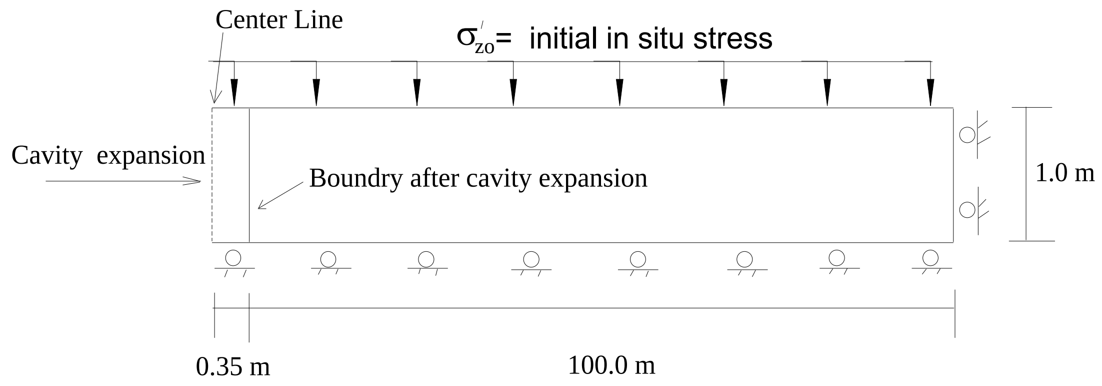

Figure 6.2: Idealization of one-layer cavity expansion

6.2.2 Material models

In this Chapter, both the MCC and SSC models are used to simulate the stone columns installed in normal soils and sensitive soils respectively. The soil parameters used for cavity expansion in normal soils are exactly the same as those in Table 5-2 of Chapter 5. Stone columns installed in sensitive soils have the same MCC parameters and their SSC parameters are the same as those listed in Table 5-3 of Chapter 5.

6.2.3 Construction consequence

A coupled analysis is adopted for the full-depth cavity expansion and the following construction sequence is modelled.

1. initialise in-situ stress of soft clay deposit under green field conditions;
2. place sand blanket in four days;
3. push the soil horizontally from 0.05m away from the centre line of the unit cell to a distance of 0.35m at a speed of 0.15m/hour.

The sand blanket is replaced first to simulate forming a platform to support the equipment required for installation of the stone columns. Its presence also remove numerical issues associated with soft clay at very low stress. Details are explained in Chapter 5 and not repeat here.

6.2.4 FEM Mesh

The finite element mesh of full-depth unit cell simulation consists of 418 Linear Strain Triangular (LST) elements with 897 nodes. The finite element mesh of one-layer consists of 38 LST elements with 117 nodes. Every LST element has 6 integration points and 3 degrees of freedom per each node of the coupled analysis using modified cam clay model and 9 integration points and 3 degrees for coupled analysis using the sensitive soft clay model.

6.2.5 One-layer cavity expansion idealization

The one-layer simulations are one meter thick soils from selected depths of the unit cell, as shown in Figure 6.2. The other dimensions, boundary conditions, soil parameters, cavity expansion speed, etc., are exactly the same as those of the typical selected soil layer in the unit cell. Three depths of the soil are selected for one-layer simulations, 9.0m-10.0m from NGL, 5.0m-6.0m from NGL and 3.0m-4.0m from NGL. The last one is only simulated in MCC soils while the first two are simulated in both MCC soils and SSC soils.

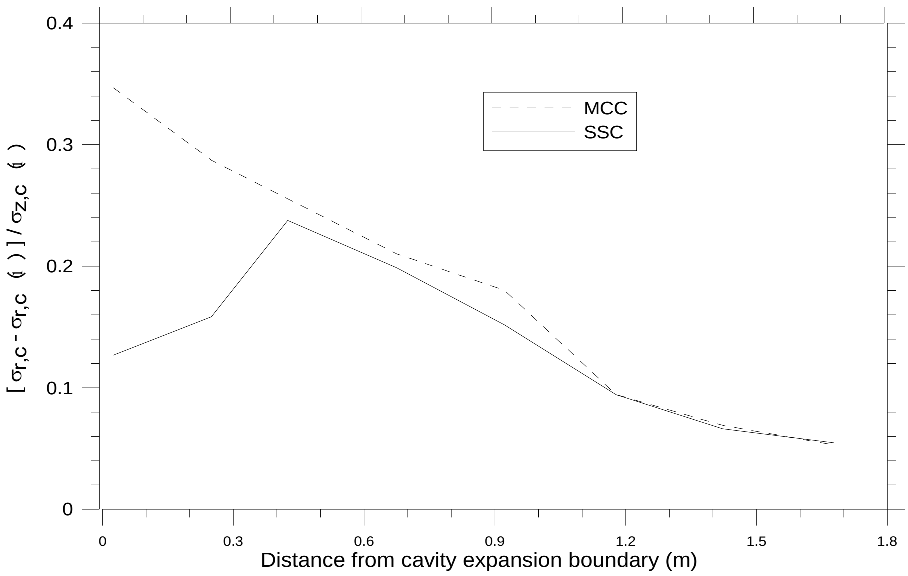

Figure 6.3: Increase of horizontal stress with distance from cavity expansion boundary at the end of cavity expansion (9.0-10.0m depth from NGL)

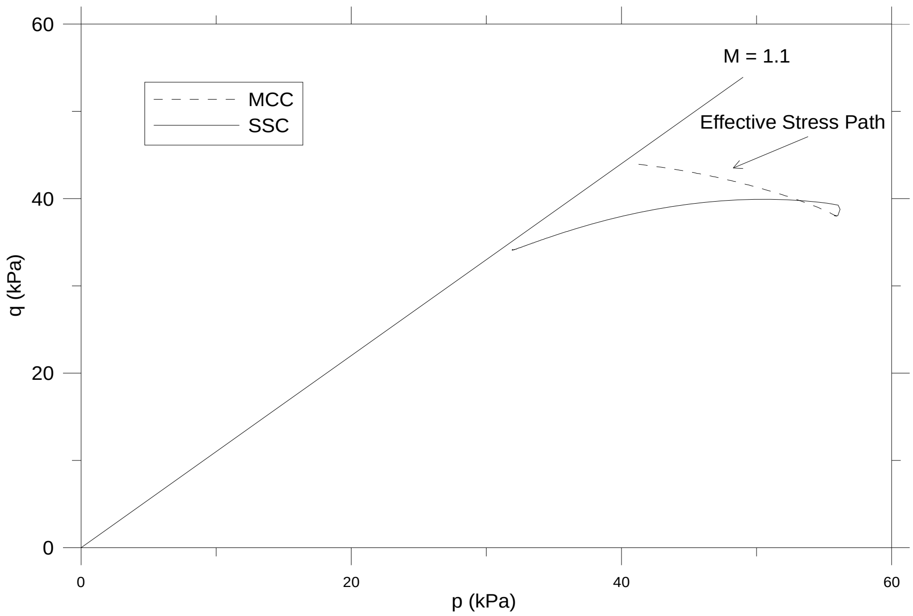

Figure 6.4: Cavity expansion stress path

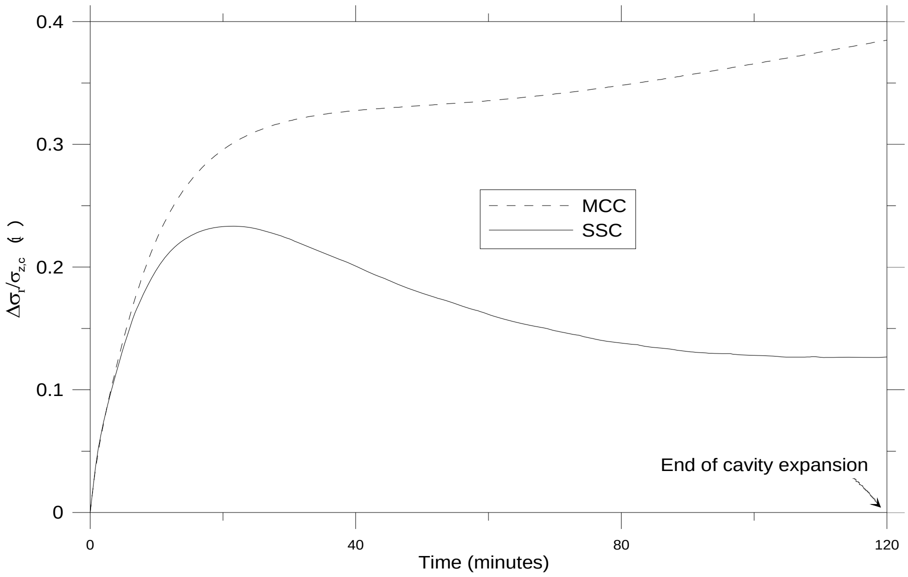

Figure 6.5: Developing of increase of horizontal effective stress

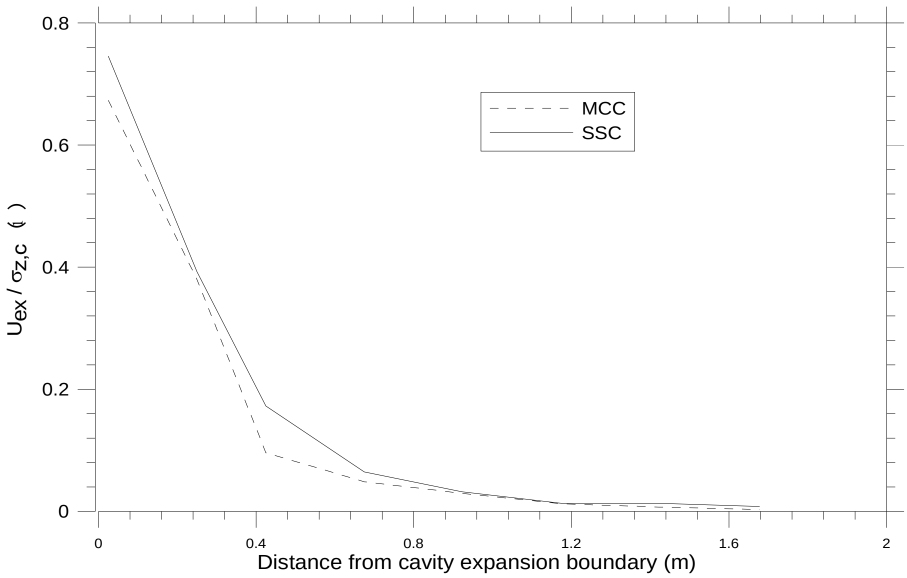

Figure 6.6: Distribution of excess pore water pressure with the distance from cavity expansion boundary at the end of cavity expansion

(9.0-10.0m depth from NGL)

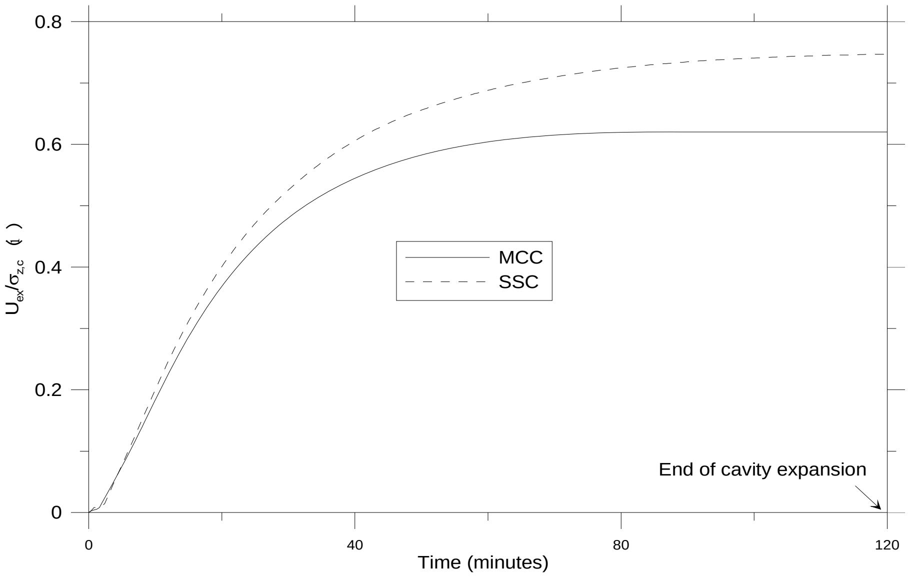

Figure 6.7: Developing of excess pore water pressure

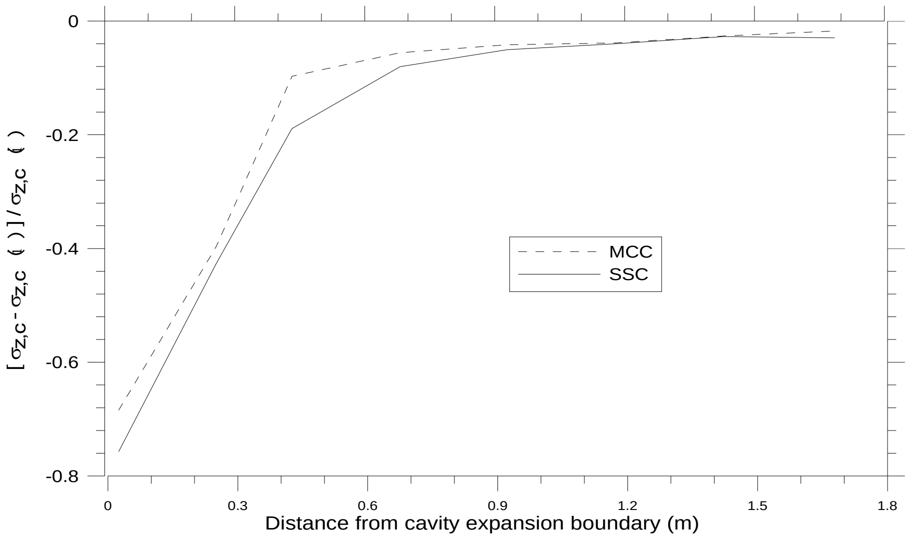

Figure 6.8: Distribution of decrease of vertical effective stress with distance from cavity expansion boundary at the end of cavity expansion (9.0-10.0m depth from NGL)

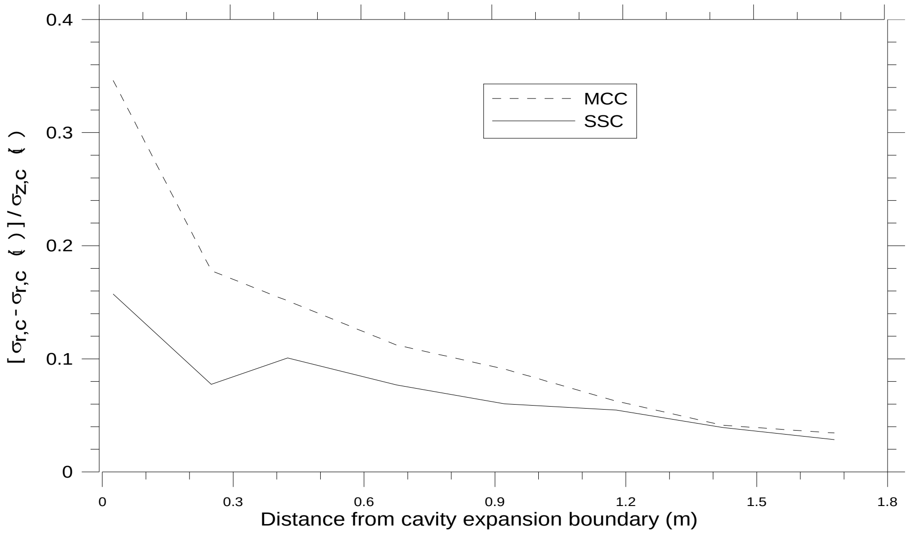

Figure 6.9: Increase of horizontal stress with distance from cavity expansion boundary at the end of cavity expansion (5.0-6.0m depth from NGL)

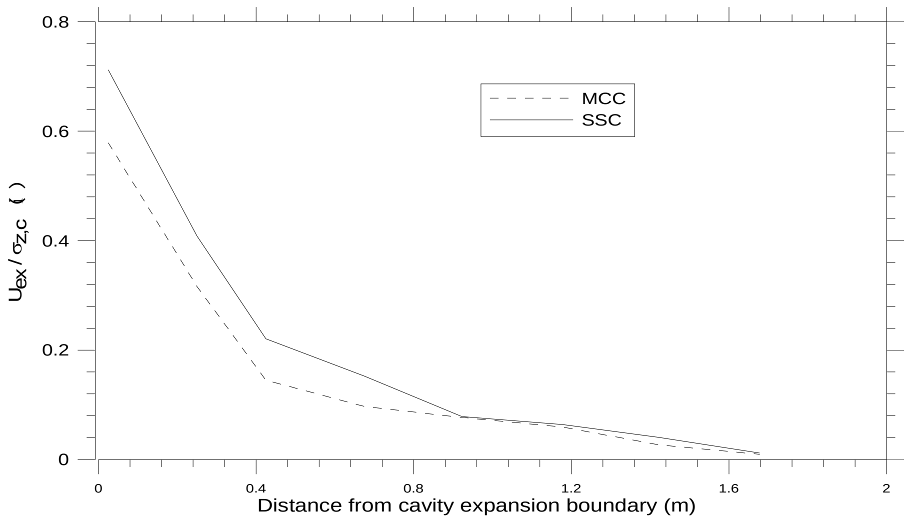

Figure 6.10: Distribution of excess pore water pressure with distance from cavity expansion boundary at the end of cavity expansion (5.0-6.0m depth from NGL)

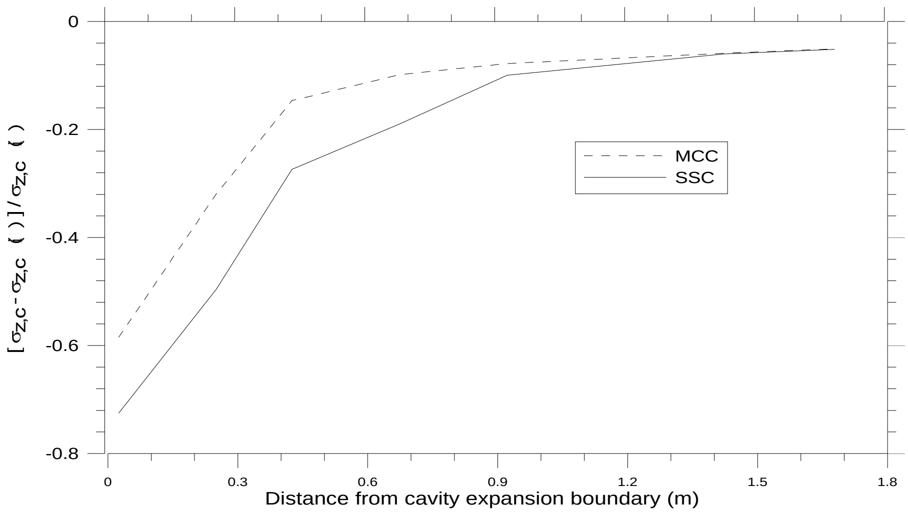

Figure 6.11: Distribution of decrease of vertical effective stress with distance from cavity expansion boundary at the end of cavity expansion (5.0-6.0m depth from NGL)

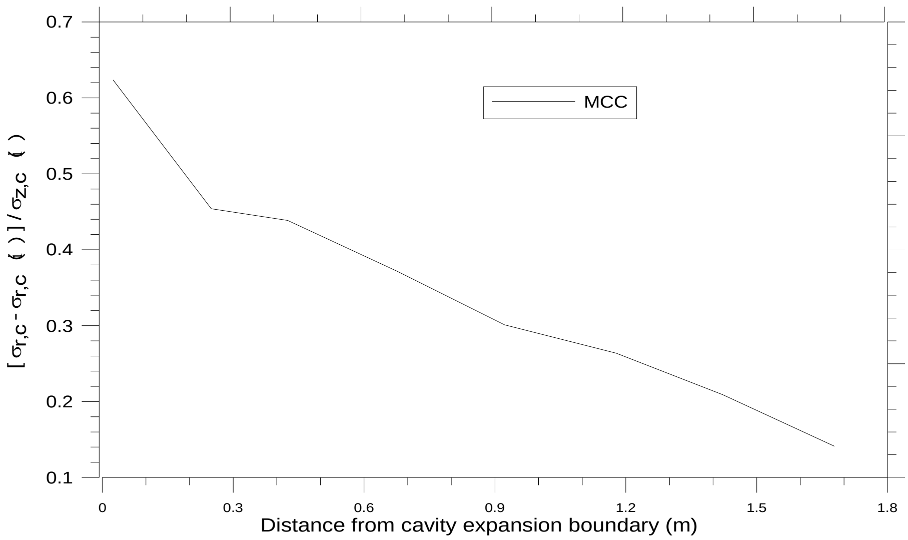

Figure 6.12: Increase of horizontal stress with distance from cavity expansion boundary at the end of cavity expansion (3.0-4.0m depth from NGL)

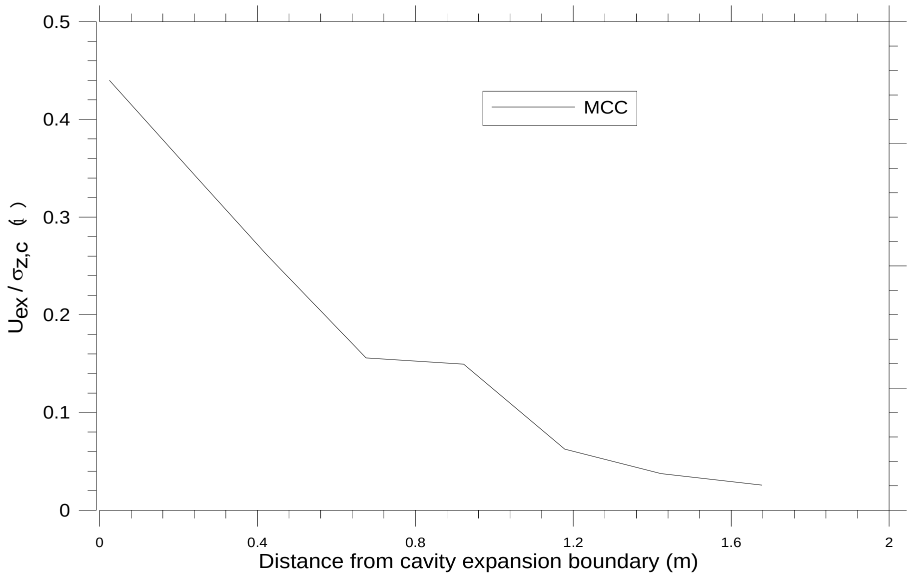

Figure 6.13: Distribution of excess pore water pressure with distance from cavity expansion boundary at the end of cavity expansion (3.0-4.0m depth from NGL)

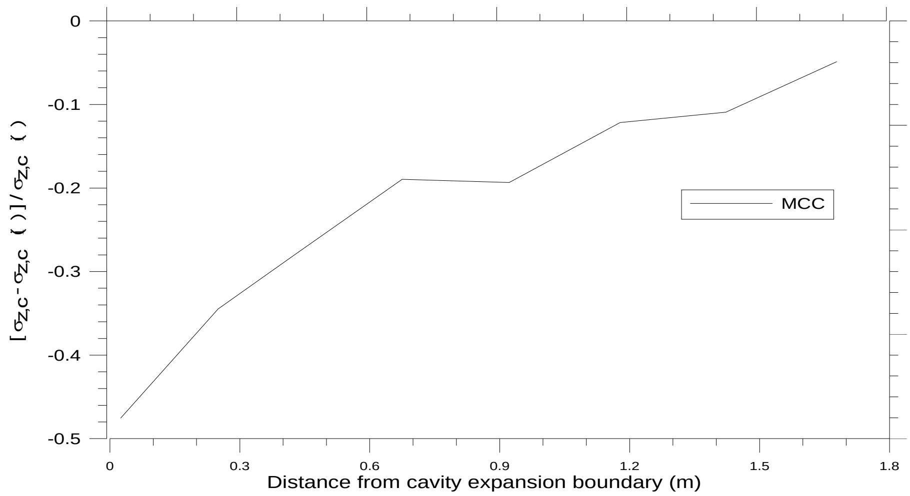

Figure 6.14: Distribution of decrease of vertical effective stress with distance from the cavity expansion boundary at the end of cavity expansion

(3.0-4.0m depth from NGL)

6.3 SIMULATION RESULTS OF ONE-LAYER CAVITY EXPANSION

For ease of comparison, the increase in horizontal effective stress, [$\sigma_{r,c}$ - $\sigma_{r,c}$(i)], is normalized relative to the average initial effective vertical stress $\sigma_{r,c}$(i) applied on the selected soil layer right before the cavity expansion begin. Note that (i) denotes start of the cavity expansion. Other than stated, the simulation results plotted in this section is at the end of the cavity expansion.

6.3.1 9.0-10.0m depth case

a) Horizontal effective stress increase

Increase of horizontal effective stress is plotted in Figure 6.3. When the soil property is MCC, the increase of horizontal effective stress generated by the cavity expansion is highest at the next to cavity expansion boundary and then decrease with the distance to the cavity expansion boundary. While in the SSC soil, the increase value of horizontal effective increases with the distance to the cavity expansion boundary, reaches the peak at about 0.5m distance and then continuously becomes lower. The Figure 6.3 also shows in the near cavity expansion boundary , increase of horizontal effective stress of MCC is significant higher than that of the SSC. After the distance of 1.2m, the two value of the MCC and SSC soil drop to about the same.

At the near the cavity expansion boundary location, the significant difference of the horizontal stress of the two types of soil is caused by the strain softening behaviour of the SSC soil. To further examine this statement, the cavity expansion stress path and the horizontal stress changes with time are plotted in Figure 6.4 and Figure 6.5.

The strain softening phenomena are quite clear in these two plots thus explain the significant less of the value of increase of horizontal stress in SSC soil than that of the MCC soil.

b) Excess pore water pressure

The excess pore water pressure distributions with the distance to the cavity expansion boundary are plotted in Figure 6.6 at the end of cavity expansion. In both MCC and SSC soils, the excess pore water pressure generated by the cavity expansion is highest at the next to cavity expansion boundary and then decreases with the distance to the cavity expansion boundary. The excess pore water pressures of the SSC is higher than that of the MCC soil at each location.

The developments of excess pore water pressure with time of the two different soils are compared in Figure 6.7. It is clear that the excess pore water pressure of SSC soil is higher than that in the MCC soil.

c) Decrease of vertical effective stress

In both two types of soils, the vertical effective stress significantly decreases after the cavity expansion. The distribution of the decreases of vertical effective stress with the distance to the cavity expansion boundary are plotted in Figure 6.8. In both MCC and SSC soils, the values of the decreases in the vertical effective stress are highest at the next to cavity expansion boundary and the value reduce with the distance to the cavity expansion boundary. The decrease of vertical effective stress of the SSC is higher than that of the MCC soil at each location.

6.3.2 5.0-6.0m depth case

a) Horizontal effective stress increase

Increases of horizontal effective stress are plotted in Figure 6.9. When the soil property is MCC, Increase of horizontal effective stress generated by the cavity expansion is highest at the next to cavity expansion boundary and then decrease with the distance to the cavity expansion boundary. While in the SSC soil, the increase value of horizontal effective stress fluctuate before 0.5m distance to the cavity expansion boundary, and then continuously drop down. The Figure 6.9 also shows that in the near expansion boundary, increase of horizontal effective stress of MCC is significant higher than that of the SSC. After the distance of 1.5m, the two value of the MCC and SSC soil drop to about the same.

b) Excess pore water pressure

The excess pore water pressure distribute with the distance to the cavity expansion boundary are plotted in Figure 6.10. In both the MCC and SSC soils, the excess pore water pressure generated by the cavity expansion is highest at the next to cavity expansion boundary and then decrease with the distance to the cavity expansion boundary. The excess pore water pressure of the SSC is higher than that of the MCC soil at each location.

c) Decrease of vertical effective stress

In both soils, the vertical effective stress significantly decreases after the cavity expansion. Distributions of the decreases of vertical effective stress with the distance of to the cavity expansion boundary are plotted in Figure 6.11. In both MCC and

SSC soils, the value of decrease of the vertical effective stress is highest at the next to cavity expansion boundary and the value reduce with the distance to the cavity expansion boundary. The decrease of vertical effective stress of the SSC is higher than that of the MCC soil at each location.

6.3.3 3.0-4.0m depth case

As this soil layer is slightly over consolidated MCC soil in the unit cell simulation., only the cavity expansion of MCC soil is simulated in it.

a) Horizontal effective stress increase

The increase of horizontal effective stress is plotted in Figure 6.12. The increase of horizontal effective stress generated by the cavity expansion is highest at the next to cavity expansion boundary and then decrease with the distance to the cavity expansion boundary.

b) Excess pore water pressure

The excess pore water pressure distribution with the distance of to the cavity expansion boundary is plotted in Figure 6.13. The excess pore water pressure generated by the cavity expansion is higher near the cavity expansion boundary and decrease with the distance to the cavity expansion boundary.

c) Decrease of vertical effective stress

The vertical effective stress significantly decreases after the cavity expansion. The distribution of the decrease of vertical effective stress with the distance of to the cavity expansion boundary was plotted in Figure 6.14. The value of decrease of the vertical effective stress is higher at the location near the cavity expansion boundary and reduces with the distance to the cavity expansion boundary.

6.3.4 Summary of the one-layer cavity expansion results

1. The impacts of the cavity expansion is reducing with the distance to the cavity expansion boundary.
2. The horizontal effective stress and the excess pore water pressure increase after the cavity expansion whereas vertical effective stress decrease.
3. The cavity expansion in SSC soil generate more excess pore water pressure and less increase of horizontal effective stress than it does in the MCC soil.
4. The general trend for all 3 depth is similar but quantitatively different.
5. no obvious trend in the impacts of the cavity expansion with the depths from NGL, a full-depth cavity expansion simulation is needed.

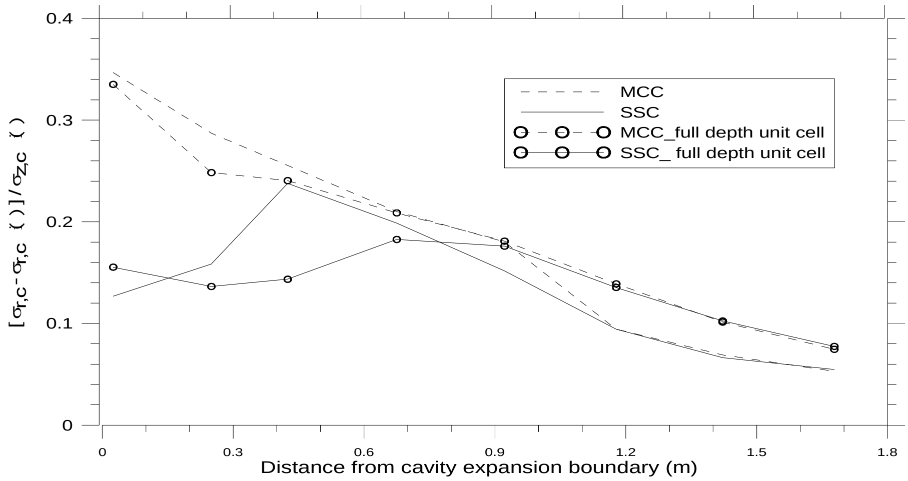

Figure 6.15: Increase of horizontal stress with distance from cavity expansion boundary at the end of cavity expansion (9.0-10.0m depth from NGL)

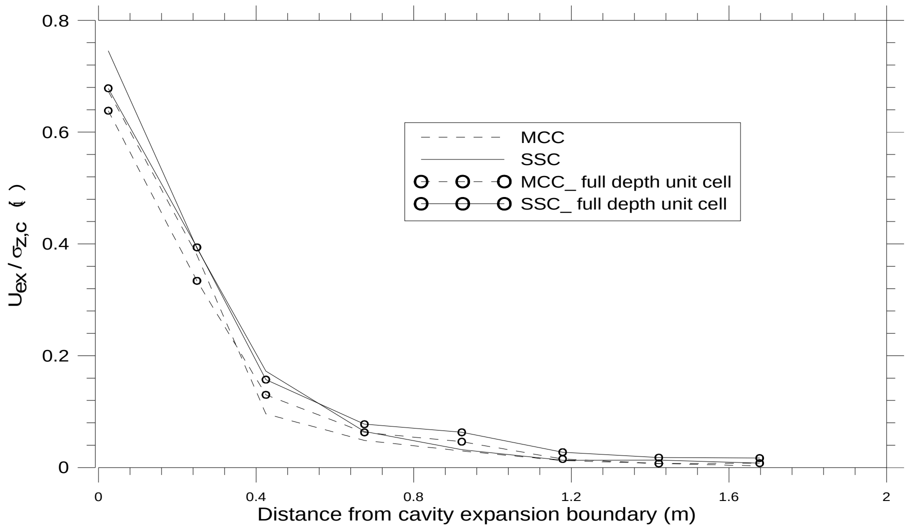

Figure 6.16: Distribution of excess pore water pressure with distance from cavity expansion boundary at the end of cavity expansion

(9.0-10.0m depth from NGL)

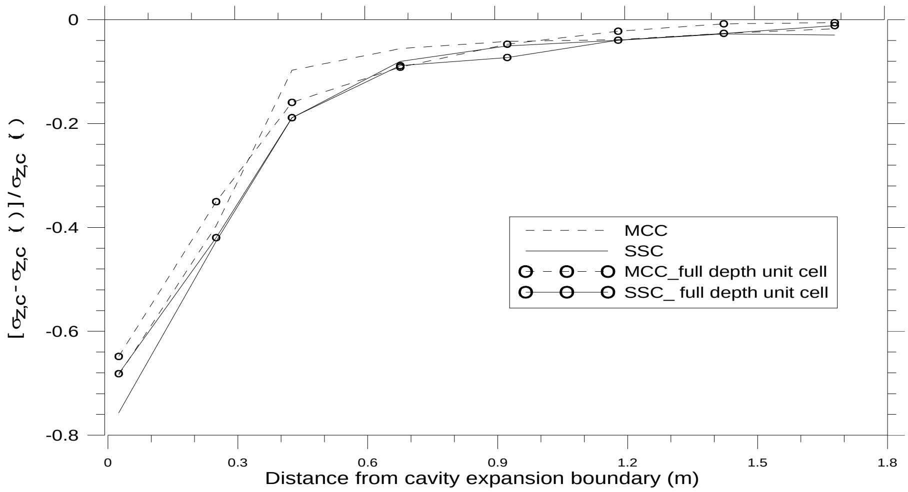

Figure 6.17: Distribution of decrease of vertical effective stress with distance from cavity expansion boundary at the end of cavity expansion (9.0-10.0m depth from NGL)

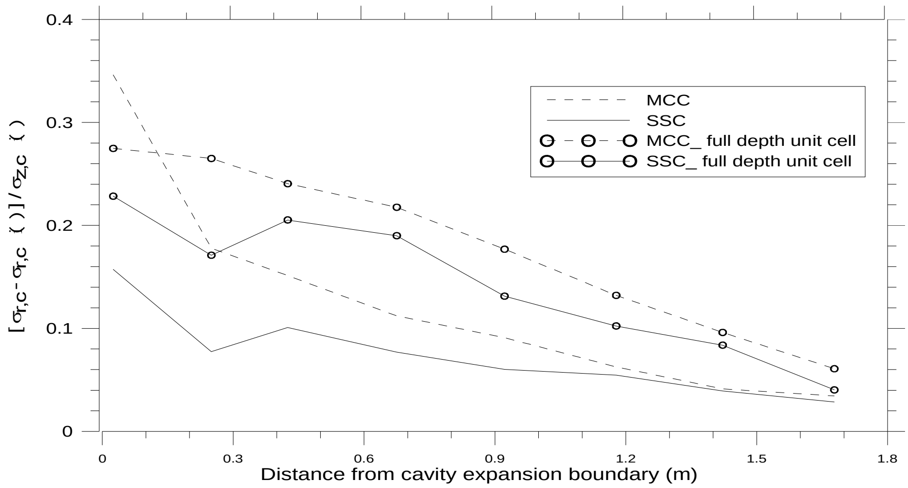

Figure 6.18: Increase of horizontal stress with the distance from cavity expansion boundary at the end of cavity expansion

(5.0-6.0m depth from NGL)

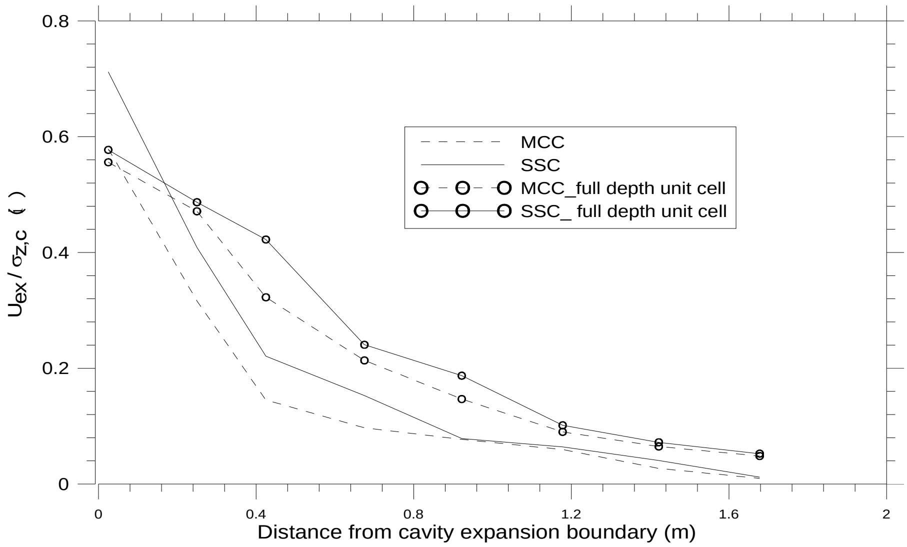

Figure 6.19: Distribution of excess pore water pressure with distance from cavity expansion boundary at the end of cavity expansion (5.0-6.0m depth from NGL)

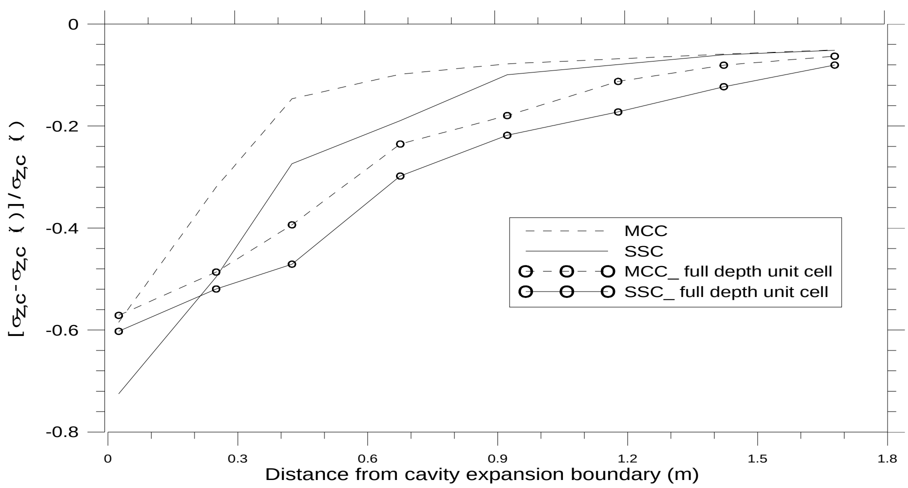

Figure 6.20: Distribution of decrease of vertical effective stress with distance from cavity expansion boundary at the end of cavity expansion

(5.0-6.0m depth from NGL)

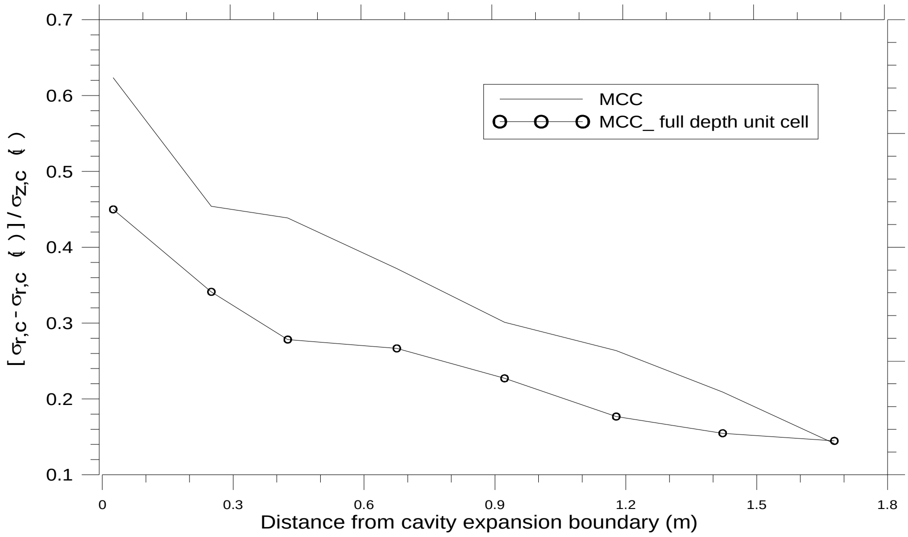

Figure 6.21: Increase of horizontal stress with the distance from cavity expansion boundary at the end of cavity expansion (3.0-4.0m depth from NGL)

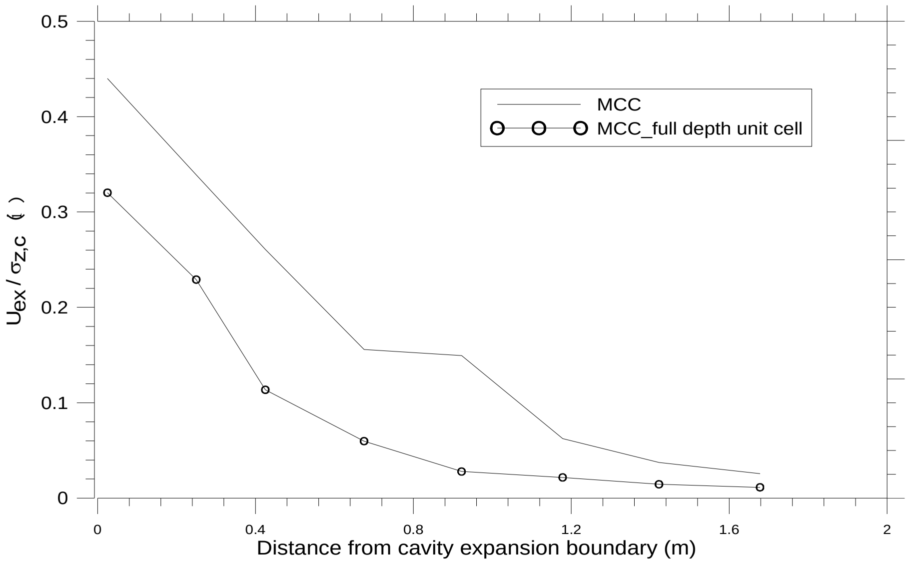

Figure 6.22: Distribution of excess pore water pressure with distance from cavity expansion boundary at the end of cavity expansion (3.0-4.0m depth from NGL)

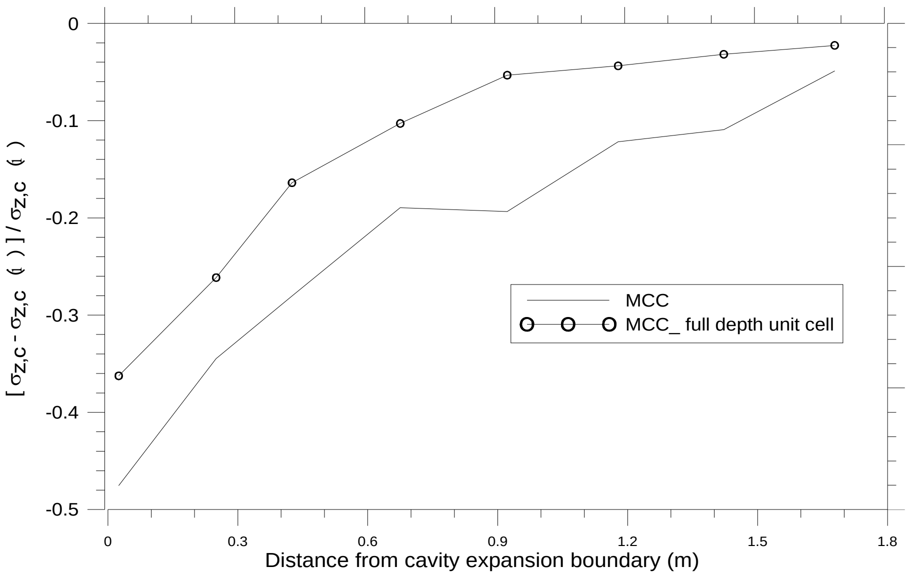

Figure 6.23: Distribution of decrease of vertical effective stress with distance from cavity expansion boundary at the end of cavity expansion (3.0-4.0m depth from NGL)

6.4 Full-depth cavity expansion results

The simulation of full-depth cavity expansion in the unit cell is conducted by adopting the numerical idealisations outlined in section 6.2. It is performed in both the MCC and SSC soils with the soil properties and expansion speed described in section 6.2. The results are obtained from three different depths: 9.0-10.0m from NGL; 5.0-6.0m from NGL; and 3.0-4.0m from NGL, and are then compared with the one-layer simulation results presented in section 6.3. The full results from the cavity expansions in both the MCC and SSC soils are used as the initial stress states for simulating the performance of geosynthetic encased stone columns installed by the full displacement installation method.

6.4.1 9.0-10.0m depth case

a) Horizontal effective stress increase

Increases in the horizontal effective stress are plotted in Figure 6.15. When the soil property is MCC, the increases generated by the cavity expansion are highest at the next-to-cavity expansion boundary and then decrease with the distance towards the cavity expansion surface. In the SSC soil, the increasing value of the horizontal effective stress fluctuates before 1.0m to the cavity expansion surface, and then continuously becomes lower. This figure also shows that, at the near cavity expansion boundary locations, increases in the horizontal effective stress of the MCC are significantly higher than those of the SSC. After the distance of 1.2m, the values of the MCC and SSC soils decrease to become about the same.

Compared with the one-layer simulation results when the MCC model is applied, increases in the horizontal effective stress are slightly lower from the full-depth simulation before 1.0m from the cavity expansion boundary. After 1.0m, values of the one-layer simulation are slightly lower than those of the full-depth simulation. When the SSC model is applied, increases in the horizontal effective stress in the full-depth simulation are, on average, slightly lower than those of the one-layer simulation.

b) Excess pore water pressure

The excess pore water pressure distributions with distance towards the cavity expansion surface are plotted in Figure 6.16. In both the MCC and SSC soils, the excess pore water pressure generated by the cavity expansion is highest at the next-to-cavity expansion boundary and then decreases with the distance towards the cavity expansion surface. The excess pore water pressures of the SSC soil are higher than those of the MCC soil at all locations.

Compared with the one-layer cavity expansion simulation, the values of the excess pore water pressure from the full-depth cavity expansion simulation are quite similar, on average, for both the MCC and SSC models.

c) Decrease in vertical effective stress

In both soils, the vertical effective stress significantly decreases after the cavity expansion. Distributions of the decreases with the distance towards the cavity expansion surface are plotted in Figure 6.17. In both the MCC and SSC soils, the values of the decreases are highest at the next-to-cavity expansion boundary and then reduce with the distance towards the cavity expansion surface. Decreases in the vertical effective stress of the SSC are higher than those of the MCC at all locations.

When compared with the one-layer cavity expansion simulation, the values of the decreases in the vertical effective stress from the full-depth cavity expansion are quite similar, on average, for both the MCC and SSC models.

6.4.2 5.0-6.0m depth case

a) Horizontal effective stress increase

Increases in the horizontal effective stress are plotted in Figure 6.18. When the soil property is MCC, these increases generated by the cavity expansion are highest at the next-to-cavity expansion boundary and then decrease with the distance towards the cavity expansion surface. In the SSC soil, the increased values of the horizontal effective stress fluctuate before 0.5m to the cavity expansion surface and then continuously become lower. This figure also shows that, at the near cavity expansion boundary locations, increases in the horizontal effective stress of the MCC are significantly higher than those of the SSC at all locations before 1.8m to the cavity expansion surface.

Compared with the one-layer simulation results from both the MCC and SSC soils, the increases in the horizontal effective stress are higher in the full-depth simulation. These differences are caused by the different boundary conditions of the two simulation methods used for this layer.

b) Excess pore water pressure

The excess pore water pressure distributions with distance towards the cavity expansion surface are plotted in Figure 6.19. In both the MCC and SSC soils, the excess pore water pressures generated by the cavity expansion are highest at the next-to-cavity expansion boundary and then decrease with the distance towards the cavity expansion surface. The excess pore water pressure of the SSC is higher than that of the MCC at all locations.

Compared with the one-layer cavity expansion simulation, the values of excess pore water pressure in the full-depth cavity expansion are higher, on average, for both the MCC and SSC models.

c) Decrease in vertical effective stress

In both soils, the vertical effective stress significantly decreases after the cavity expansion. Distributions of these decreases with the distance towards the cavity expansion surface are plotted in Figure 6.20. In both the MCC and SSC soils, the values of the decreases in the vertical effective stress are highest at the next-to-cavity expansion boundary and then reduce with the distance towards the cavity expansion surface. Decreases in the vertical effective stress of the SSC are higher than those of the MCC soil at all locations.

Compared with the one-layer cavity expansion simulation, the values of decreases in the vertical effective stress from the full-depth cavity expansion are higher, on average, for both the MCC and SSC models.

6.4.3 3.0-4.0m depth case

As this soil layer is a slightly over-consolidated MCC soil in the unit cell simulation, only the cavity expansion of the MCC soil is simulated in this layer.

a) Horizontal effective stress increase

Increases in the horizontal effective stress are plotted in Figure 6.21. Those generated by the cavity expansion are highest at the next-to-cavity expansion boundary and then decrease with the distance towards the cavity expansion surface.

Compared with the one-layer cavity expansion simulation, the values of increases in the horizontal effective stress from the full-depth cavity expansion are lower, on average, for both the MCC and SSC models.

b) Excess pore water pressure

The excess pore water pressure distributions with the distance towards the cavity expansion surface are plotted in Figure 6.22. The excess pore water pressure generated by the cavity expansion is higher near the cavity expansion boundary and decreases with the distance towards the cavity expansion surface.

Compared with the one-layer cavity expansion simulation, the values of the excess pore water pressure from the full-depth cavity expansion are lower, on average, for both the MCC and SSC models. The cause of these lower excess pore water pressure values may be due to this layer being much closer to the top drainage boundary.

c) Decrease in vertical effective stress

The vertical effective stress significantly decreases after the cavity expansion. Distributions of these decreases with the distance towards the cavity expansion surface are plotted in Figure 6.23. The values of the decreases are higher at the location near the cavity expansion boundary and reduce with the distance towards the cavity expansion surface.

Compared with the one-layer cavity expansion simulation, the values of the decreases in the vertical effective stress from the full-depth cavity expansion are lower, on average, for both the MCC and SSC models.

6.5 DISCUSSION AND SUMMARY

The full-depth cavity expansion simulation results from the bottom depth (9.0-10.0m from NGL) are similar to those from the one-layer cavity expansion simulation. At the middle depth (5.0-6.0m from NGL), increases in the horizontal effective stress and the excess pore water pressure, and decreases in the vertical effective stress of the full-depth simulation are higher than those of the one-layer simulation. At the top depth (3.0-4.0m from NGL), increases in the horizontal effective stress and the excess pore water pressure, and decreases in the vertical effective stress of the full-depth simulation are lower than those of the one-layer simulation.

The impacts of the cavity expansion reduce with the distance towards the cavity expansion surface in both the full-depth and one-layer cavity expansion simulations.

In both the full-depth and one-layer cavity expansion simulations, the horizontal effective stress and the excess pore water pressure increase after the cavity expansion while the vertical effective stress decreases.

In both the full-depth and one-layer cavity expansion simulations, the cavity expansion in the SSC soil generates more excess pore water pressure and less increase in the horizontal effective stress than it does in the MCC soil.

CHAPTER SEVEN

STONE COLUMNS WITH FULL DISPLACEMENT INSTALLATION

7.1 INTRODUCTION

As discussed in Chapter 6, the full displacement installation causes much more disturbance to the surrounding soil than the wish-in installation method does. In this chapter, the installation effects will be considered by applying the stress state of the unit cell immediately after full displacement installation as obtained from Chapter 6 as the initial stress state.

The numerical models, soil parameters, loading sequence, etc., are exactly the same as those in Chapter 5, with only the installation method being different, and this is simulated by initial stress states being different. Finite element analysis are conducted in both MCC and with SSC models. Both 2.0m and 1.3m radius unit cell representing two different stone column spacing are examined. The geosynthetic pre-strain and stiffness of stone impacts are examined in addition to the reference conditions. Circumstances and conditions to ensure the effectiveness of geosynthetic-encased stone columns are also discussed in detail in this chapter.

7.2 INITIAL STRESS STATES

The stress state of the unit cell immediately after full displacement installation as obtained from Chapter 6 are applied as the indicial stress state of the analysis. Linear interpolation is used for mapping the stress states from adjacent locations where the increases of horizontal stress, excess pore water pressure and decrease of vertical stress are known.

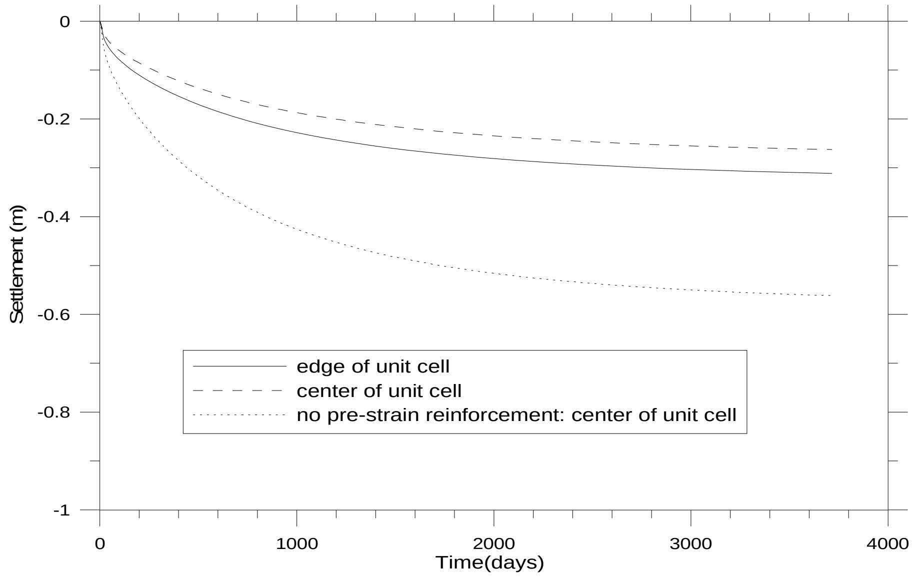

Figure 7.1(a): Settlement responses of reference analysis: Comparison of settlement-time plots (2.0m radius unit cell, MCC model only)

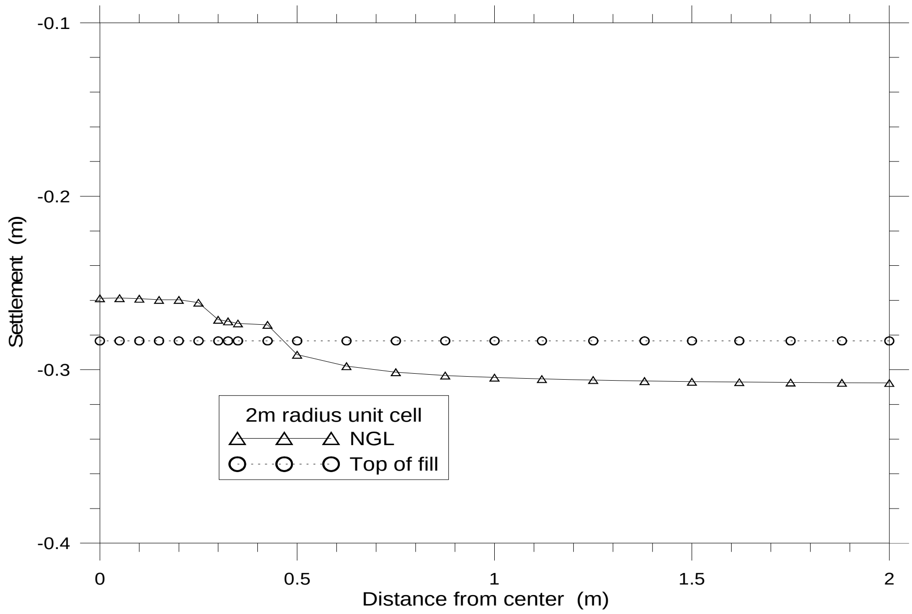

Figure 7.1(b): Settlement responses of reference analysis: Settlement profiles at 10 years

(2.0m radius unit cell, MCC model only)

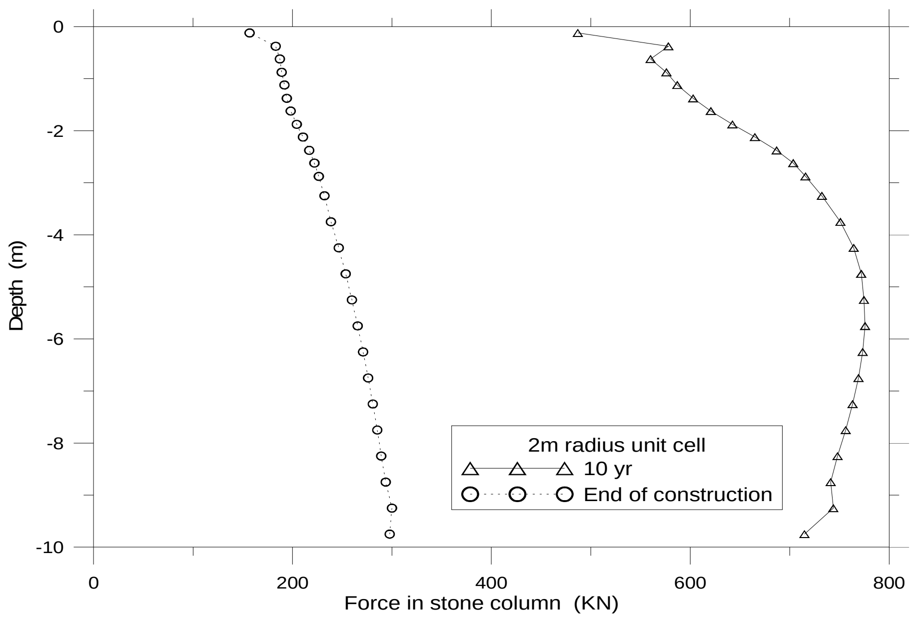

Figure 7.2: Distributions of column forces with depth:

reference analysis (2.0m radius unit cell, MCC model only)

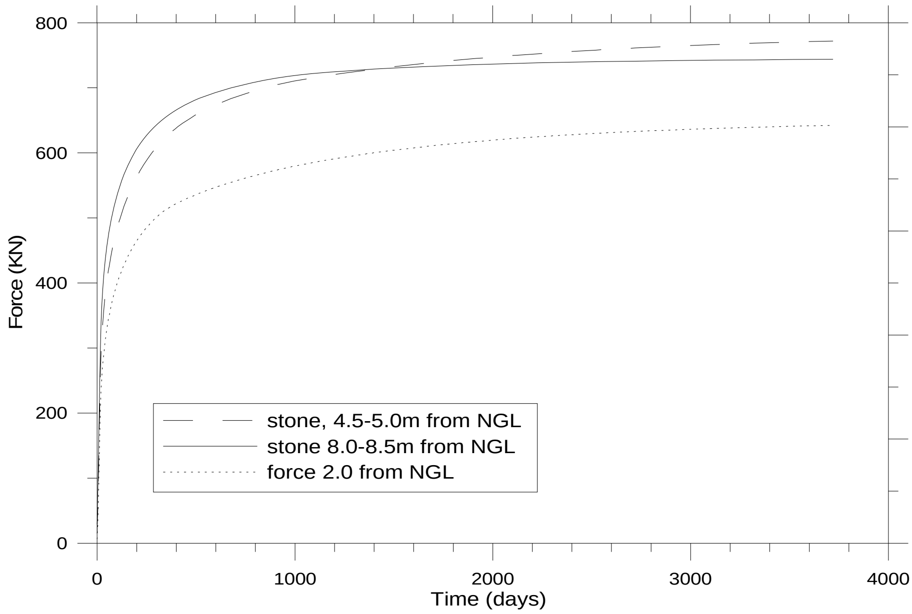

Figure 7.3: Evolutions of column forces with time: reference analysis (2.0m radius unit cell, MCC model only)

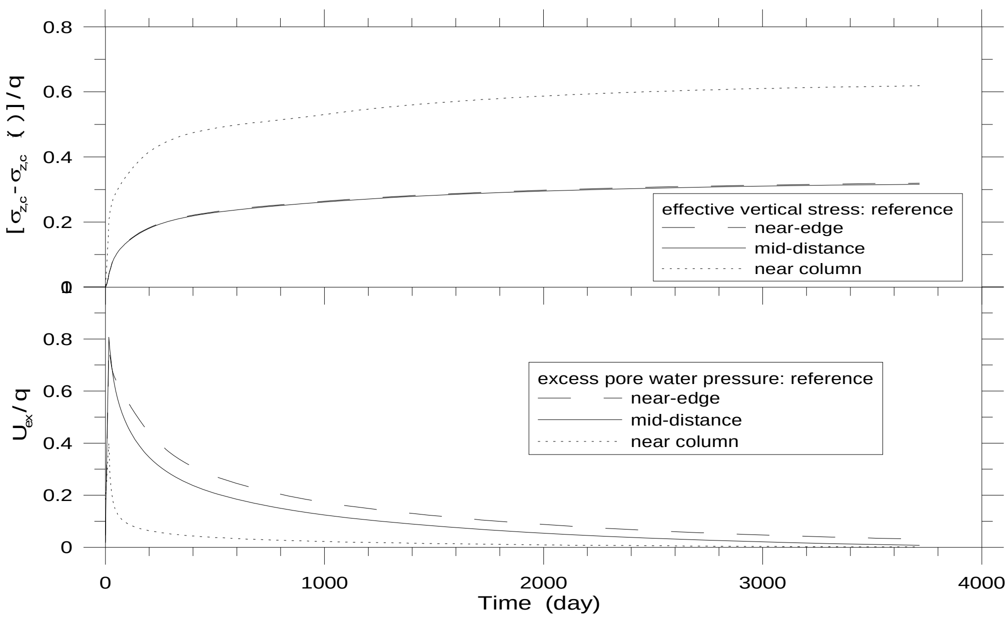

Figure 7.4: Consolidation responses in clay: reference analysis (2.0m radius unit cell, MCC model only)

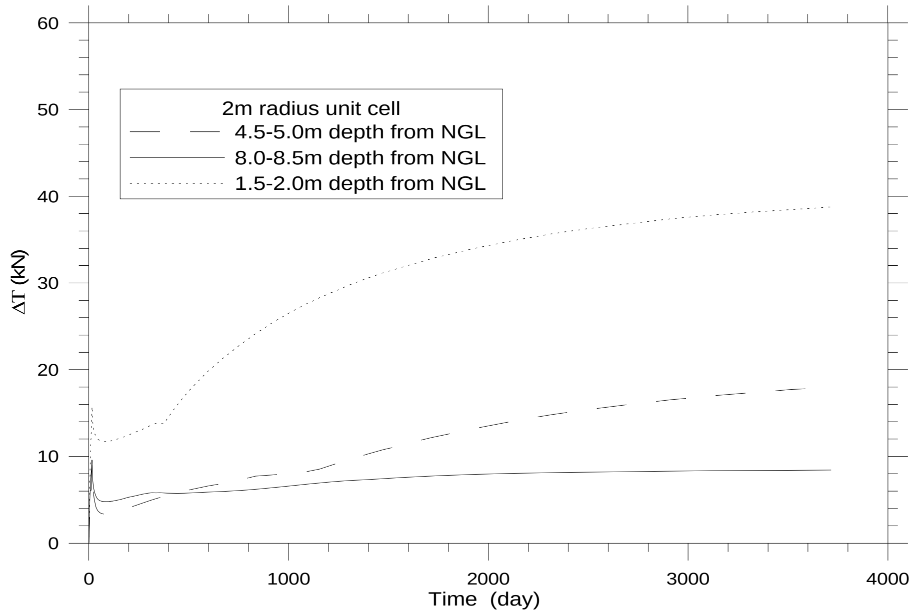

Figure 7.5: Increases in geosynthetic tension with time: reference analysis (2.0m radius unit cell, MCC model only)

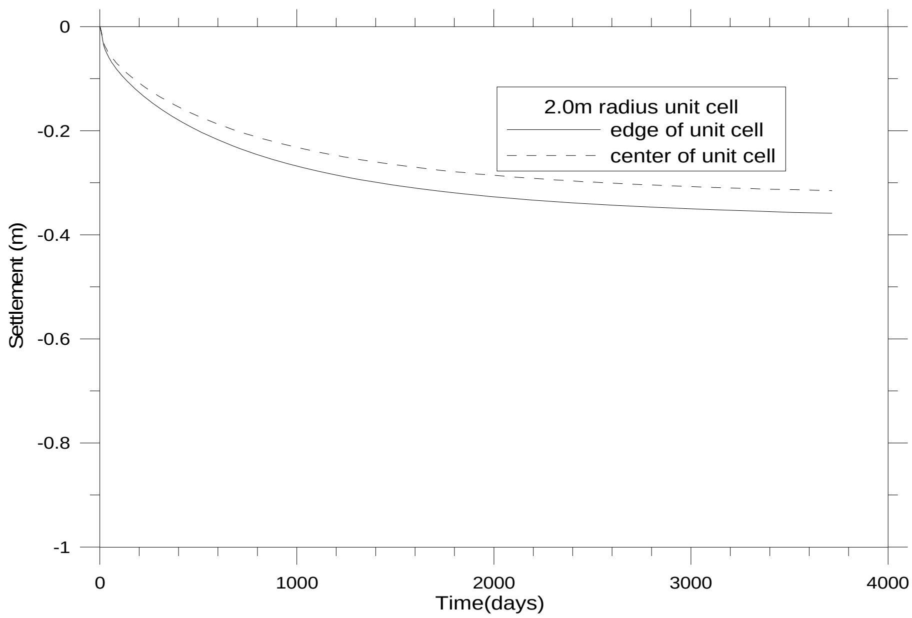

Figure 7.6(a): Settlement-time plots: reduced stone stiffness K=1000 (2.0m radius unit cell, MCC model only)

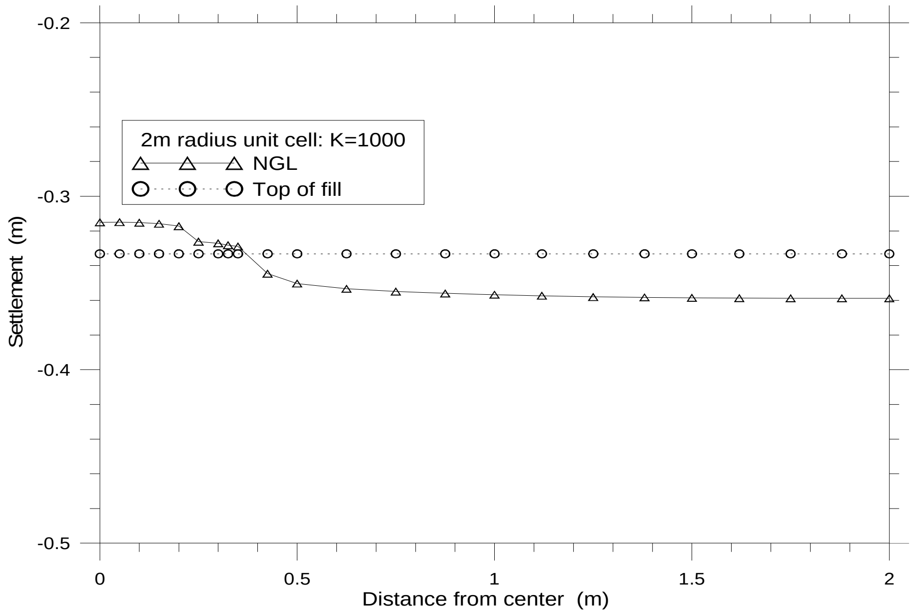

Figure 7.6(b): Settlement profiles: reduced stone stiffness K=1000 (2.0m radius unit cell, MCC model only)

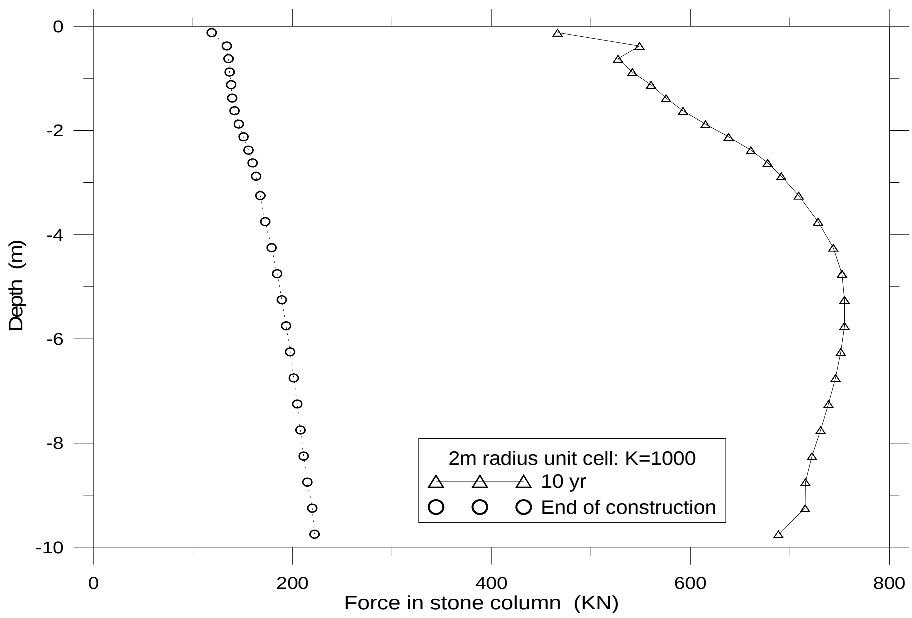

Figure 7.7: Distributions of column forces: reduced stone stiffness K=1000 (2.0m radius unit cell, MCC model only)

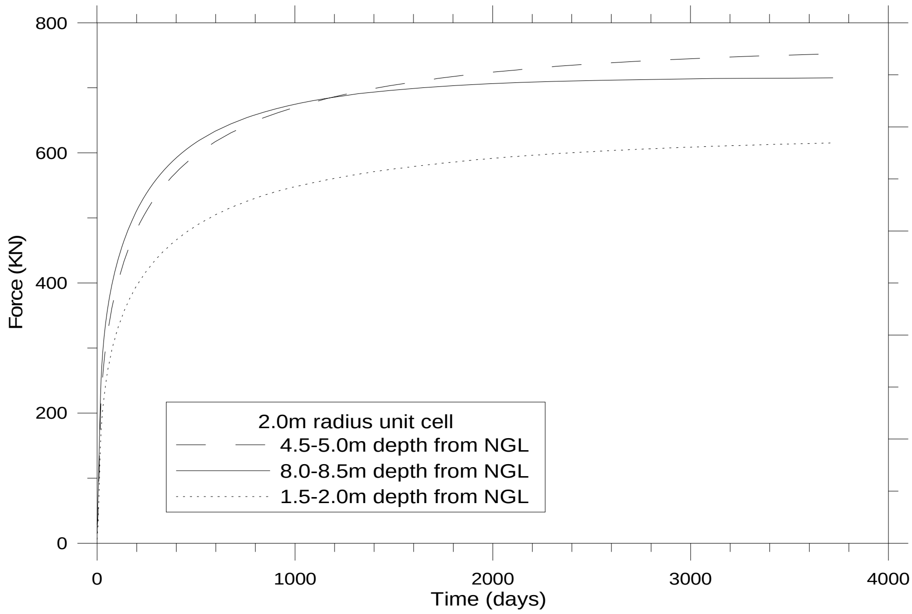

Figure 7.8: Evolutions of column forces with time: reduced stone stiffness K=1000

(2.0m radius unit cell, MCC model only)

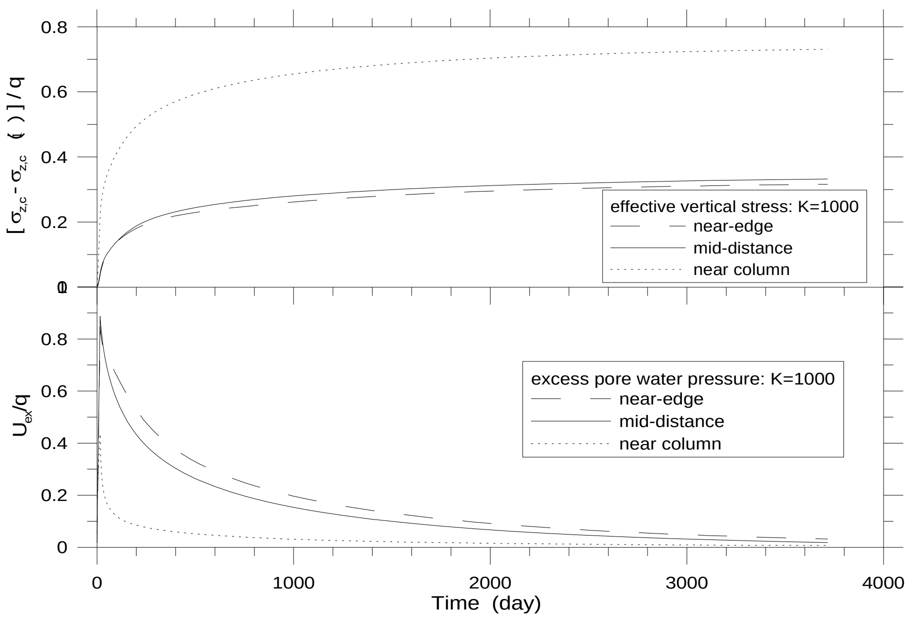

Figure 7.9: Consolidation responses in clay: reduced stone stiffness K=1000 (2.0m radius unit cell, MCC model only)

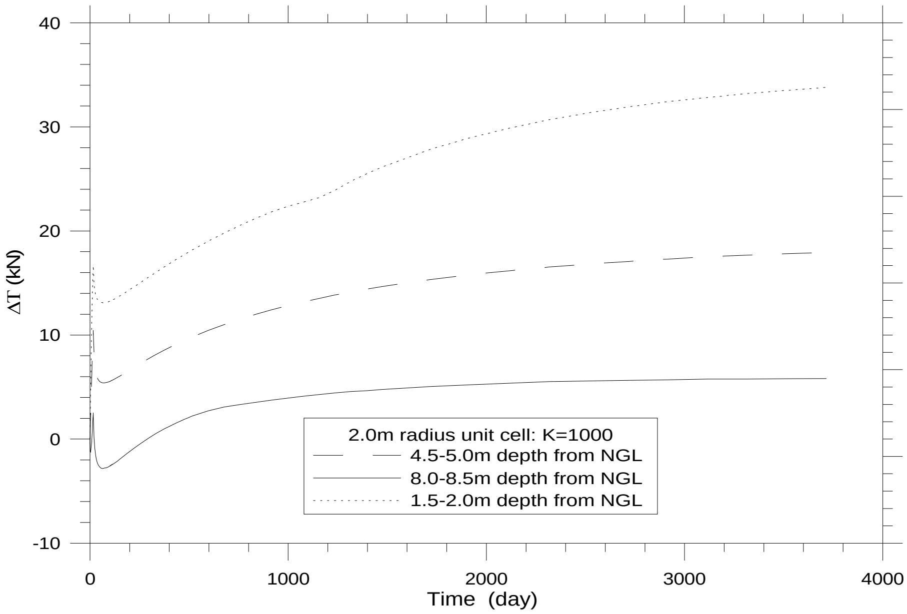

Figure 7.10: Increases in geosynthetic tension with time: reduced stone stiffness K=1000 (2.0m radius unit cell, MCC model only)

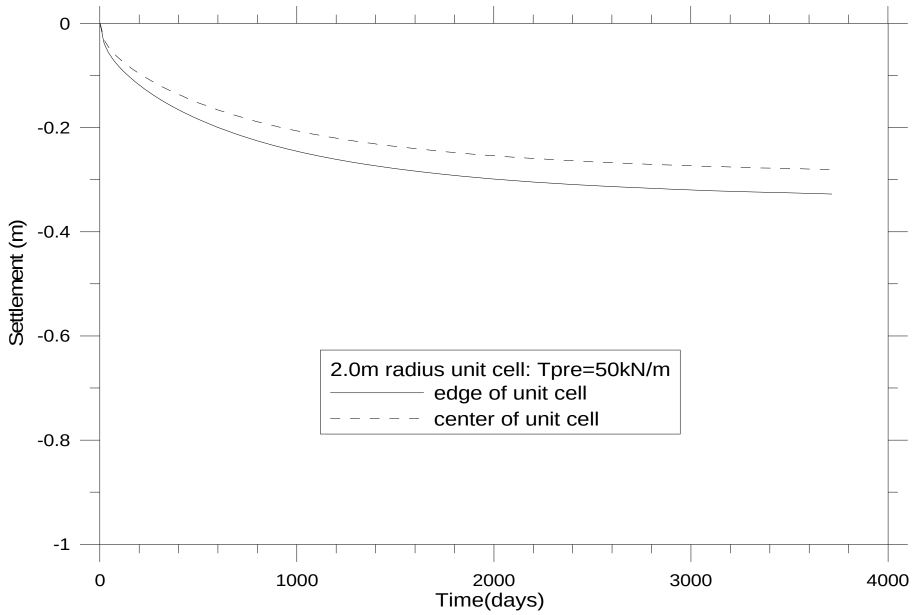

Figure 7.11(a): Settlement-time plots: reduced locked-in stress Tpre=50kN/m (2.0m radius unit cell, MCC model only)

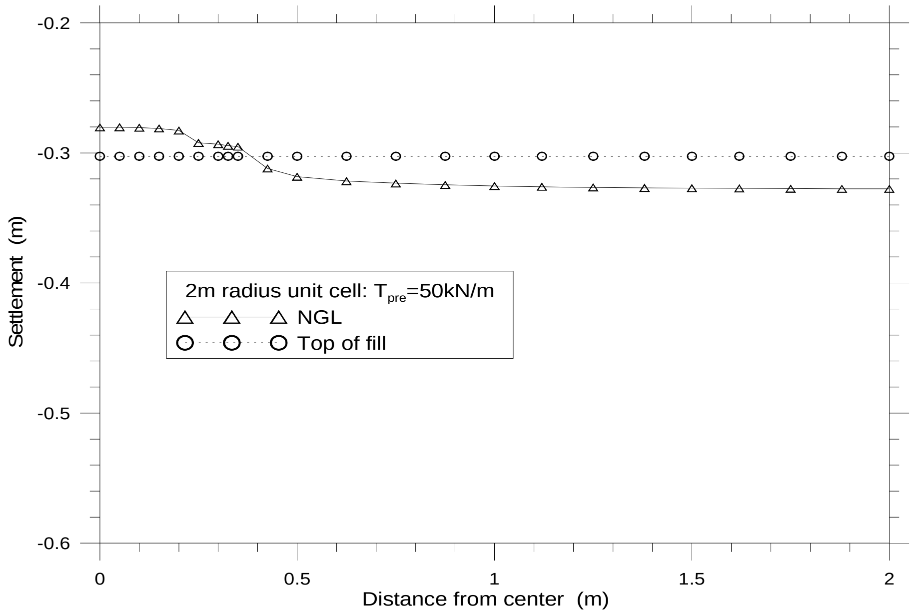

Figure 7.11(b): Settlement profiles: reduced locked-in stress Tpre=50kN/m (2.0m radius unit cell, MCC model)

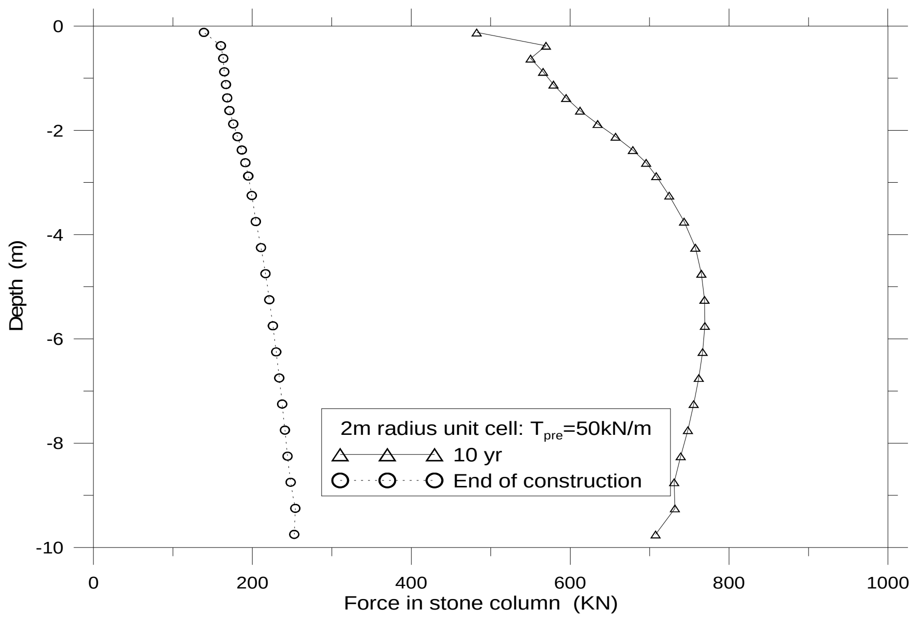

Figure 7.12: Distributions of column forces: reduced locked-in stress Tpre=50kN/m (2.0m radius unit cell, MCC model only)

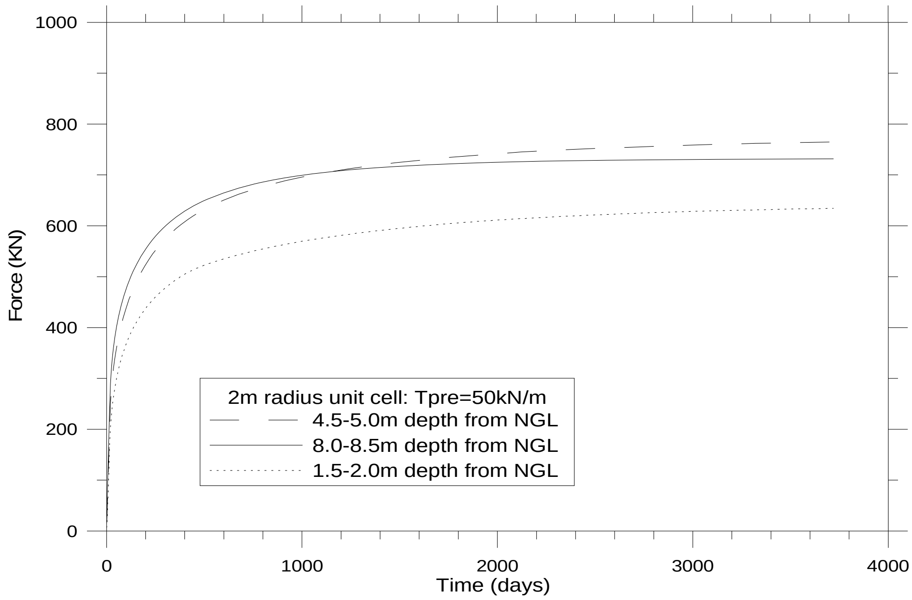

Figure 7.13: Evolutions of column forces with time: reduced locked-in stress Tpre=50kN/m

(2.0m radius unit cell, MCC model only)

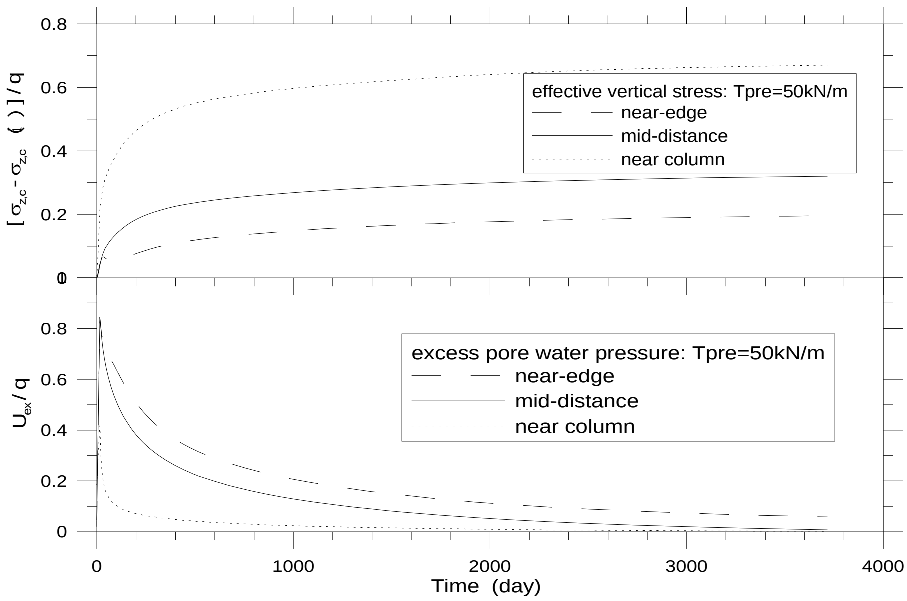

Figure 7.14: Consolidation responses in clay: reduced locked-in stress Tpre=50kN/m

(2.0m radius unit cell, MCC model only)

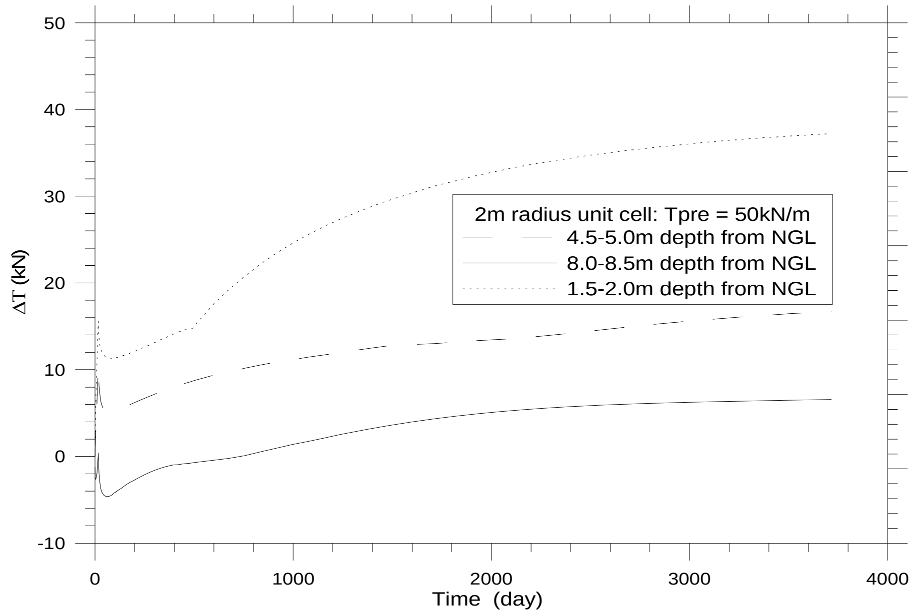

Figure 7.15: Increases in geosynthetic tension with time: reduced locked-in stress Tpre=50kN/m (2.0m radius unit cell, MCC model only)

7.3 STONE COLUMN IN MCC SOIL WITH 2.0M UNIT CELL

7.3.1 Reference parameters

Dimensions of the unit cell and the material parameters are the same as those used in Chapter 5 (Tables 5-1 and 5-2) with additional input parameters being the initial stresses which were calculated according to the method described in section 7.2. A locked-in force, T_{pre}, of 100 kN/m is referred to as the reference analysis.

<u>a) Settlement</u>

Plots showing the developments of settlement at NGL with time are presented in Figure 7.1(a). Without pre-straining of the geosynthetic encasement, settlement at the top of the stone column in 10 years is approximately 0.56m. The application of geosynthetic encasement with T_{pre}=100 kN/m reduces this settlement to 0.26m. Settlement at the edge of the unit cell attains a higher, but still relatively small, value of 0.31m at 10 years and continues after 10 years.

Settlement of the unit cell without pre-straining of the geosynthetic encasement is 27% less using the wish-in installation method which may be caused by the confining stress the latter method provides. Settlements of the unit cell of the geosynthetic encasement with T_{pre}=100kN/m are about the same for the two methods although, at NGL, the stone column settles at 0.02m more and the soil at the edge of the unit cell at 0.01m less using the full displacement installation method.

Settlement profiles at NGL and the top of the fill are plotted in Figure 7.1(b). That at foundation level manifests a "bump" near the perimeter of the stone column while that at the top of the fill is smooth. The settlement profiles and settlement with time plots show that, despite the installation method used, geosynthetic encasement with T_{pre}=100kN/m reduces settlement at 10 years to about the same level. The only difference is that, when the full displacement installation method is used, consolidation takes longer.

b) Force in stone column

Distributions of the computed column forces with depth are presented in Figure 7.2 for two time-steps: after the end of construction and at 10 years. The column forces after the end of construction increase with depth to a maximum value of about

300kN/m. The column forces at 10 years increase with depth to a maximum value of ~775 kN which is achieved at about the mid-depth. This is due to negative drag-down from the surrounding clay that tends to settle more than does that of the stone column. Evolutions of the column forces with time are examined in further detail (at three depths) in Figure 7.3. At all three depths, the column forces increase with time.

c) Coupled behaviour

The coupling between column forces and consolidation behaviour is highlighted by plotting increases in the vertical effective stress, [$\sigma_{z,c}$-$\sigma_{z,c}$(i)], and the dissipation of excess pore water pressure, u_{ex}, with time, as in Figure 7.4 for three radial locations at the mid-depth of the soft clay. Following the procedures undertaken in Chapter 5, both [$\sigma_{z,c}$-$\sigma_{z,c}$(i)] and u_{ex} are normalised relative to the average fill loading of q=80 kPa for comparison purposes. All plots commence from 16 days when the embankment is at its full height. The three radial locations are: next to the stone column; at the mid-distance between the stone column and the edge of the unit cell; and next to the edge of the unit cell.

The dissipation of excess pore water pressure proceeds with increases in the vertical effective stress, as expected, and is significantly faster next to the stone column than at the other two locations. This is due to the drainage provided by the stones. The decrease of water pressure at the mid-distance is faster than at the edge of the unit cell but increases in the effective stress are nearly the same at both locations. This may be due to the fill load being transferred to the stone column during the consolidation process. After 10 years, the excess pore water pressure at the near-stone column location approaches nearly zero while significant excess pore water pressure remains in the other two locations. The increases of the effective stress at 10 years, as indicated by the ratio $[\sigma_{z,c}-\sigma_{z,c}(i)]/q$ is ~0.61 near the column and ~0.3 at the other two locations.

Figure 7.5 presents three ΔT-time plots corresponding to three depths: near-top, mid-depth, and near-toe. All three plots show increases in ΔT with time, but increments vary at the different depth locations. The asymptotic value of ΔT after 10 years is 39 kN near the top, 18 kN at the mid-depth and only 8 kN at the bottom. The reason for the ΔT at the near-top location being much higher than at the other two locations is that, the pre-stress T(i) at the near-top location, is much smaller than T_{pre}=100 kN/m.

7.3.2 Influence of lower stone stiffness

The influence of lower stone stiffness is examined by repeating the analysis with the Duncan-Chang parameter, K, reduced to 1000, while the initial stress states and all other parameters are the same as those in the reference analysis. This stiffness value is considered to be relatively low for compacted stones.

<u>a) Settlement and force in stone column</u>

The computed evolutions of settlement with time are presented in Figure 7.6(a) and the settlement profiles at NGL and foundation level are plotted in Figure 7.6(b). The overall trends of both the settlement-time plots and settlement profiles are similar to those of the reference analysis but the computed settlement is higher and the settlement profile at the top of the fill is smooth. However, increases in settlement are only ~15% in spite of a 50% reduction in stiffness. This relatively small increase could be explained by the computed distributions of column forces with depth as shown in Figure 7.7. For both the end of construction and at 10 years, are only marginally less than are those of the reference analysis (Figure 7.2). Thus, at a high value of T_{pre} (which is the case for both analyses), the performance of the unit cell is not sensitive to the stiffness of the compacted stones. The time-dependent nature of a stone column force is illustrated in Figure 7.8. The stone column forces increase over time and the process still does not end even after 10 years.

b) Coupled behaviour

The computed $[\sigma_{z,c} - \sigma_{z,c}(i)]/q$-time and u_{ex}/q-time relationships for three radial locations at the mid-depth of the soft clay are plotted in Figure 7.9 which follows the same rationale and format as in Figure 7.4 for the reference analysis. These three plots display characteristics very similar to those of the reference analysis despite the excess water pressure dissipating a little slower and increases in the effective stress being slightly less. These similarities also explain the relatively small increase in the settlement of the soil at NGL.

The coupling between consolidation and geosynthetic tension is manifested in the ΔT versus time relationships presented in Figure 7.10. All three plots show increases in ΔT with time. The trends displayed are similar to those of the reference analysis. The asymptotic values of ΔT at the near-top and bottom locations are slightly smaller than are those in the reference analysis and, at the middle depth location.

7.3.3 Effects of locked-in stress in geosynthetic

The influence of a lower locked-in force in the stone column is studied by repeating the analysis with T_{pre} reduced to 50 kN/m, while the other parameters are identical to those of the reference analysis.

a) Settlement and force in stone column

The computed evolutions of settlement with time are presented in Figure 7.11(a) and the settlement profiles at NGL and foundation level are plotted in Figure 7.11(b). At the centre-line location, settlement is 0.28m and, at the edge location, the computed settlement is 0.33m. There is a "bump" between the top of the stone and the soil at NGL. However, the computed profile along the top of the fill is still smooth, thus giving a high-quality riding surface for the pavement. The settlement values at both of these locations are only 0.02m higher than are those of the reference analysis.

Distributions of the column forces with depth at the end of construction and at 10 years are plotted in Figure 7.12 and show that all the overall shapes of the distributions are similar to those of the reference analysis. At the end of construction, the maximum stone column force is about 40 kN less than that of the reference analysis. After 10 years, at the middle depth, the column force is only about 10 kN less than that of the reference analysis. The time-dependent nature of stone column forces is illustrated in Figure 7.13. The shapes of the increases in stone column forces with time are also similar to those of the reference analysis. The stone column forces continue increasing slightly even after 10 years, which indicates that the consolidation process is still continuing.

b) Coupled behaviour

The computed [$\sigma_{z,c}$ -$\sigma_{z,c}$(i)]/q-time and u_{ex}/q-time relationships for three radial locations at the mid-depth of the soft clay are plotted in Figure 7.14 following the same format as in Figure 7.4 for the reference analysis. The shapes of these three curves are very similar to those of the reference analysis. The ratio values of [$\sigma_{z,c}$-$\sigma_{z,c}$(i)]/q are ~0.68 near the column, ~0.32 at the middle location and ~ 0.2 at the edge of unit cell.:

The coupling between consolidation and geosynthetic tension is manifested in the ΔT versus time relationships presented in Figure 7.15 follow the same format as in the reference analysis. The ΔT values increase with time at all three locations. The shapes of the curves at all three locations are similar to those of the reference analysis with the differences being within 10%.

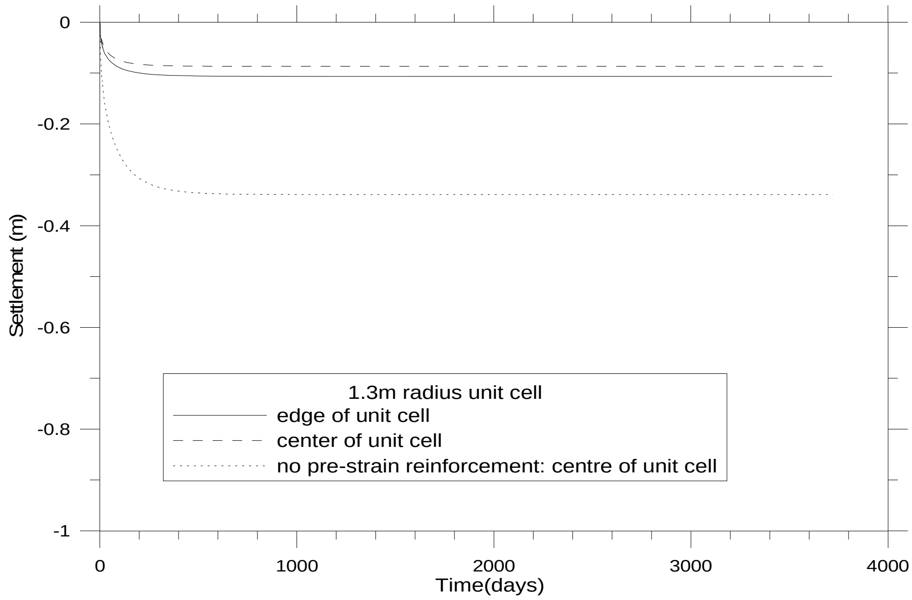

Figure 7.16(a): Settlement responses of reference analysis: comparison of settlement-time plots (1.3m radius unit cell, MCC model only)

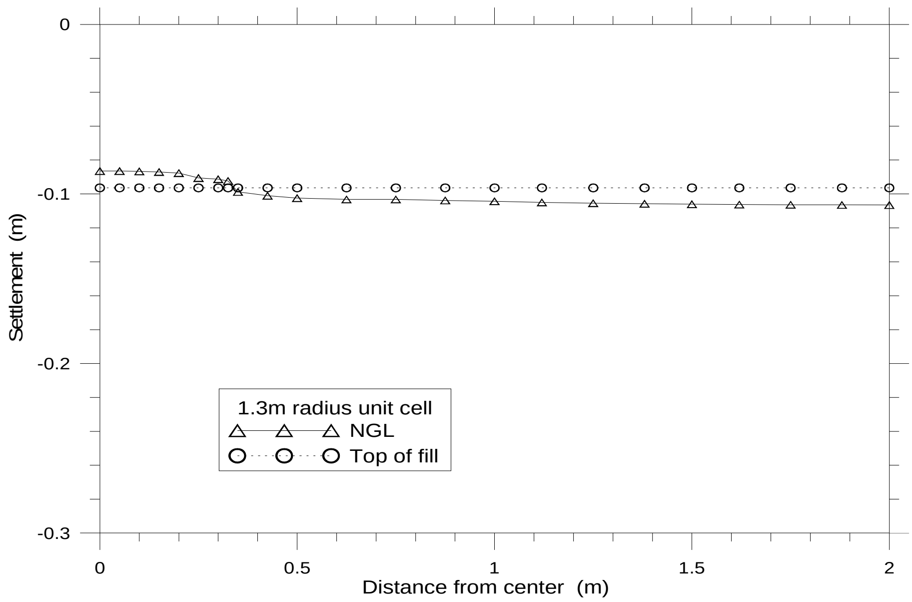

Figure 7.16(b): Settlement responses of reference analysis: settlement profiles at 10 years (1.3m radius unit cell, MCC model only)

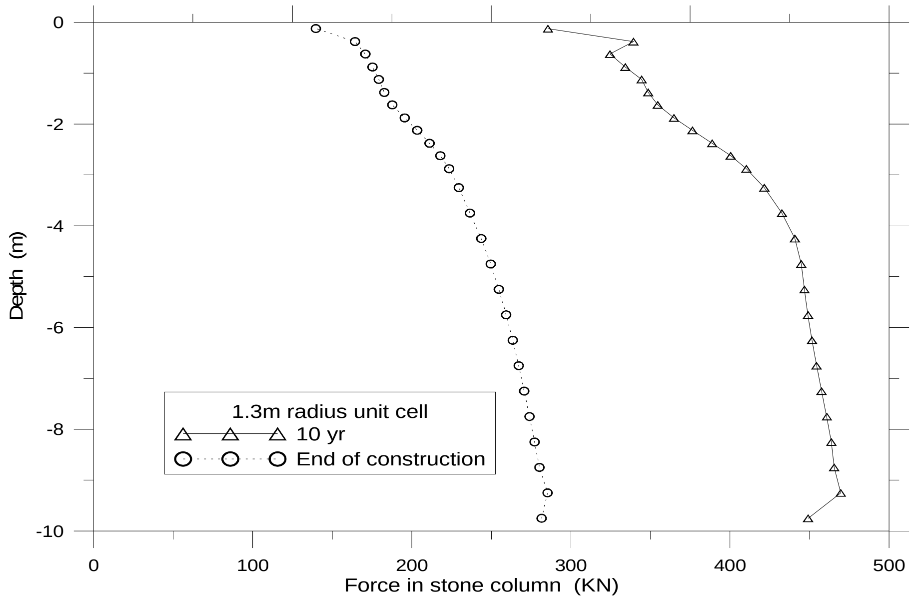

Figure 7.17: Distributions of column forces with depth:

reference analysis

(1.3m radius unit cell, MCC model only)

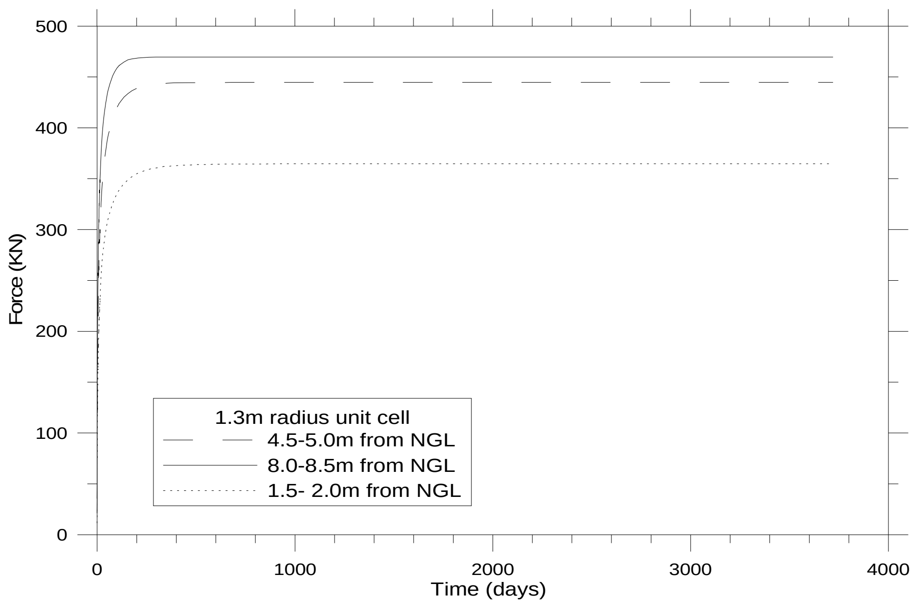

Figure 7.18: Evolutions of column forces with time:

reference analysis

(1.3m radius unit cell, MCC model only)

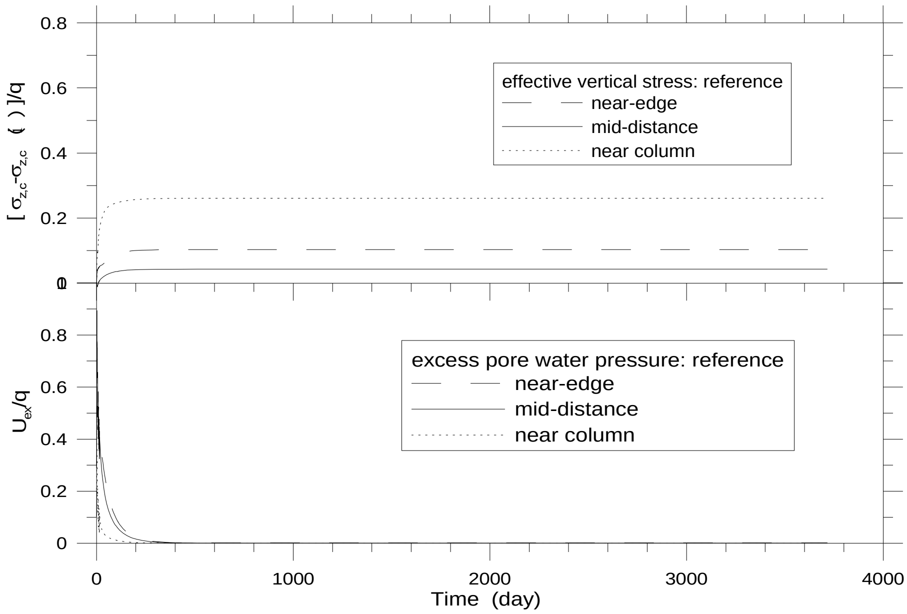

Figure 7.19: Consolidation responses in clay: reference analysis (1.3m radius unit cell, MCC model only)

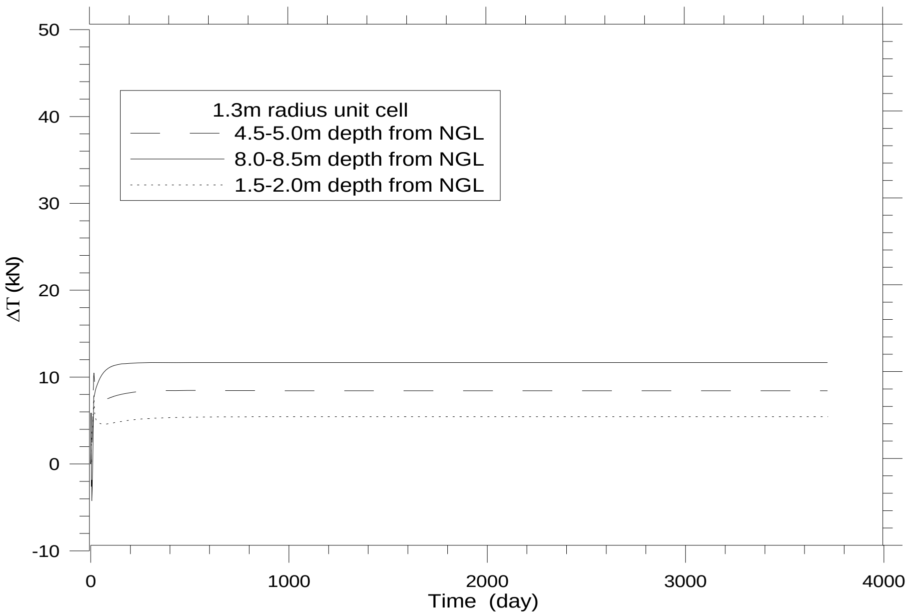

Figure 7.20: Increases in geosynthetic tension with time: reference analysis (1.3m radius unit cell, MCC model only)

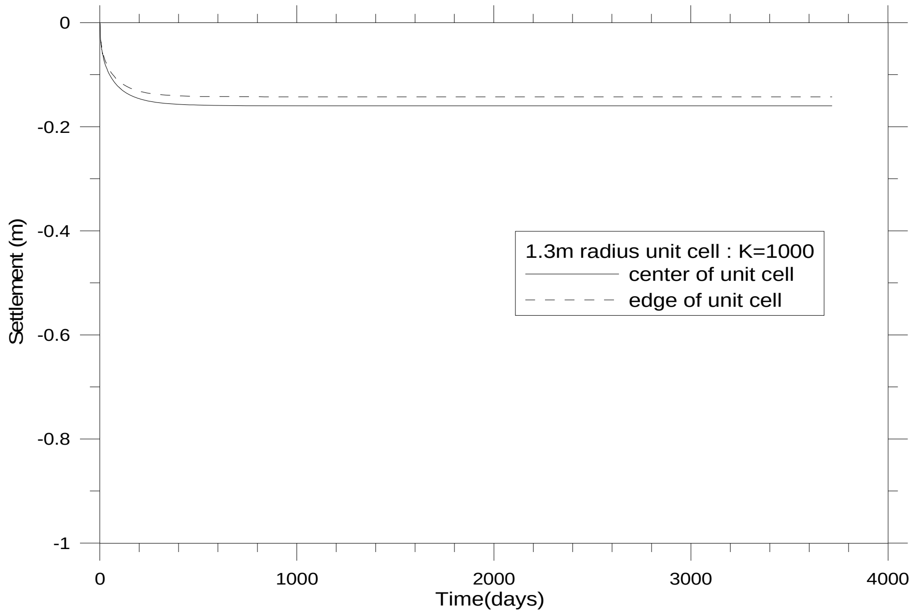

Figure 7.21(a): Settlement-time plots: reduced stone stiffness K=1000

(1.3m radius unit cell, MCC model only)

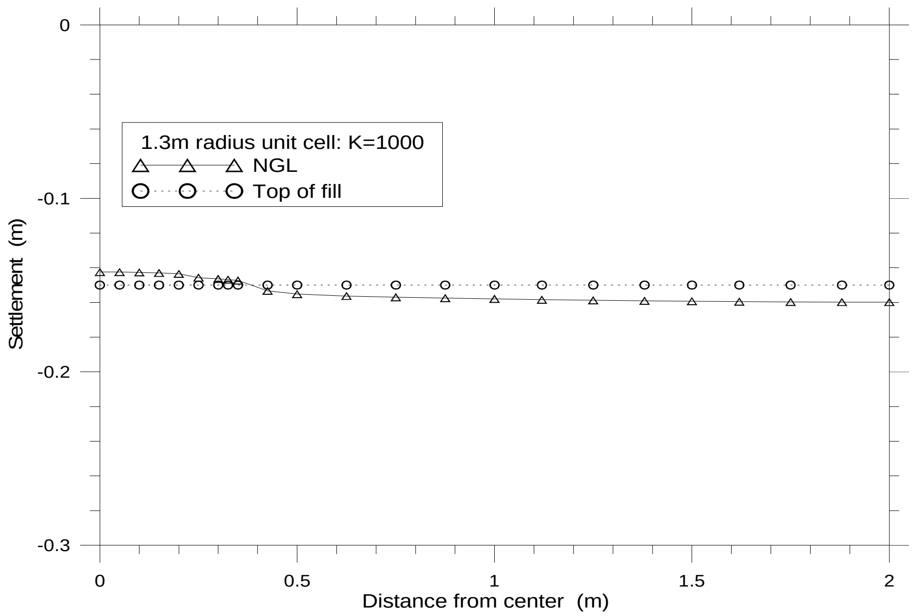

Figure 7.21(b): Settlement profiles: reduced stone stiffness K=1000

(1.3m radius unit cell, MCC model only)

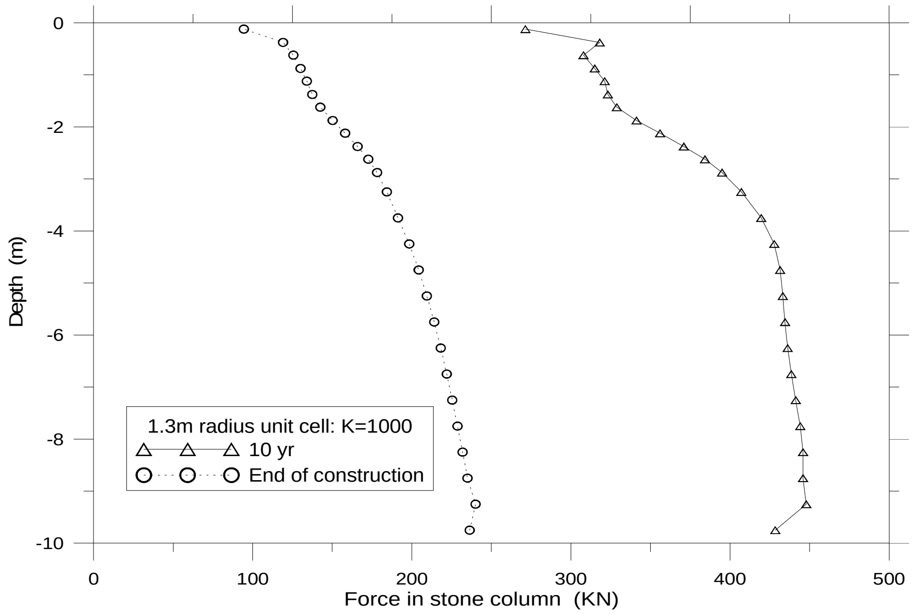

Figure 7.22: Distributions of column forces: reduced stone stiffness K=1000 (1.3m radius unit cell, MCC model only)

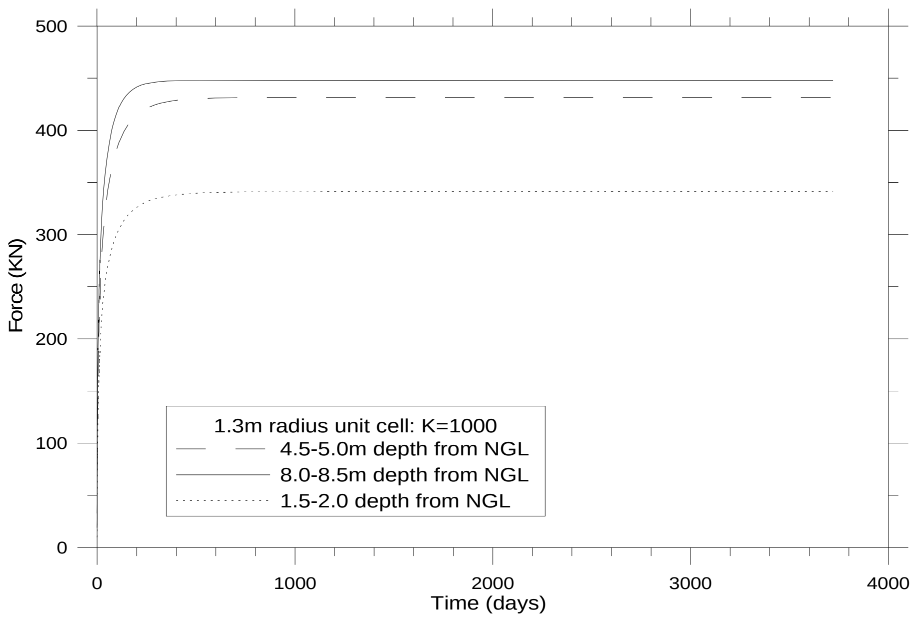

Figure 7.23: Evolutions of column forces with time: reduced stone stiffness K=1000

(1.3m radius unit cell, MCC model only)

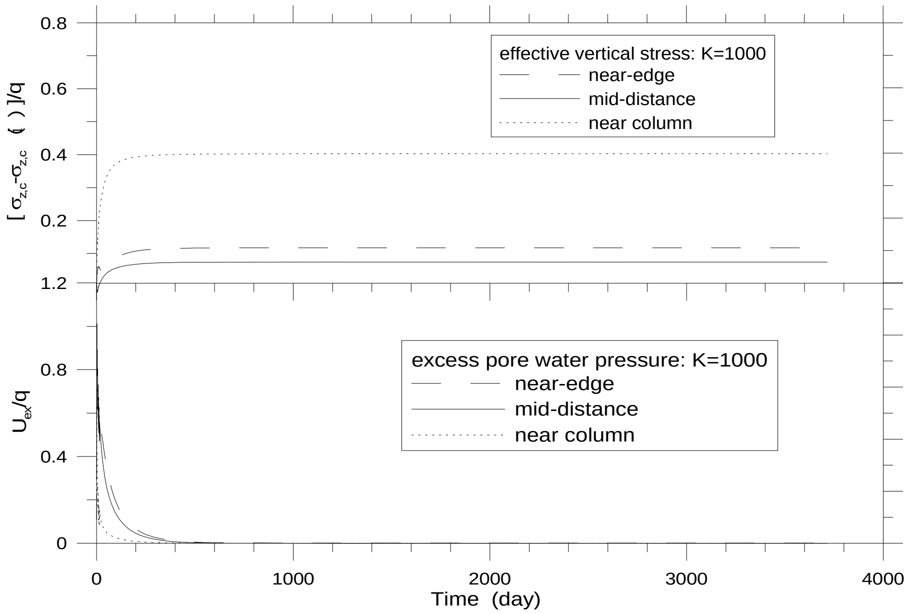

Figure 7.24: Consolidation responses in clay: reduced stone stiffness K=1000 (1.3m radius unit cell, MCC model only)

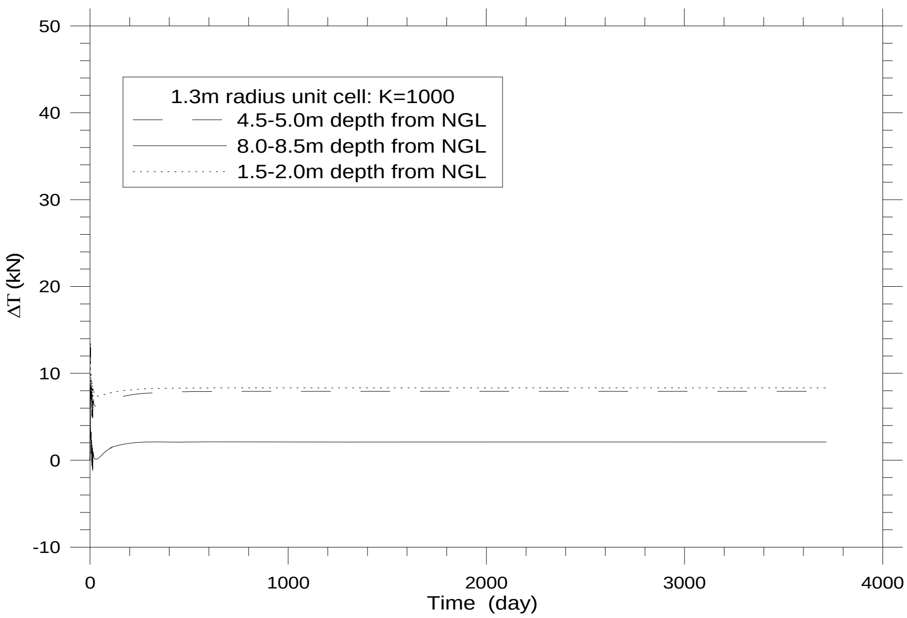

Figure 7.25: Increases in geosynthetic tension with time: reduced stone stiffness K=1000

(1.3m radius unit cell, MCC model only)

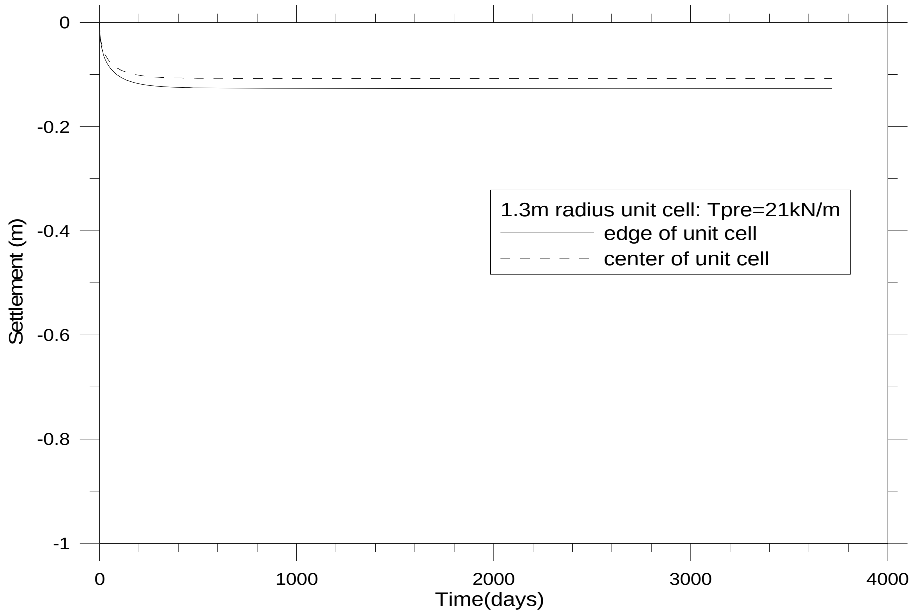

Figure 7.26(a): Settlement-time plots: reduced locked-in stress T_{pre}=21kN/m (1.3m radius unit cell, MCC model only)

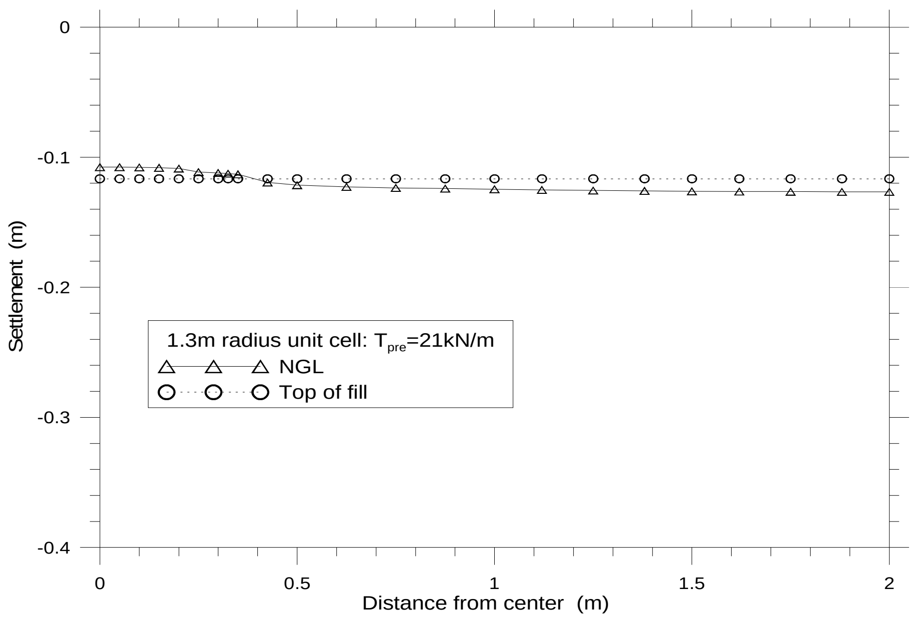

Figure 7.26(b): Settlement profiles: reduced locked-in stress T_{pre}=21kN/m (1.3m radius unit cell, MCC model only)

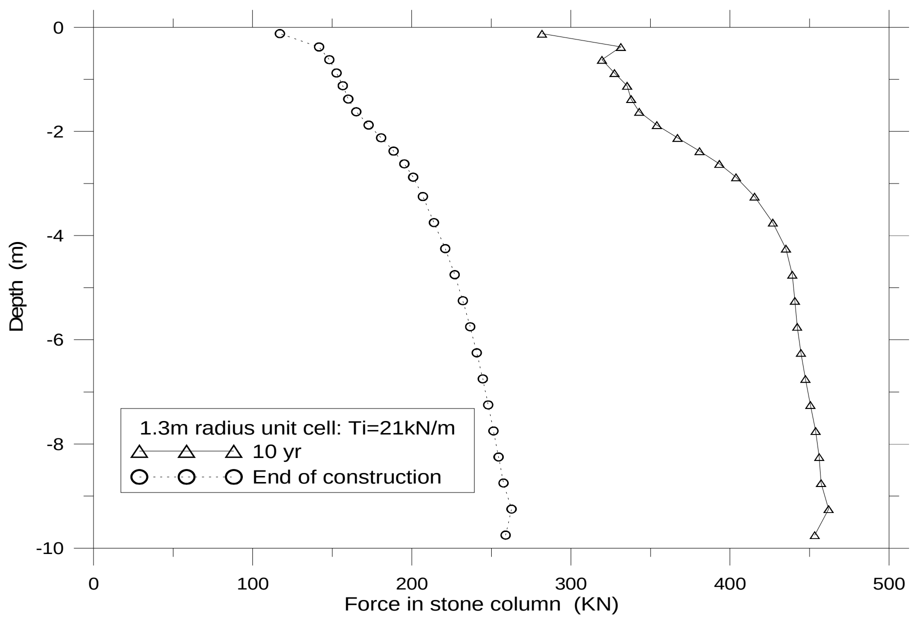

Figure 7.27: Distributions of column forces: reduced locked-in stress T_{pre}=21kN/m (1.3m radius unit cell, MCC model only)

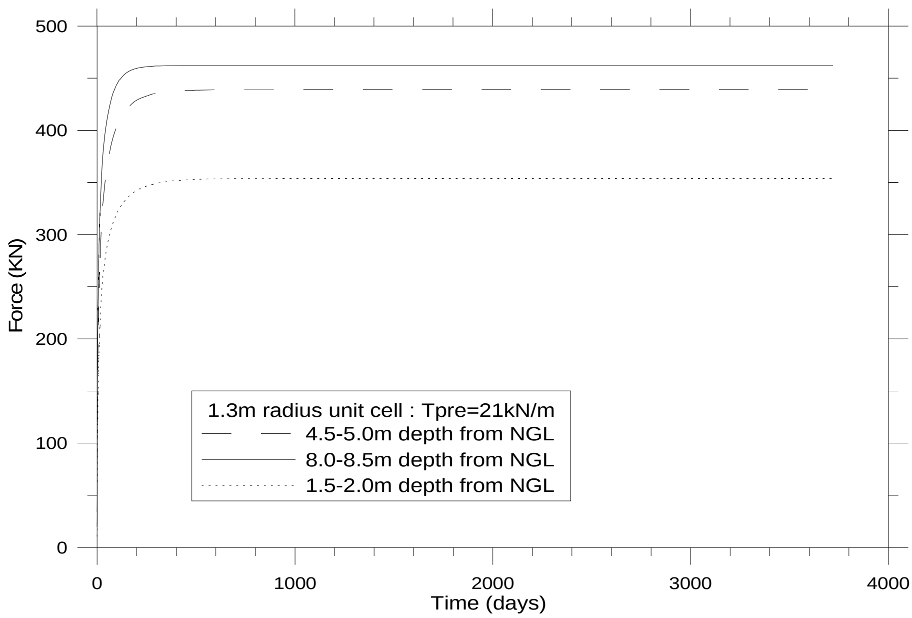

Figure 7.28: Evolutions of column forces with time: reduced locked-in stress T_{pre}=21kN/m

(1.3m radius unit cell, MCC model only)

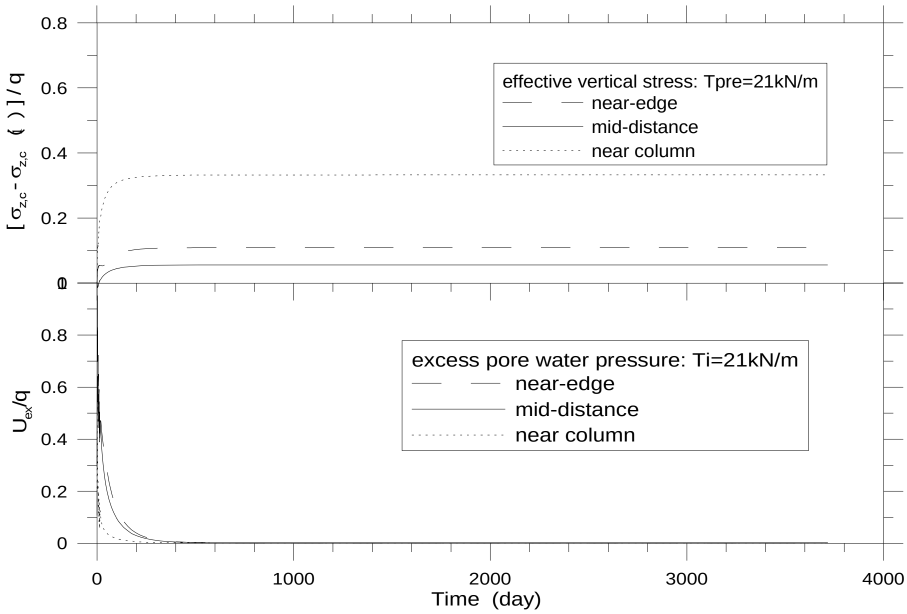

Figure 7.29: Consolidation responses in clay: reduced locked-in stress T_{pre}=21kN/m (1.3m radius unit cell, MCC model only)

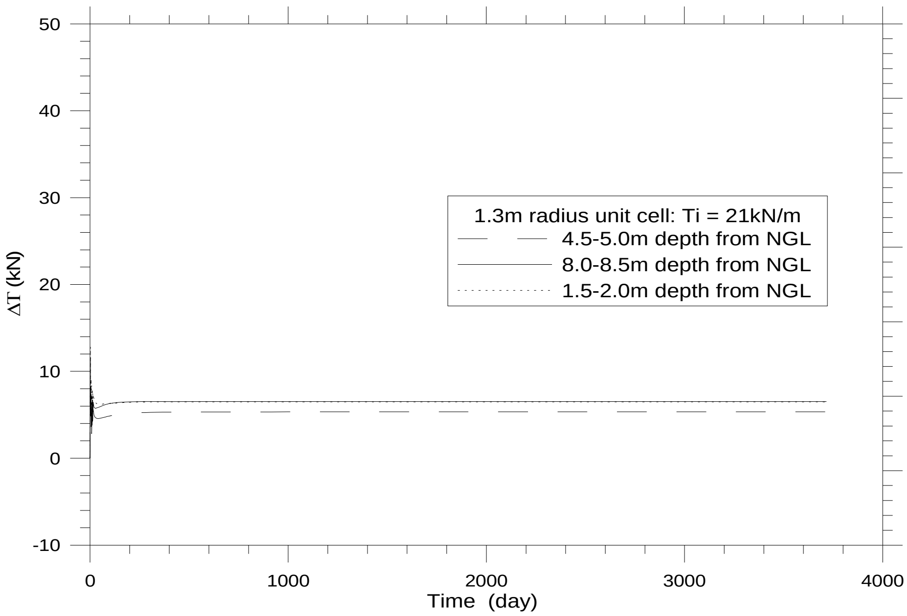

Figure 7.30: Increases in geosynthetic tension with time: reduced locked-in stress T_{pre}=21kN/m (1.3m radius unit cell, MCC model only)

7.4 STONE COLUMN IN MCC SOIL WITH 1.3M UNIT CELL

7.4.1 Reference parameters

Apart from their radii, the dimensions of the 1.3m and 2.0m radius unit cell stone columns are the same (Table 5-1) as are their material parameters (Table 5-2). Initial stresses are calculated by the methods proposed in section 7.2 with the same cavity expansion results presented in Chapter 6. Same as Chapter 5, a T_{pre} of 42 kN/m is referred to as the reference analysis.

<u>a) Settlement</u>

The numerical simulated evolutions of settlement with time are presented in Figure 7.1(a). The settlement-time relationship computed by assuming geosynthetic encasement with no non pre-straining columns is also plotted in this figure. When the encasement has no pre-straining, settlement at the top of the stone column at 10 years is approximately 0.31m, while that at NGL at the edge of the stone column is about 0.34m. These settlement values are about 60% of those of the 2.0m unit cell radius without geosynthetic encasement which is due to the dimension reduction of the unit cell radius. The application of geosynthetic encasement with T_{pre}=42 KN/m reduces settlement at the top of the stone column to only 0.09m while that at the edge of the unit cell attains a higher, but still very small, value of only 0.11m at 10 years. The stone column essentially ceases settlement after ~600 days, indicating that this consolidation process is much faster than that of the 2.0m radius unit cell.

The settlement profiles at NGL and the top of the fill are plotted in Figure 7.16(b). That at the top of the fill remains "bump-free" which is similar to that of the 2.0m unit cell stone column cases. Since settlements at both the top of the stone columns and the edges of the unit cells are very small compared with the depths of the soil, the settlement profile at NGL has only a little "bump" between the stone columns and the surrounding soil.

<u>b) Force in stone column</u>

Distributions of the computed column forces with depth at the end of construction and after 10 years are presented in Figure 7.17. The maximum column forces at the end of construction and at 10 years are about 285 kPa and 470 kPa respectively. Evolutions of the column forces with time are plotted in Figure 7.18 at three depths: the near-top, mid-depth and near-toe. At all three depths, the column forces increase with time as the excess water pressure disappears from the surrounding soil and they approach asymptotic values of about 150, 200 and 250 days at the bottom, middle and top depths respectively.

Compared with the 2.0m radius unit cell reference analysis, the 1.3m with reference parameters has the following differences:

- the maximum value of the column forces at the end of construction is only 20 kN/m less while, after 10 years, the column force is 60% less than that of the 2.0m case. This is caused by the dimensional effects because the soil volume in the stone column spacing of the 2.0m case is 2.5 times that of the 1.3m case; and

— the time needed for the stone column force to reach its maximum value is significantly shorter than that for the 2.0m case.

c) Coupled behaviour

The computed $[\sigma_{z,c} - \sigma_{z,c}(i)]/q$-time and u_{ex}/q-time relationships for three radial locations at the mid-depth of the soft clay are plotted in Figure 7.19 following the same rationale and format as the reference analysis of the 2.0m radius unit cell.

The maximum value of u_{ex}/q is less than 0.8 which can be explained by dissipation occurring during embankment construction. At all three locations, the process of dissipation of the excess pore water pressure ends up at ~400 days and the effective stress continuously increases until about 200-300 days. The asymptotic $[\sigma_{z,c} - \sigma_{z,c}(i)]/q$ values are 0.26 near the stone column, 0.1 at the middle distance and only 0.04 at the edge. This indicates that the fill load transfers from the edge of the unit cell to its centre.

The coupling between consolidation and geosynthetic tension is manifested in the ΔT versus time relationships presented in Figure 7.20 following the same format as in the reference analysis of the 2.0 m radius stone column. Unlike in the 2.0m case, the increase of ΔT is very small and the ΔT reach the asymptotic value in less than 300 days.

7.4.2 Influence of lower stone stiffness

The influence of lower stone stiffness is examined by repeating the analysis with the Duncan-Chang parameter, K, reduced to 1000, while the initial stress state and all other parameters are identical to those of the reference analysis of the 1.3m radius unit cell. This stiffness value is considered to be relatively low for compacted stones.

a) Settlement and force in stone column

The computed evolutions of settlement with time are presented in Figure 7.21(a) and the settlement profiles at NGL and foundation level are plotted in Figure7.21(b). The overall trends of both the plots and profiles are similar to those of the reference analysis. Settlement at the top of the stone column at 10 years is about 0.14m and that of the soil at the edge of the unit cell 0.16m. The computed settlement at the top of the fill is smooth with a value of 0.165 at 10 years. Compared with the reference analysis, both increases in settlement and reductions in stiffness are about 50%. This can be explained by less of the fill load being transferred to the stone columns, as shown in Figure 7.22. On average, the stone column forces reduce about 20 KN less compared with the reference analysis both after construction and at 10 years. The time-dependent nature of stone column forces is illustrated in Figure 7.23 which shows their evolutions with time at three depths. The trends in this figure are similar to those of the reference analysis with the maximum force value being only 5-10% smaller.

b) Coupled behaviour

The computed $[\sigma_{z,c}-\sigma_{z,c}(i)]/q$-time and u_{ex}/q-time relationships for three radial locations at the mid-depth of the soft clay are plotted in Figure 7.24. These plots are quite similar to those of the reference analysis but dissipation of the pore water pressure takes a little longer, about 100 days more at each location. The asymptotic values of $[\sigma_{z,c}-\sigma_{z,c}(i)]/q$ increase when the K is halved, being 0.4 at the near-column, 0.125 at the middle distance and 0.08 at the edge of the unit cell locations.

The coupling between consolidation and geosynthetic tension is manifested in the ΔT versus time relationships presented in Figure 7.25 which shows that increases in ΔT are very small after the end of construction.

7.4.3 Effects of locked-in stress in geosynthetic

The influence of a lower locked-in force in a stone column is studied by repeating the analysis with T_{pre} reduced to 21 kN/m, while the other parameters and the initial stress state are identical to those of the reference analysis.

<u>a) Settlement and force in stone column</u>

The computed evolutions of settlement with time are presented in Figure 7.26(a) and the settlement profiles at NGL and foundation level are plotted in Figure 7.26(b). The developments of settlement with time and the overall shapes of the settlement profiles follow similar patterns to those of the reference analysis. Settlement at the top of the stone column at 10 years is about 0.11m and that of the soil at the edge of the unit cell 0.13m. Settlement increases by only 20% when the T_{pre} is halved. The computed profile along the top of the fill is still smooth with a settlement value of 0.13m. Considering the 50% drop in the locked-in strain, these settlement values are only slightly higher than those of the reference analysis.

Distributions of the column forces with depth at the end of construction and at 10 years are plotted in Figure 7.27. The distribution at the end of construction remains nearly the same as in the reference analysis and the overall shape of the distribution at 10 years is similar to that of the reference analysis with slightly smaller values at each location. The maximum stone column force after 10 years is about 7 kN less than that of the reference analysis. The time-dependent nature of the stone column force is illustrated in Figure 7.28 which shows the evolutions of column forces with time at three depths. The trends in this figure are similar to those of the reference parameters with the maximum force value being less than 5% smaller.

b) Coupled behaviour

The computed $[\sigma_{z,c}-\sigma_{z,c}(i)]/q$-time and u_{ex}/q-time relationships for three radial locations at the mid-depth of the soft clay are plotted in Figure 7.29. Despite the dissipation of excess water pressure being a little slower, there are no obvious differences of u_{ex}/q–time with that of the reference analysis.

The $[\sigma_{z,c}-\sigma_{z,c}(i)]/q$–time plots are also similar except that the $[\sigma_{z,c}-\sigma_{z,c}(i)]/q$ values increase slightly at all three locations. After 10 years, the $[\sigma_{z,c}-\sigma_{z,c}(i)]/q$ values at the near the edge, middle distance and edge locations are 0.35, 0.12 and 0.05 respectively.

The coupling between consolidation and geosynthetic tension is manifested in the ΔT versus time relationships presented in Figure 7.30. The ΔT is relatively small compare to the 2.0m radius unit cell. ΔT reach its asymptotic value within 300 days.

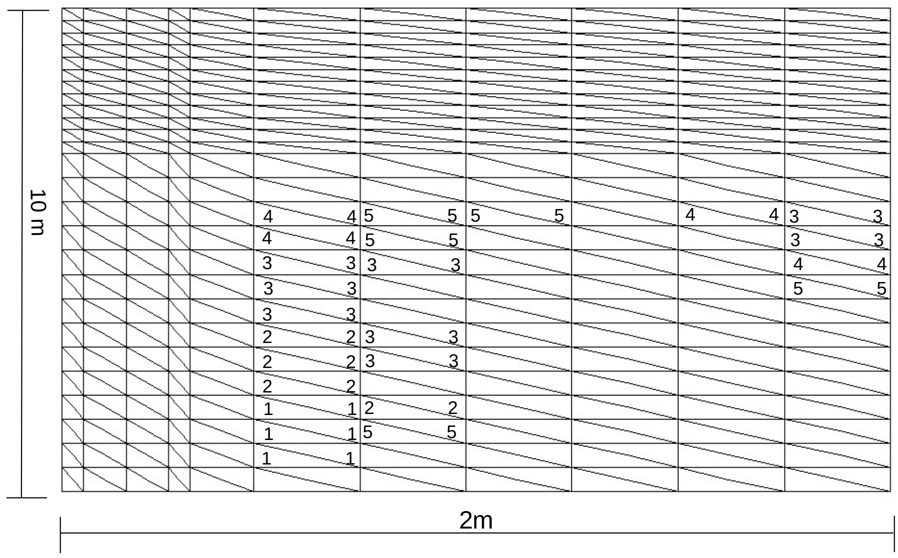

Figure 7.31: Evaluation of failure of SSC elements

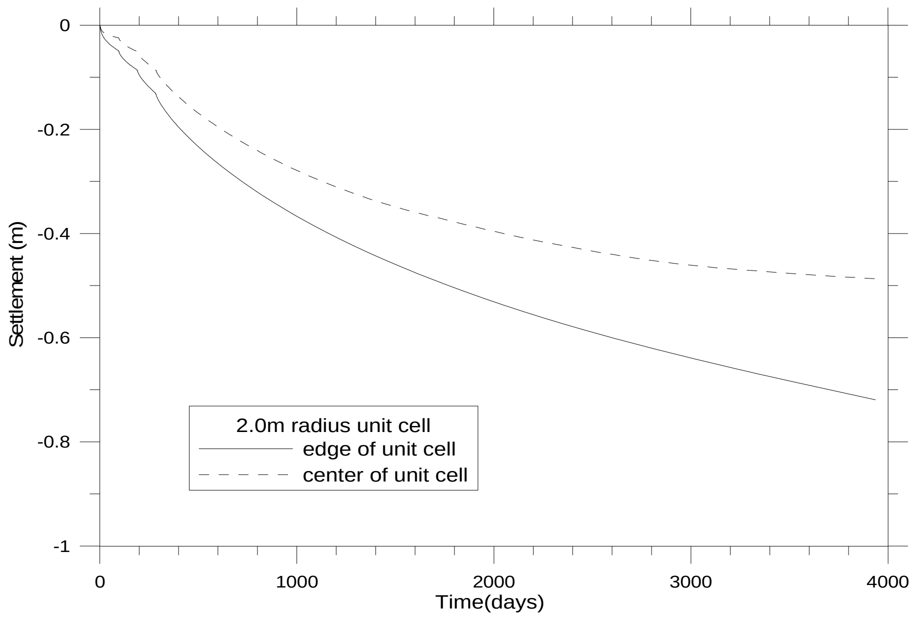

Figure 7.32(a): Settlement responses of reference analysis with waiting time applied for each metre of construction: settlement-time plots (2.0m radius unit cell, SSC model applied)

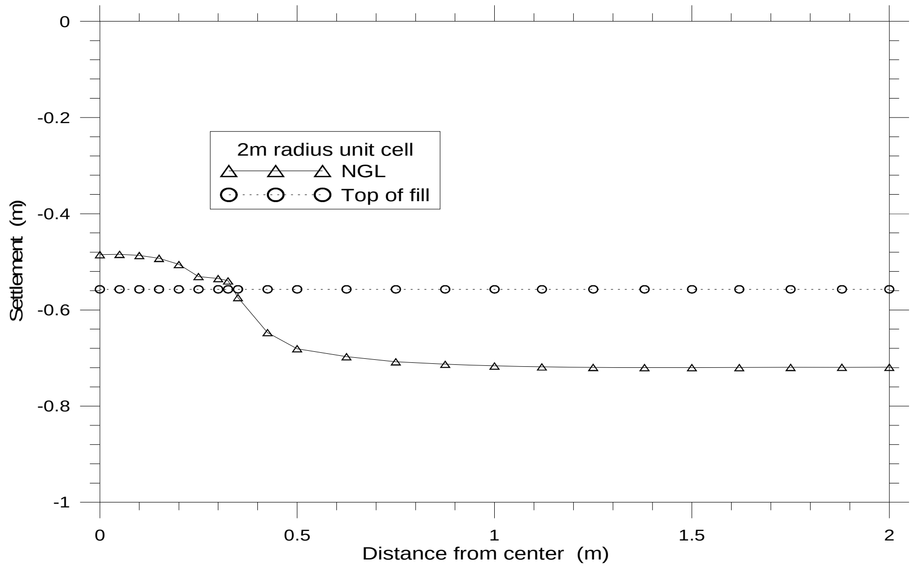

Figure 7.32(b): Settlement responses of reference analysis with waiting time applied for each metre of construction: settlement profiles at 10 years (2.0m radius unit cell, SSC model applied)

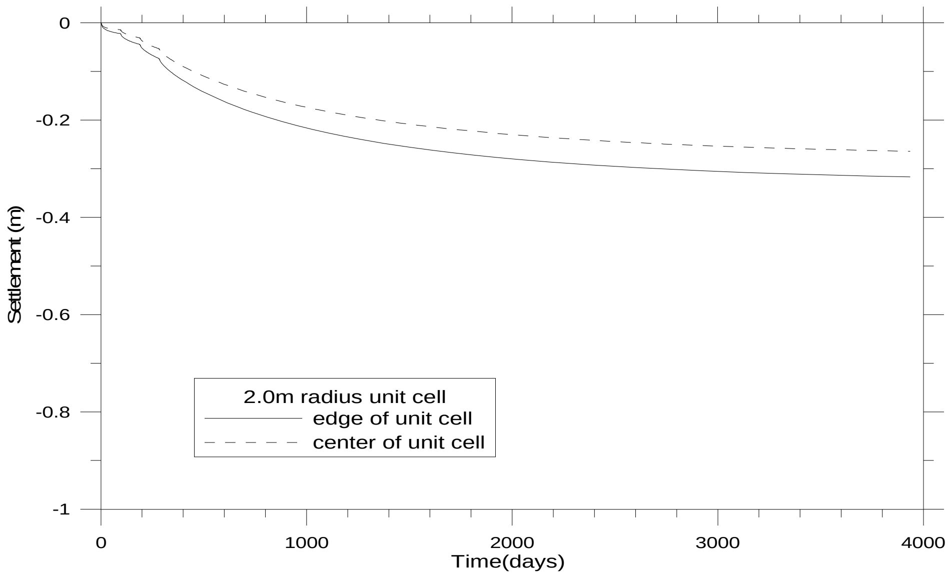

Figure 7.33: Settlement time plots of MCC reference parameter conditions with waiting time applied for each metre of construction (2.0m radius unit cell, SSC model applied)

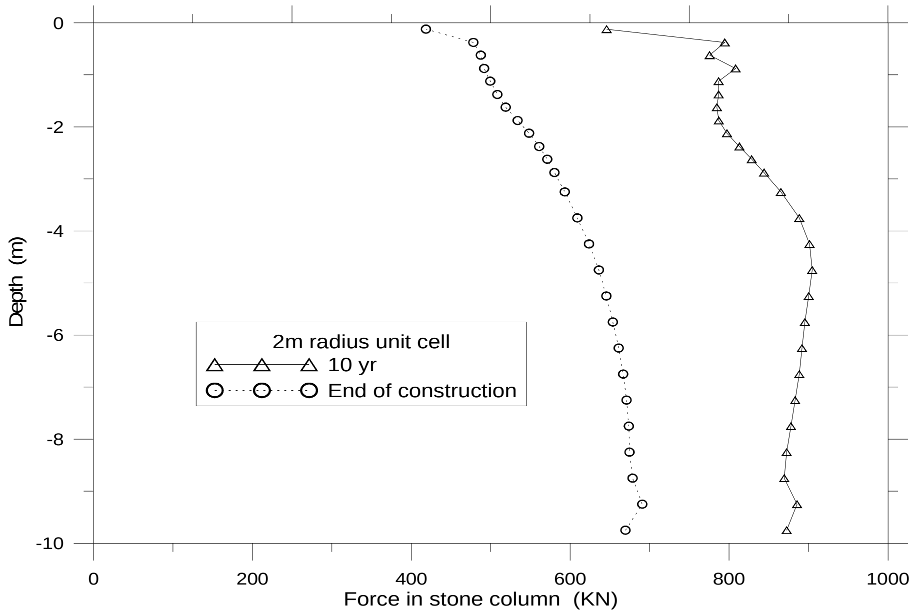

Figure 7.34: Distributions of column forces with depth: reference analysis with waiting time applied for each metre of construction (2.0m radius unit cell, SSC model applied)

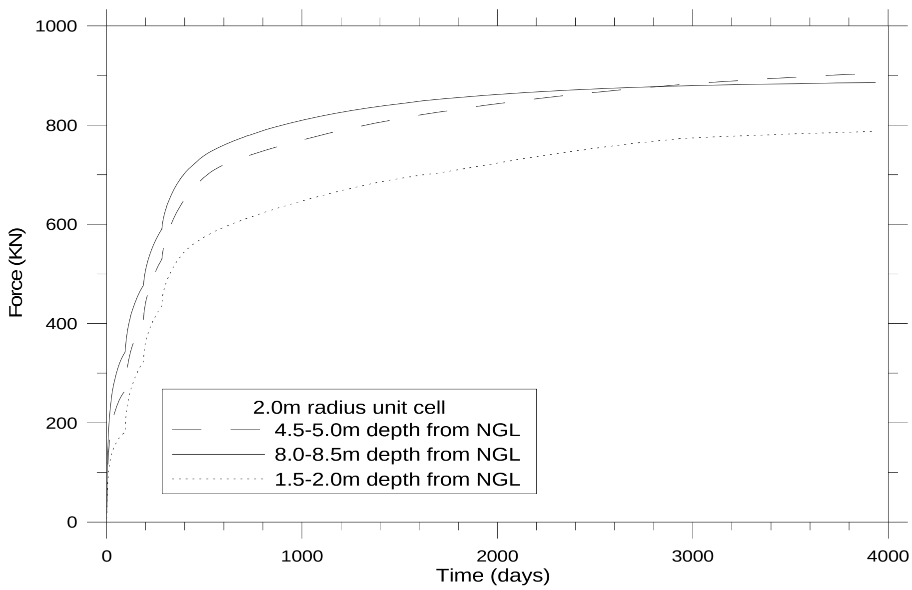

Figure 7.35: Evolutions of column forces with time: reference analysis with waiting time applied for each metre of construction (2.0m radius unit cell, SSC model applied)

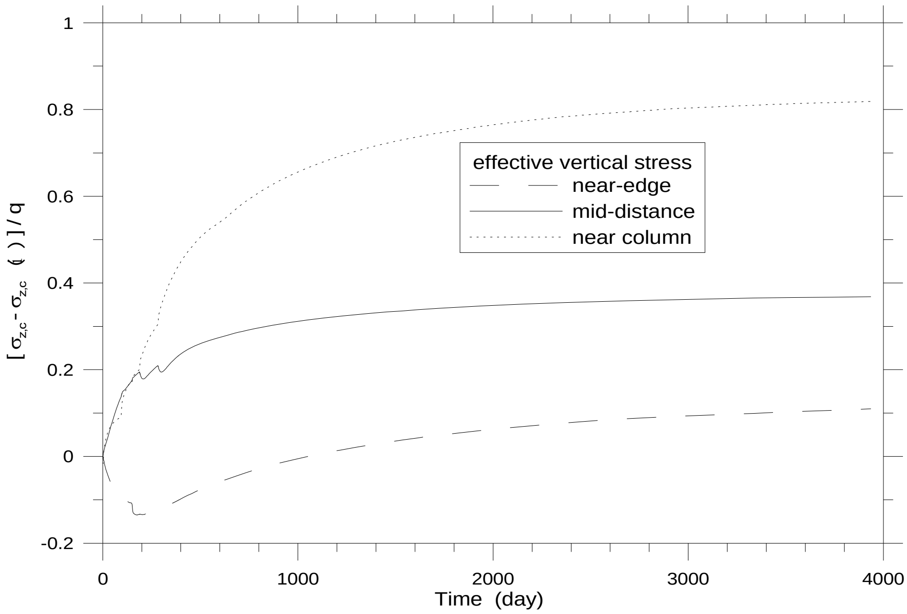

Figure 7.36(a): Consolidation responses in clay: reference analysis with waiting time applied for each metre of construction (2.0m radius unit cell, SSC model applied)

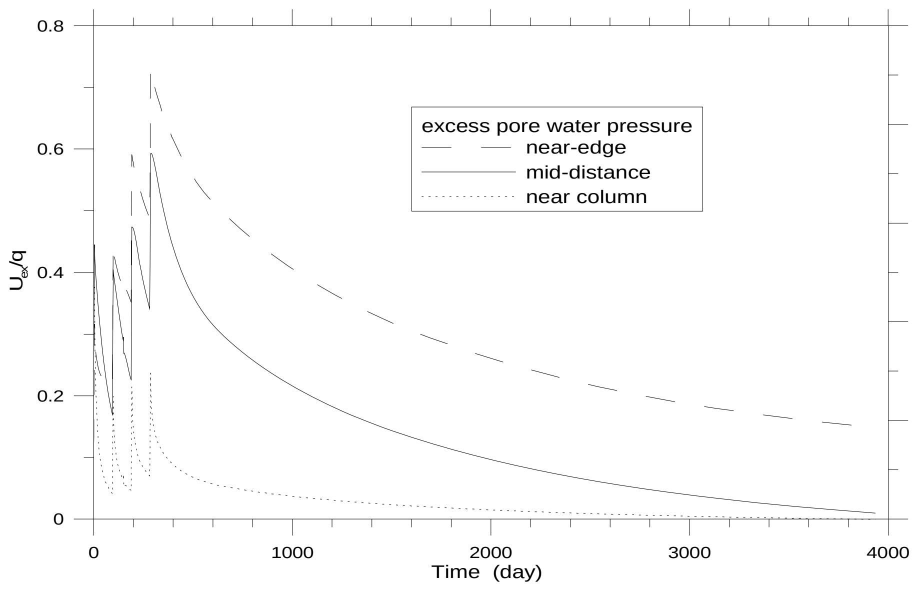

Figure 7.36(b): Excess water pressure dissipation: reference analysis with waiting time applied for each metre of construction (2.0m radius unit cell, SSC model applied)

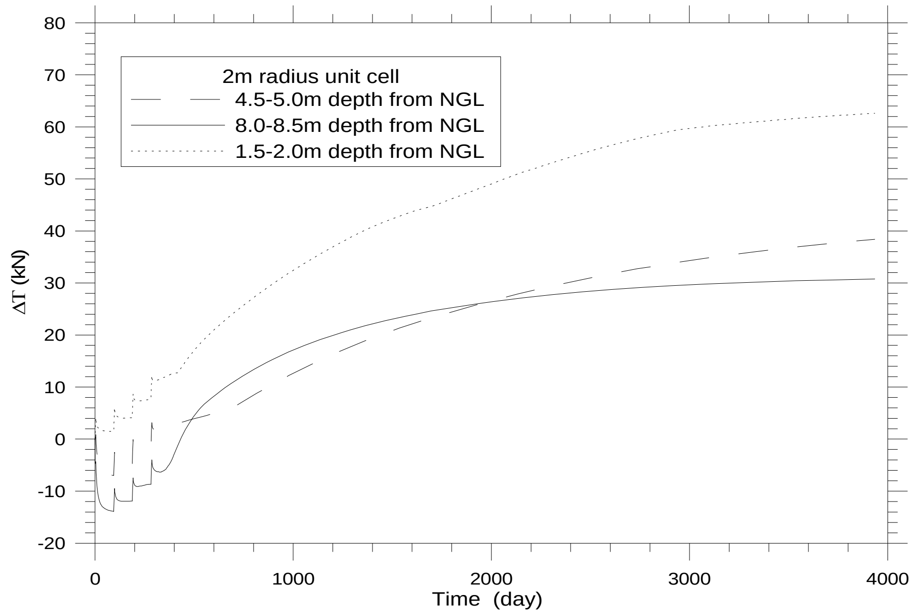

Figure 7.37: Increases in geosynthetic tension with time: reference analysis with waiting time applied for each metre of construction (2.0m radius unit cell, SSC model applied)

7.5 STONE COLUMN IN SSC SOIL WITH 2.0M UNIT CELL

The simulation using the SSC model with the full-displacement installation method employs the same parameters as that using the SSC model with the wish-in installation method presented in Chapter 5. The only difference is the initial stress state which is calculated from the results presented in Chapter 6. The first analysis was based on reference parameters. The analysis stopped shortly after the end of construction when a large number of the SSC elements are found to be approaching the critical state. To examine the process of the stop of the coupled analysis, the analysis was repeated by adopting smaller loading step and the steps before the numerical failure are examined. A number of soil elements approached the critical state as illustrated in Figure 7.31, where the number indicates the sequence of the elements approaching the critical state.

Since comparing with the wish-in installation method, only the initial stress state is different, it is more likely the excess water pressure generate by the full displacement installation method caused the numerical failure. After installation, some elements next to the stone column approach the critical state. As loading of the fill generates more water pressure, more soil elements be pushed into critical states and thus cause failure of the simulation. To identify whether the excess pore water pressure is the main cause of this problem, the construction sequence is changed to waiting after the fill loading for 90 days per meter with is about the maximum time a real construction can wait and the minimum waiting time that the numerical simulation can continue.

<u>a) Settlement and force in stone column</u>

The computed evolutions of settlement with time are presented in Figure 7.32(a) and the settlement profiles at NGL and foundation level are plotted in Figure 7.32(b). At the centre-line location, the settlement is 0.485m and, at the edge location, the computed settlement is 0.72m. These settlement values are much large than those of the “wish-in” stone columns.

To examine the influence of the construction rate, the MMC reference parameters case, using the full-displacement installation method, as explained in section 7.3, is redone with the same construction rate (90 days per meter). The settlement with time plots of the MMC reference analysis with construction rate of 90 days per meter are plotted in Figure 7.33. The figure shows that settlement at the centre-line location is 0.26m and at the edge location 0.317m after 10 years. Compared with Figure 5.6, the differences between settlement times, of the two different construction rates, are less than 0.02m at both locations. The influence of construction rate is very small on the settlement after 10 years. Thus, the main cause of high settlements is the characteristics of SSC soils.

As shown in Figure 7.32 , the “bump” between the top of the stone and the soil at NGL is also very high, being a greater than 0.2m settlement difference. However, although the computed profile along the top of the fill is still smooth, its settlement is also very high, about 0.56m after 10 years.

Distributions of the column forces with depth at the end of construction and at 10 years are plotted in Figure 7.34. At the end of construction, the maximum stone column force is about 670 kN, a very large value caused by the total construction time of one year. The maximum stone column force at the middle depth is about 900 kN. The time-dependent nature of stone column forces is illustrated in Figure 7.35. Those at three different locations increase with time, even after 10 years, which indicates that the consolidation process continues.

The higher a stone column force, the higher its displacement at NGL, as shown in Figure 7.32. A high stone column force indicates that the stone column still takes a large amount of the fill load and the soils take less. Thus, to explain the high settlement of the soil, its coupled behaviour is examined.

b) Coupled behaviour

The computed $[\sigma_{z,c}-\sigma_{z,c}(i)]/q$-time and u_{ex}/q-time relationships for three radial locations at the mid-depth of the soft clay are plotted in Figure 7.36. At all three locations, the excess pore water pressure dissipates with time, as expected. The shapes of the fluctuated curves before 400 days are caused by the "waiting" time after construction for each metre of loading. After 10 years, there is still significant excess pore water pressure remaining at the edge of the unit cell location.

The $[\sigma_{z,c}–\sigma_{z,c}(i)]/q$ increases with time at the near-column and mid-distance locations. At the mid–distance, it reaches a stable value of approximately 0.37 in about 1500 days. Its value after 10 years is about 0.81 at the near-column location and is still increasing slightly. A significant strain softening is seen in the $[\sigma_{z,c}–\sigma_{z,c}(i)]/q$ versus time curve at the edge location. The $[\sigma_{z,c}–\sigma_{z,c}(i)]/q$ decreases to about 0.13 from the beginning of construction to about 200 days. Most SSC elements at the edge of the unit cell are already at CS before 200 days; their distributions in the SSC reach the CS at about the same as those in the SSC reference analysis without any "waiting" and, then, $[\sigma_{z,c}–\sigma_{z,c}(i)]/q$ begins to increase until it reaches about 0.1. Compared with the MCC reference analysis, the $[\sigma_{z,c}–\sigma_{z,c}(i)]/q$ values at the near-column and middle distance locations increase by 10% and about 5% respectively and, at the edge location, this value dramatically reduces by 50% at 10 years. Since the edge location represents much greater soil volume than does the near-column location, the average total effective stress increase in the soil is less than that in the MCC reference analysis. This also explains why the stone column force is higher.

Compared with the MCC reference analysis, the SSC reference parameters condition has significantly more displacement, less effective stress and a significant percentage of the SSC elements approach CS. Thus, it is clear that the high displacement is caused by the failure of the SSC.

Figure 7.37 presents three ΔT-time plots corresponding to three depths: near-top, mid-depth, and near-toe. All three show increases in ΔT with time, but the increments vary with the different depth locations. The asymptotic values of ΔT after 10 years are 38 kN near the top, 62 kN at the mid-depth and only 30 kN at the bottom. The significantly high ΔT at mid-depth indicate bulging of the stone columns.

Since the geosynthetic encased stone column with reference parameters does not work, analysis of other conditions (lower T_{pre}, lower K) are not needed.

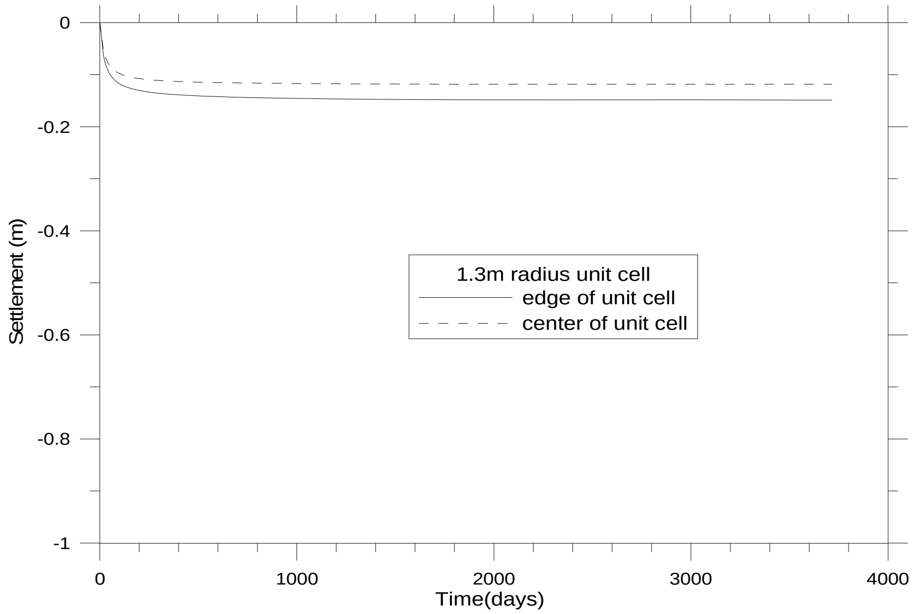

Figure 7.38(a): Settlement responses of reference analysis: settlement-time plots (1.3m radius unit cell, SSC model applied)

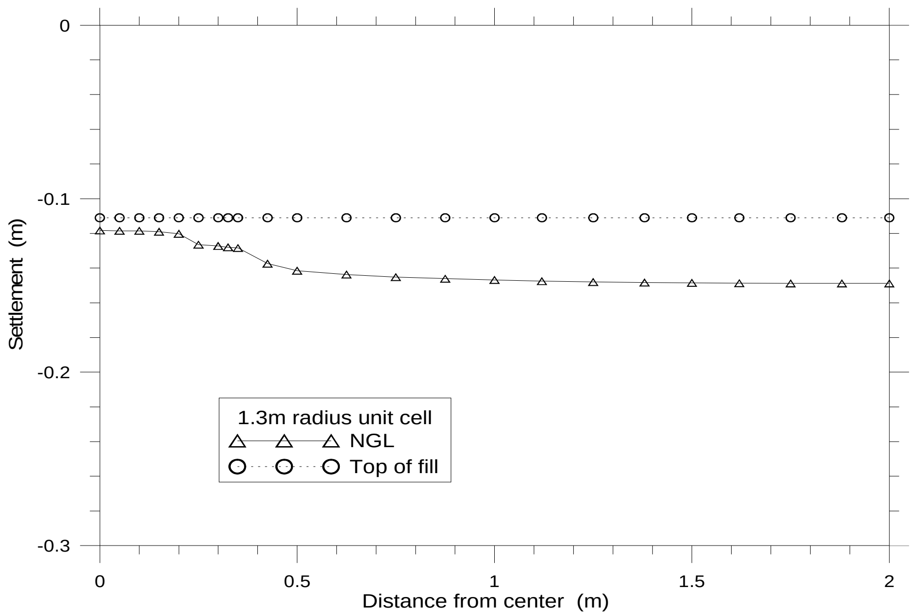

Figure 7.38(b): Settlement responses of reference analysis: settlement profiles at 10 years

(1.3m radius unit cell, SSC model applied)

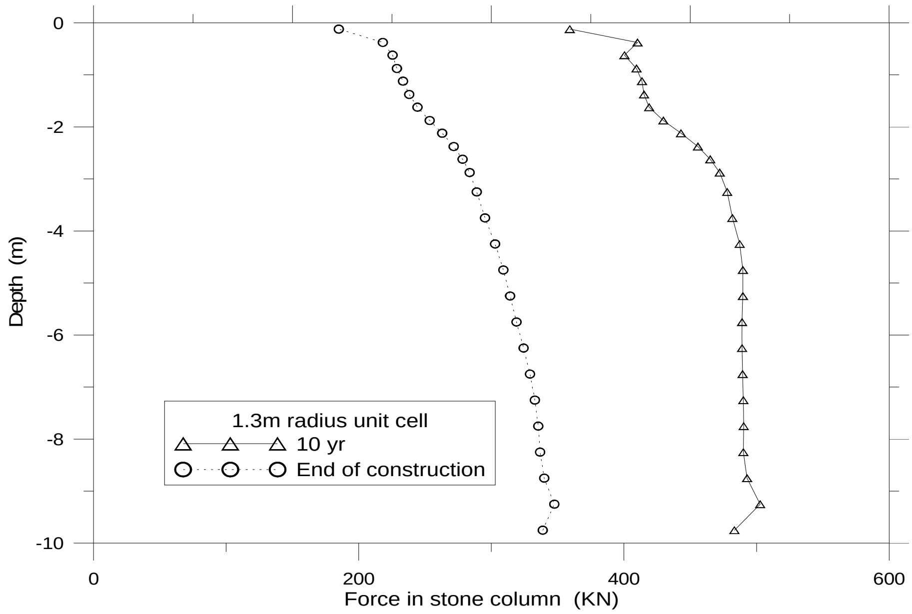

Figure 7.39: Distributions of column forces with depth: reference analysis (1.3m radius unit cell, SSC model applied)

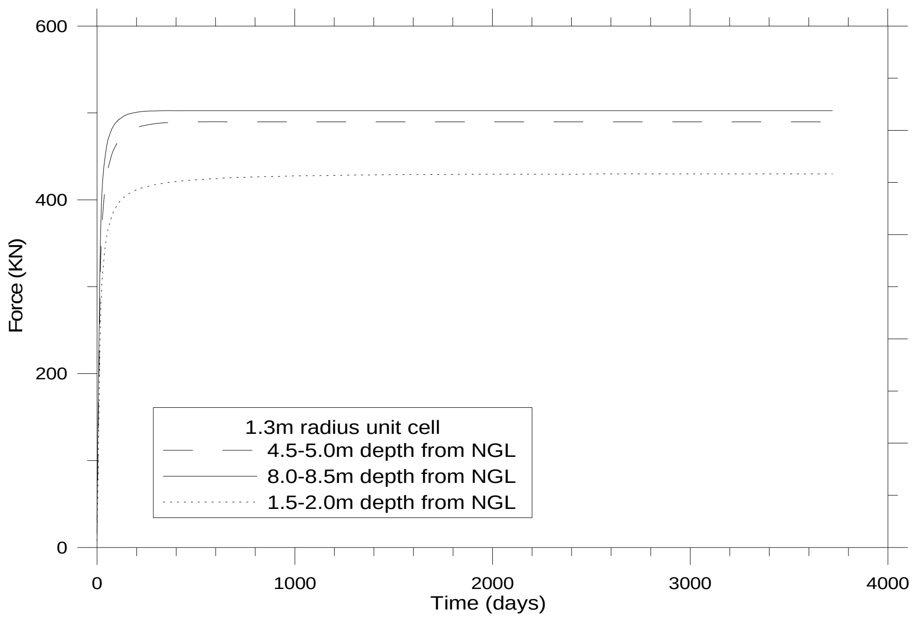

Figure 7.40: Evolutions of column forces with time: reference analysis (1.3m radius unit cell, SSC model applied)

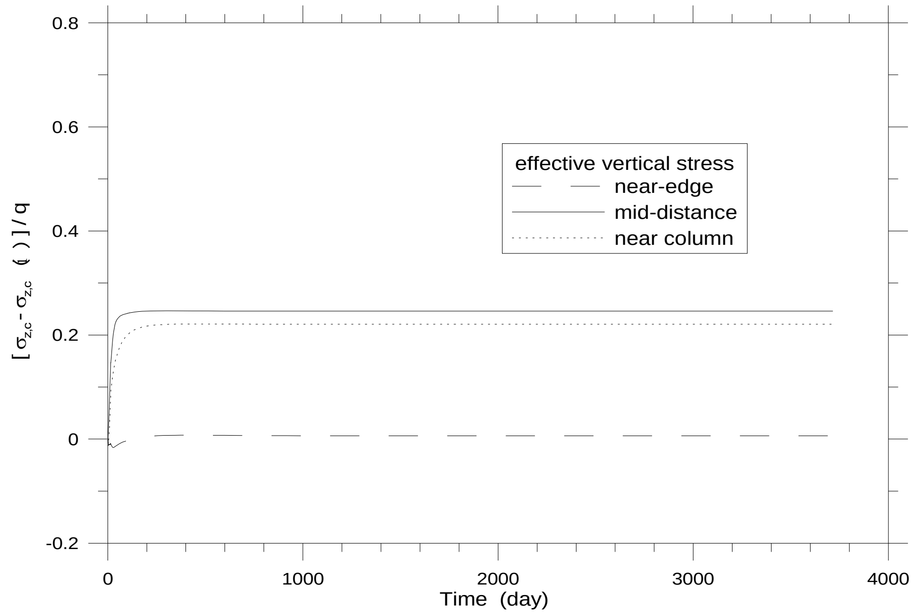

Figure 7.41(a): Consolidation responses in clay: reference analysis (1.3m radius unit cell, SSC model applied)

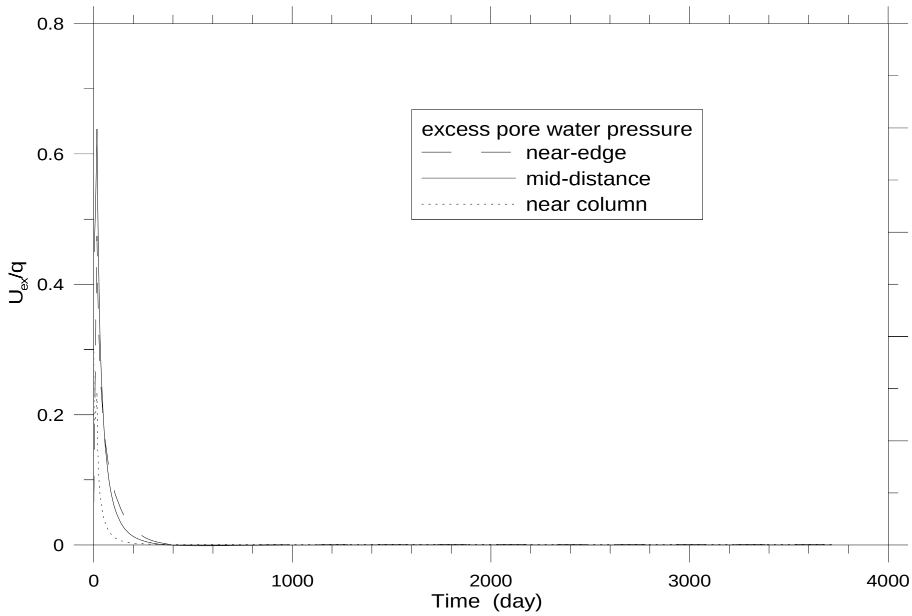

Figure 7.41(b): Excess water pressure dissipation: reference analysis (1.3m radius unit cell, SSC model applied)

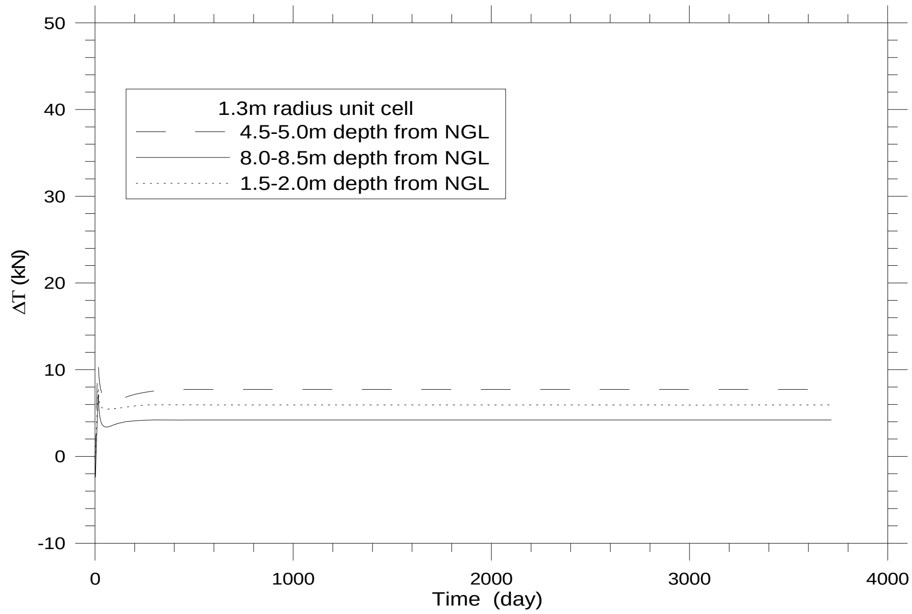

Figure 7.42: Increases in geosynthetic tension with time: reference analysis (1.3m radius unit cell, SSC model applied)

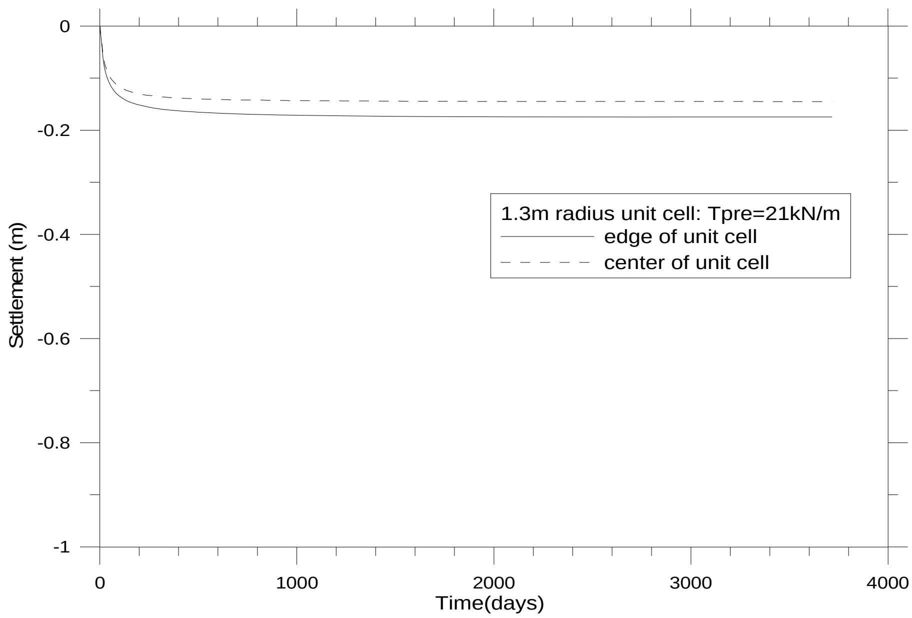

Figure 7.43(a): Settlement-time plots: reduced locked-in stress T_{pre}=21kN/m (1.3m radius unit cell, SSC model applied)

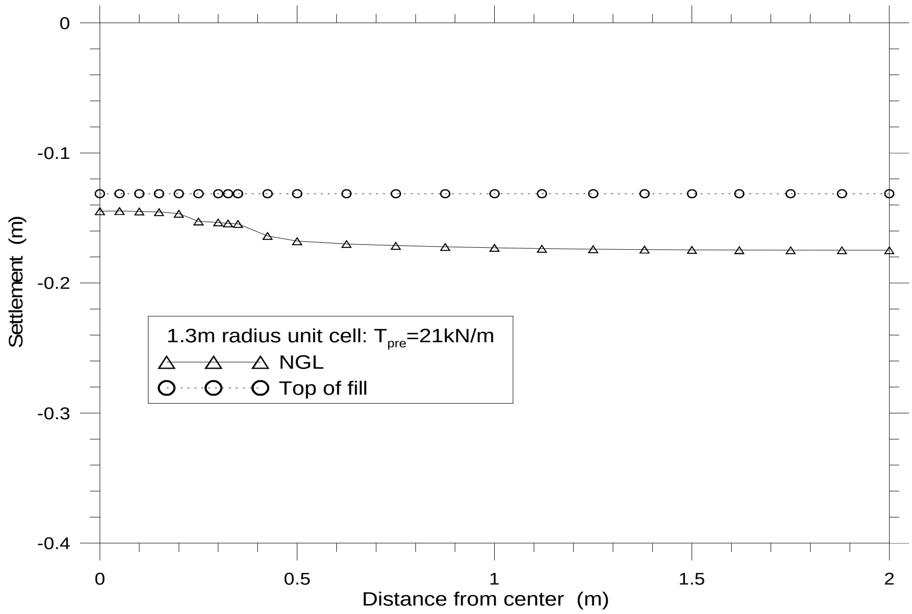

Figure 7.43(b): Settlement profiles: reduced locked-in stress T_{pre}=21kN/m (1.3m radius unit cell, SSC model applied)

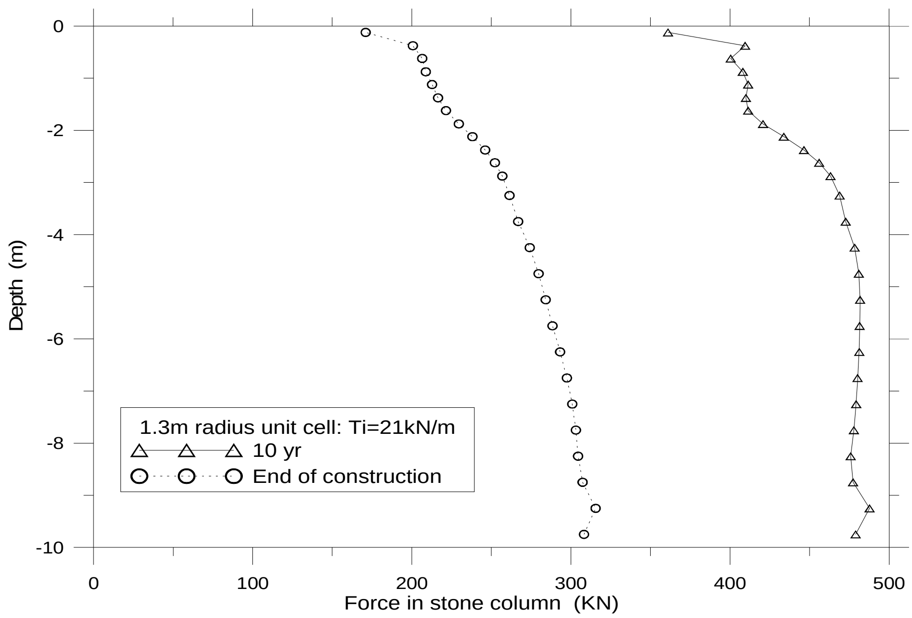

Figure 7.44: Distributions of column forces: reduced locked-in stress T_{pre}=21kN/m (1.3m radius unit cell, SSC model applied)

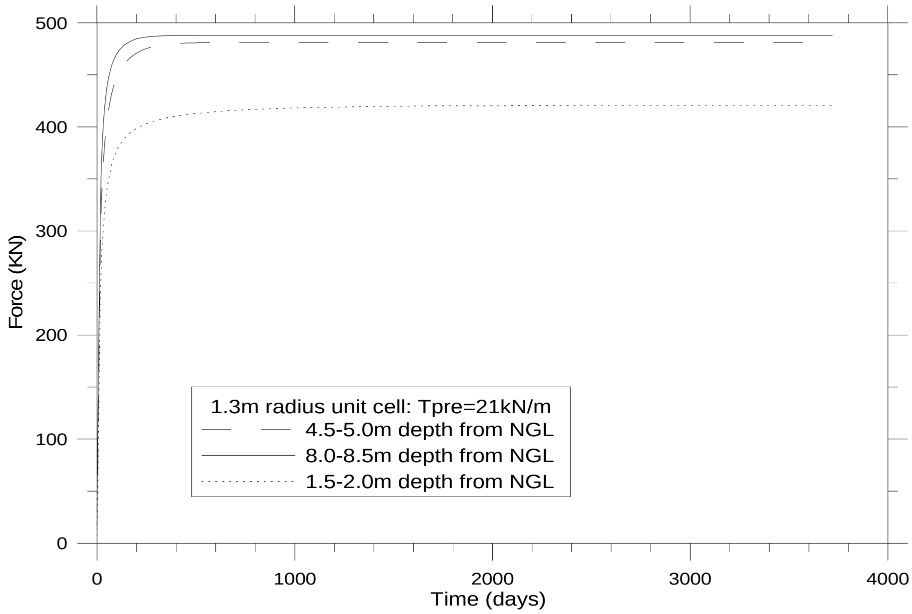

Figure 7.45: Evolutions of column forces with time: reduced locked-in stress T_{pre}=21kN/m(1.3m radius unit cell, SSC model applied)

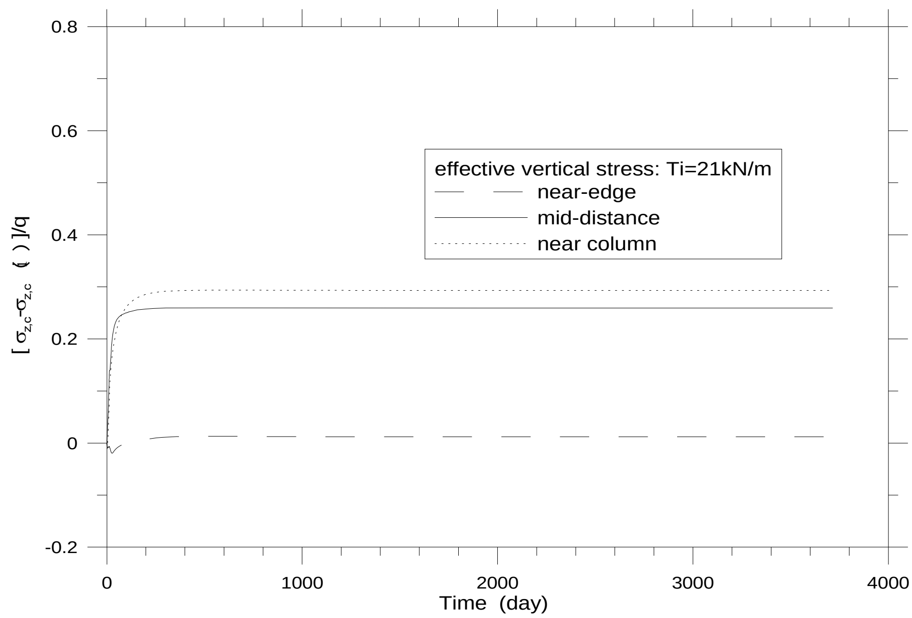

Figure 7.46(a): Consolidation responses in clay: reduced locked-in stress T_{pre}=21kN/m (1.3m radius unit cell, SSC model applied)

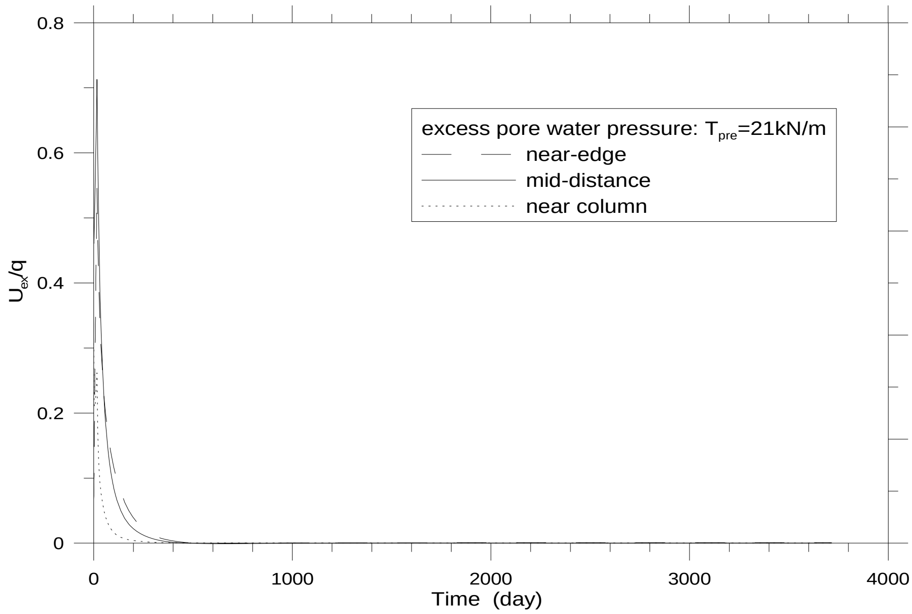

Figure 7.46(b): Excess water pressure dissipation: reduced locked-in stress T_{pre}=21kN/m (1.3m radius unit cell, SSC model applied)

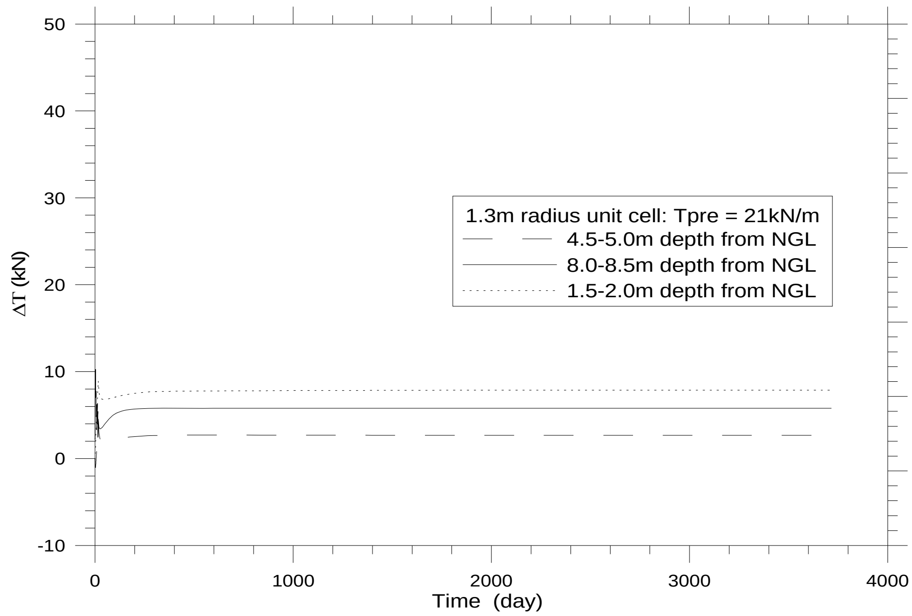

Figure 7.47: Increases in geosynthetic tension with time: reduced locked-in stress T_{pre}=21kN/m (1.3m radius unit cell, SSC model applied)

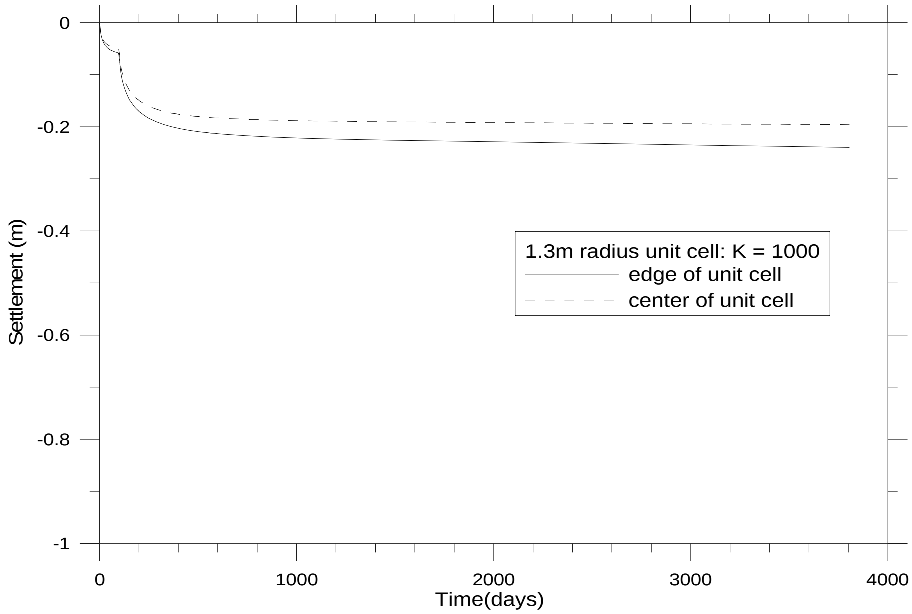

Figure 7.48(a): Settlement-time plots: reduced stone stiffness K=1000

(1.3m radius unit cell, SSC model applied)

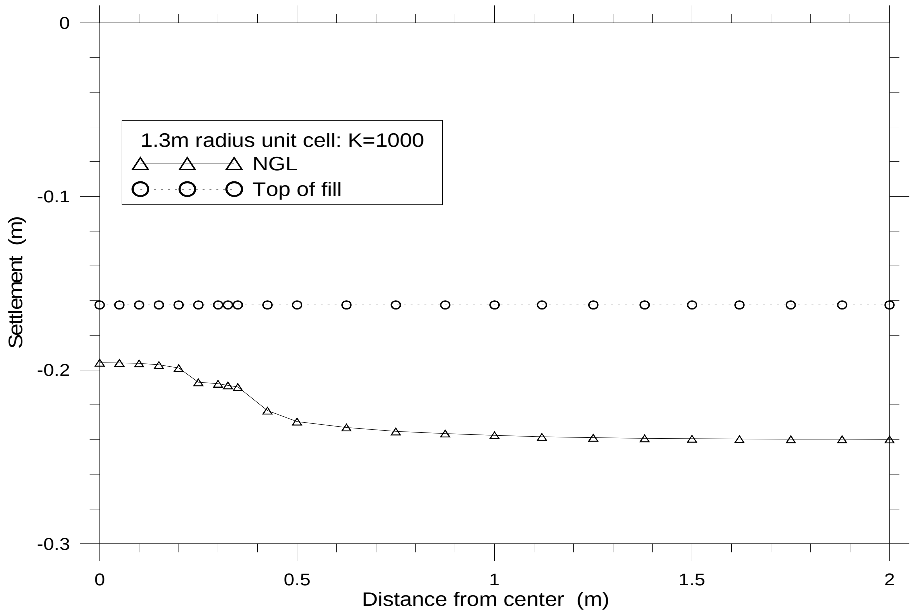

Figure 7.48(b): Settlement profiles: reduced stone stiffness K=1000

(1.3m radius unit cell, SSC model applied)

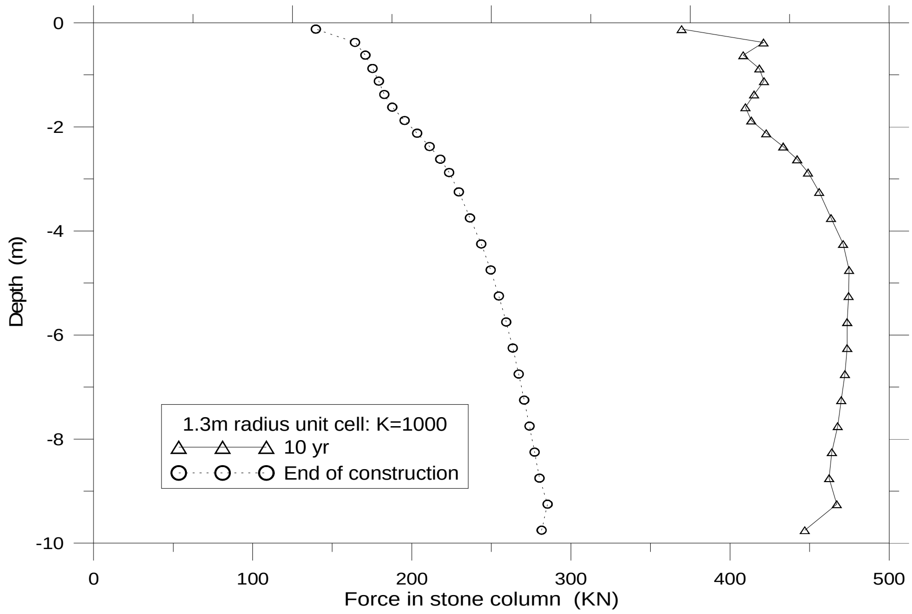

Figure 7.49: Distributions of column forces: reduced stone stiffness K=1000 (1.3m radius unit cell, SSC model applied)

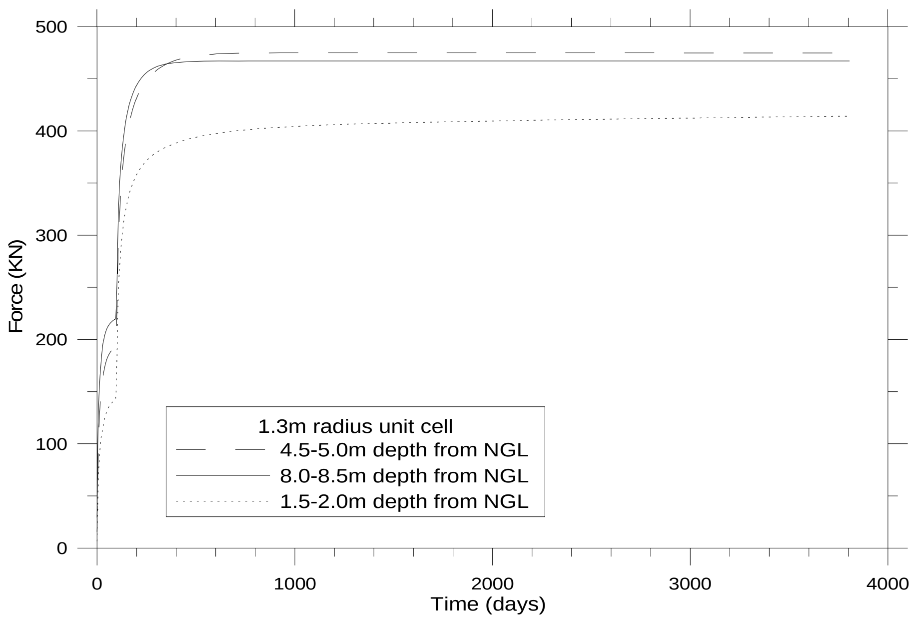

Figure 7.50: Evolutions of column forces with time: reduced stone stiffness K=1000 (1.3m radius unit cell, SSC model applied)

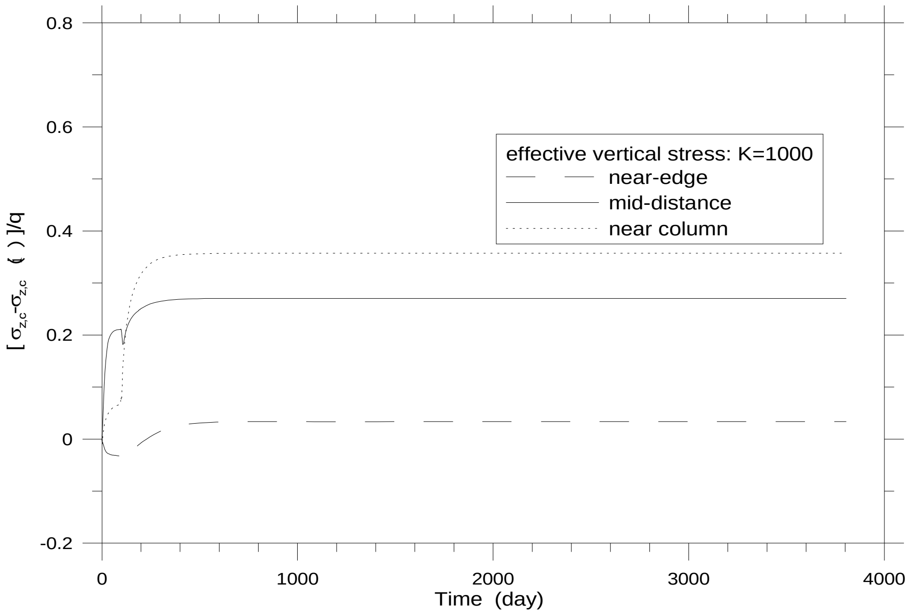

Figure 7.51(a): Consolidation responses in clay: reduced stone stiffness K=1000 (1.3m radius unit cell, SSC model applied)

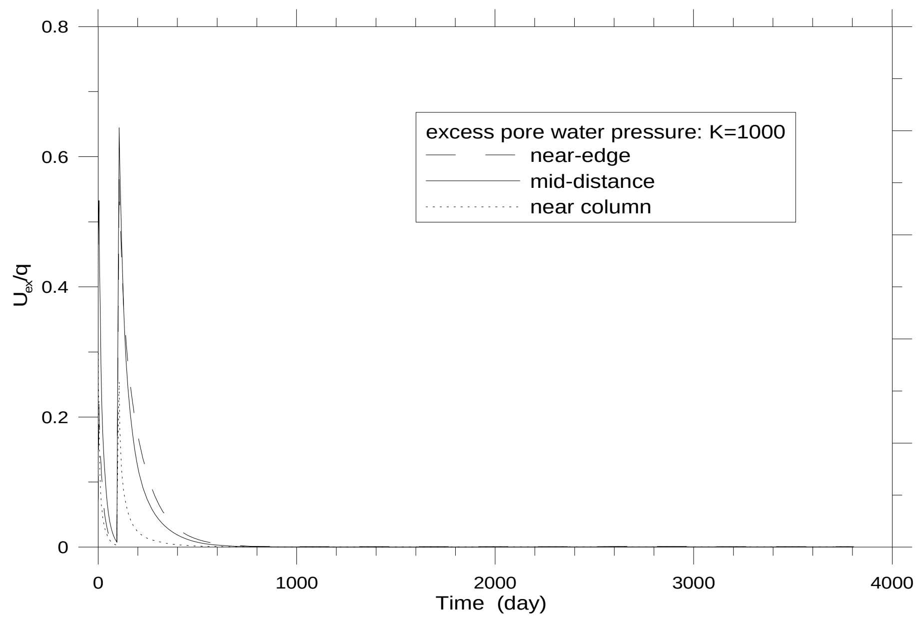

Figure 7.51(b): Excess water pressure dissipation: reduced stone stiffness K=1000 (1.3m radius unit cell, SSC model applied)

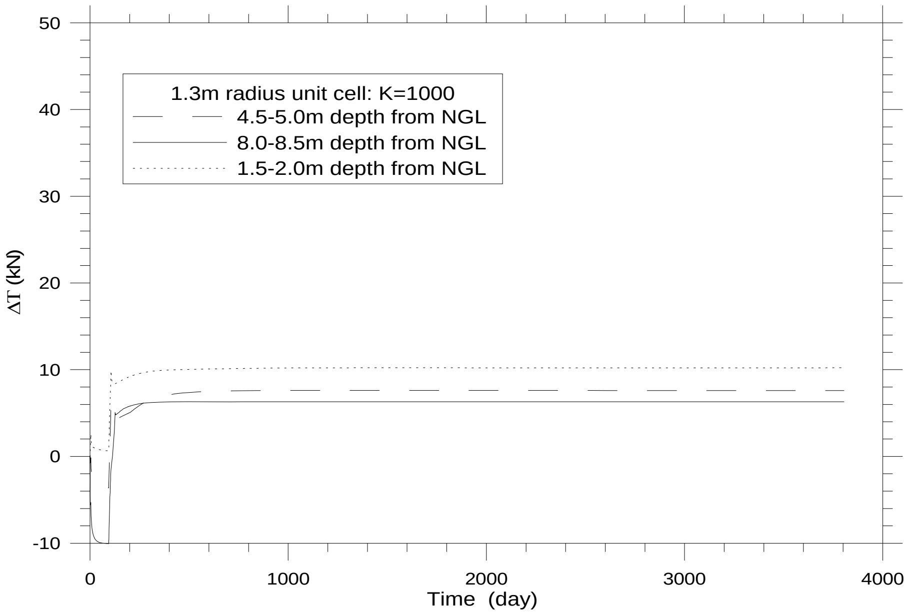

Figure 7.52: Increases in geosynthetic tension with time: reduced stone stiffness K=1000 (1.3m radius unit cell, SSC model applied)

7.6 STONE COLUMN IN SSC SOIL WITH 1.3M UNIT CELL

7.6.1 Reference parameters

Apart from their radii, the dimensions of the 1.3m and 2.0m radius unit cell stone columns are the same (Table 5-1) as are their material parameters (Table 5-2). T_{pre} = 42 kN/m is referred to as the reference analysis. The simulation is conducted using the reference parameters first. Then reducing the T_{pre} value or K by half was examined.

<u>a) Settlement</u>

The numerical simulated evolutions of settlement with time are presented in Figure 7.38(a). Settlements at the top of the stone column and at the edge of the unit cell are about 0.12m and 0.15m respectively at 10 years. The stone column essentially ceases settlement after 800 days. Compared with the corresponding MCC reference analysis, the SSC reference analysis has 25% and 37% higher settlements at the top of the stone column and at the edge of the unit cell respectively.

Settlement profiles at NGL and the top of the fill are plotted in Figure 7.38(b). Differences between settlements at the top of the stone columns and at the edge of the unit cell are larger than that of the MCC reference analysis. Thus, the “bump” between the stone columns and the surrounding soil is a little larger. The settlement profile at the top of the fill remains “bump-free” which is similar to that of the MCC parameters.

b) Force in stone column

Distributions of the computed column forces with depth at the end of construction and after 10 years are presented in Figure 7.39. The maximum column forces at the end of construction and after 10years are about 345 kPa and 500 kPa respectively. Evolutions of the column forces with time are plotted in Figure 7.40 at three depths: near-top, mid-depth and near-toe. At all three depths, the column forces increase with time as the excess pore water pressure disappears from the surrounding soil. The stone column forces approach asymptotic values at about 200, 250 and 350 days at the bottom, middle and top depths respectively.

Compared with the MCC reference analysis, using the same installation method and unit cell spacing:

The maximum value of the column force at the end of construction is 65 kN/m or 23% higher than in the corresponding MCC reference analysis but, after 10 years, it is only 30 kN/m or 6% higher than in the MCC reference analysis. This indicates that, at the beginning, SSC is much weaker than MCC and the stone columns support more of the fill load than they do in the MCC reference analysis. As the consolidation process continues, the SSC gains stiffness thus the stone column can attract more load. Thus, differences in the column forces become less. The time needed for the stone column force to reach its maximum value for the 1.3m radius stone columns is slightly shorter than it is for the corresponding MCC reference analysis.

c) Coupled behaviour

The computed $[\sigma_{z,c}–\sigma_{z,c}(i)]/q$-time and u_{ex}/q-time relationships for three radial locations at the mid-depth of the soft clay are plotted in Figure 7.41 following the same rationale and format as in the MCC reference analysis.

The maximum value of u_{ex}/q is less than 0.65 which can be explained by dissipation occurring during embankment construction. The process of dissipation of the excess pore water pressure ends up at ~600 days at all locations.

The effective stresses at the near-edge and mid-distance locations continuously increase until about 100-200 days. The stable computed $[\sigma_{z,c} – \sigma_{z,c}(i)]/q$ is 0.25 near the stone column and 0.22 at the middle distance. A small strain softening is found at the near-edge location shortly after construction. The $[\sigma_{z,c}-\sigma_{z,c}(i)]/q$ decreases to -0.01 and then increases to 0.006 at about 200 days. This small strain softening happens because the near-edge location is far from the drainage boundary and the typical undrained strain-softening feature of SSC.

The coupling between consolidation and geosyntheic tension is manifested in the ΔT versus time relationships presented in Figure 7.42. The increase of ΔT is small and the ΔT reach the asymptotic value in less than 300 days.

7.6.2 Effects of locked-in stress in geosynthetic

The influence of a lower locked-in force in a stone column is studied by repeating the analysis with T_{pre} reduced to 21 kN/m, while the other parameters and the initial stress state are identical to those of the reference analysis.

a) Settlement and force in stone column

The computed evolutions of settlement with time are presented in Figure 7.43(a) and the settlement profiles at NGL and foundation level are plotted in Figure 7.43(b). The developments of settlement with time and the overall shapes of the settlement profiles follow similar patterns to those of the reference analysis. Settlement at the top of the stone column at 10 years is about 0.145m and that of the soil at the edge of the unit cell 0.175m.Settlement only increases by 17% when the T_{pre} is halved. The computed profile along the top of the fill is still smooth with a settlement value of

0.12m. Considering the 50% drop in the locked-in strain, these settlement values are only slightly higher than that of the reference analysis.

Distributions of the column forces with depth at the end of construction and at 10 years are plotted in Figure 7.44. At the end of construction, they remain nearly the same as those in the reference analysis and their overall shapes at 10 years are similar to those of the reference analysis with slightly smaller values at each location. The maximum stone column force after 10 years is about 12 kN less than that of the reference analysis. The time-dependent nature of stone column forces is illustrated in Figure 7.45 which shows their evolutions with time at three depths. The trends in the figure are quite similar to those of the reference analysis with the maximum force value being about 5% smaller.

b) Coupled behaviour

The computed $[\sigma_{z,c}-\sigma_{z,c}(i)]/q$-time and u_{ex}/q-time relationships for three radial locations at the mid-depth of the soft clay are plotted in Figures 7.46(a) and 7.46(b). The u_{ex}/q–time plots are very similar to those of the reference conditions except that the maximum u_{ex}/q at the beginning is slightly higher. The $[\sigma_{z,c}-\sigma_{z,c}(i)]/q$–time plots are also similar except that the $[\sigma_{z,c}-\sigma_{z,c}(i)]/q$ values increase a little at all the near-column and mid-distance locations. After 10 years, the $[\sigma_{z,c}-\sigma_{z,c}(i)]/q$ values are 0.29 near the edge and 0.26 at the middle distance.

Also, the same shape, of a small strain softening, is found at the near-edge location shortly after construction. The $[\sigma_{z,c}-\sigma_{z,c}(i)]/q$ decreases to -0.011 and then increases to 0.006 at about 200 days.

The coupling between consolidation and geosynthetic tension is manifested in the ΔT versus time relationships presented in Figure 7.47. The increase of ΔT is very small and the ΔT reach the asymptotic value in less than 300 days.

7.6.3 Influence of lower stone stiffness

The influence of lower stone stiffness is examined by repeating the analysis with the Duncan-Chang parameter, K, reduced to 1000, while the initial stress state and all other parameters are identical to those of the reference analysis of the 1.3m radius unit cell. This stiffness value is considered to be relatively low for compacted stones. When using the same loading procedure as in the reference conditions, the simulation is stopped during construction because many SSC elements approach the CS. Thus a waiting time of 90 days after the installation is utilized to enable the simulation to proceed.

<u>a) Settlement and force in stone column</u>

The computed evolutions of settlement with time are presented in Figure 7.48(a) and the settlement profiles at NGL and foundation level are plotted in Figure7.48(b). The overall trends of both the settlement-time plots and settlement profiles are similar to those of the reference analysis. The small curves before 90 days are caused by the "waiting" time. Settlement at the top of the stone column at 10 years is about 0.20m and that of the soil at the edge of the unit cell is 0.24. The computed settlement at the top of the fill is smooth with a value of 0.16 at 10 years. Compared with the reference conditions, the increase in settlement is about 60% while the reduction in stiffness is 50%. This can be explained by less of the fill load being transferred to the stone columns, as shown in Figure 7.49. On average, the stone column forces reduce by about 20 KN less compared with the reference conditions both after construction and at 10 years. The time-dependent nature of stone column forces is illustrated in Figure 7.50 which shows evolutions of the column forces with time at three depths. The trends in this figure are similar to those of the reference conditions but with the ultimate force value being 5-10% smaller. The difference before 90 days is caused by the "waiting" time.

b) Coupled behaviour

The computed $[\sigma_{z,c}-\sigma_{z,c}(i)]/q$-time and u_{ex}/q-time relationships for three radial locations at the mid-depth of the soft clay are plotted in Figure 7.51(a) and Figure 7.51(b). It can be seen that, at the end of the 90-day waiting time, the excess pore water pressure caused by installation is nearly dissipated. Besides differences in the first 90 days, these plots are also quite similar to those in the reference conditions although the dissipation of excess pore water pressure takes more time, about 700 days at all three locations.

The values of $[\sigma_{z,c}-\sigma_{z,c}(i)]/q$ increase when K is halved. The asymptotic value of $[\sigma_{z,c}-\sigma_{z,c}(i)]/q$ is 0.36 at the near-column location. Obvious strain softening is found at the mid-distance and near-edge locations. At the mid-distance location, $[\sigma_{z,c}$

$- \sigma_{z,c}(i)]/q$ increases during the waiting time. A sudden drop in the value of $[\sigma_{z,c} - \sigma_{z,c}(i)]/q$ is found when the waiting period ends and construction recommences. Then, it begins to increase again after the end of construction until it reaches the asymptotic value of 0.27. At the near-edge location, the $[\sigma_{z,c} - \sigma_{z,c}(i)]/q$ value decreases to -0.036 and then increases to 0.034 at about 400 days.

The coupling between consolidation and geosynthetic tension is manifested in the ΔT versus time relationships presented in Figure 7.52 which shows that the increase of ΔT is very small and the ΔT reach the asymptotic value in less than 300 days.

Table 7-1 Simulation results of "full-displacement" stone columns

	settlement @ NGL (m)		Force (kN)		Increase of soil stress (after 10 years)		
	center	edge	EoC	After 10yr	next to column	middle-distance	near edge
MCC - 2.0m							
T_{pre} = 0	0.54	0.56	175	633			
Reference	0.26	0.31	250	775	0.61	0.3	0.3
T_{pre} halved	0.28	0.33	230	770	0.67	0.32	0.2
K halved	0.315	0.36	210	755	0.73	0.33	0.31
MCC -1.3m							
T_{pre} = 0	0.31	0.34	180	355			
Reference	0.09	0.11	285	470	0.26	0.04	0.1
T_{pre} halved	0.11	0.13	259	462	0.33	0.06	0.11
K halved	0.14	0.16	241	448	0.4	0.07	0.11
SSC- 2.0m							
Reference[1]	0.485	0.72	670	900			
SSC- 1.3m							
T_{pre} = 0							
Reference	0.12	0.15	345	500	0.22	0.25	0.006
T_{pre} halved	0.145	0.175	316	488	0.29	0.26	0.012
K halved[2]	0.2	0.24	285	475	0.36	0.27	0.034

Note: 1. Using construction rate of 90 days per meter.

2. Wait 90 days before construction.

7.7 DISCUSSION

7.7.1 Unit cell radius effects in MMC model

a) Geosynthetic encasement without pre-straining

The after 10 years settlement at NGL, stone column force and the increase of soil stress are listed in Table 7-1 for comparing purpose. From the table, the unit cell radius has a significant impact on the performance of geosynthetic encased stone columns. When the geosynthetic encasement has no pre-straining, the settlements at NGL at the centers of the 2.0m and 1.3m radius unit cells are 0.56m and 0.31m respectively. The 45% difference is due to the radius size effect.

At the end of construction, the maximum column force is about 175kN of the 2.0m unit cell radius while the value of the 1.3m radius is 180kN. The difference of the stone column force is very small. After 10 years, the maximum column force of the 2.0m unit cell radius increased to 633kN while the value of the 1.3m radius is only 355kN. The column force of the 2.0m unit cell is significantly higher than that of the 1.3m radius.

b) Reference parameters

The settlements at NGL of the 2.0m radius unit cell with reference parameters are 0.26m at the centre and 0.31m at the edge. The settlement values of the 1.3m radius unit cell with reference parameters are 0.09m at the centre and 0.11m at the edge. The settlement values of 1.3m radius are only about 35% of those of the 2.0m radius.

This comparison shows that reducing the unit cell radius can significantly enhance the performance of stone column.

At the end of construction, the maximum column force is about 250kN of the 2.0m unit cell radius while the value of the 1.3m radius is 285kN. Column force of the 2.0m radius unit cell is slightly smaller than that of the 1.3m radius. After 10 years, the maximum column force of the 2.0m unit cell radius increased to 775kN while the value of the 1.3m radius is only 470kN. The column force of the 2.0m unit cell is significantly higher than that of the 1.3m radius.

Times required for the settlement and stone column forces to reach their ultimate values are significantly reduced. This is due to the dissipation of excess pore water pressure being much faster in the 1.3m size than in the 2.0m size. As shown in Figure 7.3 and Figure 7.18, about 400 days is needed for the excess pore water pressure to dissipate out when the unit cell radius is 1.3m. Significant excess pore water pressure still remains at the mid-distance and edge when the unit cell radius is 2.0m

Increases in the effective stress of the 2.0m radius unit cell are also higher than those of the 1.3m radius unit cell. The $[\sigma_{z,c}-\sigma_{z,c}(i)]/q$ values of the 2.0m radius unit cell are more than 2.3 times higher than those of the 1.3m radius unit cell.

b) Impact on stone stiffness

The performance of stone column of less compacted stones(K reduced to half) also depends on the unit cell radius. The settlements at NGL of the 2.0m radius unit cell are 0.315m at the centre and 0.36m at the edge. The settlement values of the 1.3m radius unit cell with K reduced into half are 0.14m at the centre and 0.16m at the edge. The settlement values of 1.3m radius are about 44% of that of the 2.0m radius. This comparison shows that reducing the unit cell radius can significantly enhance the performance of stone column.

Compare with the reference analysis: When the unit cell radius is 2.0m, increases in settlement are only about 20% at the top of the stone column and 16% at the edge location in spite of a 50% reduction in stiffness; when the unit cell radius is 1.3m, the settlement value increase 55% at the centre and 45% at the edge. This comparison shown that the performance of stone column is sensitive with K when the unit cell radius is 1.3m but not sensitive with K when the radius is 2.0m.

At the end of construction, the maximum column force is about 210kN of the 2.0m unit cell radius while the value of the 1.3m radius is 241kN. Column force of the 2.0m radius unit cell is slightly smaller than that of the 1.3m radius. After 10 years, the maximum column force of the 2.0m unit cell radius increased to 755kN while the value of the 1.3m radius is only 448kN. The column force of the 2.0m unit cell is significantly higher than that of the 1.3m radius.

Increases in the effective stress of the 2.0m radius unit cell are also higher than those of the 1.3m radius unit cell. The $[\sigma_{z,c} - \sigma_{z,c}(i)]/q$ values of the 2.0m radius unit cell are more than 1.8 times higher than those of the 1.3m radius unit cell.

c) Impact of lock-in strain

The performance of a unit cell due to locked-in strain also depends on its radius. The settlements at NGL of the 2.0m radius unit cell are 0.28m at the centre and 0.33m at the edge. The settlement values of the 1.3m radius unit cell with reference parameters are 0.11m at the centre and 0.13m at the edge. The settlement value of 1.3m radius is ~ 40% of that of the 2.0m radius. This comparison shows that reducing the unit cell radius can significantly enhance the performance of stone column.

Compare with the reference analysis: When the unit cell radius is 2.0m, increases in settlement are only about 8% at the top of the stone column and 7% at the edge location in spite of a 50% reduction of T_{pre}; when the unit cell radius is 1.3m, the settlement value increase 22% at the centre and 18% at the edge. This comparison shown that the performance of stone column is not sensitive with T_{pre} for both 2.0m and 1.3m unit cell radius.

At the end of construction, the maximum column force is about 230kN of the 2.0m unit cell radius while the value of the 1.3m radius is 259kN. Column force of the 2.0m radius unit cell is slightly smaller than that of the 1.3m radius. After 10 years, the maximum column force of the 2.0m unit cell radius increased to 770kN while the value of the 1.3m radius is only 462kN. The column force of the 2.0m unit cell is significantly higher than that of the 1.3m radius.

Increases in the effective stress of the 2.0m radius unit cell are also higher than those of the 1.3m radius unit cell. The $[\sigma_{z,c}-\sigma_{z,c}(i)]/q$ values of the 2.0m radius unit cell are more than two times higher of those of the 1.3m radius unit cell.

7.7.2 Unit cell radius effects of in SSC model

The geosynthetic encased stone column cannot work when installed in the 2.0m spacing buy the full displacement installation method. When the unit cell radius is 1.3m, the geosynthetic encased stone column can still performs well in reference analysis and T_{pre} halved conditions. The “full-displacement” stone columns in 1.3m radius unit cell can afford the lock-in strain being halved but not the stiffness of the stone. This is because the confining stress generated by the full displacement installation method reduces the impact of the reduction in locked-in strain.

7.7.3 Impact of Soil models

In this sub-section, the performance changes of a stone column installed in SSC will be examined. The comparison is based on the calculation results from the above conditions using both the MCC and SSC models. Since “full-displacement” stone columns installed in SSC soil does not work for 2.0m radius unit cell, only the 1.3 m radius unit cell cases are compared.

Comparing the 1.3m unit cell radius reference analysis, settlement at the top of the stone column at 10 years is about 0.09m in the MCC case and 0.12m in the SSC case. Settlement at NGL at the edge of the unit cell at 10 years is about 0.11m in the MCC case and 0.15m in the SSC case. Settlement of SSC is higher mainly because SSC is softer than MCC with the same parameters.

When the T_{pre} is reduce into half of the reference parameters, settlement at NGL at the edge of the unit cell increases by about 20% when using MCC and by about 17%

when using SSC. This comparison shows that the impact of a reduction in the T_{pre} is about the same in both soil models.

Significant strain softening may happen at the mid-distance and near-edge locations when using the SSC model. Undrained strain softening may disappear when the consolidation process continues. Dissipation of the pore water pressure makes these SSC elements change from an undrained strain-softening state to a drained strain-hardening state.

7.8 CONCLUSION

From the above discussion, it can be concluded that:

1. The stone column radius weight has a significant impact on the performance of the stone column. The reduce of unit cell radius and significantly increase the performance of the stone column.
2. When the radius of the unit cell is 2.0m, the performance of stone column is not sensitive to either the locked-in strain or the stiffness of the stone.
3. When the radius of the unit cell is 1.3m, the performance of a stone column is more closely related to the stiffness of the stone rather than to the lock-in strain.
4. Strain softening may happen in SSC which may cause failure of stone column if the T_{pre} and the stiffness of the stone is not high enough or if its radius is too large.

CHAPTER EIGHT

OVERALL DISCUSSION OF STONE COLUMN INSTALLATION METHOD

8.1 INTRODUCTION

From the simulation results of Chapter 5 and Chapter 7, it can been seen that many factors can affect the performance of the geosynthetic encased stone columns installed in highly compressible soft clay. These factors includes:

1. The installation methods.
2. The pre-straining of the geosynthetic.
3. The stiffness of the stone in the stone columns.
4. The spacing between the stone columns installed.
5. The soft clay behaviours as reflected by using MCC or SSC model.

Comparison of the factors 2 to 5 within the wish-in installation method and full displacement installation method have been made in Chapter 5 and Chapter 7 respectively. This Chapter is comparing across Chapter 5 and Chapter 7 to discuss the effects of installation methods.

Differences between the wish-in installation method and the full displacement installation method are that the latter generated higher excess water and extra confining stress to the stone columns installed. The radius stress generated by the full displacement installation method can help the stone column to attract more fill load and reduce the total settlement of the soil. However the excess pore water pressure in the soil can cause the soil to consolidate more and thus increases its settlement. Furthermore, in some circumstances, the high excess pore water pressure generated by the full displacement method may cause failure of the soil if the soil is sensitive.

To classify the effect of the extra radial stress and excess pore water pressure generated by the full displacement installation method, detailed discussion is made in this Chapter by investigating a range of situations such as T_{pre} , K etc. Though this discussion, the performance of the stone column under varies conditions are compared for different installation methods. The circumstances that the stone columns can or can not effectively reduce the settlement and the consolidation time are made clear.

8.2 STONE COLUMNS IN MCC SOIL

8.2.1 2.0m spacing

<u>a) Geosynthetic encasement without pre-straining</u>

As shown in table 5-4 and table 7-1, when the geosynthetic encasement has no pre-straining, the radial stress generated by the full displacement installation method plays a significant role in the performance of stone column. When the wish-in installation method is adopted, the settlement at NGL after 10 years at near the edge of the unit cell 0.78m and at the top of the stone column is about 0.77m. When the full displacement installation method is used, the settlement of soil at the edge of unit cell at NGL reduce to 0.56m and at the top of the stone column is about 0.54m after 10 years. Since the excess pore water pressure generated by the full displacement method cannot help to reduce the settlement, the 25-30% reduction of settlement is due to the effects of the confining stress provided by the surrounding soil of the columns.

The significant difference of the settlement after 10 years can be further explained in the difference of the stone column force. When the wish-in installation method is used, the maximum stone column force is only about 448kN after 10 years. While when the full displacement installation method is used, the maximum stone column force is about 633kN after 10 years. It is clear that when the full displacement installation method is used, the extra radial stress generated by the installation method provides reinforcement for the stone columns. Thus the stone columns attract more fill load and reduce the long time unit cell settlement.

b) Reference parameters

The geosynthetic reinforcement of the reference parameters has a pre-straining defined by T_{pre}= 100 kN/m. When the wish-in installation method is used, the settlement at the edge of NGL was 0.3m; When the full displacement installation method is used, the settlement is 0.31m . From the results, it is clear that a high pre-straining(T_{pre}= 100 kN/m) can significantly reduce the settlement despite of which installation methods are used. There is slightly more settlement for full displacement method than that of the wish-in installation method. This is caused by the radial stress from full displacement installation method is less important as T_{pre} also provide confining stress. Furthermore, the excess pore water pressure generated by the full displacement installation method is providing extra settlement.

The values of the stone column force are also different in the reference analysis when the two installation methods are used. After installation, the value of force in the stone column of the full displacement method is significantly higher than the wished-in installation method. The value of the former is about 250kN while the value of the later is only about 198kN. The difference is due to radial stress generated by the full displacement installation method. The confining stress strengthen the geosynthetic encased stone column thus more fill load transferred to the stone column during the construction period. Meanwhile, after 10 years, the stone column force of wish-in installation method is about 750kN, and the value of full displacement installation method is about 775 kN. The difference of the stone column force is reducing as the consolidation process continues. Therefore the column force after 10 years for the two different installation method is essentially identical. This is consistent with the tiny difference of the settlement at NGL after 10 years.

c) T_{pre} reduced into half of reference parameter

When wish-in installation method is used, the after 10 years settlement is 0.4m on top of stone column and 0.445m at the edge of unit cell at NGL. When full displacement installation method is used, the settlement value is 0.28m on top of stone column and 0.33m at the edge of unit cell. The settlement of full displacement installation method is much less than that of the wish-in installation method. One possible explanation of the less settlement of the full displacement method is that the confining stress to the column generated by the installation method strengthens the stone columns.

When wish-in installation method is used, the maximum column force is 180kN at the end of construction and 676kN after 10 years. When full displacement installation method is used, the maximum column force is 230kN at the end of construction and 770kN after 10 years. The stone column force of the full displacement installation method is much larger than the wish-in installation method at both end of construction and after 10 years. This demonstrate that the confining stress strengthen the stone column and attracts more fill load. The higher column force is consistent with the less settlement at NGL after 10 years.

<u>d) K reduced into half of reference parameter</u>

When wish-in installation method is used, the after 10 years settlement is 0.297m on top of stone column and 0.35m at the edge of unit cell at NGL. When full displacement installation method is used, the settlement value is 0.315m on top of stone column and 0.36m at the edge of unit cell. The settlement of after 10 years for the two different installation method is essentially identical. The influence of the installation method is not important when K reduced into half of reference parameter.

When wish-in installation method is used, the maximum column force is 160kN at the end of construction and 740kN after 10 years. When full displacement installation method is used, the maximum column force is 210kN at the end of construction and 755kN after 10 years. The stone column force of the full displacement installation method is much larger than the wish-in installation method at end of construction. The difference is due to radial stress generated by the full displacement installation method. The difference of the stone column force is reducing as the consolidation process continues. Therefore the column force after 10 years for the two different installation method is essentially identical. This is consistent with the tiny difference of the settlement at NGL after 10 years.

e) Summary

1. when the geosynthetic encasement does not have pre-straining, the confining stress to the column generated by the full displacement method plays a significant role.
2. the influence of installation method is negligible for the reference parameters and K reduced into half conditions
3. When T_{pre} = 50 kN/m, the settlement of the "full-displacement" is significantly less than that of the "wish-in".
4. The "wish-in" stone columns is sensitive with the T_{pre} while the "full-displacement" stone columns is not. Both installation methods are not sensitive will the reduction of K.

8.2.2 1.3m spacing

a) Geosynthetic encasement without pre-straining

When the geosynthetic encasement had no pre-straining, the radial stress generated by the full displacement installation method plays a significant role in the performance of stone column. When the wish-in installation method is adopted, the settlement at NGL after 10 years at near the edge of the unit cell 0.48m and at the top of the stone column is about 0.47m. When the full displacement installation method is used, the settlement of soil at the edge of unit cell at NGL reduce to 0.34m and at the top of the stone column is about 0.33m after 10 years. Since the excess pore water pressure generated by the full displacement cannot help reduce the settlement, the ~30% reduce of settlement is due to the effects of the confining stress provided by the surrounding soil of the columns.

The significant difference of the settlement after 10 years can be further explained in the difference of the stone column force. When the wish-in installation method was used, the maximum stone column force is only about 280kN after 10 years. While when the full displacement installation method was used, the maximum stone column force is about 355kN after 10 years. It is clear that when the full displacement installation method is used, the extra radial stress generated by the installation method provide reinforcement for the stone columns. Thus the stone columns attract more fill load and reduce the long time unit cell settlement.

<u>b) Reference parameters</u>

The geosynthetic reinforcement of the reference parameters has a pre-straining defined by T_{pre}= 42 kN/m. When the wish-in installation method is used, the settlement at the edge of NGL was 0.126m; When the full displacement installation method is used, the settlement is 0.11m. There is slightly less settlement for full displacement method than that of the wish-in installation method. This is caused by the radial stress from full displacement installation method reinforced the stone columns and reduce the settlement.

The value of the stone column force are also different in the references parameters when the two installation methods are used. After installation, the value of force in the stone column of the full displacement method is significantly higher than the wished-in installation method. The value of the former is about 180kN while the value of the later is only about 142kN. After 10 years, the stone column force of wish-in installation method is about 375kN, and the value of full displacement installation method is about 470 kN. In both after construction and after 10 years, the column force of the “full-displacement” is higher than that of “wish-in”. The difference is due to radial stress generated by the full displacement installation method. It strengthen the stone columns so as to attract more fill load.

c) T_{pre} dropped into half

When wish-in installation method is used, the after 10 years settlement is 0.12m on top of stone column and 0.14m at the edge of unit cell at NGL. When full displacement installation method is used, the settlement value is 0.11m on top of stone column and 0.13m at the edge of unit cell. The settlement of full displacement installation method is less than that of the wish-in installation method.

When wish-in installation method is used, the maximum column force is 200kN at the end of construction and 371kN after 10 years. When full displacement installation method is used, the maximum column force is 259kN at the end of construction and 462kN after 10 years. The stone column force of the full displacement installation method is much larger than the wish-in installation method at both end of construction and after 10 years. This demonstrate that the confining stress strengthen the stone column and attracts more fill load. The higher column force is consistent with the less settlement at NGL after 10 years.

d) K reduced into half of reference parameter

When wish-in installation method is used, the after 10 years settlement is 0.15m on top of stone column and 0.17m at the edge of unit cell at NGL. When full displacement installation method is used, the settlement value is 0.14m on top of stone column and 0.16m at the edge of unit cell. The settlement of full displacement installation method is less than that of the wish-in installation method.

When wish-in installation method is used, the maximum column force is 173kN at the end of construction and 360kN after 10 years. When full displacement installation method is used, the maximum column force is 241kN at the end of construction and 448kN after 10 years. The stone column force of the full displacement installation method is much larger than the wish-in installation method at both end of construction and after 10 years. This demonstrate that the confining stress strengthen the stone column and attracts more fill load. The higher column force is consistent with the less settlement at NGL after 10 years.

e) Summary

1. When the geosynthetic encasement does not have pre-straining, the confining stress to the column generated by the full displacement method plays a significant role.
2. The settlement of the "full-displacement" is less than "wish-in" in reference parameters and all other three conditions.
3. Stone column force of the "full-displacement" is higher than the "wish-in" at both end of construction and after 10 years for all conditions discussed above.
4. Both installation methods are not sensitive to the change of K but not sensitive to the change of T_{pre}.

8.2.3 The influence of stone column spacing

From table 5-4 and table 7-1, the following facts can be drawn when the radius of unit cell reduce from 2.0m to 1.3m:

1. no matter which installation methods are used, the performance of the stone columns significantly increase.
2. when the geosynthetic has no pre-straining, the reduction of settlement is about 40% for both installation methods.
3. in the reference parameters conditions, the reduction of settlement of "wish-in" installation method is 58% and that of "full-displacement" is 65%. Unit cell size effect is more obvious in "full displacement" than "wish-in".

4. when T_{pre} reduced into half, the reduction of settlement is about 60% for both installation methods.
5. When K reduce into half, the reduction of settlement of "wish-in" installation method is 60% and that of "full-displacement" is 55%. Unit cell size effect is slightly obvious in "wish-in" than "full-displacement".

8.3 STONE COLUMNS IN SSC SOIL

Because of the features of the SSC soil, the stone column installed with the full displacement method generate more excess pore water pressure and less confining stress for the stone columns compare with that of MCC soil. This high excess pore water pressure may cause the SSC soil elements fail as discussed in Chapter 7. The failure of the SSC soil element depends on the spacing of the unit cell, the excess pore water pressure in the SSC soil before the construction etc.

8.3.1 2.0m spacing

When the stone column was installed by the wish-in method, the geosynthetic encased stone column performed well. The settlement of the soil at NGL is about 10-20% higher than the stone column installed in the MCC soil in general. The performance of the stone column is sensitive with the $T_{pre.}$ The settlement increase 45% when the T_{pre} reduced into half of the reference parameter. The performance of the stone column is not sensitive with the stiffness of stone. When K reduced to half , the settlement increase ~ 10%. Strain softening phenomena can be found during and shortly after the fill loading in all above conditions.

When the stone column installed by the full displacement installation method with reference parameters. Large number of soil elements will fail if the construction is done immediately after the installation. This is because of high excess pore water pressure generated by the full displacement installation method and the strain softening feature of the SSC soil. When alternative construction rate(waiting 3 month after one meter construction) to dissipate some of the excess pore water pressure generated by the full displacement installation method, the settlement is 0.48m on top of stone column and 0.72m at edge of unit cell at NGL. The settlement value is more than double of that of the “wish-in”. Since the “waiting 3 month after one meter construction” is a very slow construction rate, it is highly likely that the geosynthetic encased stone column cannot work properly if installed in the SSC soil with the full depth full displacement method.

In a word, for the SSC 2.0m radius unit cell conditions, the “wish-in” stone columns perform well while the “full-displacement” stone columns are unlikely to work.

8.3.2 1.3m spacing

When the unit cell spacing is 1.3m, the stone column installed with the wished-in installation method function well of all analysed cases. When the full displacement installation method is used, the no pre-straining and the K reduced into half of reference parameter conditions will fail shortly after the end of construction. Thus in this sub-section, compassion of “wish-in” and “full-displacement” stone columns will be restricted to reference parameters and T_{pre} reduced into half.

a) Reference parameters

Considering the size effect, the T_{pre} of the reference parameters condition of 1.3m unit cell spacing is 42kN/m. The after 10 years settlement at the edge of unit cell at NGL is about 0.13m when the wished-in installation is used. When the full displacement installation method is used, the settlement value is about 0.15m. The value is slightly higher than that of the “wish-in” stone columns. The consolidation process of the full displacement installation method takes slightly longer time. This may due to the excess pore water pressure generated by the installation method.

Although the settlement after 10 years is about nearly the same, the force in the settlement of the two installation method have obvious difference. After 10 years, the maximum stone column force of the full displacement installation method is about 500 kN while the value of the wished-in installation method is only about 420 kN. The stone column installed by the full displacement installation method generate confining stress which help the stone columns attracts more fill load. The reason why the settlement is still about the same as that of the “wished-in” columns is that the extra excess pore water pressure of the “full-displacement” columns cause more settlement.

b) T_{pre} reduced to half of reference parameter

When wish-in installation method is used, the after 10 years settlement is 0.135m on top of stone column and 0.16m at the edge of unit cell at NGL. When full displacement installation method is used, the settlement value is 0.145m on top of stone column and 0.175m at the edge of unit cell. The settlement of full displacement installation method is slightly higher than that of the wish-in installation method.

When wish-in installation method is used, the maximum column force is 215kN at the end of construction and 410kN after 10 years. When full displacement installation method is used, the maximum column force is 316kN at the end of construction and 488kN after 10 years. The stone column force of the full displacement installation method is much larger than the wish-in installation method at both end of construction and after 10 years.

8.3.3 The influence of stone column spacing

From table 5-4 and table 7-1, the following facts can be drawn when the radius of unit cell reduce from 2.0m to 1.3m:

1. Despite which installation methods are used, the performance of the stone columns significantly increase.
2. When the geosynthetic has no pre-straining, the reduction of settlement is about 40% for “wish-in” columns; The “full-displacement” columns not work for both unit cell radius.

3. In the reference parameters conditions, the reduction of settlement of “wish-in” installation method is 60%. The “full-displacement” columns turn from not work to work.
4. When T_{pre} reduced into half, the settlement of “wish-in” columns reduce ~70%. The “full-displacement” columns cannot work in 2.0m radius but work in 1.3m radius.
5. When K reduce into half, the settlement of “wish-in” columns reduce ~70%. The “full-displacement” columns not work for both unit cell radius.

8.4 CONCLUSION ON INFLUENCE OF INSTALLATION METHODS

<u>a) 2.0 m unit cell spacing</u>

1. When the geosynthetic encasement has no pre-straining, the settlement of the “full-displacement” columns is significantly less than that of the “wish-in” columns if the soil is MCC.
2. For both installation methods, the performance of stone columns is not sensitive with the stiffness of stone when soil is MCC.
3. The performance of “wish-in” stone column is sensitive with T_{pre} while the “full-displacement” stone column is not when the soil is MCC.
4. The “full-displacement” stone column does not work for the SSC soil and the “wish-in” stone column works well.

<u>b) 1.3 m unit cell spacing</u>

1. When the geosynthetic encasement has no pre-straining, the settlement of the "full-displacement" columns is significantly less than that of the "wish-in" columns if the soil is MCC.
2. For both installation methods, the performance of stone columns is sensitive with the stiffness of stone when soil is MCC.
3. For both installation methods, the performance of stone columns is not sensitive with T_{pre} , no matter the soil is MCC or SSC
4. If high quality stone is not used, the "full-displacement" stone column may not function well if installation in SSC soil.

<u>c) Unit cell size effects</u>

1. For both installation methods, the settlement and stone column force reduce when the unit cell radius reduce from 2.0m to 1.3m.
2. The size effects are not sensitive to the stiffness of stone and T_{pre} when the wished-in installation method is used. The size effects are sensitive to the stiffness of stone and T_{pre} when the full displacement installation method is used.

CHAPTER NINE

CONCLUSION AND RECOMMENDATIONS

9.1 SUMMARY

A constitutive model was developed to simulate the typical features of soft sensitive clay: a curved e-lnp for ICL, strain softening in the undrained shearing and strain hardening in drained shearing. A set of incremental differential $\sigma - \varepsilon$ equations were deducted. These incremental differential equations can be solved in a spread sheet for various triaxial conditions. Thus a series of bench mark analyses which was done with the excel worksheet to check the ability of the SSC model in predicting triaxial behaviors. The numerical model was then incorporated into a fully-coupled Biot consolidation analysis and this was then was implemented into a general purpose FE code AFENA. These bench mark analyses were repeated using the FE code as a verification process.

Since the effectiveness of stone column installed in the SSC soil was questioned by a recent field trial, the performance of stone column in SSC was selected as the problem for the application of the SSC model and corresponding coupled FE analysis. Stone column element and geosynthetic encasement element are developed and coded into AFENA program. The problem was idealised by a unit-cell analysis. The FE analyses include: i) two soil models for the very soft clay, MCC and SSC; and ii) two different column spacing as represented by different unit cell radii were analysed.

Both wish-in installation method and full displacement installation method were examined. Different stone stiffness and pre-strain level are also checked to examine sensitive of the changes of these factors. Detailed comparison was then done after the simulation of different spacing, soil properties and installation method are done. Circumstances that the geosynthetic encased stone column cannot perform well in SSC soil is clarified and detail explanation are made.

9.2 CONCLUSIONS

9.2.1 From the simulation of bench mark cases done by both finite difference and coupled Finite element analysis.

1. The SSC model can simulate the typical features of the SSC soils.
2. There is no significant difference between FEM simulation results and simulation results of FD method for triaxial test simulations. No obvious numerical problem occurred when SSC soil parameters are selected to simulate a "transitioned" to MCC soil. Thus the FEM code of SSC model implemented into AFENA can be used for the simulation of the SSC soils.

9.2.2 From coupled FEM analysis of geosynthetic encased stone column.

3. The geosynthetic encased stone columns can serve the function of reducing the settlement and consolidation time of the soil under embankment if the soils are not SSC soils or if the wish-in installation method is used.

4. When the stone column was installed by the full displacement installation method, the geosynthetic encased stone columns only work only if the spacing between the stone columns is not large and the pre-straining of geosynthetic encasement is high enough and the stiffness of the stone column is corresponding to that of well compacted high quality stones.

9.3 RECOMMENDATIONS FOR FUTURE RESEACH

a) Field trial embankment verification

Numerical simulation is done in this thesis, but this simulation results are not verified by field data. Thus trial embankment will be need to be built, and long term settlement need to be measured to compare with the numerical simulation results. It is also of utmost important to have high quality sampling and laboratory testing for the trial site so that input parameters for FE prediction can be objectively established.

b) Numerical modelling

Since creep is very importance for the long time performance of the SSC soils, the SSC model may need to be extended to consider the creep effects of the soft soils.

REFERENCE

Adachi, T., F. Oka and M. Koike (2005). "An elasto-viscoplastic constitutive model with strain-softening for soft sedimentary rocks." Soils and Foundations 45(2).

Adachi, T., F. Oka and F. Zhang (1998). "An elasto-viscoplastic constitutive model with strain softening." Soils and Foundations 38(2): 27-35.

Alexiew, D., D. Brokemper and S. Lothspeich (2005). "Geotextile Encased Columns (GEC): load capacity, geotextile selection and pre-design graphs." Proceedings of GeoFrontiers , Austin, Texas, United States: 497-510.

Ambily, A. P. and S. R. Gandhi (2007). "Behavior of stone columns based on experimental and FEM analysis." Journal of geotechnical and geoenvironmental engineering 133(4): 405-415.

Asaoka, A., M. Nakano and T. Noda (2000). "Superloading yield surface concept for highly structured soil behavior." Soils and Foundations 40(2): 99-110.

Asaoka, A., M. Nakano, T. Noda and K. Kaneda (2000). "Delayed compression/consolidation of natural clay due to degradation of soil structure." soil and Foundations 40(3): 75-85.

Ayadat, T. and A. M. Hanna (2005). "Encapsulated stone columns as a soil improvement technique for collapsible soil." Ground Improvement 9(4): 137-147.

Barksdale, R. D. and R. C. Bachus (1983). "Design and Construction of Stone Columns, Volume I." Washington D.C, Federal Highway Administration, Office of Engineering and Highway Operations, Research and Development.

Baudet, B. and S. E. Stallebrass (2004). "A constitutive model for structured clays." Geotechnique 54(4): 269-278.

Baumann, V. and G. E. A. Bauer (1974). "The performance of foundations on various soils stabilised by the vibro-compaction method." Can. Geotech. Journal 3(11): 509-530.

Black, J. A. and J. Brown (2006). Ground improvement by vibrated stone columns - ‘Case histories within Ireland’. The proceedings of the 9th Young Geotechnical Engineers Conference. ‘Geotechnical Engineering - New Frontiers and Challenges’, Belfast, Northern Ireland.

Britto, A. M. and M. J. Gunn (1987). "Critical state soil mechanics via finite elements." Ellis Horwood Ltd., Chichester, England.

Bruce, D. A. and M. ASCE (1996). "The Return of Deep Soil Mixing." Civil Engineering-ASCE 66(12): 44-46.

Burland, J. B. (1990). "On the compressibility and shear strenth of natural clays." Geotechnique 40(3): 329-378.

Burland, J. B., S. Rampello, V. N. Georgiannou and G. Calabresi (1996). "A laboratory study of the strength of four stiff clays." Geotechnique 46(3): 491-514.

Butterfield, R. (1979). "A natural compression law for soils(an advance on e-log p')." Geotechnique 29: 469-480.

Callisto, L., A. Gajo and D. Muir Wood (2002). "Simulation of triaxial and true triaxial tests on natural and reconstituted Pisa clay." Geotechnique 52(9): 649-666.

Castro, J. and C. e. Sagaseta (2009). "Consolidation around stone columns. Influence of column deformation." International Journal for Numerical and Analytical Methods in Geomechanics 33: 851-877.

Callisto, L. and S. Rampello (2002). "Shear strength and small-strain stiffness of a natural clay under general stress conditions." Geotechnique 52(8): 547-560.

Carter, J. P. and N. P. Balaam (1995). "AFENA." A general finite element algorithm: user's manul. Centre of Geotechinical Research, Univercity of Sydney, NSW, 2006, Australia.

Chai, J. C., J. P. Carter, N. Miura and K. Hino (2004). "Coefficient of consolidation from piezocone dissipation test result." Proc. of Inter. Symp. on Lowland Technology. Bangkok, ISLT2004: 1-6.

Chai, J. C., N. Miura and K. Onitsuka (2004). "Adsorption characteristics of Ariake clays to Chromium and the effect of pH-value." Proc. of 9th Australia New Zealand Conference on Geomechanics. 1: 467-472.

Chang, M. F., V. Choa, L. F. Cao and M. B.W (1997). "Overconsolidation ratio of a seabed clay from In-situ Tests." In proceeding of the 14th international conference on soil mechanics and foundation engineering, Hamburg 1(453-456).

Chazallon, C. and P. Y. Hicherp (1998). "A constitutive model coupling elastoplasticity and damage for cohesive-frictional materials " Mechanics of Cohesive-frictional Materials 3: 41- 63.

Chen, Y. M., X. W. Tang and J. Wang (2004). "An analytical solution of one-dimensional consolidation for soft sensitive soil ground." International Journal of Numerical and Analytical Methods in Geomechanics 28: 919-930.

Christoulas, St., Giannaros Ch., Tsiambaos G (1997). "Stabilization of embankment foundations by using stone columns. Geotechnical and Geological Engineering," 15(3), 247-258

Chu, J., M. W. Bo and V. Choa (2004). "Practical considerations for using vertical drains in soil improvement projects." Geotextiles and Geomembranes 22: 101-117.

Chu, J., S.-C. R. Lo and I. K. Lee (1992). "Strain-softening behaviour of granular soil in strain path testing. ." J. Geotech. Engng, ASCE 118(2): 191-208.

Chu, J., W. B. Myint, M. F. Chang and V. Choa (2002). "Consolidation and permeability properties of Singapore marine clays." Journal of Geotechnical and Geoenvironmental Engineering 128(9): 724-732.

Chu, J., S. W. Yan and H. Yang (2000). "Soil improvement by the vacuum preloading method for an oil storage station." Geotechnique 50(6): 625-632.

Cotecchia, F. (2003). "Mechanical behaviour of the stiff clays from the Montemesola Basin in relation to their geological history and structure." Proceedings of the international conference on characterisation and engineering properties of natural soils,Lisse: Swets & Zeitlinger 2: 817-850.

Cotecchia, F., F. CAFARO and B. Aresta. (2007). "Structure and mechanical response of sub-Apennine Blue Clays in relation to their geological and recent loading history." Geotechnique 57(2): 167-180.

Cotecchia, F. and R. J. Chandler (2000). "A general framework for the mechanical behaviour of clays." Geotechnique 50(4): 431-447.

Dennes, T. B., A. S. Balasubramaniam, F. R. Jonathan and D. H. Robert (2002). "Prefabricated vertical drains(PVD) in soft bangkok clay: a case study of the new bangkok international airport project." Can. Geotech. J 39: 304-315.

Duncan, J. M. and C. Chang (1970). "Nonlinear analysis of stress and strain in soils." Journal of Soil Mechanics and Foundations Division, ASCE 96: 1629-1653.

FHWA (1983) Design and construction of stone columns. FHWA Report No. RD-83/026, 194p.

Garga, V. K. and L. V. medeiros (1995). "Field performance of the port of Sepetiba test fills." Can. Geotech. Journal 32(1): 106-121.

Greenwood, D. A. (1991). "Load tests on stone columns. In Deep foundation improvements: design, construction and testing," ASTM STP1089, Philadelphia: 148-171.

Han, J. and S. L. Ye (2001). "Simplified metod for consolidation rate of stone column reinforced foundations." Journal of geotechnical and geoenviromental engineering, ASCE 127(7): 597-603.

Hawlader, B. C., B. Muhunthan and G. Imai (2008). "State-dependent constitutive model and numerical solution of self-weight consolidation." Geotechnique 58(2): 133-141.

Hird, C. C., I. C. Pyrah and D. Russell (1992). "Finite element modelling of vertical drains beneath embankments on soft ground." Geotechnique 42(3): 499-511.

Hong, Z., S. Liu, S. Shen and T. Negami (2006). "Evaluation of Sample Quality of Sensitive Clay Using Intrinsic Compression Concept." Journal of geotechnique and geoenviroment engineering 132(2): 272-275.

Hu, L. M. and J. L. Pu (2004). "Testing and modeling of soil-structure interface." J. Geotech. Geoenviron. Eng. ASCE 130(8): 851-860.

Hughes, J. M. O., N. J. Withers and D. A. Greenwood (1975). "A field trial of the reinforcing effect of a stone column in soil." Geotechnique 25(1): 31-44.

Indraratna, B., A. S. Balasubramaniam and P. Ratnayake (1994). "Performance of Embankment Stabilized with Vertical Drains on Soft Clay." ASCE, Journal of Geotechnical Engineering 120(2): 257-273.

Kavvadas, M. (1995). "A plasticity approach to the mechanical behaviour of bonded soils." Proc. 4th Int. Conf. on Computational Plasticity, Barcelona,Spain.

Kavvadas, M. and A. Amorosi (2000). "A constitutive model for structured soils." Geotechnique 50(3): 263-273.

Kempfert, H. G. and M. Raithel (2002). "Experiences on Dyke Foundations and Land Fills on Very Soft Soils." Proc. Intern. Workshop ISSMGE - Techn.

Committee TC 36 “Foundation in Difficult Soft Soil Conditions”. Mexico City, SMMS.

Kerry R., C. J. Gnanendran, A. Landva and A. Valsangkar (1996). "Construction and performance of a full scale geotextile reinforced test embankment - Sackville, New Brunswick." Canadian Geotechnical Journal 32(3): 512-534.

Kimoto, S., F. Oka and Y. Higo (2004). "Strain localization analysis of elasto-viscoplastic soil considering structural degration." Comput. Methods Appl. Mech. Engineering 193: 2845-2866.

Konrad, J. M. and R. Ayad (1997). "Desiccation of a sensitive clay:Field experimental observations." Can. Geotech. Journal 34: 929-942.

Ladd, C. C. and R. Foot (1974). "New design procedure for stability of soft clays." Journal of Geotechnical and Geoenvironmental Engineering, ASCE 100(7): 763-786.

Lagioia, R. and R. Nova (1995). "An experimental and theoretical study of the behaviour of a calcarenite in triaxial compression." Geotechnique 45(4): 633-648.

Lambe, T. W. and R. V. Whitman (1969). "Soil Mechanics, ." Wiley, New York, .

Leroueil, S. and D. W. Hight (2002). "Mechanical behaviour and properties of natural soils and soft rocks." Proc. Int. Workshop on Characterisation and Engineering Properties of Natural Soils, Singapore.

Leroueil, S., F. Kabbaj, F. Tavenas and R. Bouchardr (1985). "Stress - strain - strain rate relation for the compressibility of sensitive natural clays." Geotechnique 35: 159-180.

Leroueil, S. and P. R. Vaughan (1990). "The general and congruent effects of structure in natural soils and weak rocks." Geotechnique 40(3): 467-488.

Liu, M., S. Horpibulsuk, J. Suebsook and A. Chinkulkijniwat (2007). "A theoretical study of the behaviour of clays in reconstituted, naturally structured and cemented states." Proceedings of International Symposium on Engineering, Ground Improvement and Geosynthetics for Human Security and Environmental Preservation, Bangkok,Thailand. 469-493.

Liu, M. D. and J. P. Carter (1999). "Virgin compression of structure soils." Geotechnique 49(1): 43-57.

Liu, M. D. and J. P. Carter (2000). "Modelling the destructuring of soils during virgin compression." Geotechnique 50(4): 479–483.

Liu, M. D. and J. P. Carter (2002). "A structured Cam clay model." can.Geotech 39: 1313-1332.

Liu, M. D. and J. P. Carter (2003a). "A general strength criterion for geo-materials " International J. of Geomechanics, ASCE 3 236-252.

Liu, M. D., J. P. Carter (2003b). "Modelling the compression behaviour of geo-materials " International J. of Geomechanics, ASCE 3(3/4): 191-204

Liyanapathirana, D. S. and H. G. Poulos (2005). "Seismic Lateral Response of Piles in Liquefying Soil." Journal of Geotechnical and Geoenvironmental Engineering 131(12): 1466-1479.

Lo S. R., Mak J. and R. Zhang. (2007). "Geosynthetic Encased Stone Columns in Soft Clay." Proc of International symposium on earth reinforcement, Kyushu, Taylor and Francis: 751-756.

Locat, J. and G. Lefebvre (1985). "The compressibility and sensitivity of an artificially sedimented clay soil: The Grande-Baleine marine clay, Quebec." Canada. Marine Geotechnology 6: 1-28.

Lohani, T. N., K. Matsushima, U. Aqil, Y. Mohri and F. Tatsuoka (2006). "Evaluating the strength and deformation characteristics of a soil bag pile from full-scale laboratory tests." Geosynthetics International 13(6): 246–264.

Lumb, P. and J. Holt (1968). "Undrained Shear Strength of A Soft Marine Clay From Hong Kong." Geotechnique 18(1): 25-36.

Marshall, T. and H. JW (1979). "Soil Physics." Cambridge University Press

Masia Mark John, Kleeman Peter Wallace and M. R. Erich (2004). "Modelling Soil/Structure Interaction For Masonry Structures." Journal of Structural Engineering 130: 641-649.

McKenna, J. M., W. A. Eyre and D. R. Wolstenholme (1975). "Performance of an embankment supported by stone columns in soft ground." Geotechnique 25(1): 51-59.

Mesri, G. (1975). "Discussion: New design procedure for stability on soft clays by Ladd and Foott." ASCE Journal of the Geotechnical Engneering Division 101(GT4): 409-412.

Mitchell, J. K. and T. R. Huber (1985). "Performance of a stone column foundation." Journal of Geotechnical Engineering, ASCE 11(2): 205-223.

Murugesan, S. and K. Rajagopal (2006). "Geosynthetic encased stone columns: Numerical Evaluation." Journal Geotextiles and Geomembranes 24: 349-358.

Noda, T., M. Tashiro, T. Takaine and A. Asaoka (2005). "Deformation analyses of piled paft foundation in terms of settlement reduction and load sharing ratio " Japan society of civil engineers 799: 37-49.

Nova, R. (1977). "On the hardening of soils." Archiw. Mech. Stos. 29(3): 445-458.

Oh, E. Y. N., A. S. Balasubramaniam, C. Surarak, M. Bolton, G. W. K. Chai, M. Huang and M. Braund (2007a). "Behaviour of A Highway Embankment on Stone Column Improved Estuarine Clay." Proceedings of 16th Southeast Asian Geotechnical Conference, Malaysia. Vol. 1, 567-572

Oh, E. Y. N., C. Surarak, A. S. Balasubramaniam and M. Huang (2007b). "Observed Field Behaviour of Soft Clay Due to Embankment Loading: Case Study in Queensland, Australia." Proceedings of 16th Southeast Asian Geotechnical Conference, Malaysia.

Pastor, M., O. C. Zienkiewicz and A. H. C. Chan (1990). "Generalised plasticity and the modelling of soil behaviour." Int. J. Numer. Anal. Methods Geomech 14 151-90.

Pedroso, D. M., M. M. Farias and T. Nakai (2005). "An interpretation of subloading tij model in the context of conventional elastoplasticity theory." Soils and Foundations 45(4): 61-78.

Perzyna, P. (1963). "The Constitutive Equations for Workhardening and Rate Sensitive Plastic Materials." Proc. of Vibrational problems, Warsaw 4(3): 281-290.

Pitts, J. (1983). "The origin, nature and extent of recent deposits in Singapore." Proc. int. Seminar, Construction Problems in Soft Soils: 1-18.

Prasad, K. N., B. S. Murthy, A. Vatsala and T. Sitharam (1998). "Yielding of sensitive clays: micromechanical considerations " In: Canadian Geotechnical Journal 35(01): 169-174.

Raithel, M., H. G. Kempfert and A. Kirchner (2002). Geotextile-Encased Columns (GEC) for Foundation of a Dyke on very Soft Soils. Proc. 7th Intern. Conf. On Geosynthetics, Nizza.

Rosco, K. H. and J. B. Burland (1968). "On the generalized stress-Strain Behaviour of 'wet ' clay." Engineering plasticity: 535-609.

Rowe, R. K., C. T. Gnanendran, A. O. Landva and A. J. Valsangkar (1996). "Calculated and observed behaviour of a reinforced embankment over soft compressible soil." Canadian Geotechnical Journal 33(2): 324-338.

Santagata, M. C. and J. T. Germaine (2005). "Effect of OCR on Sampling Disturbance of Cohesive Soils and Evaluation of Laboratory Reconsolidation Procedures." Canadian Geotechnical Journal 42(2): 459-474.

Schofield, A. N. and C. P. Wroth (1968). "Critical State Soil Mechanics." McGraw Hill, Maidenhead.

Shogaki, T. (2006). "Microstructure, Strength, and Consolidation Properties of Ariake Clay Deposits Obtained from Samplers." Journal of ASTM International 3: 7.

Suzuki, Y. (1982). "Deep chemical mixing method using cement as hardening agent." Proceedings of the International Symposium on Soil and Rock Improvement Techniques Including Geotextiles, Reinforced Earth and Modern Piling Methods. Bangkok, Balkema Publishers,Rotterdam.

Thevanayagam, S. and S. Mohan (2000). "Intergranular state variables and stressstrain behaviour of silty sands." Geotechnique 50(1): 1-23.

Watts, K. S. and C. J. Serridge (2000). "A trial of vibro bottom-feed stone column treatment in a soft clay soil." Proc 4th Int Conf on Ground Improvement Geosystems - grouting- soil improvement and geosystems including reinforcement, Helsinki.

Wood, C. W., S. B. Marshall and M. L. Cabrera (2000). "Improved method for field-scale measurement of ammonia volatilization." Communications in soil science and plant analysis 31(5&6): 581- 590.

Wood, C. W. and D. E. Pettry (1989). "Initial pedogenic progression in a drastically disturbed prime farmland soil." Soil Science 147(3): 196-207.

Wood, D. M., K. BeLKHEIR and D. F. Liu (1994). "Strain softening and state parameter for sand modelling." Geotechnique 44(2): 335-339.

Wu, C. and H. Hao (2008). "Numerical derivation of averaged material properties of hollow concrete block masonry." Engineering Structures 30: 870-883.

Wu, C. S. and Y. S. Hong (2008a). "The behavior of a laminated reinforced granular column." Geotextiles and Geomembranes 26: 302-316.

Wu, C. S. and Y. S. Hong (2008b). "Laboratory tests on geosynthetic-encapsulated sand columns " Geotextiles and Geomembranes 27: 107-120.

Xie, K.-H., M.-M. Lu and G.-B. Liu (2009). "Equal strain consolidation for stone columns reinforced foundation." International Journal for numerical and analytical method in geomechanics 33: 1721-1735.

Yamamuro, J. A. and P. V. Lade (1998). "Steady-state concepts and static liquefaction of silty sands." Journal of Geotech. Geoenviroment engineering 124(9): 868-877.

Yan, S. W. and H. Chen (1986). "Mechanism of vacuum preloading method and the numerical method." Chinese Journal of Geotechnical Engineering 8(2): 35-44.

Zhang, R. and S.-C. R. Lo (2008). "Analysis of Geosynthetic Reinforced Stone Columns in Soft Clay " Geosynthetics Asia 2008 Proceedings of the 4th Asian Regional Conference on Geosynthetics in Shanghai, China

Zienkiewicz, O. C. and R. L. Tayler (1987). "The finite element method." McGraw-Hill book company.